Thermoelectric transport properties of nanostructured FeSb2 and Ce-based heavy-fermions CeCu6 and CeAl3

Author: Mani Raj Pokharel

Boston College

The Graduate School of Arts and Sciences

Department of Physics

THERMOELECTRIC TRANSPORT PROPERTIES OF NANOSTRUCTURED $FeSb_2$ AND Ce-BASED HEAVY-FERMIONS $CeCu_6$ and $CeAl_3$

a dissertation

by

Mani R. Pokharel

submitted in partial fulfillment of the requirements

for the degree of

Doctor of Philosophy

January 2015

Abstract

Title: THERMOELECTRIC TRANSPORT PROPERTIES OF NANOSTRUCTURED $FeSb_2$ AND Ce-BASED HEAVY-FERMIONS $CeCu_6$ and $CeAl_3$

Author: Mani R. Pokharel

Advisor: Dr. Cyril P. Opeil, S.J.

Committee Members: Dr. Michael J. Graf, and Dr. Stephen D. Wilson

Thermoelectric (TE) energy conversion is an all-solid-state technology which can convert waste thermal energy into useful electric power and cool ambience without using harmful gases like CFC. Due to their several advantages over traditional energy conversion technologies, thermoelectric generators (TEG) and coolers (TEC) have drawn enormous research efforts. The objective of this work is to find promising materials for thermoelectric cooling applications and optimize their thermoelectric performances. Finding a material with a good value for the thermoelectric figure-of-merit (*ZT*) at cryogenic temperatures, specifically below 77 K, has been of great interest. This work demonstrates that $FeSb_2$ [1], $CeCu_6$ [2] and $CeAl_3$ [3], all belonging to a class of materials with strongly correlated electron behavior; exhibit promising thermoelectric properties below 77 K.

In general, ZT of a TE material can be increased using two basic approaches: lattice thermal conductivity reduction and power factor (PF) enhancement. The results of this study indicate that nanostructuring effectively decreases the thermal conductivity of $FeSb_2$, $CeCu_6$ and $CeAl_3$ leading to improved *ZT*. The approach of introducing point-defect scattering to further reduce the thermal conductivity is successfully implemented for Te-substituted $FeSb_2$ nanostructured samples [4]. A semiconductor/metal interface has long been proposed to exhibit enhanced thermoelectric properties. We use this technique by introducing Ag-nanoparticles in the

host $FeSb_2$ which further increases ZT by 70% [5].

Additionally, a detailed investigation is made on the phonon-drag effect as a possible mechanism responsible for the large value of the Seebeck coefficient of $FeSb_2$ [6]. We show that the phonon-drag mechanism contributes significantly to the large Seebeck effect in $FeSb_2$ and hence this effect cannot be minor as was proposed in literatures previously. A model based on Kapitza-resistance and effective medium approach (EMA) is used to analyze the thermal conductivities of nanostructured $FeSb_2$ samples [7]. We find a notably large value for Kapitza length at low temperatures indicating the dominance of inter-grain thermal resistance over bulk thermal resistance in determining the thermal properties of $FeSb_2$.

[1]Huaizhou Zhao, Mani Pokharel, Gaohua Zhu, Shuo Chen, Kevin Lukas, Qing Jie,Cyril Opeil, Gang Chen, and Zhifeng Ren, Appl. Phys. Lett. 99, 163101 (2011).

[2]Mani Pokharel, Tulashi Dahal, Zhifeng Ren, and Cyril Opeil, Journal of Alloys and Compounds 609 (2014) 228–232.

[3]Mani Pokharel, Tulashi Dahal, Zhensong Ren, Peter Czajka, Stephen Wilson, Zhifeng Ren, and Cyril Opeil, Energy Conversion and Management, 87 (2014) 584-588.

[4]Mani Pokharel, Machhindra Koirala, Huaizhau Zhao, Zhifeng Ren, and Cyril Opeil, J. Low Temp. Phys., 176 (2014) 122–130.

[5]Mani Pokharel, Huaizhou Zhao, Shuo Chen, Kevin Lukas, Hui Wang, Cyril Opeil1, Gang Chen, and Zhifeng Ren, Nanotechnology 23 (2012) 505402.

[6]Mani Pokharel, Huaizhou Zhao, Kevin Lukas, Bogdan Mihaila, Zhifeng Ren, and Cyril Opeil, MRS Communications 3 (2013) 31-36.

[7]Mani Pokharel, Huaizhau Zhao, Zhifeng Ren, and Cyril Opeil, International Journal of Thermal Science, 71 (2013) 32-35.

Table of Contents

Dedication

To my late father Dilli Ram Pokharel.

Quotation

A happy family is but an earlier heaven.

(George Bernard Shaw)

Acknowledgements

I would like to take this opportunity to express my gratitude to all those who helped me throughout the process which brought this thesis project to fruition. First of all, my sincere thanks go to my advisor Fr. Cyril P. Opeil, S.J. for giving me an opportunity to do research in his laboratory and also for supporting, guiding and encouraging me during my graduate years at Boston College.

Secondly, I would like to express my sincere thanks to Prof. Michael Graf and Prof. Stephen Wilson for their kindness in agreeing to participate on my dissertation committee and for their valuable guidance and suggestions throughout this work.

I would also like to express my thanks to Prof. Zhifeng Ren and his group members Dr. Huaizhou Zhao, Mr. Machhindra Koirala and Mr. Tulashi Dahal for their continuous collaborative support.

I would like to extend acknowledgement to my colleagues, especially Dr. Kevin Lukas, for teaching me many experimental skills and for being a source of inspiration for my work. Mr. Mengliang Yao and Mr. Nawa Raj Dahal have been fantastic friends and colleagues for years.

To my friends at Boston College Binod Rizal, Chetan Dhital and Sovit Khadka for their wonderful company while sipping caffeine.

Finally and most importantly, I would like to thank my wife Nirmala Ojha and daughters Anima and Ashmi for their love, support, and patience throughout my graduate years.

Mani R Pokharel

List of Figures and Tables

Chapter 1

Chapter 2

Chapter 3

Chapter 4

Chapter 5

Chapter 1: Introduction to Thermoelectricity

1.1 Introduction

Thermoelectricity involves a fundamental interplay between the electronic and thermal properties of a system. These effects are most often observed by measuring electrical quantities like voltage and current induced by thermal gradients. Although the thermoelectric phenomena were observed by Peltier as early as18^{th} century, renewed interest in the recent decades is due to the potential application of these phenomena in solid state energy conversion. The demand for energy resources in a modern world, particularly fossil fuels increases as the populations rise. . Simultaneously, increased population results in the emission of harmful gases like carbon dioxide, and chlorofluorocarbons etc., which contribute to the problem of global warming. In order to alleviate this problem for future generations some technological innovations will be necessary. Direct solid-state conversion between thermal and electrical energy could be part of the solution to the approaching crisis in our demand for future energy. In this chapter the three fundamental thermoelectric principles will be introduced: the Seebeck effect, the Peltier effect and the Thomson effect. The factors affecting the efficiency of thermoelectric energy conversion, specifically material properties, will be discussed.

1.2 Basic Thermoelectric Phenomena

1.2.1The Seebeck Effect

In 1821, Thomas Seebeck discovered a phenomenon in which a voltage develops

when two different conductors are joined together and the junction is heated [1-4] as shown in Figure 1.1. For a pair of metals (semimetals or semiconductors) as depicted in Figure 1.1, the thermal emf ΔV is given by,

$$\Delta V = (S_A - S_B)\,\Delta T = S_{AB}\,\Delta T \qquad (1.1)$$

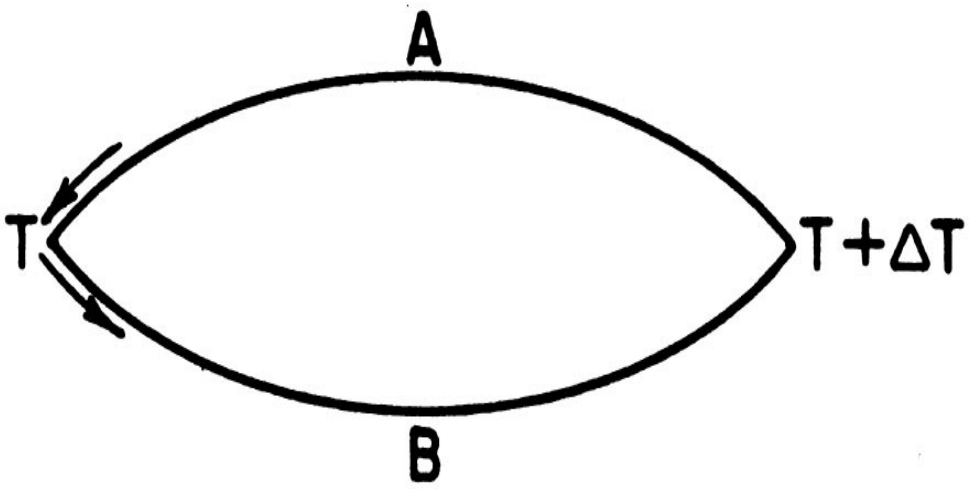

Figure 1.1 A junction is formed by using two dissimilar metals A and B. When the junction is heated an amount □T, a thermal emf is developed across the junction at the left.. Figure was taken from reference [5].

The quantity S_{AB} is called the relative Seebeck coefficient and is the difference between absolute Seebeck coefficients of the two materials A and B. The ΔT in Fig. 1.1 is the temperature difference between hot and cold ends. Although the Seebeck coefficient becomes apparent at junctions, it is essentially a property of bulk material. A Seebeck voltage develops in a single bulk material when its two ends are kept at different

temperatures as shown in Figure 1.2. For a single bulk material, the relation for the Seebeck coefficient is given as,

$$\Delta V = S\,\Delta T \tag{1.2}$$

where S is the absolute Seebeck coefficient of the bulk material, where ΔT represents the temperature difference along the sample . Polarity of the Seebeck voltage depends upon whether the bulk material has electron (n) or hole (p) charge carriers, normally referred to n-type or p-type materials (Figure 1.2).

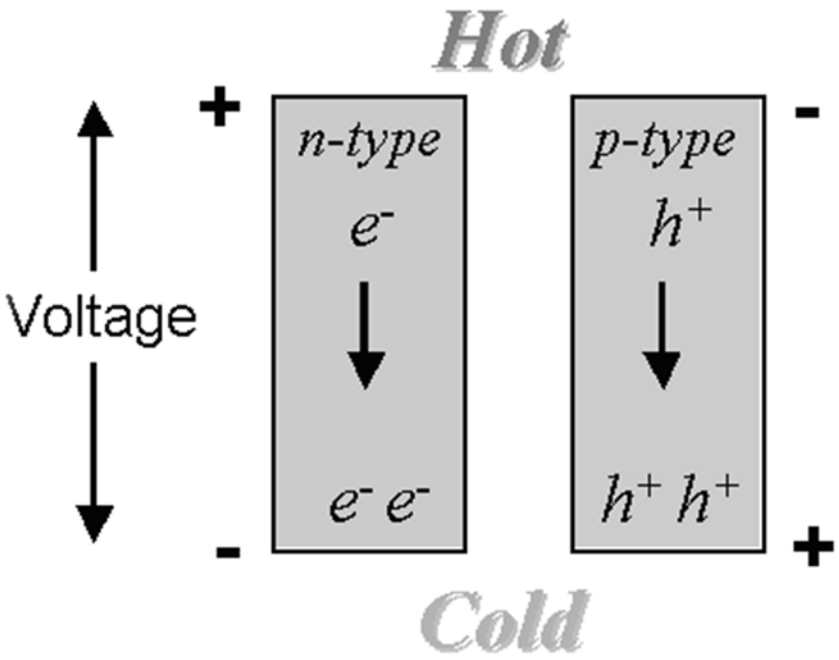

Figure 1.2 Both n-type and p-type thermoelectric materials are subject to a thermal gradient. In both the materials majority carriers (electrons: e- and holes: h+) flow from hot to cold side but the sign of induced Seebeck voltage is different.

Generation of the Seebeck voltage in a material is due to the difference in carrier energy (entropies) at hot and cold ends. At the hot end, the energy of carriers is higher

with higher carrier density above Fermi level [6]. This will cause a net diffusion of carriers from the hot to the cold side until there is a sufficiently large electric field generated to stop the further diffusion. The density and energy of carriers at two ends of the material with temperature gradient is shown in Figure 1.3.

The most common application of the Seebeck effect is in thermoelectric thermometry *i.e.* thermocouples, where the induced thermoelectric emf is used to measure temperature. This same principle can be used to produce a useful electrical output wherever there is a thermal differential and the material possesses a significant Seebeck coefficient.

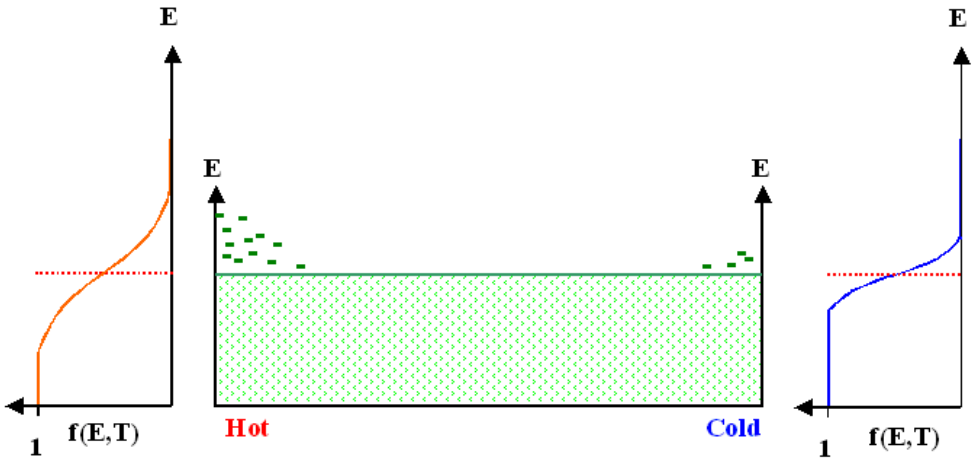

Figure 1.3 Schematic diagram showing density of states (DOS) at hot and cold ends of a thermoelectric material. The shape of the DOS at each end changes due to the temperature differential. Picture is taken from reference [7].

1.2.2 The Peltier Effect

In 1834, the French scientist, Jean-Charles Peltier discovered a reverse effect of the Seebeck effect in which, when an electric current passes through the junction between two different conductors, heat is liberated or absorbed across that junction depending upon the direction of the current flow [8]. A thermodynamic circuit demonstrating this effect is shown below in Figure 1.4. This effect is quantified by Peltier coefficient (π_{AB}). For a pair of material as shown in Figure 1.4, π_{AB} is given by the relation,

$$\pi_{AB} = \pi_A - \pi_B \tag{1.3}$$

Here π_A and π_B are absolute Peltier coefficients (equivalent to entropies) of the two conductors A and B respectively. Thus, the Peltier effect (like Seebeck effect) arises as a result of the entropy difference between the components of the junction [5]. The rate of heating or cooling (Q) at one of the junctions when an electric current I passes around the circuit is related to the Peltier coefficient, $\pi_{AB,}$ as

$$\pi_{AB} = \frac{Q}{I} \tag{1.4}$$

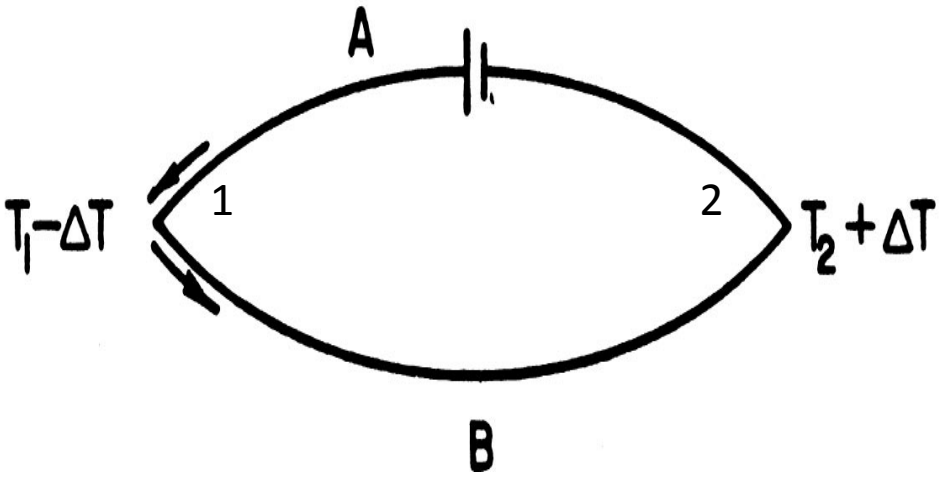

Figure 1.4 Thermoelectric circuit connecting two dissimilar metals A and B. An external electrical source drives a current through the circuit which causes liberation of heat at one junction and absorption at the other [5].

π_{AB} is regarded as positive if junction 1 becomes heated and junction 2 becomes cooled when the electric current in A passes from 1 to 2 [9].

1.2.3 The Thomson Effect

In 1851, W. Thomson established a relationship between the Seebeck coefficient and Peltier coefficient predicting a third thermoelectric phenomenon called the Thomson Effect [10-13]. In this effect, when a current carrying conductor is subjected to a temperature gradient, the conductor absorbs or emits heat as shown in Figure 1.5. This effect is quantified by the Thomson coefficient (τ). For a conductor carrying a current *I*, Thomson coefficient (τ) is defined as,

$$\tau = \frac{dq/dx}{I\ dT/dx} \tag{1.5}$$

where *dq/dx* is the rate of heating per unit length and *dT/dx* is the temperature gradient.

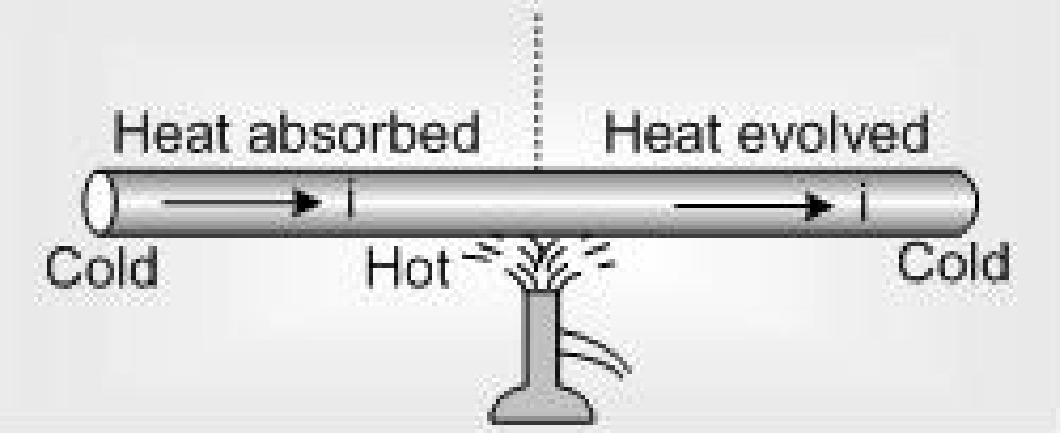

Figure 1.5 A demonstration of the Thomson Effect where a temperature gradient across a current carrying conductor causes heat absorption and a current evolution in the conductor.

The absorption or emission of heat depends on the direction of flow of electrical carriers with respect to a temperature gradient [5]. The carriers absorb heat when they are flowing in a direction opposite to a thermal gradient, and when flowing in the same direction as a thermal gradient, they liberate heat.

1.2.4 Kelvin Relations

The Thompson effect combines the Seebeck and Peltier coefficients by the Thompson -Kelvin relations. For a pair of materials A and B as explained above, these relationships are

$$\tau_A - \tau_B = T\frac{dS_{AB}}{dT} \tag{1.6}$$

and

$$\pi_{AB} = S_{AB}\,T \tag{1.7}$$

From an experimental point of view the Seebeck coefficient can be measured directly and hence is more readily determined than the Peltier coefficient. The second Thompson - Kelvin relation, Equation 1.7, is important in the sense that it shows the Peltier coefficient can be determined by measuring the Seeback coefficient.

1.3 Thermoelectric Generation (TEG) and Thermoelectric Cooling (TEC)

As mentioned previously, although the principle of thermoelectric phenomena was discovered in the 18th century, significant research in thermoelectricity and its applications started only after 1950 when Iofee [14] pointed out that semiconductors can be used as alternatives to the traditional power generation and refrigeration processes. Thermoelectric phenomenon can be used either to generate electrical power (thermoelectric generators (TEG)) utilizing waste heat or to pump heat for cooling (thermoelectric coolers (TEC)) below ambient temperatures [15-16].

Figure 1.6 shows typical model sketches for both the TEG and TEC. To improve efficiency, a *p*-type thermoelectric material is coupled with an *n*-type. By pairing the materials, the thermoelectric emfs are added and the conversion efficiency of the module increases. The majority carriers both in *n*-type (electrons) and *p*-type (holes) materials flow in the same direction to effectively increase the current. In the cooling mode (Figure 1.6 (a)), the carriers take heat away from the top end and dump it to the lower end which results in cooling at the upper end. In the power generation mode (Figure 1.6 (b)), the majority carriers get energy from the hot end and diffuse towards the cold end. The Seebeck voltage developed across the two legs (*n*- and *p*-type) add up resulting in a net electric current in the circuit.

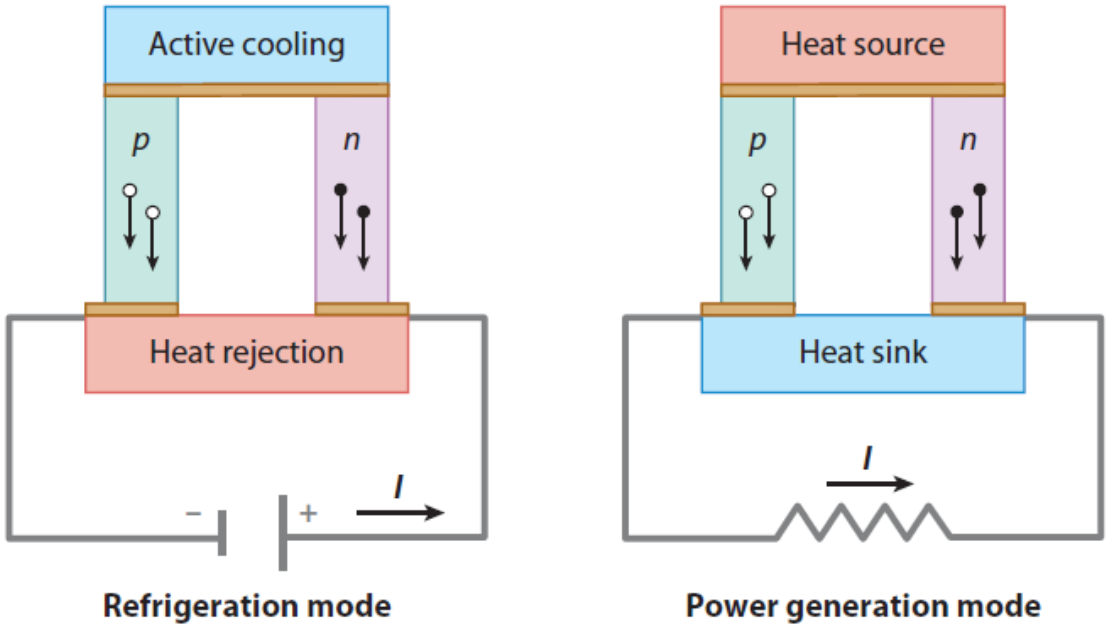

(a) (b)

Figure 1.6 Model sketches for thermoelectric cooling (a) and thermoelectric power generation (b) modes using a pair of *n*-type and *p*-type materials. Red represents hot and blue represents cold temperatures (From reference [17]).

Thermoelectric converters (TEG and TEC) have the potential to be quite useful to solve the problem of energy-crisis. Since the majority of the waste energy is in the form of heat, TEGs can be used to recover that waste heat to produce useful electrical output. Specifically, utilizing the waste heat from automobile exhaust, heat generated by industrial furnaces (*e.g.* iron smelting) and geothermal sources could significantly boost clean energy production in the world. For this reason, recently large investments have been made in research on thermoelectric materials which can be used in power generation applications [18]. The progress made to improve the thermoelectric performance of new

materials can be found in several review articles [19-21]. Presently, due to low efficiency, thermoelectric generators are available only in niche applications, the most well-known being for deep space missions [18, 22]. On the other hand, the TECs based on Peltier effect can be used for cooling below ambient temperatures without using the harmful gases like CFCs. Presently there are several commercially available TE cooling devices employed in electronics, lasers, and even small household refrigerators [23].

Thermoelectric energy conversion has several advantages over conventional electric generators and refrigerators. They are economically friendly, can be of compact size, contain no moving parts, are more accurate and have low production cost. Despite these advantages, thermoelectric devices are not yet able to replace the conventional generators or refrigerators due to low energy conversion efficiency and the slow pace of technological innovation.

1.4 Thermoelectric Figure-of-merit

The efficiency of a TE generator (η) and coefficient of performance (ϕ) of a TE refrigerator (as shown in Figure 1.6) are given by the expressions [5],

$$\eta = \frac{\frac{\Delta T}{T_h}(\sqrt{1+ZT}-1)}{\sqrt{1+ZT}+\frac{T_C}{T_H}} \tag{1.8}$$

$$\phi = \frac{T_C}{T_H - T_C}\frac{(\sqrt{1+ZT}-\frac{T_H}{T_C})}{\sqrt{1+ZT}+1} \tag{1.9}$$

where T is the average temperature, T_C and T_H are the temperatures of the cold and hot reservoirs, respectively. The quantity ZT is called dimensionless figure-of-merit and for a single material it is defined as,

$$ZT = \left(\frac{S^2 \sigma}{\kappa} \right) T \tag{1.10}$$

Here S is the Seebeck coefficient, σ is the electrical conductivity and κ is the total thermal conductivity of the material. The numerator $S^2\sigma$ is also referred as the power factor (PF). From the equations (1.8) and (1.9), it is apparent that both η and ϕ depend directly on ZT. In fact, the ZT-dependent η and ϕ relations for a given ΔT have been calculated [17]. Figure 1.7 shows the ratio of thermoelectric efficiency ($\eta_{TE)}$ to Carnot efficiency (η_C) as a function of ZT. As ZT increases, so does the η and ϕ. While the temperature gradient ($\Delta T = T_H - T_C$) also effects the quantities η and ϕ, the primary focus of thermoelectric research community at present is to find a material with large ZT.

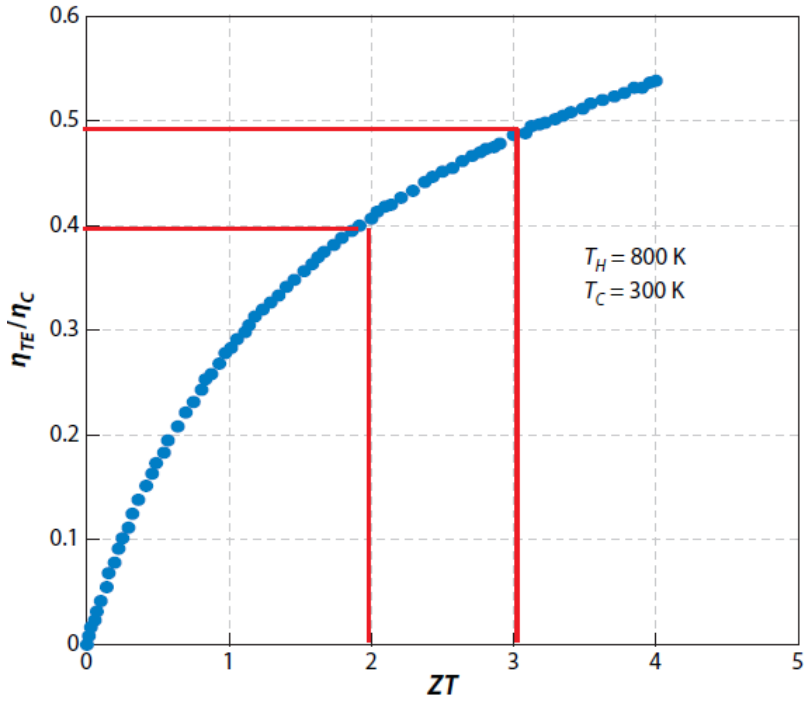

Figure 1.7 Ratio of thermoelectric efficiency to Carnot efficiency as a function of *ZT*. The figure is taken from reference [17].

The dimensionless figure-of-merit (*ZT*) is material dependent. Also different materials exhibit their optimum *ZT* at different temperatures. Figure 1.8 shows several of the highest performing TE materials with their maximum *ZT* at operating temperatures. The time evolution of *ZT* values in the past few decades is also presented.

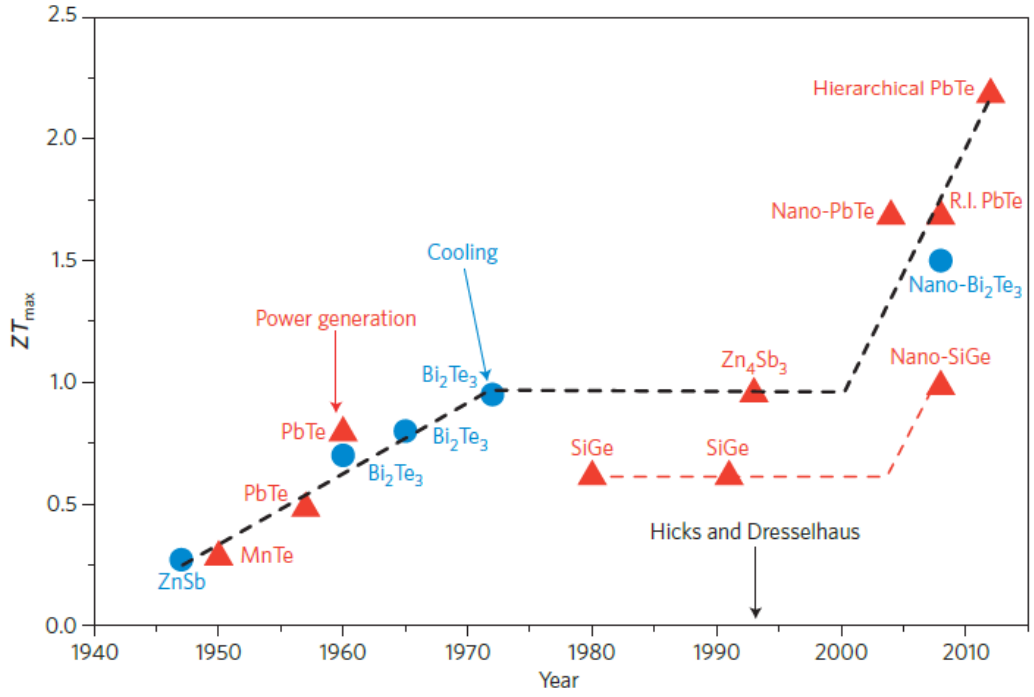

Figure 1.8 Maximum ZT values of some of the best TE materials and evolution of ZT over time in past few decades. Blue dots stands for materials suitable for cooling and red triangles stand for materials suitable for power generation. (From reference [19])

To be commercially competitive a *ZT* value of 3 is desirable while the present state-of-art materials possess only a ZT of ≈ 2 at their operating temperature near or above room temperature. At cryogenic temperatures (77 K), however, the maximum values of *ZT* are around 0.5. This is due, in part, to the reason that most thermoelectric research has focused on power generation applications rather than cooling applications. In this context, we strongly believe that more rigorous and more extensive research efforts in low temperature thermoelectrics are required. This thesis is the result of several of the research efforts to investigate several thermoelectric materials for cryogenic

cooling applications.

References

1. T. J. Seebeck, Ueber den magnetismus der galvenische kette, Abh. K. Akad. Wiss. Berlin, **289** (1821).
2. T. J. Seebeck, Magnetische polarisation der metalle und erze durck temperatur-differenz, Abh. K. Akad. Wiss. Berlin, **265** (1823).
3. T. J. Seebeck, Ann. Phys. (Leipzig), **6**, 1, (1826).
4. T. J. Seebeck, Methode, Platinatiegel auf ihr chemische reinheit durck thermomagnetismus zuprufen, Schweigger's J. Phys., **46**, 101 (1826).
5. CRC Handbook of Thermoelectrics, Edited by D. M. Rowe, CRC Press, Boca Raton (1995).
6. C. Kittel, Introduction to Solid State Physics, Wiley (1996).
7. K.C. Lukas, Ph. D. Thesis, Boston College (2010).
8. J. C. Peltier, Ann. Chim. LV, **1**, 371 (1834).
9. H. J. Goldsmid, Semiconductor and Semimetals, Vol **69**, Chap 1
10. W. Thomson, An account of Carnot's theory of the motive power of heat, Proc. R. Soc. Edinburgh, **16**, 541 (1849).
11. W. Thomson, On a mechanical theory of thermo-electric currents, Philos. Mag., **3**, 529, (1852).
12. W. Thomson, Account of researches in thermo-electricity, Philos. Mag. **8**, 62, (1854).

13. W. Thomson, On the electrodynamic qualities of metals, Philos. Trans. R. Soc. London, **146**, 649, (1856).

14. A. F. Ioffe, Semiconductor Thermoelements and Thermoelectric Cooling, Infosearch, London (1957**)**.

15. C.J. Vineis, A. Shakouri, A. Majumdar, et al., Nanostructured thermoelectrics: big efficiency gains from small features, Advanced Materials (Weinheim, Germany) **22** (36), 3970– 3980 (2010).

16. L.E. Bell, Cooling, heating, generating power, and recovering waste heat with thermoelectric systems, Science (New York, NY) **321** (5895), 1457–1461 (2008).

17. T. M. Tritt, Annu. Rev. Mater. Res. **42**, 433-448 (2011).

18. D. M. Rowe (Ed.) CRC Handbook of Thermoelectrics, CRC Press, Boca Raton (1995).

19. J. P. Heremans, M. S. Dresselhaus, L. E. Bell and D. T. Morelli, Nature Nanotechnology, **8** (2013).

20. G. J. Snyder and E. S. Toberer, Nature Materials, **7** (2008).

21. Z. G. Chen, G. Han, L. Yang, L. Cheng, and J. Zou, Progress in Natural Science: Materials International, 22 (6): 535 – 549 (2012).

22. D. M. Rowe, Proc. VIIIth Int. Conf. Thermoelectric Energy Conversion, France **133** (1989).

23. H. J. Goldsmid, Thermoelectric Refrigeration, Plenum Press, New York (1964).

Chapter 2: The Theory of Thermoelectric Transport

2.1 Introduction

Systematic research to find thermoelectric materials with high efficiency involves the study of transport parameters, the Seebeck Coefficient (S), electrical conductivity (σ), and thermal conductivity (k) in terms of more fundamental properties such as band gap (E_g), carrier concentration (n), mobility (μ) and effective mass (m^*). The thermoelectric conversion efficiency of a material is quantified by the dimensionless quantity "ZT". Improving ZT of bulk materials is complex due to the interrelation among σ, S, and k. Under one band model [1], one can write $\sigma = ne\mu$ so that ZT given in equation 1.10 can be expressed as,

$$ZT = (S^2 n)e\left(\frac{\mu}{\kappa}\right)T \tag{2.1}$$

Here e is the electronic charge. The two quantities in brackets are counter-indicated. For instance, n can be increased by adding more carriers to the system, but at the same time the Seebeck coefficient decreases. Additionally, increased mobility of the carriers not only increases the electrical conductivity but also increases the thermal conductivity particularly if the electronic component of thermal conductivity is high with respect to the phonon contribution. This scenario is expressed more clearly in Figure 2.1 where σ, S, k, and ZT vary as a function of carrier concentration (n).

Generally, heavily doped semiconductors show the most promising TE properties as indicated in Figure 2.1. As a result, the theory of thermoelectric transport is essentially the domain of transport in semiconductors. To optimize the thermoelectric performance

of a material it is desirable to have a clear understanding of the physics associated with the related parameters. In this chapter, the basic theoretical details of thermoelectric transport will be discussed.

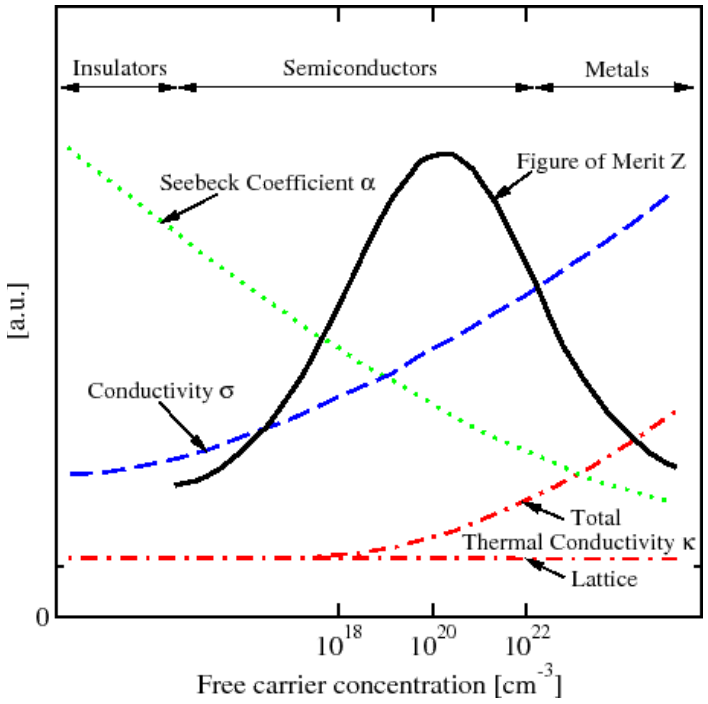

Figure 2.1 Seebeck coefficient, electrical conductivity, thermal conductivity, and figure-of-merit as a function of free carrier concentration. (Figure taken from reference [2])

2.2 Electronic Transport

2.2.1 Electrical Conductivity

Boltzmann transport theory describes both electronic and thermal transport in the vast majority of solid materials. With the relaxation time approximation, the Boltzmann's transport equation can be written as [3],

$$\frac{\partial f}{\partial t} + \vec{v} \bullet \nabla f + q\vec{E} \bullet \frac{\partial f}{\partial \vec{p}} = \frac{f_0 - f}{\tau} \tag{2.2}$$

where f is the distribution function, E is the strength of the electric field, p is the momentum and τ is the relaxation time. The charge $q = -e$ for electrons and $q = +e$ for the holes. When the number of charge carriers becomes large, the carriers can no longer be treated as non-interacting particles and Fermi-Dirac statistics should be used. The equilibrium Fermi-Dirac distribution (f_0) is [4],

$$f_0(\vec{k}) = \frac{1}{\exp(\eta) + 1}; \qquad \eta \equiv \frac{E - \mu}{k_B T} \tag{2.3}$$

Here μ is the chemical potential and k_B is the Boltzmann constant. For an isotropic and parabolic energy band, the dispersion relation is given as [5],

$$E(\vec{k}) = \frac{\hbar^2 (k_x^2 + k_y^2 + k_z^2)}{2m} \tag{2.4}$$

Assuming that there is zero temperature gradient ($dT/dr = 0$) and zero carrier concentration gradient ($d\mu/dr = 0$), and solving equations (2.2) – (2.4), one arrives to the following general expression for the electrical conductivity [3].

$$\sigma \equiv -\frac{2q^2}{3m} \int_{E=0}^{\infty} \frac{\partial f_0}{\partial E} D(E) E \tau dE \tag{2.5}$$

The quantity $D(E)$ is called the density of states. $\frac{\partial f_0(E)}{\partial E}$ is non-zero only when E is close to μ, and can be approximated to as a delta function

$$\frac{\partial f_0(E)}{\partial E} \approx -\delta(E - \mu) \tag{2.6}$$

Combine equations 2.5 and 2.6,

$$\sigma \equiv \frac{2q^2}{3m}\int_{E=0}^{\infty}\delta(E-\mu)D(E)E\tau dE = \frac{2e^2}{3m}D_{E=\mu}\mu\tau_{E=\mu} = \frac{2q^2}{3m}D_F\mu\tau_F \tag{2.7}$$

We can use $\mu \approx E_F = m{v_F}^2/2$ to reduce eq. 2.7 to

$$\sigma = \frac{q^2}{3}D_F{v_F}^2\tau_F \tag{2.8}$$

The charge carrier concentration can be calculated as,

$$\begin{aligned} n &= \int_{E=0}^{\infty} f_0(E)D(E)dE = \int_{E=0}^{\infty} f_0(E,T=0)D(E)dE = \int_{E=0}^{E_F} D(E)dE \\ &= \int_{E=0}^{E_F} \frac{1}{2\pi^2}\left(\frac{2m}{\hbar^2}\right)^{2/3} E^{1/2}dE = \frac{1}{3\pi^2}\left(\frac{2m}{\hbar^2}\right)^{2/3} {E_F}^{3/2} = \frac{2}{3}D_F E_F \approx \frac{2}{3}D_F\mu \end{aligned} \tag{2.9}$$

Substituting for D_F in equation 2.7 using equation 2.9, we obtain

$$\sigma = \frac{q^2}{m}n\tau_F \tag{2.10}$$

If we define mobility as,

$$\mu_q = \frac{q}{m}\tau_F \tag{2.11}$$

we obtain

$$\sigma = nq\mu_q \tag{2.12}$$

This is a general expression for electrical conductivity (used in equation 2.1) of a material. In semiconductors, both electrons and holes contribute to the electrical conductivity and the following relation should be used.

$$\sigma = n_e e\mu_e + n_h e\mu_h \tag{2.13}$$

where “e” stands for electron and “h” stands for hole.

2.2.2 Seebeck coefficient

The Seebeck coefficient is defined as the ratio between the voltage gradient and the temperature gradient for an open loop configuration with zero net current flow. In the case of non-zero temperature gradient and no current, the Boltzmann transport equation leads to an expression for the Seebeck coefficient as given below [29].

$$S = -\frac{k_B}{q}\left(\eta - \frac{\left(r+\frac{5}{2}\right)F_{r+3/2}(\eta)}{\left(r+\frac{3}{2}\right)F_{r+1/2}(\eta)}\right) \tag{2.14}$$

In the above expression, r is the scattering parameter defined by,

$$\tau = \tau_0 E^r \tag{2.15}$$

where τ_0 is a constant independent of E. The Fermi-Dirac integral $F_n(\eta)$ is,

$$F_n(\eta) = \int_0^\infty f_0(\zeta,\eta)\zeta^n d\zeta \tag{2.16}$$

and $\zeta = E/k_B T$ is the reduced energy.

For metals, q = - e and $\eta = \mu / k_B T >> 0$. In this case the Fermi-Dirac integral can be expressed in the form of a rapidly converging series and taking only the first two terms in the equation 2.14 reduces to,

$$S = -\frac{\pi^2 k_B}{3e}\left(\frac{k_B T}{\mu}\right)\left(\frac{3}{2}+r\right) \tag{2.17}$$

In non-degenerate semiconductors, μ is located within the band gap with a distance from the conduction or valence band edges larger than $3k_B T$ so that $\frac{E-\mu}{k_B T} = \zeta - \eta > 3$. In this case the Fermi-Dirac integrals become a gamma function and

we arrive at the following formula,

$$S = -\frac{k_B}{q}\left(\eta - \left(r + \frac{5}{2}\right)\right) \tag{2.18}$$

In this equation, □ is measured from the conduction band edge E_C for electrons and from the valence band edge E_v for holes. Located within the band gap, □ is negative for electrons, and is also negative for holes because the hole energy is higher when the energy level is moved further down. Also q = -e for electrons and +e for holes, so that the Seebeck coefficient is negative for electrons in the conduction band and positive for holes in the valence band.

If □ is measured from a global reference instead of the band edge as the zero energy point, we can express equation 2.18 for electrons and holes separately as follows.

$$S_e = -\frac{1}{eT}(E_c - \mu + (r + 5/2)k_B T) < 0, \qquad \text{for electrons} \tag{2.19}$$

$$S_h = \frac{1}{eT}(\mu - E_v + (r + 5/2)k_B T) > 0, \qquad \text{for holes} \tag{2.20}$$

The effective Seebeck coefficient in a nondegenerate semiconductor has a contribution coming from both electrons and holes. In this case, the total Seebeck coefficient is given by,

$$S = \frac{n\mu_e S_e + p\mu_h S_h}{n\mu_e + p\mu_h} \tag{2.21}$$

where n and p are electron and hole concentrations, respectively, and □$_e$ and □$_h$ the mobility of electrons and holes, respectively.

2.3 Thermal Transport

2.3.1 Thermal Conductivity

Thermal conductivity characterizes the heat transport in solids as electrical conductivity does in electric conduction. By definition, thermal conductivity ($\vec{k}$) is given as

$$\vec{j} = -\vec{k}(\frac{\partial T}{\partial \vec{r}}) \tag{2.22}$$

where $\vec{j}$ is the heat current density flown through the material, and $\partial T / \partial \vec{r}$ is the temperature gradient in the material. Since the heat conduction in solids is carried by carriers and lattice vibrations (phonons), the total thermal conductivity of the material is a sum of both carrier and lattice contributions.

$$\kappa_{total} = \kappa_{lattice} + \kappa_{carrier} \tag{2.23}$$

The above relation is also referred to as independent approximation in the sense that it assumes that electrons and phonons do not interact. In a semiconductor, the carrier contribution to the thermal conductivity comes from both the electrons and holes. In such a case, the total carrier contribution is given by [7],

$$\kappa_{carrier} = \kappa_e + \kappa_h + \frac{(\sigma_e \sigma_h)}{(\sigma_e + \sigma_h)}(S_e - S_h)^2 T \tag{2.24}$$

where “e” stands for electron and “h” stands for hole. The first two terms in the above equation represents independent contributions from electrons and holes. The third term represents bipolar contribution which manifests itself at temperatures near or exceeding

the energy of the band gap (E_g). At these temperatures electrons have a much higher probability of jumping from the valence band to the conduction band thereby creating electron-hole pairs, which propagate along the material and upon recombination energy is released in the form of photons.

The carrier contribution to the thermal conductivity can be derived from the Boltzmann equation. Assuming zero electric current and non-zero temperature gradient, a general expression for electronic contribution to thermal conductivity can be written as [5],

$$k_e = \frac{1}{3}\int_{E=0}^{\infty} \frac{\partial f_0(E)}{\partial T} D(E) v^2 (E-\mu)\tau dE \tag{2.25}$$

When E is far away from μ, $f_0(E)$ remains to be either 0 or 1 as the temperature changes, so that $\frac{\partial f_0(E)}{\partial T}$ is non-zero only when E is close to μ. Therefore, equation 2.25 can be approximated by taking $v = v_F$ and $\tau = \tau_F$, i.e. the Fermi velocity and the scattering mean free time of Fermi electrons,

$$k_e = \frac{1}{3} v_F{}^2 \tau_F [\int_{E=0}^{\infty} \frac{\partial f_0(E)}{\partial T} D(E)(E-\mu) dE] = \frac{1}{3} v_F{}^2 \tau_F C_e = \frac{1}{3} C_e v_F l_F \tag{2.26}$$

Here C_e is the electronic heat capacity and l_F is the electron mean free path. Equation 2.25 is essentially the kinetic theory expression of the thermal conductivity. For metals the expression 2.27 can be written [5, 6],

$$C_e = \frac{1}{2}\pi^2 n k_B T / T_F \tag{2.27}$$

In this way, the energy of the lattice vibration is quantized and the quanta are called phonons. The kinetic theory expression for the lattice contribution to thermal

conductivity of a solid can be written by the approximation [8],

$$k_{lattice} = \frac{C_v v_s l}{3} \tag{2.28}$$

Here C_v is the specific heat at constant volume, v_s is the average velocity of sound and l is the mean free path of phonons. At very low temperatures ($T << \theta_D$), where θ_D signifies the Debye temperature, the behavior of $k_{lattice}$ is dominated by the Debye T^3 law whereas at high temperatures ($T > \theta_D$), $k_{lattice}$ is primarily dominated by phonon scattering mechanisms.

2.3.2 Wiedemann-Franz law

We can use equations 2.10 and 2.26 to calculate the ratio between the electron thermal conductivity and electrical conductivity.

$$\frac{k_e}{\sigma} = \frac{\frac{1}{3} v_F{}^2 \tau_F C_e}{\frac{e^2}{m} n \tau_F} = \frac{m C_e v_F{}^2}{3ne^2} \tag{2.29}$$

Here it is assumed that τ_F (mean free scattering time of electrons) is the same for the thermal conductivity and electrical conductivity expressions. Also, equation 2.27 can be rearranged as follows,

$$C_e = \frac{\frac{1}{2}\pi^2 n k_B T}{\frac{m v_F{}^2}{2k_B}} = \frac{\pi^2 n k_B{}^2 T}{m v_F{}^2} \tag{2.30}$$

Combining equations 2.29 and 2.30, we obtain

$$\frac{k_e}{\sigma} = \frac{m v_F{}^2}{3ne^2} \frac{\pi^2 n k_B{}^2 T}{m v_F{}^2} = \frac{\pi^2 k_B{}^2 T}{3e^2} = LT \tag{2.31}$$

where

$$L = \frac{\pi^2 k_B^{\ 2}}{3e^2} = 2.45 \text{ x } 10^{-8} \text{ W}\Omega/\text{K}^2 \qquad (2.32)$$

is the Lorenz number. Equation 2.31 holds that at a given temperature the ratio of electronic thermal conductivity to electrical conductivity is constant for a metal. This relation is referred as Wiedemann-Franz Law [5] and is a valid approximation for all good metals.

2.4 Optimizing Power Factor

Enhancing the ZT (where $ZT = S^2 \square\square\square\square_{total}$) in a material can be achieved either by reducing thermal conductivity ($\square_{total} = \square_{electronic} + \square_{phononic}$) while keeping the power factor ($PF = S^2\square$) relatively unaffected or increasing the power factor without adversely effecting the thermal conductivity. Since the Seebeck coefficient and the electrical conductivity are predominately determined by the electronic band structure of the material, improving the power factor requires modification in the band structure, also referred to as "band structure engineering". Current efforts target the modification of the electronic structure in order to achieve sharp features in the density of states function and strong energy dependence in the transmission coefficients. One of the initial ideas to improve he power factor was proposed by Hicks and Dresselhaus [9]. They suggested that low dimensional materials could provide improvements in the Seebeck coefficient and the power factor due to the sharp features in their density-of-states function. Mahan and Sofo [10] have predicted that infinitely large *ZT* values could be achieved in zero-dimensional structures in the limit of zero lattice thermal conductivity. Another approach (other than reducing the dimensionality) to improve the power factor is "doping". For a

three dimensional bulk material, “doping” offers one of the easiest and most effective ways to modify band structure [1]. In the recent years “resonant doping” has become the focus of the thermoelectric research community [1, 11]. Additionally, electronic correlations have also shown to produce large power factor values in some compounds [12, 13]. In this section, some of the fundamental methods on how to improve the power factor will be discussed.

2.4.1 Mott Relation

The constituent parameters S and σ of the thermoelectric power factor ($S^2\sigma$) are all functions of carrier concentration and are interrelated with each other. It is a general rule that a rise in thermopower implies a decrease in electrical conductivity due to decrease in the carrier density. As a result, it is very difficult to simultaneously achieve an increased S and σ. Originally, Mott and Cutler [14] proposed a dependence of *S* on logarithmic derivative of σ, known as Mott formula, given by

$$S = -\frac{\pi^2}{3}\frac{k_B^2 T}{e}\left[\frac{d\ln\sigma(E)}{dE}\right]_{E=E_F} \tag{2.33}$$

The above equation can be rewritten in expanded form as,

$$S = -\frac{\pi^2}{3}\frac{k_B^2 T}{e}\left[\frac{1}{n}\frac{dn(E)}{dE} + \frac{1}{\mu}\frac{d\mu(E)}{dE}\right]_{E=E_F} \tag{2.34}$$

Equation 2.34 suggests that Seebeck coefficient can be increased by augmenting the energy dependences of carrier density and mobility. The increased energy dependence of *n* can be realized in the situations where the density of states is increased locally [1]

whereas any scattering mechanism that strongly depends on the energy of the charge carriers will increase energy dependence of the mobility [15].

2.4.2 Effective Mass and Role of Correlations

In the ground state of a system of N free electrons, the occupied energy levels of the system fill a sphere of radius [5],

$$k_F = \sqrt{\frac{2mE_F}{\hbar^2}} \tag{2.35}$$

where m is the free electron mass. However, when an electron in a periodic potential is accelerated relative to the lattice in an applied electric or magnetic field, that electron feels as if its mass were equal to an effective mass (m^*) [5]. Then m of equation 2.35 is to be replaced by m^*. For degenerate semiconductors [16], the Seebeck coefficient can be expressed in terms of effective mass m* by combining equations 2.17 and 2.35 as shown,

$$s = \frac{8\pi^2 \kappa_B^2 T}{3e\hbar^2} m^* \left(\frac{\pi}{3n}\right)^{2/3} \tag{2.36}$$

The effective mass is highly enhanced because of electron-electron interaction in strongly correlated rare–earth compounds including heavy Fermions. Since enhanced m^* leads to an increased S, the correlated systems possess a potential to be a good thermoelectric at low temperatures.

In the case of rare-earth compounds, the effective mass, $m*$, of quasi-particles is enhanced mainly due to Kondo local fluctuations around each f-electron atom [17]. A new temperature scale called characteristic Kondo temperature (T_k) appears for these compounds which scales as a function of the effective mass (m^*) [17].

$$T_k \sim \frac{1}{m^*} \tag{2.37}$$

In these compounds, not only the Kondo interaction but also the crystal electric field (CEF) excitations may generate large anomalies in $S(T)$ [18]. For a CEF level at $T_{CEF} >> T_k$, theoretical calculations predict a large thermopower with an extremum at temperature T^* [19],

$$T^* = (0.3 \ldots .).6) T_{CEF} \tag{2.38}$$

In fact, experiments [20, 21, 22] have shown that several Ce and Yb systems show deviations from a simple $S(T)$ dependence (equation 2.17) with a Kondo peak and a CEF peak reflecting Kondo scattering on the ground state and the excited CEF levels.

Although the correlations seem to enhance Seebeck coefficient, due to large effective mass the mobility of the carriers may be reduced simultaneously. As a result, the gain from Seebeck coefficient may be negated by loss in electrical conductivity. Recently, there have been some studies concluding that correlations in some materials cannot lead to an increase of ZT [23]. Nevertheless, many heavy-fermion compounds exhibit good thermoelectric power factor at the characteristic temperature T^*.

2.4.3 Phonon-drag Effect

In all of above sections, the Seebeck coefficient (S) was defined using classical theory of thermoelectricity which assumes that the flow of charge carriers and phonons can be treated independently. Under this assumption, the Seebeck coefficient arises due solely to spontaneous electron diffusion. However, when the flow of charge carriers and

phonons are linked, the effect of electron-phonon scattering should be taken into account. Hence, in general, the Seebeck coefficient is given as the sum of two independent contributions [24],

$$S_{Total} = S_d + S_p \tag{2.39}$$

where S_d is the conventional electron-diffusion part (denoted as S in the sections above) and S_p is the phonon-drag contribution. The diffusion part is caused by the spatial variation of the electronic occupation in the presence of a thermal gradient, whereas the drag part arises due to the interaction between anisotropic lattice vibrations and mobile charge carriers. Herring [24] showed that the higher than expected value of thermopower in germanium [25] as shown in Figure 2.2 and other semiconductors could be explained assuming that the carriers are preferentially scattered by the phonons toward the cold end of the sample. Thus the effective "drag" of some of the charge carriers along the thermal gradient (hence phonon-drag) gives rise to an additional thermoelectric electromotive force (emf). Because the additional emf and the emf induced by diffusion have the same sign, the overall phonon-drag effect is to increase the Seebeck coefficient. Generally, this effect becomes stronger at lower temperatures where the phonon mean free path becomes longer.

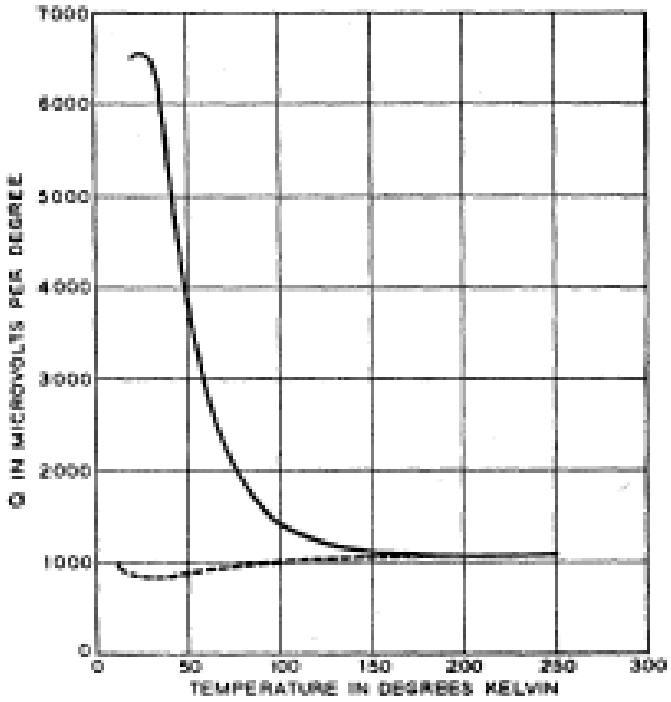

Figure 2.2 Comparison of observed thermoelectric power (|*S*|) with the theoretically predicted electronic contribution for p-type germanium with carrier density of 1.5×10^{14} cm^{-3} [7]. Solid line represents the observed values and dashed curve represents calculated contribution from diffusion part.

Following Herring [24], the phonon-drag thermopower for semiconductors, in the first-order approximation, can be written as,

$$S_p = \frac{\beta v_s \lambda_p n e}{\sigma T} \ , \tag{2.40}$$

where v_s is the velocity of sound, λ_p the mean free path of the interacting phonons, n the charge carrier density, σ the electrical conductivity, T is the absolute temperature and β is the dimensionless parameter with its value ranging from 0 to 1 depending upon the strength of the interaction. It is implied by Eq. 2.38 that a significant phonon-drag

contribution increases the total Seebeck coefficient.

Since the phonon-drag component depends directly with the mean free path of interacting phonons, an increase in S_p would essentially imply an increase in thermal conductivity. Due to this fact, phonon-drag may not be useful for a good TE material. According to Keyes *et al*. [26], the value of the figure of merit (Z_p) that can be reached using phonon drag is rather low. Based on their argument, H. J. Goldsmid [27] shows that Z_pT is less than ¼ for a bulk thermoelectric material. Ivanov *et al*. [28] reported recently a similar conclusion for low-dimensional structures.

2.5 Reducing Thermal Conductivity

The recent trend in thermoelectric research is to reduce thermal conductivity of a material without adversely affecting the power factor. This is, however, a difficult task. For instance, a large energy band gap is generally required for a good TE material to minimize the effect of the minority carriers [29]. On the other hand, usually a large energy band gap means large lattice thermal conductivity. For doped semiconductors, not only the lattice contribution but also the carrier contribution to the total thermal conductivity is large enough to be important. The present work of this thesis is mainly devoted to the efforts made to reduce the lattice thermal conductivity. Therefore, discussions to follow will mainly focus on the lattice part. To effectively reduce the lattice thermal conductivity of a material, a deeper understanding of the different scattering mechanisms involved during heat conduction is required. In the following section, we discuss different scattering mechanisms associated with the heat conduction in a material.

2.5.1 Scattering mechanisms

The physics of the lattice thermal conductivity is commonly interpreted using the Debye approximation [30],

$$\kappa_{lattice} = \frac{k_B}{2\pi^2 v}\left(\frac{k_B}{\hbar}\right)^3 T^3 \int_0^{\frac{\theta_D}{T}} \frac{\tau_c x^4 e^x}{(e^x-1)^2}\, dx \tag{2.41}$$

where $x = \frac{\hbar w}{k_B T}$, w is the frequency, k_B is the Boltzmann constant, $\hbar$ is the Planck constant, v is the speed of sound, θ_D is the Debye temperature and τ_c is the relaxation time. The overall time constant (τ_c) is given by the Matthiessen's rule,

$$\tau_c^{-1} = \tau_{defect}^{-1} + \tau_{umklapp}^{-1} + \tau_{boundary}^{-1} \tag{2.42}$$

Here τ_{defect}, $\tau_{umklapp}$ and $\tau_{boundary}$ are the relaxation times associated with the three scattering mechanisms: the phonon-defect scattering, the umklapp process and phonon-boundary scattering respectively. Different scattering processes usually dominate in different temperature ranges with different temperature dependences as shown in Figure 2.3. At high temperatures ($T \approx \theta_D$), umklapp is the dominant scattering mechanism. Boundary and point-defect scattering dominate at low and intermediate temperatures respectively.

From second order perturbation theory, the relaxation time for three phonons Umklapp scattering is given by [29],

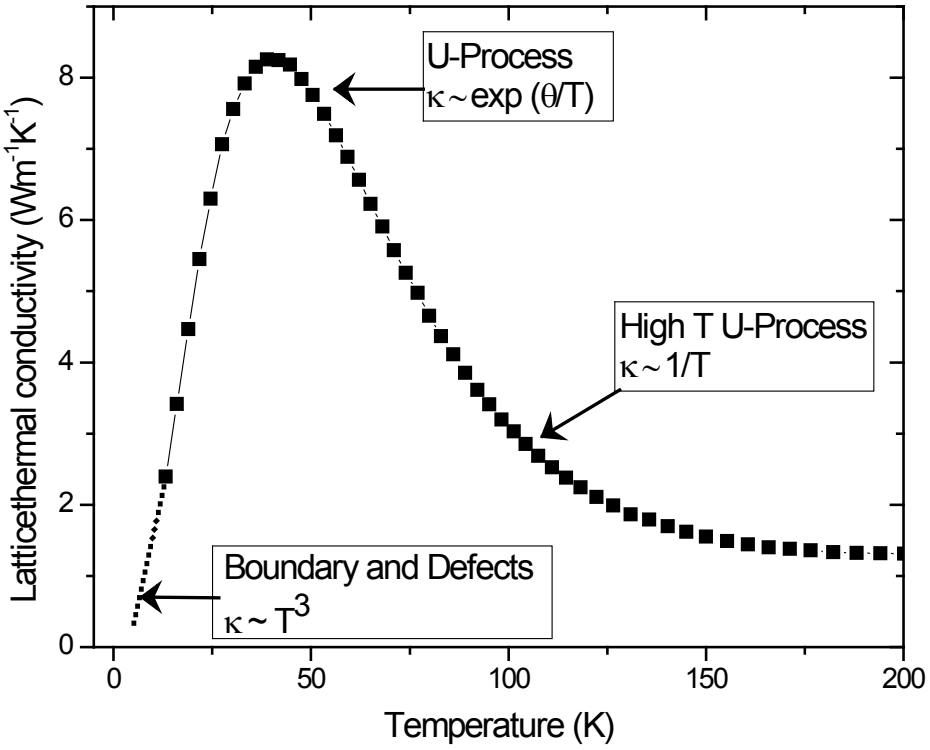

Figure 2.3 Lattice thermal conductivity as a function of temperature for ingot sample of $FeSb_2$ used in this study. The different scattering mechanisms at different temperature regions are shown.

$$\tau_{umklapp}^{-1} = 2\gamma^2 \frac{k_B T}{\mu V_0} \frac{\omega^2}{\omega_D} \tag{2.43}$$

Here γ is the Gruneisen anharmonicity parameter μ is the shear modulus and V_0 is the volume per atom and ω_D is the Debye frequency. In the case of purely diffusive scattering, the relaxation time for the boundary scattering assumes the well-known Casimir limit [29].

$$\tau_{boundary}^{-1} = \frac{\nu}{D} \tag{2.44}$$

where D is the average grain size, ν is the group velocity of the phonon. On the other hand, the defect scattering process involves the scattering of phonons by a variety of crystal defects, impurity sites and different isotopes of the host material [29]. The phonon relaxation time for this type of point defect scattering is

$$\tau_{defect}^{-1} = \frac{V_0 \Gamma \omega^4}{4\pi v^3} \tag{2.45}$$

$$\Gamma = \sum_i f_i \left[\left(1 - \frac{M_i}{M} \right)^2 + 2\left\{ 6.4\gamma \left(1 - \frac{R_i}{R} \right) \right\}^2 \right] \tag{2.46}$$

Here M_i and R_i are the mass and Pauling ionic radius of the ith impurity atom, and f_i is the fractional concentration of impurity atoms.

2.5.2 Mechanical Nanostructuring

Equation 2.44 implies that the relaxation time associated with the boundary scattering scales with the size of the grain (or crystallite). This type of scattering becomes appreciable at low temperatures where the phonon mean free paths are usually large. An ideal case for improving ZT of a thermoelectric material would be to obtain the crystallite size smaller than the phonon mean free paths (l_{phonon}) but larger than electron mean free paths (l_{electron}), i.e.

$$l_{electron} < D < l_{phonon} \tag{2.47}$$

Under above condition, the phonons are effectively scattered off the grain-boundaries

whereas electrons are not as shown in Figure 2.4. In other words, the thermal conductivity of the system decreases without affecting electronic properties (power factor). This situation is illustrated in the following figure.

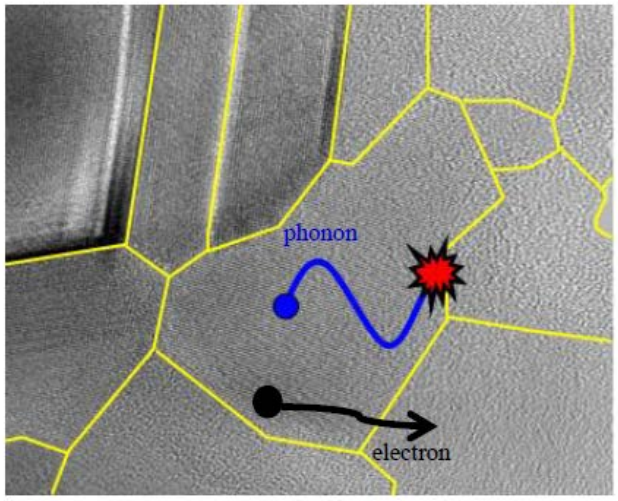

Figure 2.4 Schematic illustration of grain-boundary scattering mechanism. The long wavelength phonons (blue) are scattered off the boundaries. Figure was borrowed from Dr. Kevin Lukas and edited.

In general, electron mean free paths are of the order of few nanometers whereas the phonons mean free paths at low temperature fall in the range of microns. One of the ways to achieve the condition implied in the Eq. 2.47 is to introduce nano-sized grains in the samples using ball-milling and hot-pressing technique, usually referred as "mechanical nanostructuring". This technique utilizes a distribution of small grain sizes rather than a uniformity of grain size to suppress the thermal conductivity, because the phonon mismatch across many grain sizes and boundaries will serve to lower the overall lattice thermal conductivity.

As discussed in section 3.3, original goal of nanostructuring was to increase the power factor by employing quantum confinement of carriers [9, 31]. However, experiments [32, 33, 34] have shown that the main reason for the *ZT* improvement in several nanostructured TE materials was the reduction of thermal conductivity rather than power factor improvement.

References

1. J. P. Heremans, V. Jovovic, E. S. Toberer, A. Saramat, K. Kurosaki, A. Charoenphakdee, S. Yamanaka, and G. J. Snyder, Science **321**, 554 (2008).
2. Figure adopted from http://www.iue.tuwien.ac.at/phd/mwagner/node49.html
3. N. W. Ashcroft and N. D. Mermin, Solid State Physics, Brooks/Coles Cengage Learning, Chapter 16 (1976).
4. R. K. Pathria, Statistical Mechanics, Butterworth-Heinemann, 2nd Edition, Chapter 8 (1996).
5. C. Kittel, Introduction to Solid State Physics, John Wiley and Sons, 7th Edition, Chapter 6 (1996).
6. D. M. Rowe, Thermoelectrics Handbook: Macro to Nano , Taylor & Francis, New York (2006).
7. G. S. Nolas, J. Sharp, and H. J. Goldsmid, Thermoelectrics: Basic Principles and New Materials Developments, Springer (2001).
8. T. M. Tritt, Thermal Conductivity Theory, Properties, and Applications, Kluwer Academic/ Plenum Publishers, New York (2004).
9. L.D. Hicks, M. S. Dresselhaus, Phys. Rev. B, **47**, 16631 (1993).
10. G. D. Mahan, J. O. Sofo, Proc. Natl. Acad. Sci. USA, **93**, 7436-7439 (1996).

11. Q. Zhang, H. Wang, W. Liu, H. Wang, B. Yu, Q. Zhang, Z. Tian, G. Ni, S. Lee, K. Esfarjani, G. Chen and Z. F. Ren, Energy Environ. Sci., **5**, 5426 (2012).
12. G. D. Mahan, Solid State Physics, **51**, 81 (1998).
13. A. Bentien, S. Johnson, G.K.H. Madsen, B.B. Iversen and F. Steglich, EPL, **80**, 17008 (2007).
14. N. Cutler, and N. F. Mott, Phys. Rev., **181**, 1336 (1969).
15. J.M. Ziman, Electrons and Phonons, Oxford, Cambridge (1960).
16. G. J. Snyder, and S. Toberer, Nature materials, **7**, 105 (2008).
17. K. Behnia, D. Jaccard and J. Flouquet, J. Phys.: Condens. Matter **16**, 5187–5198 (2004).
18. U. K¨ohler, Thermoelectric transport in rare-earth compounds, der Fakult¨at Mathematik und Naturwissenschaften der Technischen Universit¨at Dresden (1977).
19. V. Zlatić, A. C. Hewson, Properties and Applications of Thermoelectric Materials: The Search for New Materials for Thermoelectric Devices, Springer (2009).
20. P. Paschen: Thermoelectric Handbook, chapter 15, ed. D. M. (CRC Press, Taylor and Francis, Boca Raton, FL (2006).
21. G. Sparn, W. Lieke, U. Gottwick, F. Steglich, and N. Grewe, J. Magn. Magn. Mater **47**, **48**, 521-523 (1985).
22. Amato D. Jaccard, J. Sierro, F. Steglich, and N. Grewe, J. Magn. Magn. Mater **76**, **77**, 263-264 (1988).
23. M. K. Fuccillo, Q. D. Gibson, Mazhar N. Ali, L. M. Schoop, and R. J. Cava, APL Materials **1**, 062102 (2013).

24. C. Herring, Phys Rev **96**, 5 (1954).

25. T. H. Geballe, and G. W. Hull, Phys. Rev. **94**, 5 (1954).

26. R. W. Keyes, Thermoelectricity: Science and Engineering, Interscience, New York, p. 389 (1961).

27. H. J. Goldsmid, Introduction to Thermoelectricity, p. 41 (2010).

28. Y. U. V. Ivanov, Thermoelectric Handbook: Macro to Nano, CRC Taylor and Francis, Boca Raton, p. 18-19 (2006).

29. CRC Handbook of Thermoelectrics, Edited by D. M. Rowe, CRC Press, Boca Raton (1995).

30. J. Callaway: Model for lattice thermal conductivity at low temperatures. Phys. Rev. **113**, 1046 (1959).

31. L. D. Hicks and M. S. Dresselhaus, Phys. Rev. B, **47**, 12727 (1993).

32. . R. Venkatasubramanian, E. Silvola, T. Colpitts, and B. O'Quinn, Nature, **413**, 597-602 (2001).

33. T. C. Harman, P. J. Taylor, M. P. Walsh, and B. E. LaForge, Science, **297**, 2229-2232 (2002).

34. K. F. Hsu, S. Loo, F. Guo, W. Chen, J. S. Dyck, C. Uher, T. Hogan, E. K. Polychroniadis, and M. G. Kanatzidis, Science, **303**, 818-821 (2004).

Chapter 3: Sample Preparation and Measurement

3.1 Introduction

In this chapter an overview of different experimental techniques e.g. TE sample preparation and characterization, utilized throughout this study are presented. Sections 3.2 and 3.3, describe the preparation techniques for stoichiometric sample ingots and how nanostructured sample pellets were produced.. In section 3.4, material characterization methods are reviewed. Section 3.5 discusses the theory of operations for a cryogenic refrigerator, a Physical Properties Measurement System (PPMS) manufactured by Quantum Design, where most of the measurements for this thesis were made. Since the details of the theory of operation of PPMS are given in reference [1-3], only a brief overview will be presented. In section 3.6, details on a home-built ac magnetic susceptometer will be given.

3.2 Ingot Preparative Methods

A diverse array of methods is available to synthesize solid compounds and metallic alloys. Some details of the synthesis methods employed in this thesis will be given below. Further reference information on synthesis methods can be found in the literature [4, 5, 6]. Some of the most important factors to be taken into account during synthesis are: purity of the starting materials, proper stoichiometric quantities, ensuring that the reaction has gone to completion, homogenization of the sample and creating a good vacuum in the quartz ampule to avoid oxidation states in the starting materials/sample. The ingot samples used for this thesis were prepared by two methods (quartz tube and arc melting) and will be discussed in the following sections.

3.2.1 Melt-quenching Method

The ingots of $FeSb_2$ samples used for this work were prepared by direct melting of the constituent elements in a furnace followed by quenching [7, 8] in water or liquid nitrogen. In this method, the pure starting elements with appropriate atomic percentages are loaded inside a quartz tube which has been sealed at one end by a hydrogen/oxygen torch. Nominally, the diameter of a typical quartz tube was ½" or ¾" depending on the volume of sample material under consideration. The contents of the quartz tube were initially stoppered using an ultra-torr vacuum fitting and a needle valve assembly to perform the initial pump-down. Using a turbo pump the tube and the valve assembly

(a)

(b)

(c) (d)

Figure 3.1 Shown here are the different steps and essential apparatus for material synthesis using the quart tube method. (a) A quartz tube with stoichiometric mixture of elements ($FeSb_2$) being evacuated to 10^{-6} mbar. (b) A sealed quartz tube sealed for the furnace. Hydrogen/oxygen torch was used to melt and seal quartz tube at low pressure. (c) Horizontal tube furnace for melting materials. (d) Sample ingot obtained from this process.

were pumped to the vacuum level of ~ 10^{-6} mbar (shown in Figure 3.1 (a)) and sealed (Figure 3.1 (b)). The sealed quartz tube is heated in a furnace (Figure 3.1 (c)) to a temperature to melt the components and consistent with the desired phase of the material. The quartz tube is gently shaken during the melt to improve the sample mixing/homogeneity. The molten samples were then rapidly quenched in cold water. Figure 3.1 (d) shows a typical ingot sample which resulted from this process.

For $FeSb_2$, Fe (99.9%, Alfa Aesar) and Sb (99.9% Alfa Aesar) metal chunks with the molar ratio of 1:2 were inserted in a 1/2 inch quartz tube and the steps explained in the above paragraph were followed.

The binary phase-diagram for the Fe-Sb system is as shown in the Figure 3.2 below. The ingot sample of $FeSb_2$ used in this work was prepared by heating a sealed quartz tube up to 1050 ^{o}C for 5 hrs with intermittent stirring.

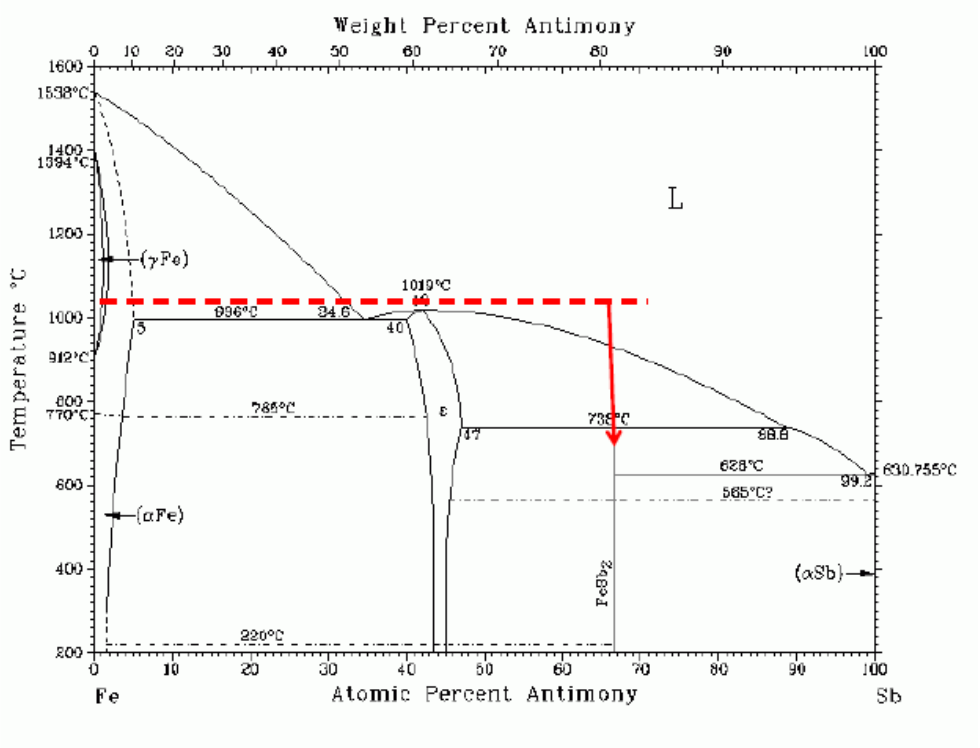

Figure 3.2 Binary phase diagram of Fe-Sb system. The image was taken from reference [9].

3.2.2 Arc-melting

Arc-melting is an effective method to prepare alloys by melting the constituent elements together. The heat needed for this purpose is produced by discharging a voltage arc in the presence of a noble gas. The process consists in melting the pure elements of the alloy or compound in the desired stochiometry by discharging an electrical arc caused

by the application of a large current between two electrodes. The actual arc-melting furnace (you need to write the manufacturer name and number of this device) available in the laboratory is pictured in Figure 3.3 (a). A continuous flow of argon gas (AR PP 300) is maintained through the furnace chamber at a pressure of 1-1.5 bar during the arc discharge and the melting process. The synthesis process consists of melting the materials into a button, then flipping it over and re-melting it to ensure sample homogeneity. . Figure 3.3 (b) shows a picture of an ingot sample ($CeCu_6$) obtained by this process.

The ingots of heavy-fermion compounds $CeCu_6$ and $CeAl_3$ were prepared by arc-melting method as explained in the paragraph above. Stoichiometric amounts of Ce (99.9%), and Cu (99.999 %, Alpha Aesar), as well as, Ce (99.9%, Alpha Aesar), and Al (99.99%, Alpha Aesar) were mixed and arc-melted together to form the binary alloy samples.

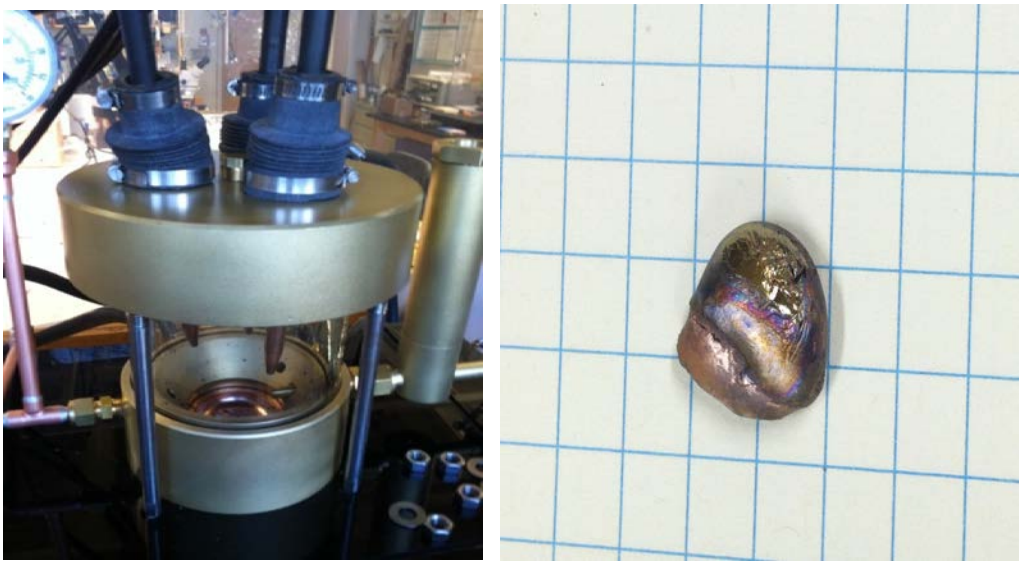

(a) (b)

Figure 3.3 (a) A view of the arc-melting furnace used in this work. (b) The ingot button for a typical sample obtained after melting.

3.3 Mechanical Nanostructuring

Mechanical nanostructuring is a sample technique where materials are pulverized or powdered by mechanical means (ball-milling) to reduce the particle size and the resulting material (powder) is pressed together (hot-pressing) into a pellet to increase the material density. The ingot samples obtained as explained in sections 3.2.1 and 3.2.2 are enclosed inside an air- tight ball-milling jar [25] along with stainless steel balls (Figure 3.4 (a)). All this is done inside a glove box so the ball-milling occurs in an argon atmosphere. The jar is then put in the ball milling machine (SPEX 8000D) shown in Figure 3.4 (b) and the machine is run for a desired period of time to get the nanopowders. During this high energy ball milling process mechanical alloying and nanostructuring occurs basically through a sequence of collision events between the balls and the material to be ground. Average temperature inside the ball milling jar is usually less than 100 ^{o}C. However the local temperature can be raised to the temperature high enough to form some binary alloys like SiGe.

(a) (b)

Figure 3.4 Stainless steel jars, balls, and a ball mill machine (8000D Dual Mixer/Mill from SPEX).

The number of ball-milling hours depends on both the brittleness of the ingot and the desired size of nano-grains. In this work, ball-milling time was 15 hrs for $FeSb_2$ whereas it was only 5 hrs for $CeCu_6$ and $CeAl_3$. Often the powdered materials stick to the walls of the jar after a certain time and limit the effectiveness of further ball-milling. The remedy for materials which stick to the walls is to remove the jars from the ball milling machine, re-introduce the jar to the glovebox and mechanically loosen the powder from the walls and then continue the balling milling process.

The nanopowder obtained from ball-milling is then consolidated into dense pellets. This was done by using a DC-current controlled hot-press method, more commonly known as the "spark plasma sintering (SPS)" method. Figure 3.4 (a) show a schematic diagram for hot-press and Figure 3.4 (b) shows the schematic representation of the SPS mechanism. As shown in fig 3.4 (a),

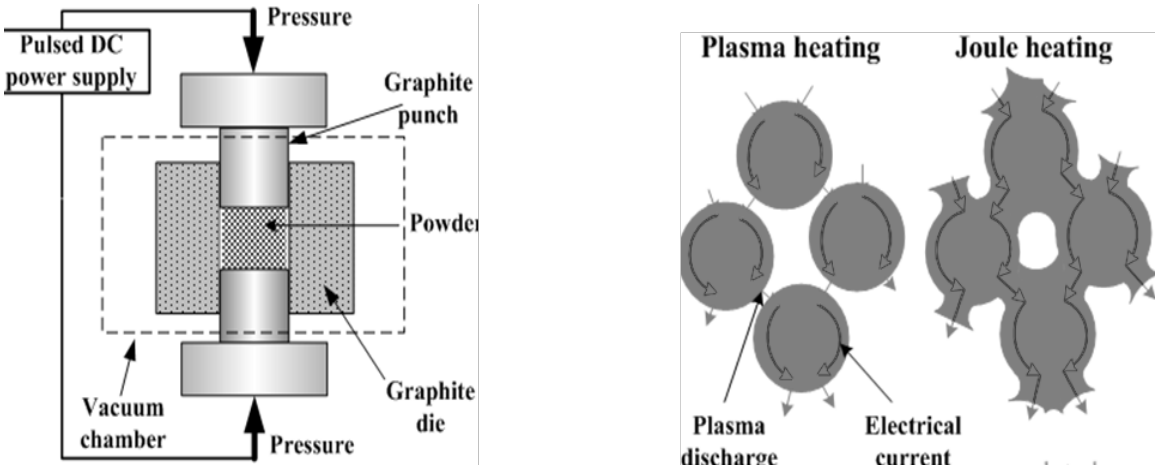

(a) (b)

Figure 3.5 Schematic pictures of hot-press method (a) and schematic representation of the SPS mechanism (b). Figure was taken from reference [10] and edited.

nanopowder is loaded in a cylindrical hole of a graphite die and sealed with graphite rods on top and bottom in a glove box. Then, the die with powder is put on a hot-press system. The powder is then pressed for 2 minutes for all the samples using a uniaxial pressure of around 78 MPa. For $FeSb_2$ nanocomposite samples the hot-pressing temperature ranged from 200 ^oC to 600^oC whereas for $CeCu_6$ and $CeAl_3$ it ranged from 400 ^oC to 800 ^oC. While pressing, a current is discharged through the material which produces both a strong electric field along the sample and Joule heating in the gaps of the powdered materials upon applying an ON-OFF DC pulse (see Figure 3.5 (b)). A rapid and thorough heat distribution throughout the specimen results in dense pellets with high homogeneity. The advantage of this technique is that it can produce a variety of grain sizes from nanopowders by varying the hot-pressing temperature (proportional to current and pressing time), and pressure. Varying the grain size of a material and measuring its thermal conductivity can lead to an optimization of its thermoelectric efficiency as a function of grain size. In fact, major portion of this thesis involves analyzing the grain-size dependence of thermoelectric properties of the samples obtained as explained above.

3.4 Material Characterization

Material characterization, in general, refers to the use of external techniques to probe into the internal structure and properties of the material. Several characterization techniques are available for studying materials. In this work, two of them, namely, X-ray diffraction (XRD) and Scanning Electron Microscopy (SEM) techniques were extensively used.

3.4.1 X-ray Diffraction

X-ray diffraction (XRD) is an analytical technique where one looks at X-rays scattered from a crystalline material. A commercially available XRD device from Bruker AXS shown in Figure 3.6 (a) was used. Details on the theory of operation of the XRD device can be found in reference [11]. Each material produces a unique X-ray fingerprint of intensity versus scattering angle which is characteristic of the material's atomic structure. The XRD pattern shown in Figure 3.6 (b) was taken for a typical $FeSb_2$ sample used in this work and corresponds to the orthorhombic crystal structure.

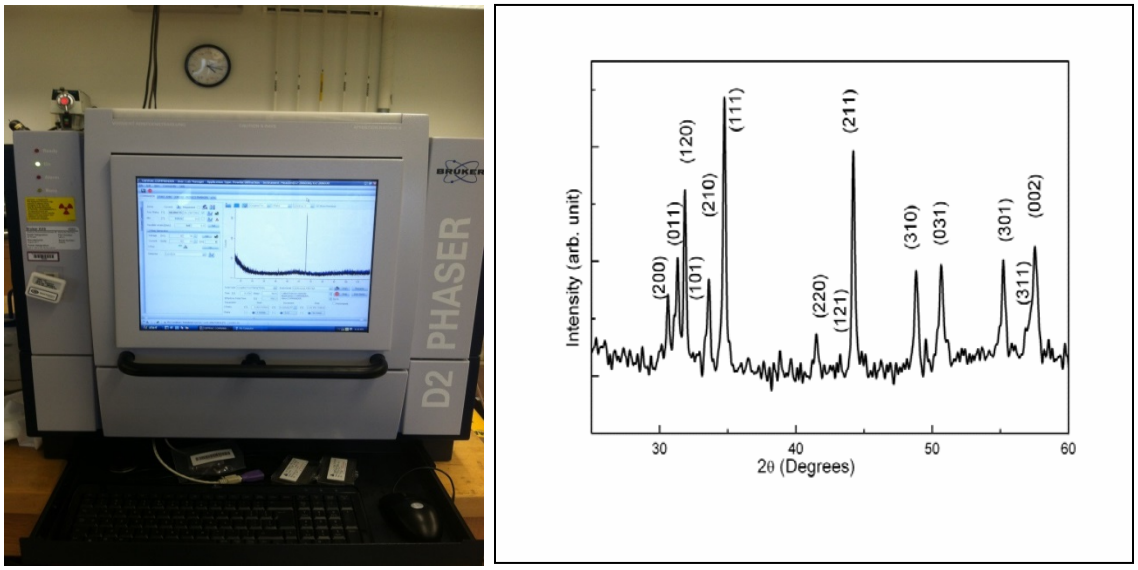

(a) (b)

Figure 3.6 (a) X-ray diffraction spectrometer used in this work and (b) XRD diffraction pattern of a typical $FeSb_2$ sample used in this study.

The X-ray diffraction technique offers several useful applications like determining

lattice parameter, strain, grain size, epitaxy, phase composition, preferred orientation, order-disorder transformation, thermal expansion etc. As discussed above, distribution of peak positions in XRD pattern (intensity vs. 2θ plot) enables one to determine the different chemical phases present in the sample. For the purpose of this work, obtaining a single phase material was essential to evaluating our material for thermoelectric efficiency.

3.4.2 Scanning Electron Microscopy

Scanning electron microscopy (SEM) is one of the most versatile techniques available for the examination and analysis of the microstructure morphology and also for chemical composition characterizations. A JEOL 6340F SEM available at Boston College was used throughout this thesis work to determine grain size, morphology, *etc.* The system is pictured in Figure 3.7 (a). The SEM technique uses a focused electron probe to extract structural and chemical information point-by-point from a region of interest in the sample. Due to its high spatial resolution, a wide range of specimens ranging from nanometer to micrometer length scales can be characterized. For nanostructured polycrystalline samples used in this work, SEM images provided information about the grain-size distribution, grain-orientation, texture and porosity. A typical SEM image of a polycrystalline sample used in this study is shown in Figure 3.7 (b).

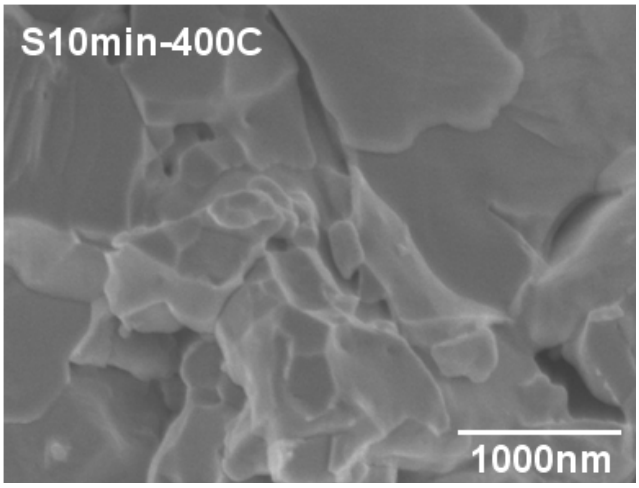

Figure 3.7 (a) A commercially available SEM device (JEOL 6340F) used in this work. (b) SEM image of a typical nanostructured $FeSb_2$ sample.

3.5 Physical Property Measurement System (PPMS)

The thermal conductivity, electrical resistivity, Seebeck coefficient, Hall coefficient, Hall mobility and magnetization of the samples used in this work were measured by a commercially available Physical Property Measurement System (PPMS) from Quantum Design. The PPMS dewar available in Opeil lab, Boston College is pictured in Figure 3.8. The system offers accurate and precise material characterization [1] in a temperature range of 2 – 400 K with a magnetic field up to 9 T. Two of the available PPMS options, namely, thermal transport option (TTO) and AC Transport (ACT) were extensively utilized during this research work. The measurement procedures used for this work will be briefly described in the following sections.

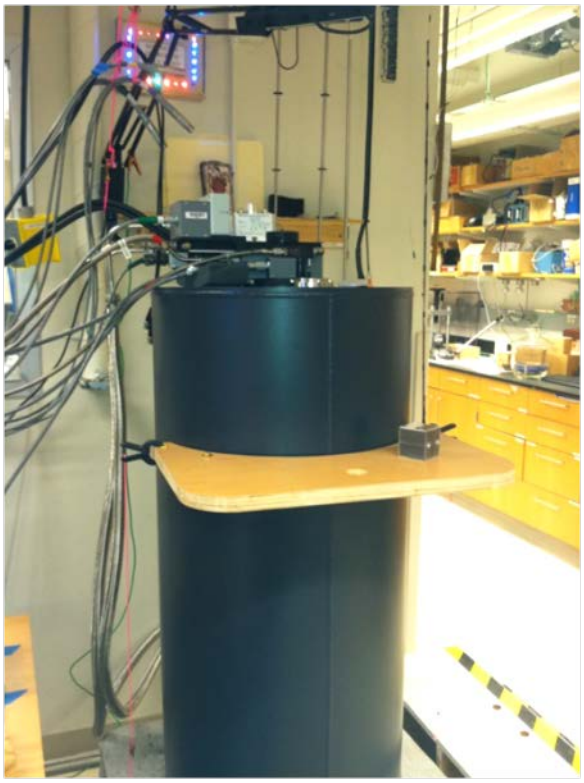

Figure 3.8 Picture of physical property measurement system (PPMS) dewar located in Opeil lab (Higgins 130, Boston College).

3.5.1 Thermal Transport Option

The thermal transport option (TTO) of the PPMS enables measurements of thermal properties, including thermal conductivity and the Seebeck coefficient and electrical resistivity simultaneously. The option measures thermal conductivity and the Seebeck coefficient by applying heat from the heater shoe in order to create a user-specified temperature differential between the two thermometer shoes [2]. The electrical resistivity is measured by using precision DSP current source and phase sensitive voltage detection. Figure 3.9 shows the schematic representation of heat and current flow across

the sample and different physical quantities to be taken into account during the measurement.

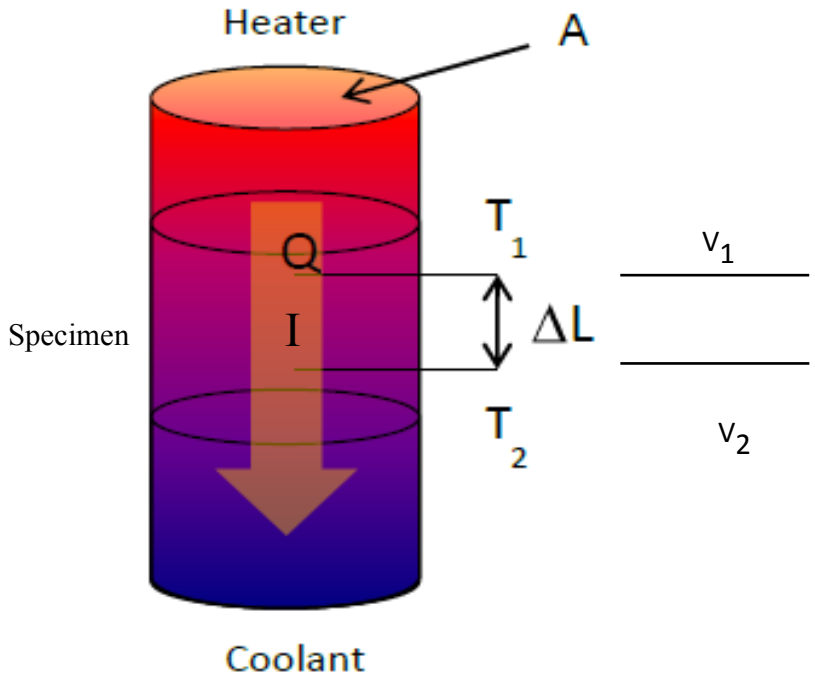

Figure 3.9 Schematic representations of heat and current flow across the sample during simultaneous measurement of the thermal conductivity, the Seebeck coefficient and the electrical resistivity in steady state method. The relevant physical parameters are also shown.

The quantities κ, *S* and ρ are calculated based on the following basic relations.

$$\kappa = \frac{Q/A}{\Delta T/\Delta L} \tag{3.1}$$

$$S = \frac{\Delta V}{\Delta T} \tag{3.2}$$

$$\rho = \frac{\Delta V}{I}\frac{R}{A} \tag{3.3}$$

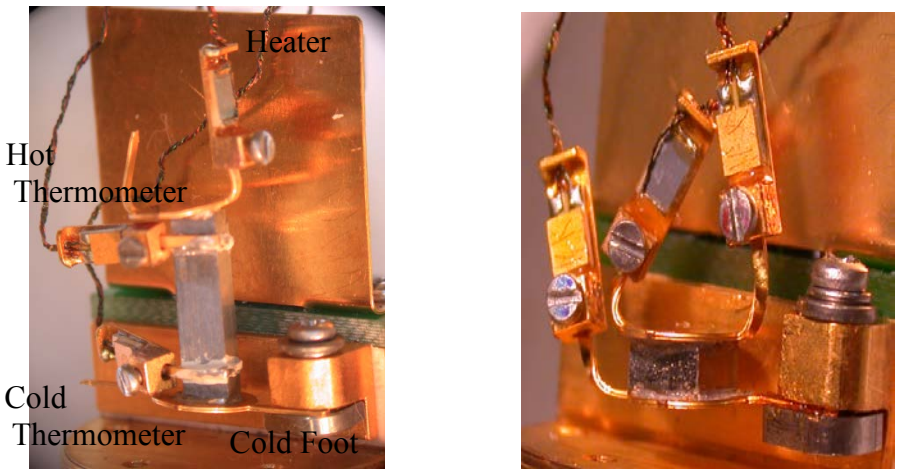

Figure 3.10 A sample of thermoelectric material mounted in a TTO puck of the PPMS in (a) 2-point configuration and (b) 4-point configuration.

The actual experimental arrangement with a sample mounted in a TTO puck is pictured in Figure 3.10. Both the two-point (see Figure 3.10 (a)) and four-point (Figure 3.10 (b)) configurations were used. Although two-point configuration is often used, a four-point configuration can help to minimize contact resistance. To compare the 2 and 4 point methods the same $FeSb_2$ sample was measured in both in configurations. It is noted that two datasets are highly consistent as shown in Figure 3.11. The consistency of data is likely due a minimization of contact resistance by using sputtered (Ti-Ni-Au layers) contacts and solder connections.

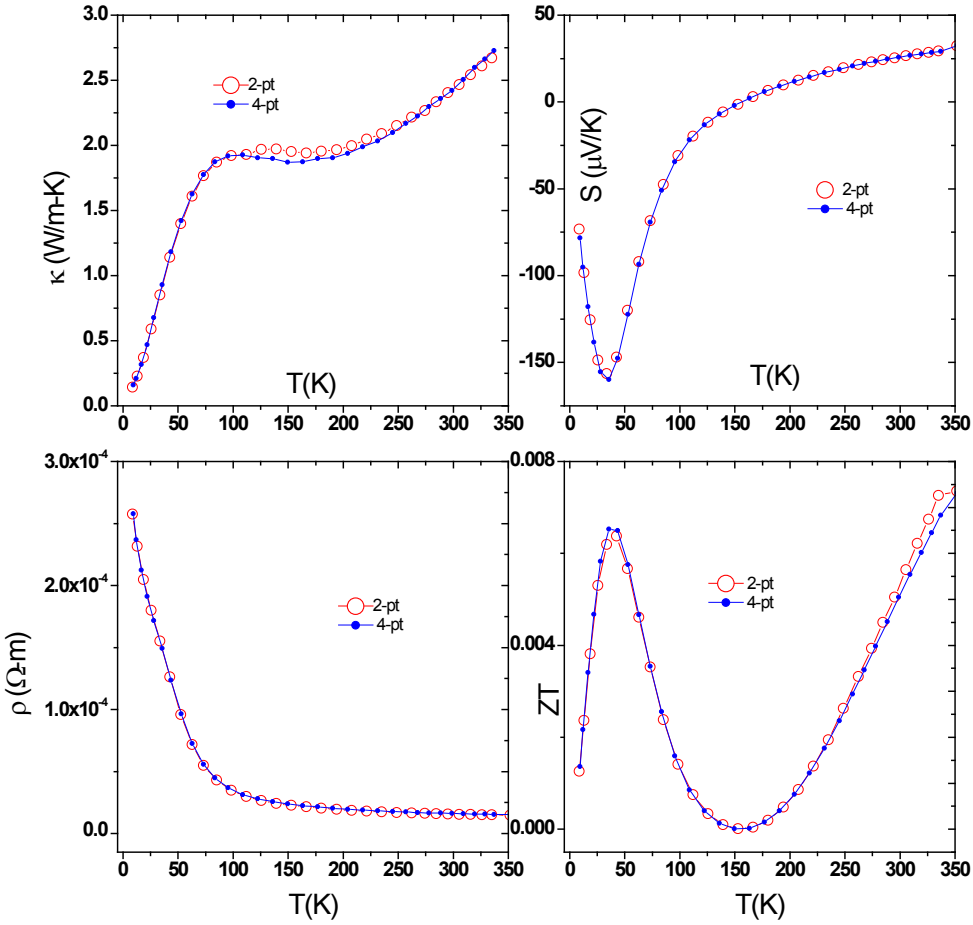

Figure 3.11 Comparison between the observed values of κ, *S* and ρ measured under 2-point configuration and 4-point configuration.

3.5.2 Horizontal Rotator Option

The horizontal rotator option of the PPMS enables determination of the Hall coefficient (R_H), which quantifies the Hall Effect for a given sample. The Hall effect is basic to solid-state physics and is an important diagnostic tool for the characterization of materials, particularly semi-conductors. It provides a direct determination of both the sign

of the charge carriers and their density in a given sample. The Hall coefficient R_H for a parallelepiped shaped specimen of cross-sectional area A and width l as shown in Figure 3.12(a) is given by,

$$R_H = \frac{V_H A}{IlB} \tag{3.4}$$

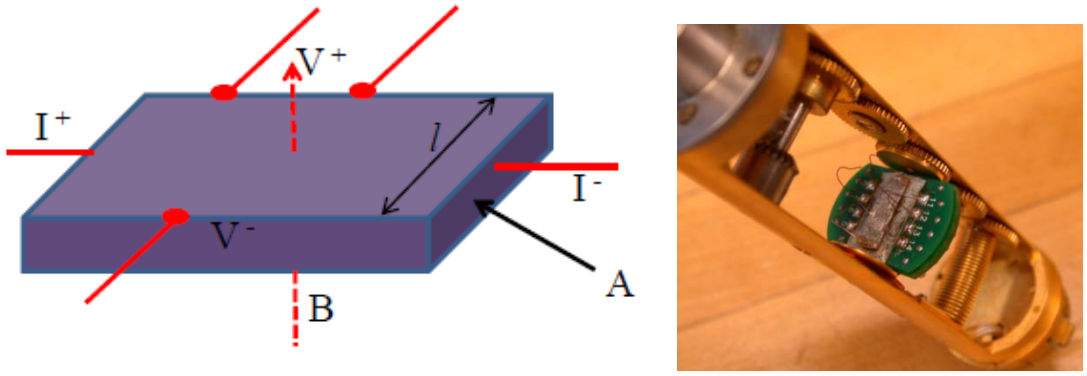

(a) (b)

Figure 3.12 (a) Geometrical representation of the Hall coefficient measurement of a rectangular slab. (b) Actual sample mounted on the sample stage in five-point configuration of the horizontal rotator.

where $V_H = V^+ - V^-$, I is the current and B is the transverse magnetic field. The actual sample mounted on the horizontal rotator platform looks as shown in Figure 3.12 (b). The five-point configuration helps to eliminate the offset voltage created due to misalignment of the voltage leads. The horizontal rotator option also allows sample rotation around an axis that is perpendicular to the magnetic field. The Hall coefficients both in positive (+B) and negative (-B) magnetic fields can be measured by rotating the sample stage by 180°. The actual Hall coefficient is then calculated as an average of the two values.

$$R_H = \frac{R_H(+B)+R_H(-B)}{2} \tag{3.5}$$

The purpose of flipping the sample and averaging the two Hall coefficient values as explained above is to eliminate the contribution from a magnetic field symphethetic component [3]. All the Hall coefficient measurements were carried out following a five-point configuration and 180^o rotation arrangements. Figure 3.13 shows temperature dependent Hall-coefficient values for a typical $FeSb_2$ sample used in this work. In an ideal case, the two curves should lie symmetrically about the line $R_H = 0$.

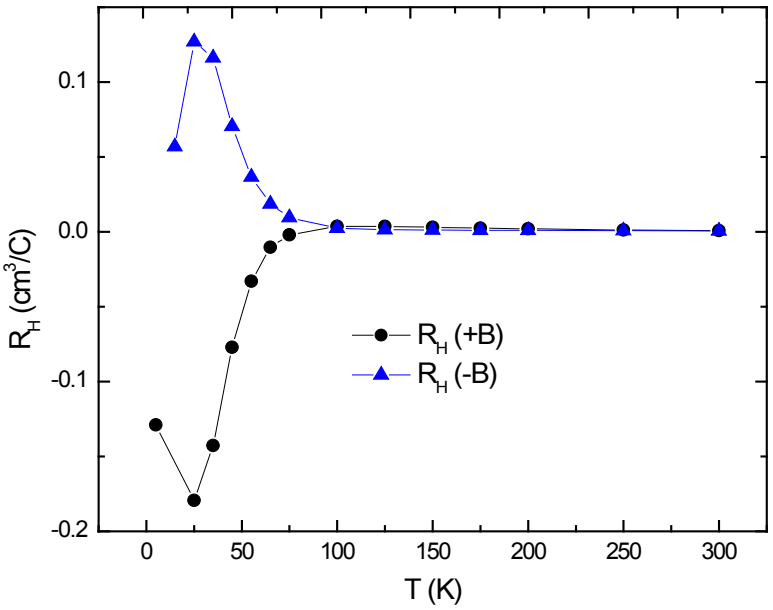

Figure 3.13 The Hall coefficient values as a function of temperature for a typical $FeSb_2$ sample. The black dots and the green triangles represent the values when the sample stage is set to 0^o and 180 ^{o} position respectively.

3.6 AC magnetic susceptibility measurement

In order to gain experience in fundamental measurement techniques in physics and to determine the superconducting transition temperature of experimental samples derived from the Meissner Effect, a device to measure AC magnetic susceptibility, also called a "susceptometer" was developed. The design employed here follows ref. [12] and the details can be found elsewhere [13, 14, 15]. A common experimental procedure used to characterize the magnetic susceptibility is to apply an external DC field to the sample and determine the induced field within the sample. This method measures DC magnetic susceptibility of the sample. Alternatively, an AC excitation on top of the DC external field is applied and the AC response of the material is measured. In this case, the complex magnetic susceptibility is given by,

$$\chi = \chi' - i\chi'' \tag{3.6}$$

where χ' and χ'' are real and imaginary parts of the total susceptibility. A typical ac-susceptometer often consists of a primary excitation field coil, a secondary pick-up coil and a secondary compensation coil as shown in Figure 3.14 (a). The coil set adapted to fit on a Quantum Design PPMS Multi-Purpose Probe is shown in Figure 3.14 (b).

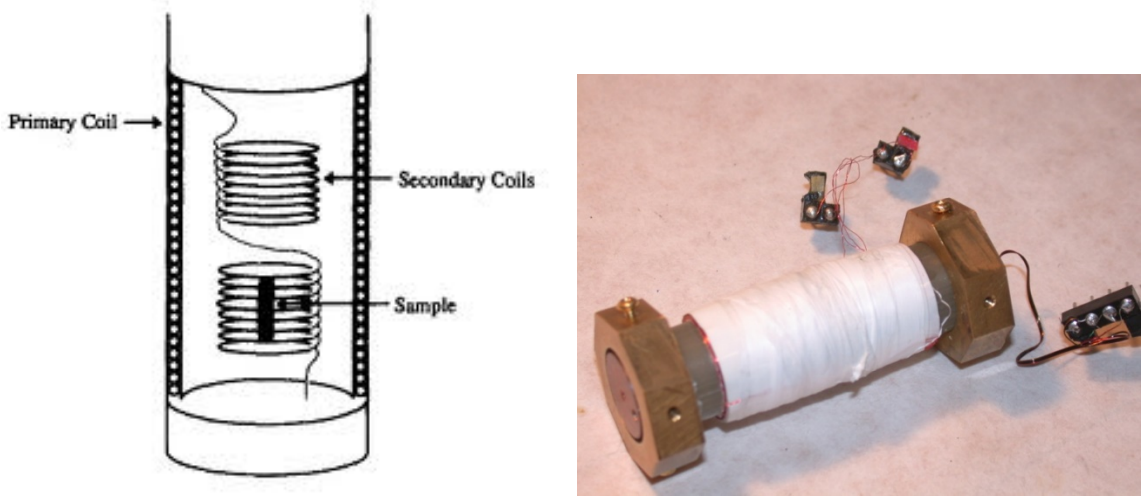

(a) (b)

Figure 3.14 (a) Schematic representation of coil configuration (Figure taken from reference [15]). (b) The actual coil assembly used in this work.

For our device, the number of turns in secondary coils is 1100 each whereas the primary coil has 3000 turns. When an ac current $I = I_o$ Sin(wt) is sent through the primary, a voltage (V_{rms}) is induced across the pick-up coil which is proportional to the magnetic moment of the sample. The induced voltage is related to the magnetic susceptibility by the equation [12],

$$\chi = \frac{\alpha}{\upsilon f I_o} V_{rms} \qquad (3.7)$$

Here α is the calibration constant and υ is the volume fraction of the pick-up coil. Knowing α, υ and real (V') and imaginary (V") part of the induced voltages, χ' and χ" can be determined using Equation 3.7.

AC susceptibility measurement has been proven to be a useful technique to characterize high T_C superconductors [16, 17] and to explore superparamagnetism in

nano-sized particles [18, 19, 20]. The original goal of this project was to separate the real and imaginary parts of the AC magnetic susceptibility and see the effect of grain sizes on magnetic properties of the samples. Since most of the samples used in this thesis are composed of nano-sized grains, a significant change in the magnetic moment may be expected due to increased surface to volume ratio of available spins [21]. The system was calibrated using two superconducting samples of niobium. Detail of the calibration can be found in Appendix A.

Figure 3.15 shows the total induced voltage across the pick-up coil as a function of temperature for a 2.5 % Sb-doped $Ca_3Ir_4Sn_{13}$ sample. This sample exhibits a

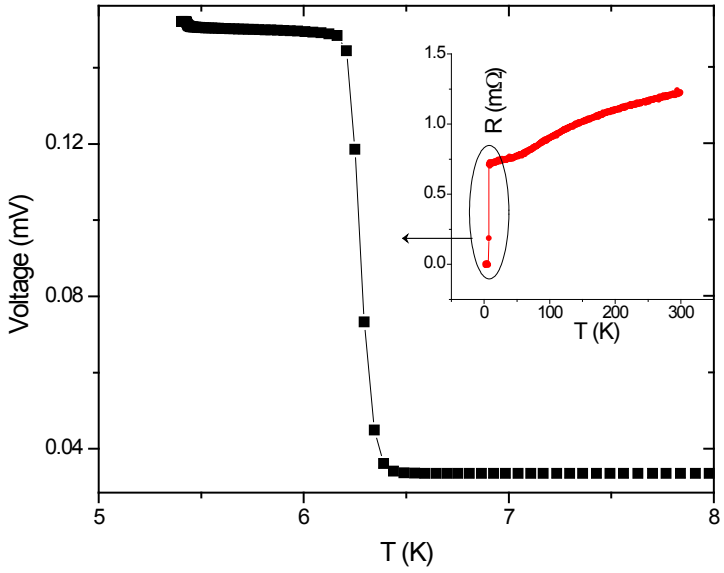

Figure 3.15 Temperature dependent voltage induced across the secondary coil for a sample of $Ca_3Ir_4Sn_{13}$. The temperature dependent resistance of the sample was measured using DC resistivity option of the PPMS.

superconducting transition at around 6.5 K [22] as shown in the inset. The inset data was

measured using DC resistivity option of the PPMS. The susceptometer data shows a corresponding superconducting transition derived from the Meissner effect.

In figure 3.16 (a), I plot the magnetic susceptibility (in arbitrary units) as a function of temperature for a polycrystalline gadolinium. For gadolinium an

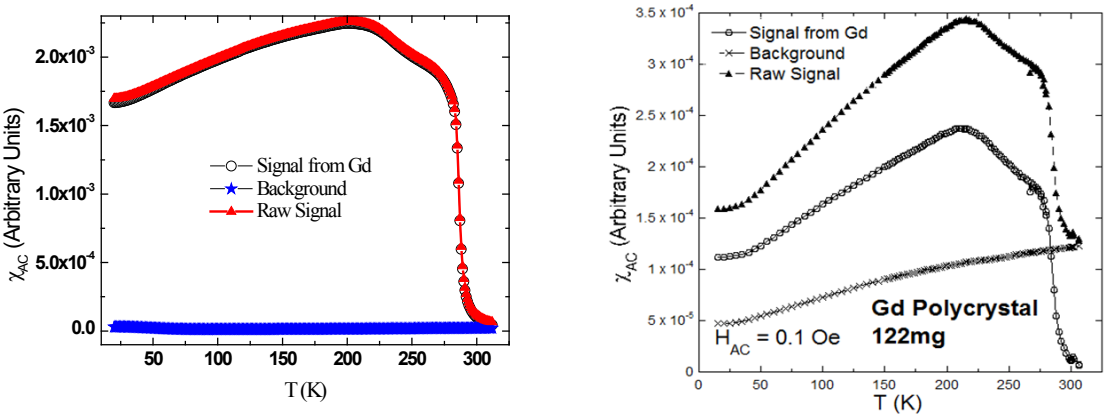

(a) (b)

Figure 3.16 (a) Temperature dependent ac magnetic susceptibility of a gadolinium polycrystalline sample measured using home-built susceptometer and (b) similar data taken from reference [24].

antiferromagnetic transition at 293 K was reported earlier [23] which was also seen in work by Fukuda *et al*. [24] (shown in the inset of Figure 3.15 (b)). The data from the home-built susceptometer is consistent with the literature data.

References

1. M.Y. Tang, Ph. D. thesis, Massachusetts Institute of Technology, (2011).
2. Quantum Design, San Diego, CA, Physical Property Measurement System: Thermal Transport Option User's Manual, Third edition, (2002**).**
3. Quantum Design, San Diego, CA, Physical Property Measurement System: AC Transport Option User's Manual, Third edition, (2002).
4. B. Cushing, V. Golub, and C. O'Connor; Journal of Physics and Chemistry of Solids **65**, 825–829 (2004).
5. Alloys. Preparation, Properties and Applications, edited by Fathi Habashi, Wiley (1998).
6. W. Alexander and A. Street; Metals in the Service of Man (1969).
7. H. Zhao, M. Pokharel, G. Zhu, S. Chen, K. Lukas, Q. Jie, C. Opeil, G. Chen, and Z. Ren, Appl. Phys. Lett. **99**, 163101 (2011)
8. M. Pokharel, H. Zhao, Z. Ren, and C. Opeil, International Journal of Thermal Science, **71**, 32-35 (2013).
9. The phase diagram for Fe-Sb system was taken from the website: http://www.himikatus.ru/art/phase-diagr1/Fe-Sb.php
10. The picture was taken from the website http://www.substech.com/dokuwiki/doku.php?id=spark_plasma_sintering , and edited.

11. D2 Phaser, Bruker AXS, Diffraction Solutions manual, http://chemistry.harvard.edu/files/chemistry/files/d2_phaser_doc-b88-exs017_en_high.pdf
12. R. C. Johnson, Ph. D. Dissertation, Boston College (2012).
13. J. K. Krause and J. R. Bergen, Superconductor Industry, **3**, 23-26 (1990)
14. C. P. Bidinosti and W. N.Hardy, Review of Scientific Instrument, **71**, 10 (2000).
15. M. Nikolo, American Journal of Physics, **63**, 1 (1995).
16. P. Laurent, J. F. Fagnard, B. Vanderheyden, N. Hari Babu, D. A. Cardwell, M. Ausloos and P. Vanderbemden, Meas. Sci. Technol.**19**, 085705 (2008).
17. M. Zeisberger, A. M. Campbell, Wai Lo and D. A. Cardwell, IEEE Transactions on Applied Superconductivity, **7**, 2 (1997).
18. K. Nadeem, H. Krenn, T. Traussing, and I. Letofsky-Papst, Journal of Applied Physics **109**, 013912 (2011).
19. V. B. Barbeta, R. F. Jardim, P. K. Kiyohara, F. B. Effenberger, and L. M. Rossi, Journal of Applied Physics, **107**, 073913 (2010).
20. S. H. Masunaga, R. F. Jardim, P. F. P. Fichtner, and J. Rivas, Physical Review B **80**, 184428 (2009).
21. B. D. Cullity, C. D. Graham, Introduction To Magnetic Materials, John Wiley & Sons, Inc., Hoboken, New Jersey (2009).
22. Kefeng Wang and C. Petrovic, Physical Review B, **86**, 024522 (2012).
23. H. E. Nigh, S. Legvold, and F.H. Spedding, Physical Review, **132**, 1094 (1963).
24. Ryan H. Fukuda, Smitha Sunny Proceedings on the National Conference on Undergraduate Research (NCUR) (2012).

25. Jars for our experiments were designed and machined out of O-1 tool steel (McMaster-Carr), hardened at 800 ^{o}C for 45 minutes, oil-quenched until 60 ^{o}C, and tempered at 260 ^{o}C for 2 hours. This produced jars of Rockwell hardness ~ 65.)

Chapter 4: Thermoelectric Properties of Nanostructured $FeSb_2$

4.1 Introduction to $FeSb_2$

$FeSb_2$ has been one of the extensively studied thermoelectric compounds in the past few decades [1-4]. This compound crystallizes in *Pnnm* orthorhombic structure as shown in Figure 4.1 [5] with lattice parameters a ≈ 5.8328 A^o, b ≈ 6.5376 A^o and c ≈ 3.1973 A^o [1]. The basic structural unit is made of Fe ions surrounded by deformed Sb octahedra. The Sb octahedra form edge sharing chains along the c- axis, sharing corners between chains.

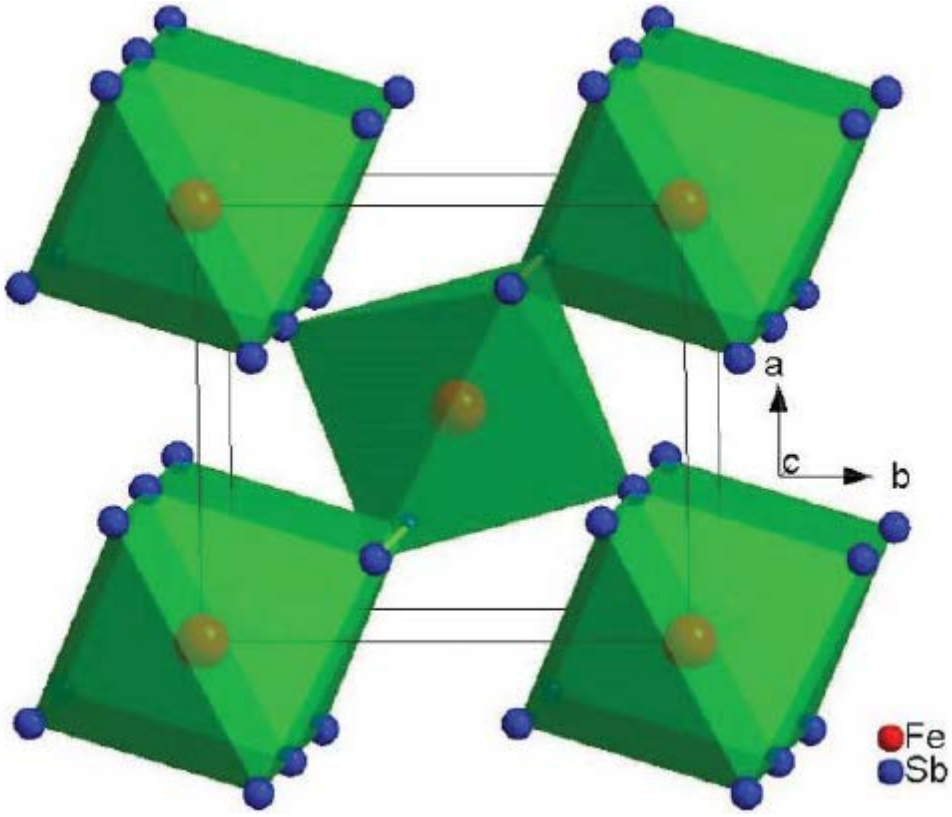

Figure 4.1 Crystal structure of $FeSb_2$.

The crystal structure of $FeSb_2$ plays a key role in the development of its electronic and magnetic properties at low temperatures. For example, the structural anisotropy of

the crystal structure leads to highly anisotropic electronic [6] and magnetic [4] properties in this compound as shown in Figure 4.2. Additionally, the anisotropies (Figure 4.2 (a)) of this compound exhibit unusual magnetic behavior. Single crystal $FeSb_2$ is known to be paramagnetic; having unusual temperature dependence of magnetic susceptibility with a diamagnetic to paramagnetic crossover at ~ 100 K. Petrovic *et al*. [4] reported such a crossover for the magnetic field applied along all the three crystallographic axes whereas Hu *et al*. [8] reported the crossover only along the c-axis. It should be pointed out that that the magnetic properties exhibit weaker anisotropy when compared to the electronic properties.

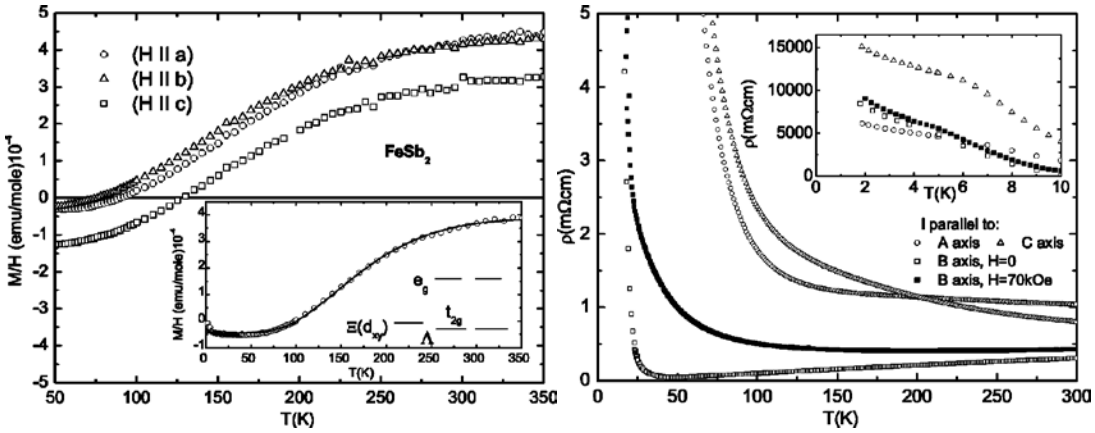

Figure 4.2 Magnetic susceptibility (a) and electrical resistivity (b) of a single crystal $FeSb_2$ as a function of temperature [4].

Below 50 K, a secondary transport gap is observed in pure $FeSb_2$ single crystals from temperature-dependent resistivity measurements. This gap is believed to originate from strong hybridization of Fe 3*d* orbitals with Sb 5*s* and 5*p* (*sp*3 hybridized) valence states due to the edge- and corner-sharing configurations present in the crystal structure, similar to what was seen in FeSi [4,8]. Figure 4.3 shows a depiction of the hybridization mechanism [11].

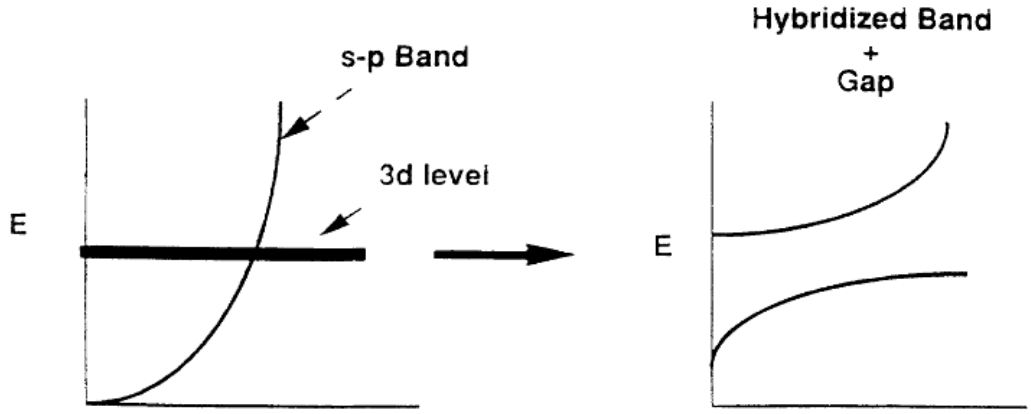

Figure 4.3 Depiction of band gap formation due to hybridization between 3*d* and *sp3* orbitals in FeSi [11].

Optical investigations on $FeSb_2$ give an estimated optical gap of 300 cm^{-1} [9] whereas the electrical transport gap is ~ 170 cm^{-1} [6]. This discrepancy is usually understood by assuming a small indirect gap for transport and a large direct gap for optical response [10]. Based on the structural analysis of marcasite by Goodenough [12], the magnetic and electrical properties may be accounted for by considering temperature induced transitions within the 3d multiplet. The five 3d orbitals split in the octahedral crystal field into a high energy e_g doublet ($d_{z^2}, d_{x^2-y^2}$) and a low energy t_{2g} triplet ($d_{xy}, d_{zx}\ and\ d_{yz}$). The e_g orbitals are left unoccupied above the Fermi level (E_F) and the t_{2g} orbitals remain below the Fermi level.

4.2 Thermoelectricity of Single Crystal $FeSb_2$

Investigations on $FeSb_2$ were conducted initially because of its unusual magnetic properties [13]. Research interests on this compound as a thermoelectric material emerged after Bentien *et al*. [6] reported a colossal value of the Seebeck coefficient of -

45,000 μVK^{-1}. A record high value of the power factor (PF) of 2,300 $\mu WK^{-2}cm^{-1}$ at around 10 K in single crystal samples was reported. These measurements along with its low resistivity suggested this material as a potential candidate for the Peltier cooling applications at temperatures near 10 K. Figure 4.4 shows the temperature dependent power factor (*PF*) of single crystal of $FeSb_2$ grown by flux method [6]. The authors also demonstrated that the peak value of the Seebeck coefficient changes with the crystal orientations. As a result, the power factor is is highly anisotropic. Also note significant magneto-thermopower of the sample. Despite the huge *PF* value, the dimensionless figure of merit (*ZT*) values for single crystal samples are limited by a very high thermal conductivity. As seen in the inset of Figure 4.4, $\kappa \sim 500$ $Wm^{-1}K^{-1}$ at ~ 10 K. Based on this data, one can calculate the temperature dependent dimensionless figure-of-merit (*ZT*) which is shown in Figure 4.5. The largest value of *ZT* is ~ 0.005 at low temperatures, much less than the state-of-art requirement for a $ZT = 1$ of conventional thermoelectric systems working above room temperature [14].

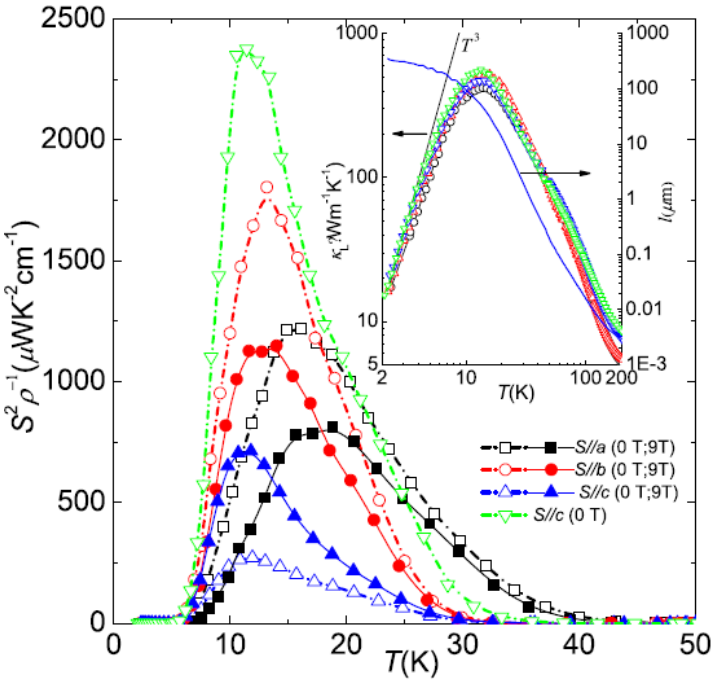

Figure 4.4 Power factor of single crystal $FeSb_2$ as a function of temperature. The inset shows temperature dependent thermal conductivity. Figure was taken from reference [6].

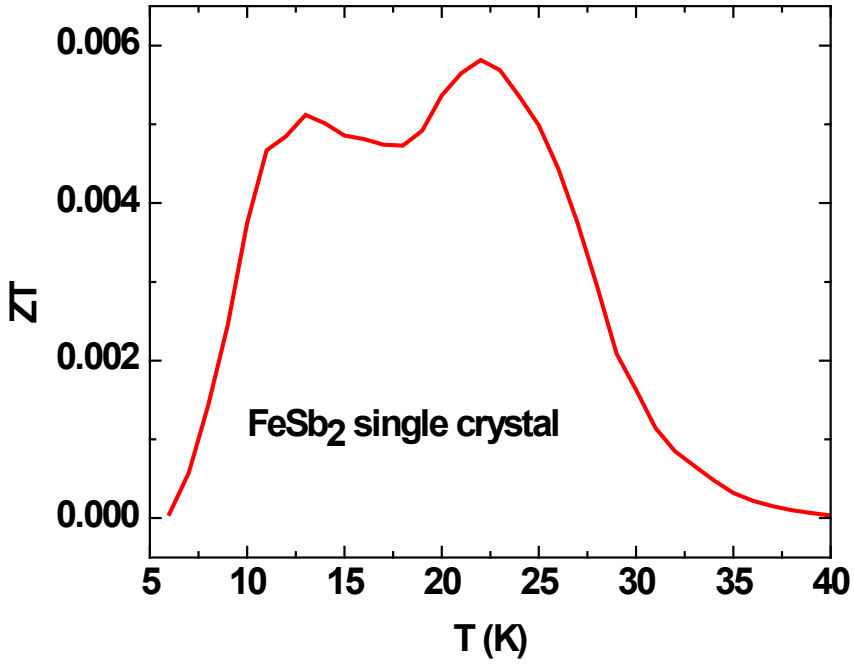

Figure 4.5 Dimensionless figure-of-merit (*ZT*) of $FeSb_2$ single crystal sample as a function of temperature. The temperature dependent power factor and thermal conductivity were drawn from Figure 4.4 and interpolated data was used to calculate the *ZT*.

Reducing the thermal conductivity without affecting the power factor of $FeSb_2$ system has been a real challenge. Initial attempts to reduce thermal conductivity employed doping or elemental substitution of $FeSb_2$ [15, 16, 17, 18]. Significant thermal conductivity reduction was achieved from these efforts, which in some case reaches 10 W/K-m below 50 K. However, other issues emerged with these doping efforts *i.e.* a semiconductor-metal transition was introduced, a modest reduction of thermal

conductivity, and the magnitude of the Seebeck coefficient was severely decreased, with its peak position shifting to higher temperature ranges. Thus, to some extent, the significance of *ZT* enhancement was degraded by its peak shifting from 12 K to above 100 K.

In principle, thermal conductivity suppression can be realized through impurity defects and lattice boundary scattering in a crystal. Indeed, for single crystal $FeSb_2$, its reported electron mean free path is less than 10 nm at all temperatures, and its phonon mean free path was determined to be 40 μm at 15K [19]. This suggests that it would be advantageous to tune the material's electrical and thermal conductivity properties by either doping or nano-engineering approaches. The nano composite approach, which has been approved as very efficient way to reduce the lattice contribution portion of thermal conductivity in many thermoelectric systems [20-23], appears inevitable for the *ZT* improvement of $FeSb_2$. In a review of the literature, among all the low temperature thermoelectric systems, especially those working at cryogenic temperatures, materials like FeSi [24], $RuSb_2$ [25], CeB_6 [26], $FeAs_2$ [27] have not yet gone through significant thermal conductivity suppressions by the nanocomposite approach.

A temperature scale called Debye temperature (θ_D) governs important information regarding dominant phonon scattering mechanisms in different temperature regions (2.5.1). In general,

$$\theta_D = \left(\frac{1944n}{\beta}\right)^{\frac{1}{3}} \tag{4.1}$$

where β coefficient is derived from the low temperature heat capacity (C_p) given by,

$$C_P = \gamma T + \beta T^3 \tag{4.2}$$

where n denote the atom number density [28]. The minimum limit of lattice thermal

conductivity has been calculated as low as less than 0.3 W/m-K at 50K [29] through the model proposed by Cahill *et al.* [30]. Therefore a significant ZT enhancement through nanocomposite approach in $FeSb_2$, which is a phonon dominated system, can be expected. In the following sections thermoelectric properties of nanostructured $FeSb_2$ samples will be discussed.

4.3 Effect of nanostructuring

4.3.1 Experimental

$FeSb_2$ nanocomposites were synthesized and processed by the procedure described in section 3.2.1.Further details of the sample preparation procedure can also be found in reference [31]. For a typical sample a total amount of 50 g of Fe and Sb metal pellets with the molar ratio of 1:2 of Fe to Sb was sealed in an evacuated quartz tube and then heated to 1050 ^{o}C in a furnace for 5 hours with intermittent stirring. Next the tube was removed from the furnace and quenched in water. The resulting ingot was resealed in an evacuated quartz tube and annealing at 600 ^{o}C for 24 hours. The final annealed ingot was ball milled prior to hot-pressing.

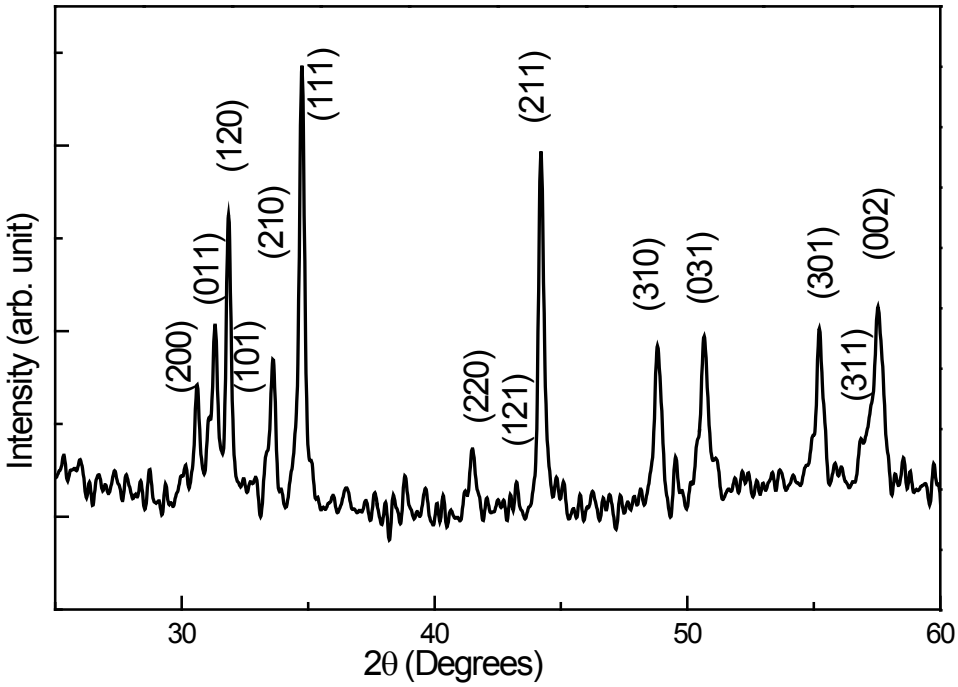

Figure 4.6 X-ray diffraction pattern of $FeSb_2$ nanopowder obtained after 15 hours of ball-milling

The final powder products were characterized by X-ray diffraction (XRD, Bruker AXS) to determine if the desired stoichiometry was achieved. Figure 4.6 shows the XRD pattern obtained for the final powder. The pattern showed that all the powders were pure phase $FeSb_2$ within the resolution of the equipment. All peaks of the pattern can be indexed as the orthorhombic *Pnnm* $FeSb_2$.

Table 4.1 Processing parameters, densities and IDs for the samples.

Powder ball milling time	Press temperature ^{o}C (at 1 ton)	Density (% of single crystal)	Average grain size with deviations (nm)	Sample ID
10 minutes	400	95.2	5000 ± 3000	S10min-400C
1 hour	400	96.3	300 ± 200	S1hr-400C
15 hours	200	77.2	20± 5 (Aggregates)	S15hr-200C
	300	85.6	30 ± 15	S15hr-300C
	400	97.7	100 ± 20	S15hr-400C
	600	98.9	20,000 ± 2000	S15hr-600C
	Room temperature (9 ton)	85.4	20 ± 5	S15hr-room temperature (RT)

In order to understand the role of the grain sizes in the thermoelectric properties of nano composite $FeSb_2$ system, we tuned the sample grain sizes both by varying the ball milling time and by changing the hot pressing temperature while keeping the other one unchanged. We prepared the following powders with different ball milling time: 10 minutes, 1 hour and 15 hours. DC current hot press method (as discussed in section 3.3) was used to prepare disk samples from the aforementioned $FeSb_2$ powders. The pressing force was usually at 1 ton. For the cold-pressed (room temperature pressed) sample a nine ton force was used. A one ton force exerting on a 1/2" pressing die produces a uniaxial pressure equivalent to

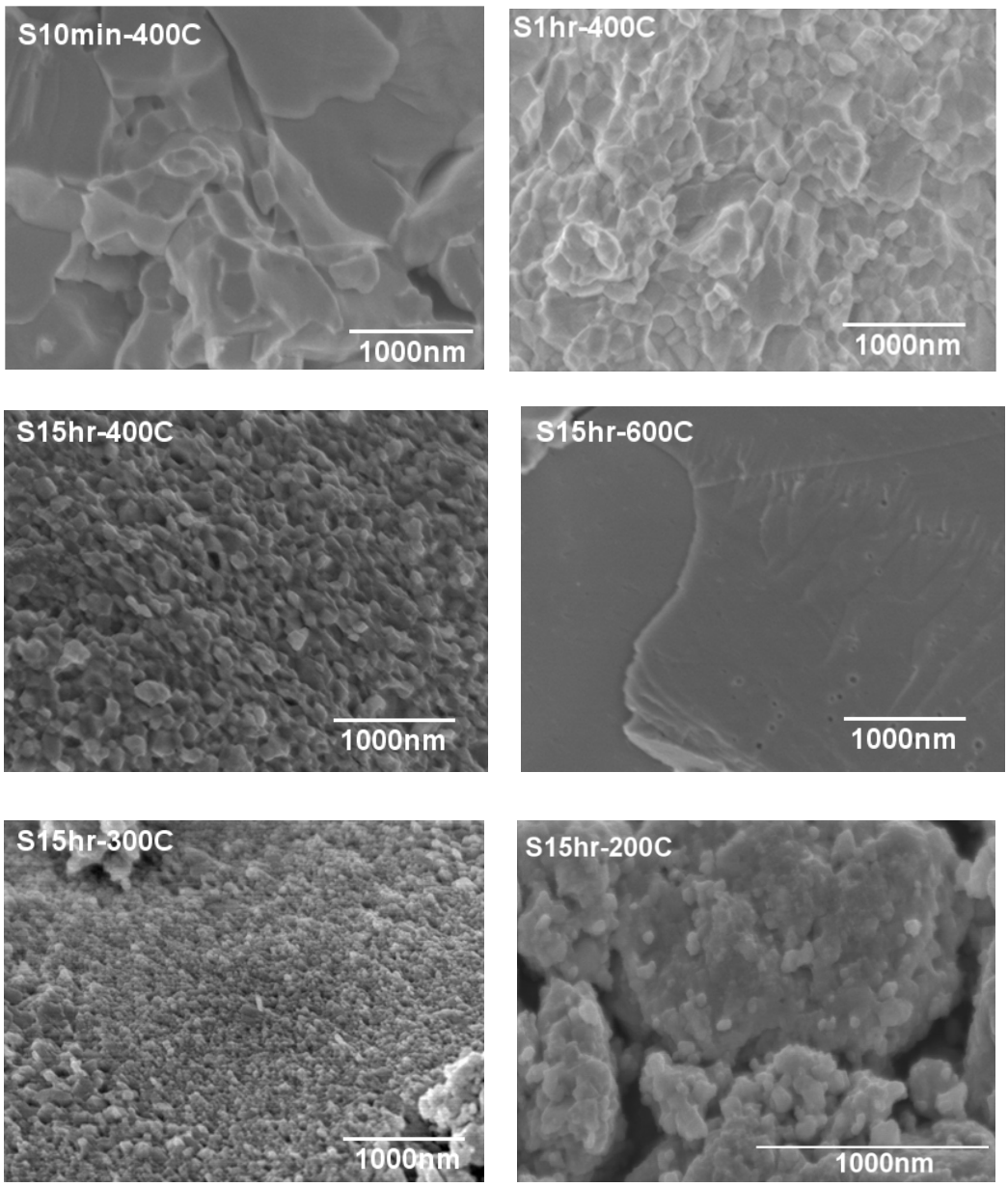

Figure 4.7 SEM images for nano composite samples, processing parameters for each sample were listed in Table 1.

78 MPa. The density of the palletized samples was measured by using the Archimedes method. Table 4.1 summarized the processing parameters, relative density and average

grain sizes and IDs for samples.

The grain sizes were estimated from images (see Figure 4.7) obtained from scanning electron microscopy (SEM). Images were all taken from the fresh fractures of the broken sample pieces. SEM images show how the grain size changes as a function of ball milling time and hot press temperature. From the images it can be seen that samples pressed at higher temperatures or with shorter ball milling times have much larger grains. It is also noticed that unlike those samples pressed under higher temperatures, S15hr-200C was composed of grain aggregates. The sizes of the small grain component of the aggregates were around 20 ± 5 nm estimated from HRSEM images. With the increasing of the pressing temperatures, the boundaries between small grains became clear.

The electrical resistivity (ρ), Seebeck Coefficient (S), thermal conductivity (K) and Hall coefficient (R_H) were all measured on a Physical Property Measurement System (PPMS) from Quantum Design. Thermoelectric properties ρ (T), S (T) and K (T) were determined with normal two point method using Thermal Transport Option (TTO). For a TTO sample, the ends of the samples were sputtered with three consecutive layers of titanium, nickel and gold. The two sputtered ends were then soldered on disk-shaped gold plated copper leads. For Hall coefficient measurement, five Platinum wires were spark welded onto the sample as depicted in Figure 3.12(a). The Hall Effect R_H (T) measurements were performed on samples S15hr-600C and S15hr-300C.

4.3.2 Results and Discussions

Figure 4.8 shows the temperature dependence of thermal conductivity for all samples and includes thermal conductivity of single crystals grown from vapor transportation and self-flux methods as reported in the literature [25]. A substantial

decrease of thermal conductivity was found for all samples throughout the temperature range. The thermal conductivity decreases as grain size decreases. For instance, the thermal conductivity of sample S15hr-600C is 17 W/m-K at 40K, compared with 0.34 W/m-K for S15hr-200C at the same temperature. Such a drastic reduction is mainly attributed to the decrease in the lattice portion of the thermal conductivity due to increased scattering of the phonons off the grain boundaries. The data indicates that the lattice thermal conductivity decreases with decreasing hot-pressing temperature and increasing ball milling time.

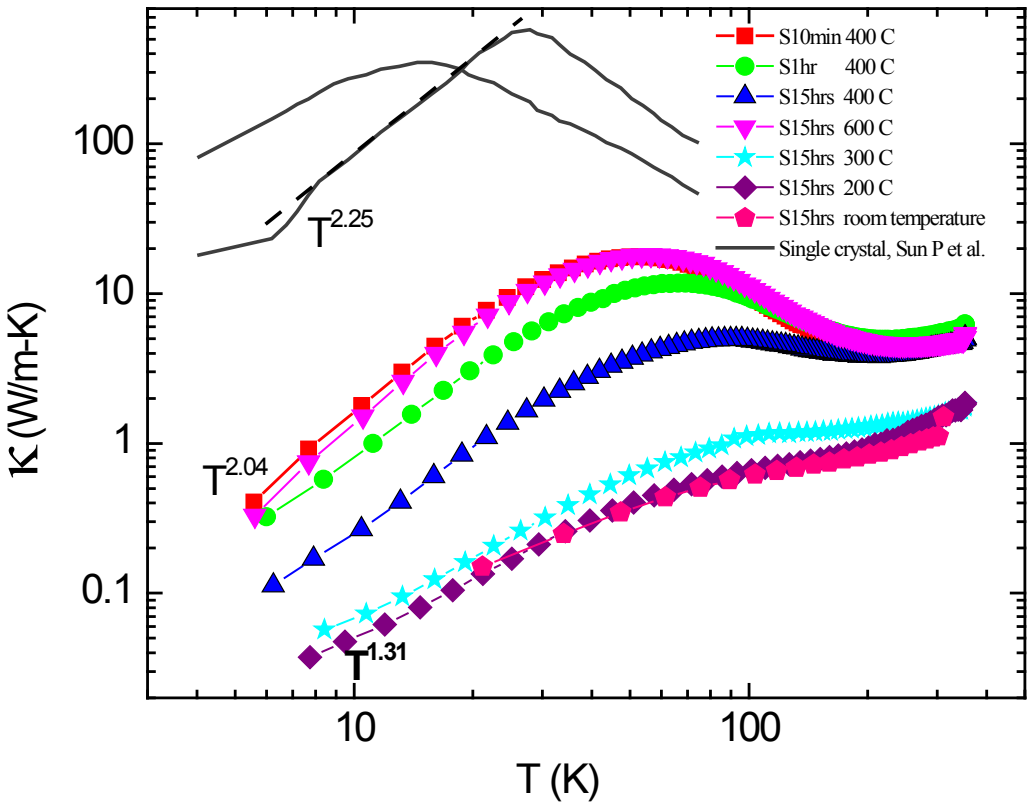

Figure 4.8 Temperature dependence of thermal conductivity for nano composite samples. Fittings were applied to sample S10min-400C and S15hr-200C respectively. Two solid

curves correspond to thermal conductivity from single crystal samples, data were extracted from reference [25].

Sample S15hr-200C has thermal conductivity reduced to 0.4 W/m-K at 50K, which almost reaches the theoretical minimum as calculated for thermal conductivity by Cahill *et al.* [30]. The peak positions of □, which reveal the competition between the phonon-phonon (umklapp) scattering and the grain boundary scattering (Figure 2.3), shift to higher temperatures and nearly disappear on samples S15hr-200C and S15hr-room temperature. This demonstrates that grain boundary scattering is the dominant scattering mechanism in samples with smaller grain sizes. Moreover, fitting the thermal conductivity data for temperatures below 100 K shows a shift from $T^{2.04}$ to $T^{1.31}$ with the decreasing of grain sizes, similar trends are indicated in nanocrystalline silicon [20]. This decreasing exponent in the temperature dependence indicates that other parameters besides C_V such as porosity, phonon frequency (ω), and the effective mean free path (Λ_{eff}) also play important roles in thermal conductivity reduction. When compared with single crystal $FeSb_2$, there is a reduction by more than three orders of magnitude, from 500 W/m-K down to around 0.1 W/m-K at 20 K in the nano composite system S15hr-200C. In comparison with the literature, such large scale thermal conductivity suppression by nanostructuring had never been reported in any other thermoelectric materials. Nano composite *p*-type BiSbTe bulk alloy achieved 83% thermal conductivity reduction compared with its ingot counterpart at 250^{o}C [21], half-Heuslers achieved 33% in high temperature ranges [23], and for *p*-type silicon germanium alloy, 100 % thermal conductivity reduction was reported through the nanocomposite approach [32]. Effectiveness of mechanical nanostructuring in reducing thermal conductivity of $FeSb_2$

was further corroborated by calculating Kapitza resistance using effective medium approach (EMA) [33], to be discussed later.

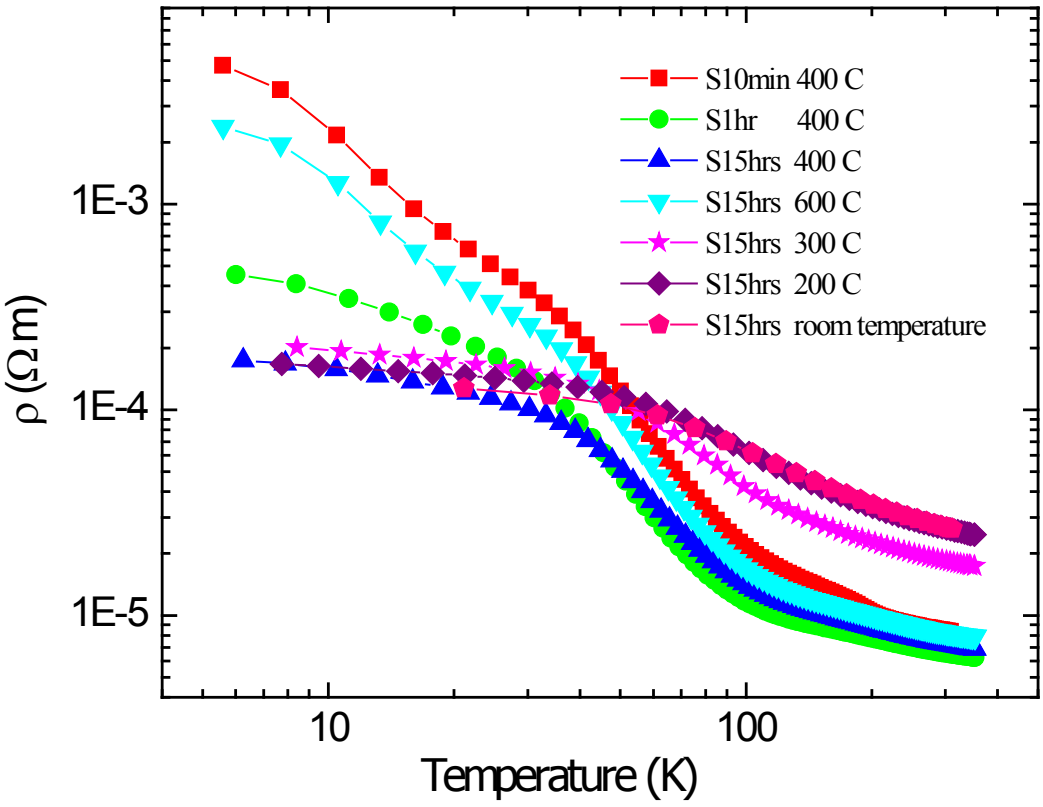

Figure 4.9 Electrical resistivity of the nanocomposite $FeSb_2$ samples as a function of temperature.

Figure 4.9 shows the temperature dependence of electrical resistivity for all the samples. The data was fitted using Arrhenius' law [28],

$$\rho(T) = \rho_0 \exp[-\frac{E_g}{k_B T}] \tag{4.3}$$

Here ρ_0 is the electrical resistivity at absolute zero, E_g is the thermally activated energy gap and k_B is the Boltzmann constant. Sample $FeSb_2$ S15hrs-600C has two gaps of 28.2

meV and 4.2 meV respectively. $FeSb_2$ S10min-400C also has two energy gaps of 28 meV and 2.5-5 meV respectively. But for sample S15hrs-300C, only one gap appears with a value of 21 meV. The change in the band gaps correspond to increasing crystal defects due to decreasing grain size. The lower temperature energy gap located in the temperature range of 7-20K gets completely suppressed upon decreasing grain size whereas the higher temperature gap depletes but does not disappear. For the sample pressed at room temperature, the gap is reduced to 18 meV.

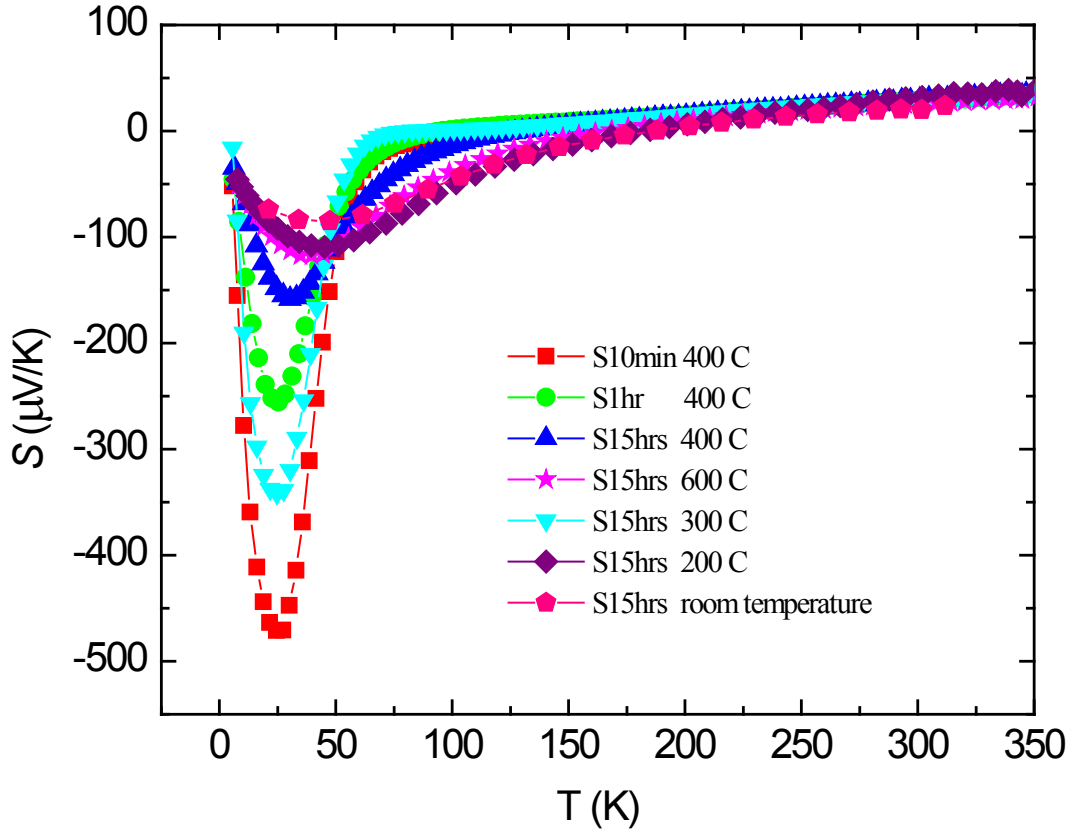

Figure 4.10 Seebeck coefficients of the nanocomposite $FeSb_2$ samples as a function of temperature.

The temperature dependent Seebeck coefficients (*S(T)*) are shown in Figure 4.10.

It can be seen that the peak value of the Seebeck coefficient (S_{max}) goes down as ball milling time is increased. It is also noted that the S_{max} decreases as pressing temperature decreases. For the most part, this shows that S decreases as grain size is decreased. This is not the case for S10min-400C, which has smaller grains than S15hr-600C. From the relationship of the resistivity and the quality of crystal, it is believed that S10min-400C has fewer defects than that of S15hr-600C due to the longer ball milling time. Defects typically increase carrier concentration, which will in turn decrease the S.

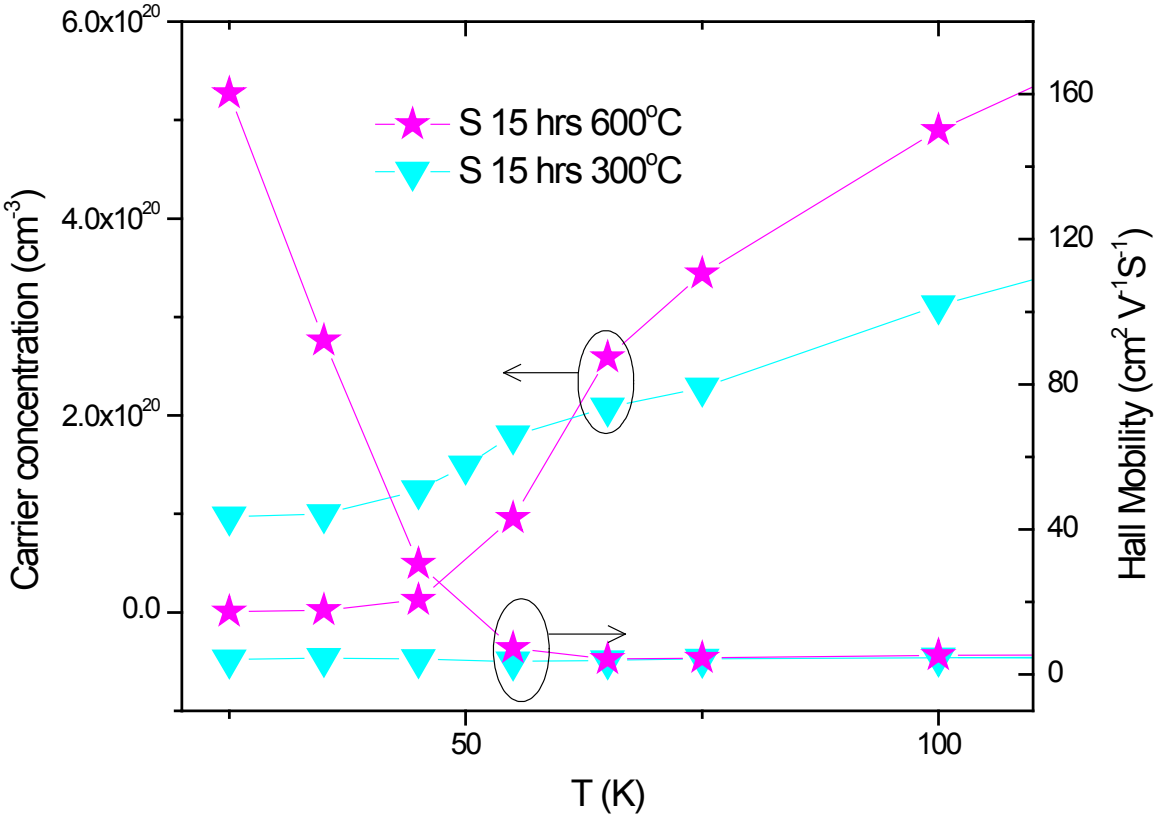

Figure 4.11 Hall carrier concentration and Hall mobility derived from measured values of Hall coefficient and electrical resistivity as a function of temperature for the samples S15hr-600C and S15hr-300C. Note the arrows showing corresponding axes.

Mobility and carrier concentration measurements are shown for two samples S15hr-600C and S15hr-300C in Figure 4.11. For S15hr-300C at 25 K, carrier concentration is 9.75×10^{19} cm^{-3} and the mobility is 4.52 cm^2/V- s. On the other hand, for S15hr-600C at 25 K, carrier concentration is decreased to 8.36×10^{17} cm^{-3} while the mobility is as high as 160 cm^2/V- s. This directly correlates to the increase seen in the *S* in Figure 4.10. There is a cross over between the two samples in the Seebeck coefficient found at 65 K. This cross over is also seen in the measurements for carrier concentration at 65 K while the mobility remains relatively constant confirming both measurements. Since S15hr-600C has better crystallization, and therefore a band gap of 4.2 meV in the temperature range 7-20 K which is not seen in S15hr-300C, and induces higher resistivity than that of S15hr-300C below 50 K. For the same reason, peak values of the Seebeck coefficient of S15hr-600C, which is 352 μV/K at 20 K, is much larger than 117 μV/K for S15hr-300C at 35 K.

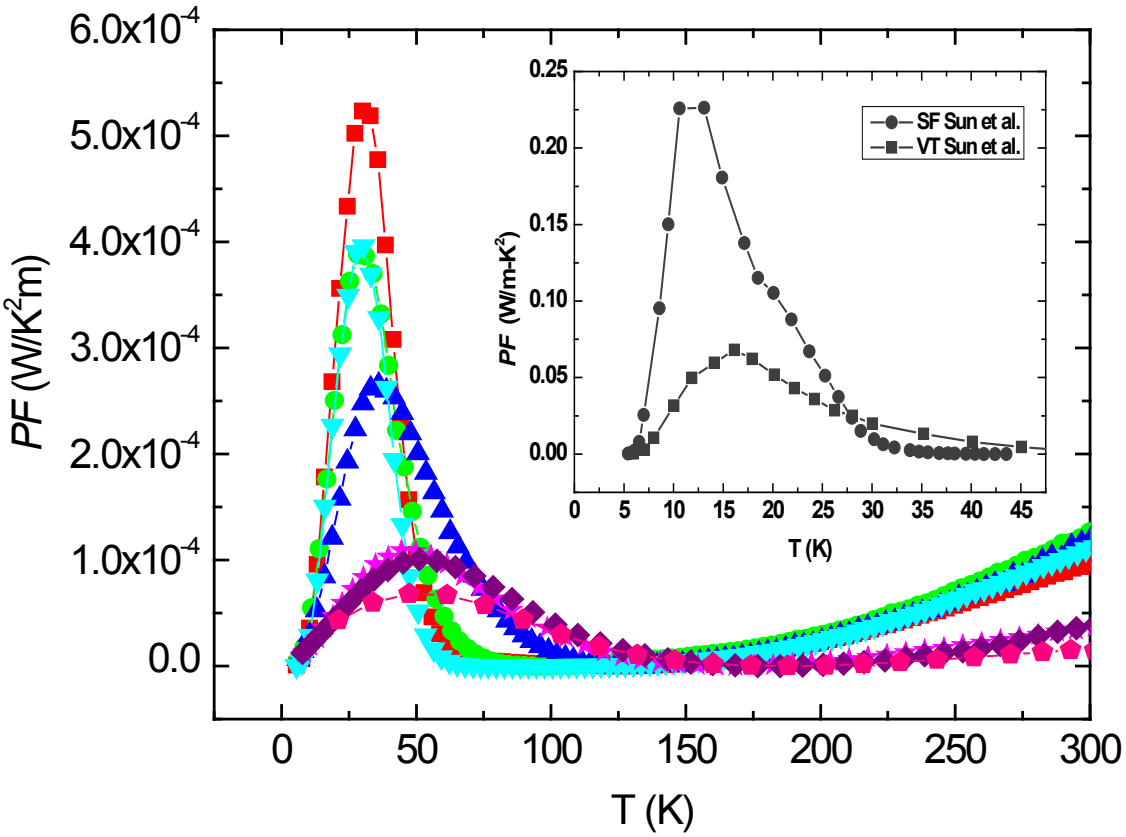

Figure 4.12 Temperature dependent power factor for $FeSb_2$ nanocomposite samples. Inset refers to the power factor for single crystal data taken from reference [25].

In $FeSb_2$ systems, the relation between carrier concentration and Seebeck coefficient has been intensively investigated recently by Sun *et al.* [5, 16, 19]. It was found that an enhancement by a factor of 30 or larger could be applied to the calculated Seebeck coefficient based on the free-electron model thereby suggesting a strong electron-electron correlation as a possible cause for large value of the Seebeck coefficient in $FeSb_2$. However, based on our analysis [34], a substantial phonon-drag contribution to the Seebeck coefficient exists in this system which will be discussed in later section.

Figure 4.12 shows the temperature dependence of power factor (*PF*) for all samples. The *PF* from single crystal samples grown by VT and SF [25] are plotted as the inset to Figure 4.12. It can be seen that the *PF* values from polycrystalline samples are far from comparable to their single crystal counterpart. This can be fully ascribed to the much lower value for *S* of the polycrystalline (nanocomposite) samples. As for the resistivity, polycrystalline samples all show typical semiconductor behavior, which is consistent with most reported results in the literature [5, 6, 16]. In some reports of single crystal $FeSb_2$ the Kondo effect was observed [4, 13]. The b- axis of single crystal $FeSb_2$ exhibits a metal-semiconductor crossover around 40 K. The *PF* peak along b axis was measured to be 0.78 W/m-K^2 due to the much lower resistivity [35].

Figure 4.13 shows the temperature dependence of *ZT* for the nanocomposite samples. It can be noted that there is significant enhancement, by a factor of more than 2, over that of single crystal samples. The figure of merit increases as grain size decreases except for the sample pressed at room temperature. However the difference in thermal conductivity from S15hr-200C to S15hr-RT is negligible due to the fact that the lower limit of thermal conductivity has been reached. Therefore, any further reduction in grain size will only degrade thermopower with no enhancement in thermal conductivity

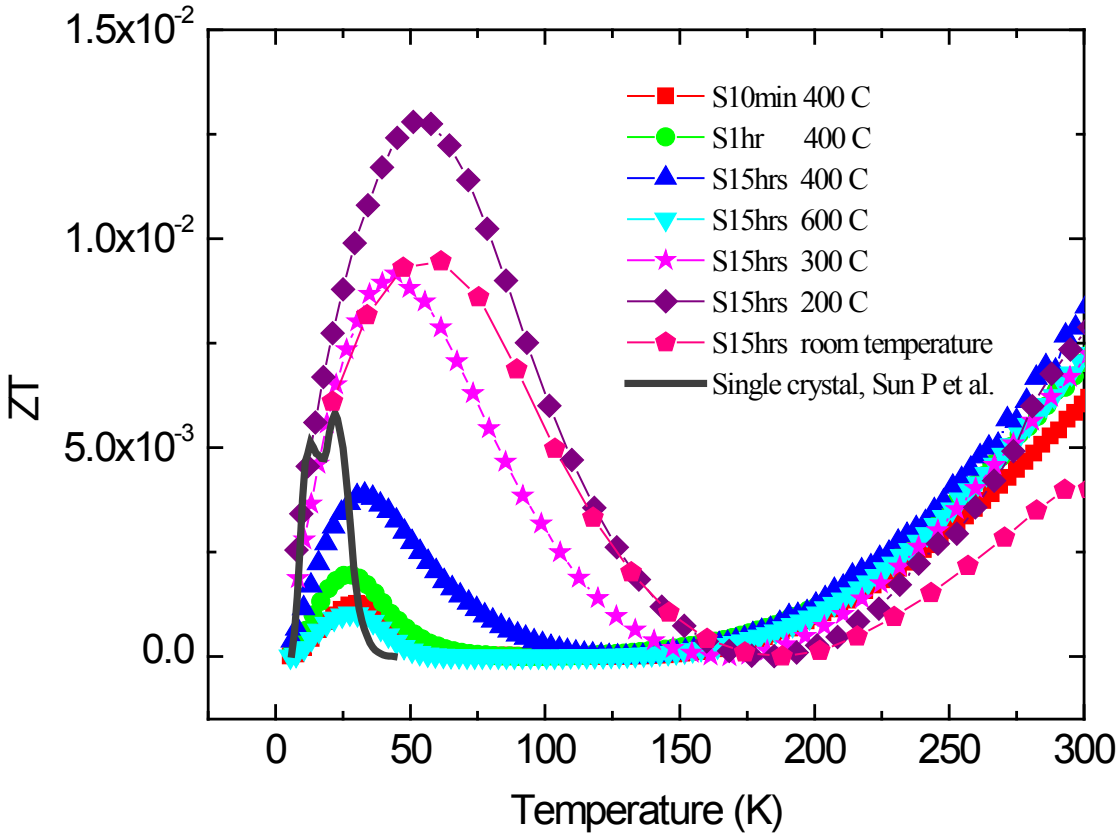

Figure 4.13 Dimensionless figure-of-merit (*ZT*) of the $FeSb_2$ nanocomposite samples as a function of temperature. The thick and black curve represents temperature dependent *ZT* for single crystal sample, taken from reference [25].

leading to lower values for *ZT*. The optimal *ZT* value from S15hr-200C which reaches 0.013 at 50 K, is higher than *ZT* = 0.005 at 10 K for single crystal samples. Though the power factor is much less than that of the single crystal, the drastic reduction in thermal conductivity contributes to the increase in *ZT*. A *ZT* value greater than 0.1 at cryogenic temperatures (< 77 K) has rarely been reported. Single crystal FeSi has *ZT* of 0.01 at 50 K, which can be slightly raised to 0.07 at 100 K by 5% Ir doping [11].

4.3.3 Conclusions

In conclusion, substantial thermal conductivity suppression for the strongly correlated system $FeSb_2$ through a nano composite approach is reported. Thermal conductivity was reduced by more than three orders of magnitude over its single crystal counterpart. Through the optimization of ball milling time and pressing temperature it was shown that as grain size decreases from tens of microns to around 20 nm, the corresponding thermal conductivity decreases 50 times, reaching its minimum limit, 0.34 W/m-K at 50 K. The optimized nanocomposite sample characteristic *ZT* was found to be 0.013, compared to 0.005 for single crystal $FeSb_2$. Although this is small when considering a nominal $ZT = 1$ desirable for room temperature thermoelectrics, it is clear that nanostructuring reduces thermal conductivity in $FeSb_2$ and can be combined with other methods *e.g.* doping or composition adjustment to greatly increase the figure of merit. This method can be easily extended to other strongly correlated low temperature thermoelectric materials, paving the way for future cryogenic temperature cooling systems.

4.4 Effect of Doping

4.4.1 In, Te, Sn, Ru, Co and Cr-doped $Fesb_2$

Several attempts to optimize the thermoelectric performance of $FeSb_2$ have been made previously. Some of the typical dopants were Sn [15], In [29], Se [36], Te [16, 37], Cr [37], Co [37]. All of the above studies were performed either in single crystal or polycrystalline samples. Few of these doping studies show significantly enhanced thermoelectric properties of $FeSb_2$. Furthermore, it was shown that the Seebeck coefficient decreases sharply upon doping and thus in turn dramatically reduced the

power factor (S^2□□. Tellurium [16, 37] was found one of the best dopants by reducing thermal conductivity while maintaining a reasonably large value of the power factor. In this work, doping was combined with the mechanical nanostructuring with the anticipation that the reduced thermal conductivity may lead to increased ZT values.

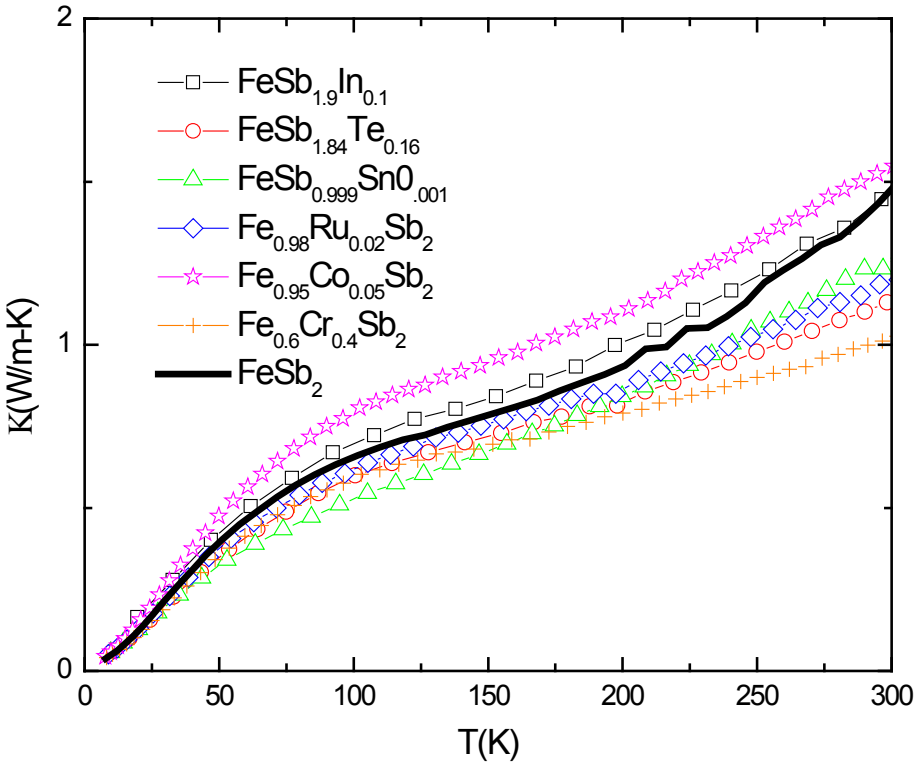

Figure 4.13 Thermal conductivity of doped nanocomposite samples of $FeSb_2$ as a function of temperature. All the samples are hot-pressed at same temperature of 200 ^oC.

From the previous work (section 4.3), the lowest hot-pressing temperature of 200 ^oC presents the lowest thermal conductivity and optimized ZT. Therefore, to maintain low thermal conductivity all the doped samples to be discussed below were pressed at 200 ^oC. The dopant concentrations were chosen from the literatures mentioned above. In our

substitution studies, three samples were doped on the Sb site and three were doped on the Fe site.

In Figure 4.13, temperature dependent thermal conductivity of the doped nanostructured samples are presented. No significant change in thermal conductivity is induced by doping. Co and In-doped samples exhibit increased thermal conductivity whereas other four samples have slightly reduced thermal conductivity when compared to the undoped sample.

Figure 4.14 shows the temperature dependence of the power factor for the samples. When compared to the undoped samples, doped samples exhibit decreased values of the power factor. Additionally, for Te and In-doping the peaks in *PF* shift to higher temperature. A similar shifting of the peak in power factor with increasing Te-content has been reported also in the litrature [16]. The decrease in Seebeck coefficient in doped samples is due

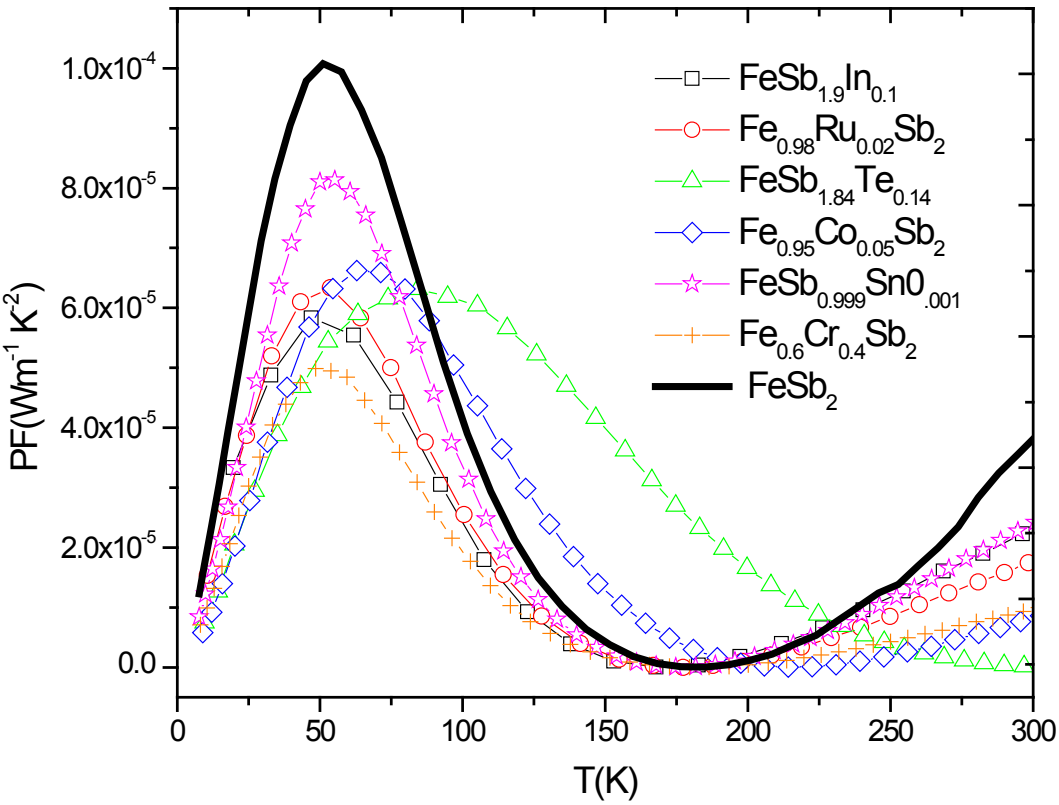

Figure 4.14 Thermoelectric power factors of doped nanocomposite samples of $FeSb_2$ as a function of temperature.

mainly to the increased concentration of the carriers. However, this data does not show a clear trend of how Fe and Sb-substitutions effect the carrier concentration.

In Figure 4.15, calculated values of ZT as a function of temperature are shown. All the doped samples exhibit ZT_{max} values smaller than that of undoped counterpart. Te-doped samples has a relatively tall peak in ZT when compared with other doped samples. Also the ZT peak for Te-doped sample is shifted to the temperature ~ 100 K when compared to ~ 50 K for the undoped sample. Moreover, the ZT peak in Te-doped sample is broader and is an important factor in terms of practical application in TE cooler. In the

following section, details about the effect of Te-doping will be discussed. . Details can also be found in reference [38].

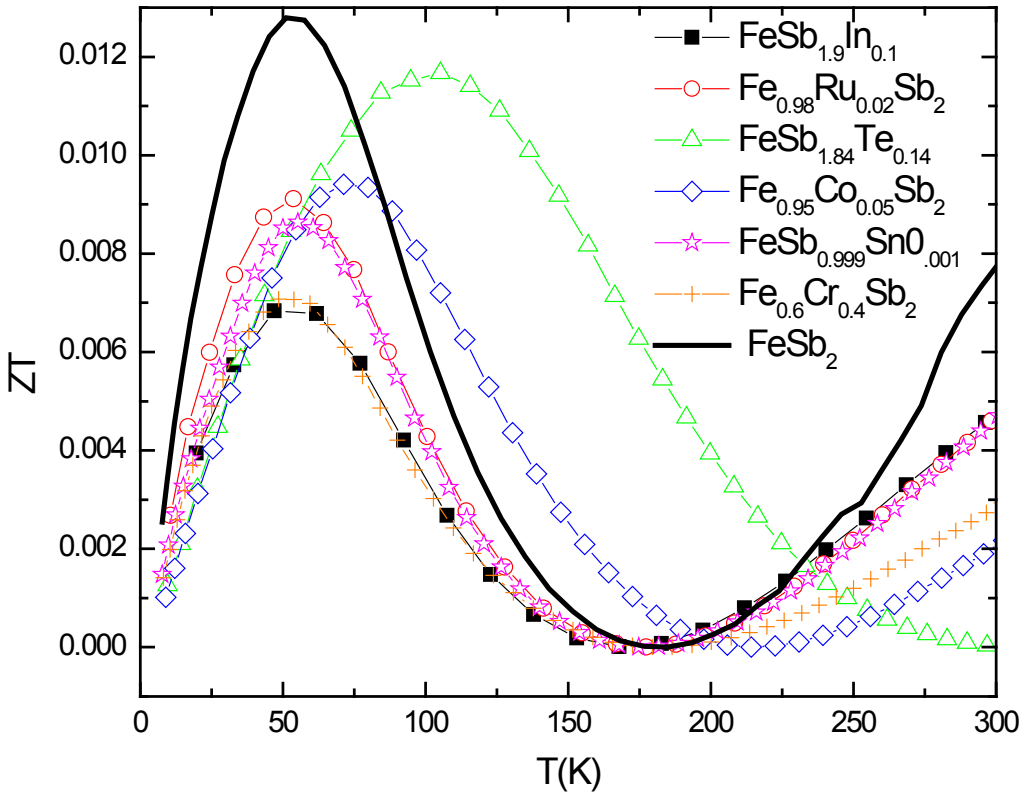

Figure 4.15 ZT of doped nanocomposite samples of $FeSb_2$ as a function of temperature.

4.4.2 Optimizing Thermoelectric Properties of Te-doped $FeSb_2$ nanocomposites

In our earlier work [31] explained in section 4.3.2, we were able to reduce the thermal conductivity of $FeSb_2$ by three orders of magnitude using the technique of nanostructuring. Unfortunately, the values of the Seebeck coefficient were drastically reduced in these nanostructured samples possibly indicating a significant phonon-drag contribution [34]. As a result, *ZT* was increased by only one order of magnitude. Data from our earlier work clearly showed that a significant increase in *ZT* of $FeSb_2$ through

nanostructuring alone cannot be expected. On the other hand, studies have shown tellurium to be an effective dopant for improving *ZT* of single crystal $FeSb_2$ by reducing the thermal conductivity via point defect scattering. Sun *et al*. [16] reported a *ZT* value of ~ 0.013 at around 100 K in $FeSb_{2-x}Te_x$ single crystal samples for their optimized doping concentration of x = 0.16. The following paragraphs discuss the combined effect of nanostructuring and Te-doping on the thermoelectric properties of $FeSb_2$. To conduct this research, the previously reported [16] optimized Te-doped stoichiometric composition ($FeSb_{1.84}Te_{0.16}$) was used. The thermoelectric properties of this particular stoichiometry were tuned by changing the hot pressing temperature.

The sample preparation and measurement methods are similar to that explained in section 4.3.1 and can also be found in reference [38]. Five nanostructured samples of $FeSb_{1.84}Te_{0.16}$ were prepared by hot-pressing nanopowder at five different temperatures namely, 200, 400, 500 and 600 ^{o}C. The samples are given IDs based on their corresponding hot-pressing temperature. For example, $FeSb_{1.84}Te_{0.16}$ HP 200 means nanostructured sample of $FeSb_{1.84}Te_{0.16}$ hot-pressed at 200 ^{o}C.

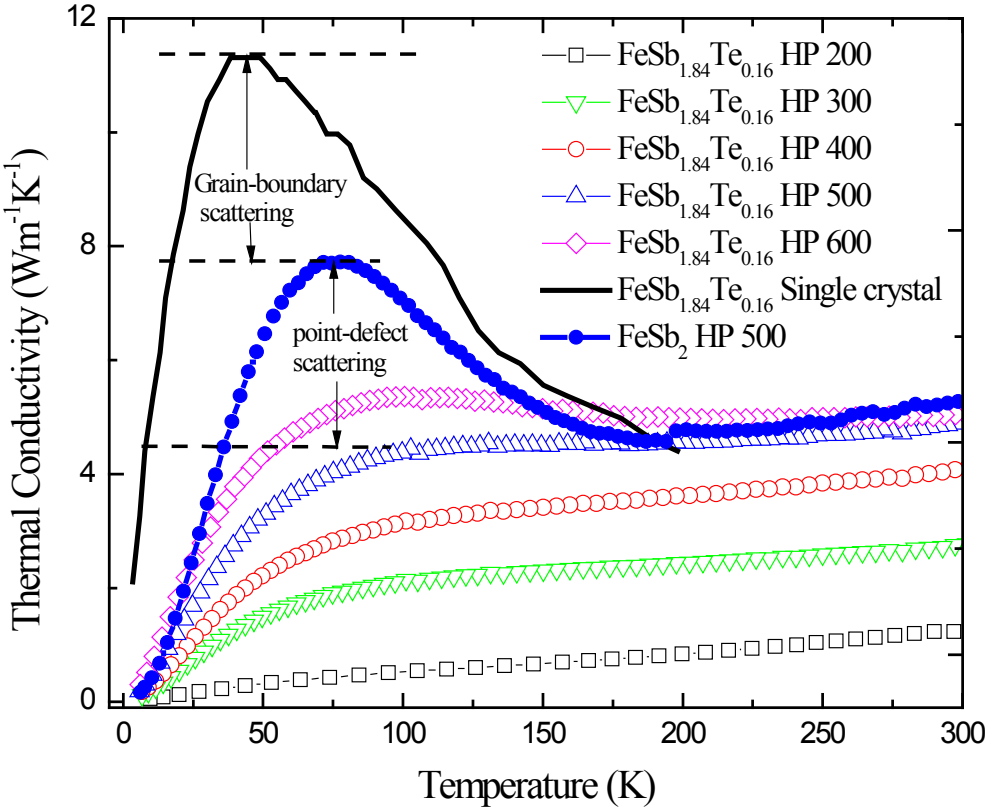

Figure 4.16 Thermal conductivity of the nanostructured $FeSb_{1.84}Te_{0.16}$ samples as a function of temperature. The data for single crystal of $FeSb_{1.84}Te_{0.16}$ (from reference [34]) and undoped $FeSb_2$ sample hot-pressed at 500 ^{o}C are also shown for comparison.

Figure 4.16 shows the temperature dependence of the thermal conductivity for the samples. The thermal conductivity values of all the nanostructured samples are significantly lower than the values reported for single crystal [6]. For the sample $FeSb_2$ HP 500, κ = 7.08 W m^{-1} K^{-1} at 100 K which is 76% lower than the value reported for single crystal $FeSb_2$ (~30 W m^{-1} K^{-1}). By doping with Te, the thermal conductivity was further reduced to 4.38 W m^{-1} K^{-1} in the representative sample $FeSb_{1.84}Te_{0.16}$ HP 500; a

reduction by 38%. In this way an overall reduction in thermal conductivity by 85% was achieved.

In general, $\kappa = \kappa_{carrier} + \kappa_{lattice}$. Here $\kappa_{carrier}$ and $\kappa_{lattice}$ are the carrier and lattice contributions respectively. Calculations based on the Wiedemann-Franz law ($\kappa_{carrier} = L_0\rho^{-1}T$) show that more than 99% of the total thermal conductivity of $FeSb_2$ comes from lattice vibrations (phonons). Therefore any reduction in the total thermal conductivity of this system is due to reduction in lattice contribution. The physics of the lattice thermal conductivity is commonly interpreted using the Debye approximation as explained in Chapter 2.The reduced (by 76%) thermal conductivity in our nanostructured samples is due primarily to scattering of the phonons off the grain boundaries. On the other hand, since addition of a small amount of Te should not change the Umklapp process and grain-boundary scattering that much, the additional reduction (by 38%) comes mainly from the point-defect scattering. It should be noted that the mass difference between Sb (121.75) and Te (127.60) is considerably small; therefore the difference in interatomic coupling force constants probably plays a dominant role in scattering of phonons in doped samples. The contributions of nanostructuring and defect scattering are depicted in Figure 4.16. A significant reduction of thermal conductivity in Te-doped $FeSb_2$ single crystals has been previously discussed in detail by Sun *et al* [16]. They attributed the thermal conductivity reduction to the introduced charge carriers rather than chemical disorder whereas Wang *et al.* [37] attributed the reduction to the enhanced point defect scattering caused by both the different bonding tendency and different thermal conductivities of Sb and Te.

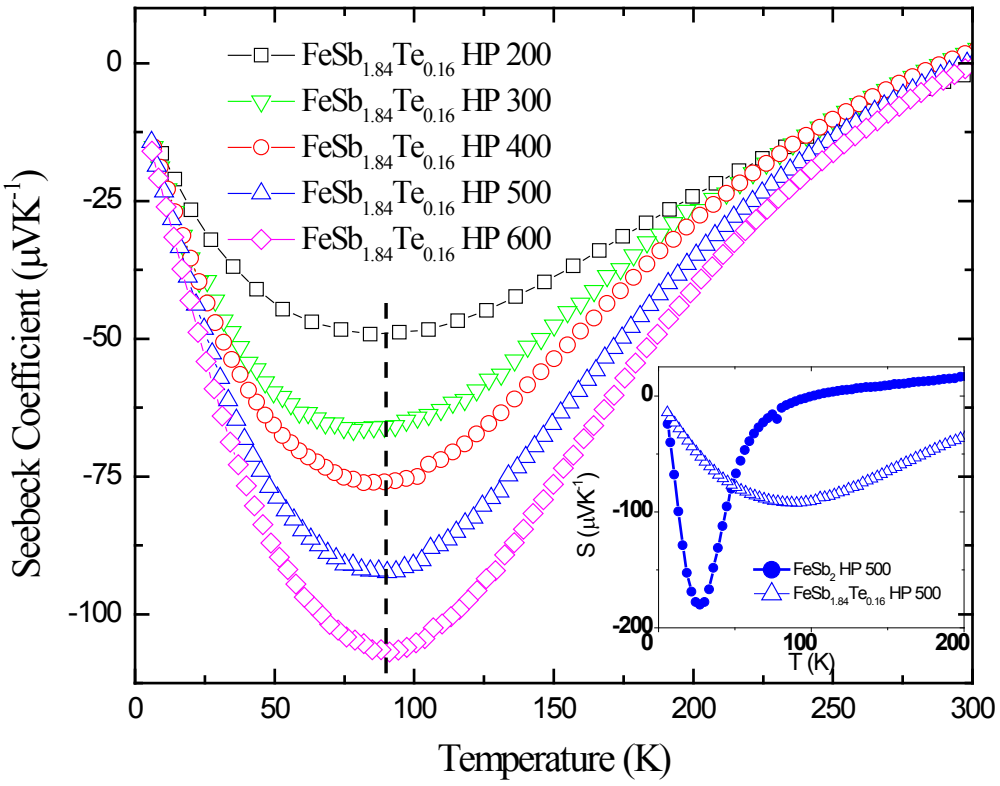

Figure 4.17 Seebeck coefficient of the nanostructured $FeSb_{1.84}Te_{0.16}$ samples as a function of temperature. The data for undoped $FeSb_2$ sample hot-pressed at 500 ^oC is also shown in the inset for comparison.

Figure 4.17 shows temperature dependence of the Seebeck coefficient. At 300 K, the Seebeck coefficient has a small positive value (p-type) ~2 μV K^{-1} for all the Te-doped samples. This value of Seebeck coefficient is significantly less than 31 μV K^{-1} observed for undoped samples. As the temperature decreases, the Seebeck coefficient decreases and changes to a negative (n-type) value at ~290 K. The Seebeck coefficient assumes a peak value at 90 K for all the samples. The largest peak value for the Seebeck coefficient among our samples is ~ -107 μV K^{-1} for sample $FeSb_{1.84}Te_{0.16}$ HP 600 which is two

orders of magnitude less than the reported value for undoped $FeSb_2$ single crystals [6] and is one-fourth of the value (~ - 400 μVK^{-1}) for $FeSb_{1.84}Te_{0.16}$ single crystals [16]. The peak value of the Seebeck coefficient decreases with decreasing hot pressing temperature. This decrease, based on our analysis, comes from two factors: increased carrier density and suppression of the phonon-drag contribution due to increased grain boundary scattering at lower hot-pressing temperatures [34]. The inset of Figure 4.17 shows the temperature dependent Seebeck coefficient for representative sample $FeSb_{1.84}Te_{0.16}$ HP 500 and its undoped counterpart $FeSb_2$ HP 500. Upon Te-doping, peak value of the Seebeck coefficient decreases and shifts to a higher temperature. A similar shifting of the Seebeck peak with increasing Te-content has been reported also in reference [16].

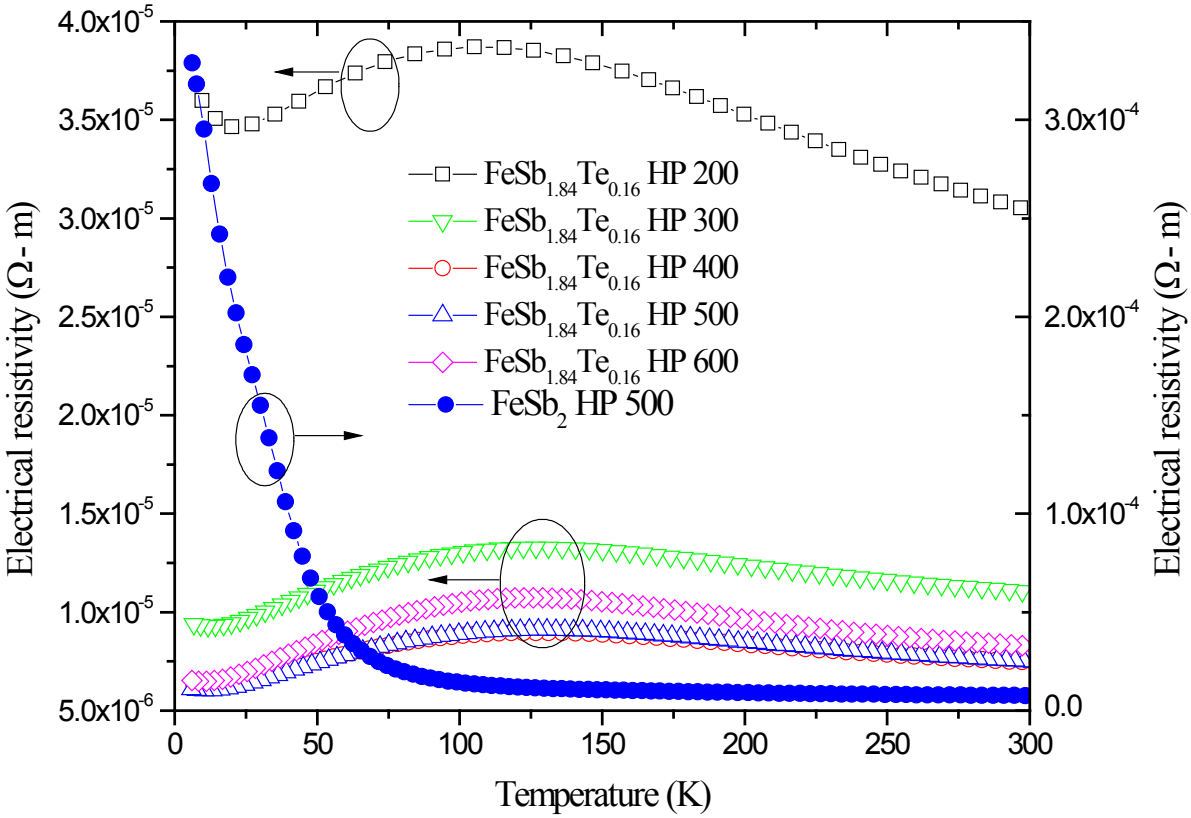

Figure 4.18 Electrical resistivity (left y-axis) as a function of temperature for the five Te-doped samples. The right y-axis corresponds to the electrical resistivity for the undoped sample $FeSb_2$ HP 500.

Figure 4.18 shows the temperature dependence of the electrical resistivity for the samples. The electrical resistivity of the sample $FeSb_2$ HP 500 is represented by the right y-axis. The undoped sample exhibits semiconducting behavior throughout the temperature range 5-300 K with increasing resistivity as temperature decreases. A sharp increase in resistivity below 70 K indicates an insulating ground state. In contrast to the undoped $FeSb_2$, the Te doped samples exhibit suppressed electrical resistivity with a metallic ground state. The electrical resistivity decreases by one order of magnitude at

100 K. The semiconductor to metal transition temperature for the different samples falls within the range of 100 – 130 K.

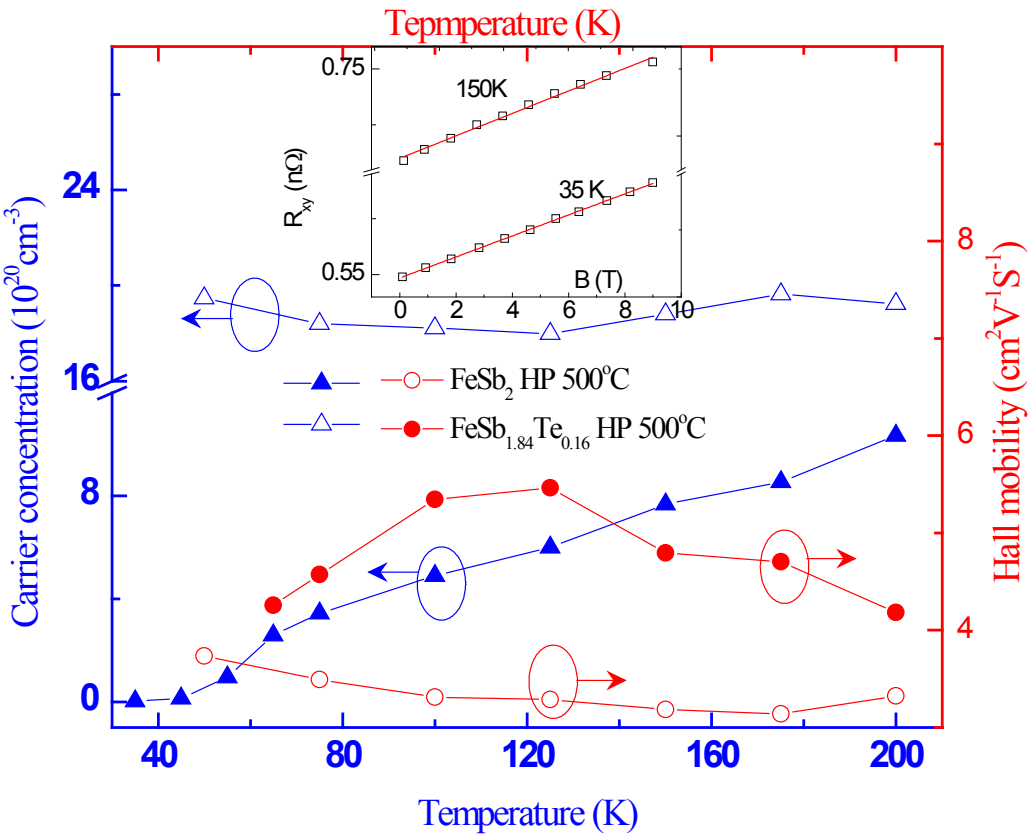

Figure 4.19 Hall carrier density and Hall mobility of the nanostructured $FeSb_{1.84}Te_{0.16}$ samples as a function of temperature. The inset shows linear dependence of Hall resistance on applied magnetic field.

Figure 4.19 shows the temperature dependence of the carrier concentration (n) and the Hall mobility (μ) for the undoped and doped nanostructured samples pressed at 500 °C. n and μ were estimated from the Hall coefficient (R_H) and electrical resistivity (ρ) measurements using $n = 1/|R_H|e$ and $\mu = |R_H|/\rho$, under the single parabolic band model. Here $e = 1.6 \times 10^{-19}$ C is the electronic charge. At 100 K, the carrier concentration of the doped sample is increased by one order of magnitude when compared with that of

undoped sample. Also, the carrier concentration is less temperature sensitive for doped samples, a result consistent with the metallic nature seen in the electrical resistivity data at lower temperatures. The Hall mobility is reduced in the doped sample. For example, μ = 5.3 $cm^2\ V^{-1}\ S^{-1}$ and 3.3 $cm^2\ V^{-1}\ S^{-1}$ for samples $FeSb_2$ HP 500 and $FeSb_{1.84}Te_{0.16}$ HP 500, respectively at 100 K.

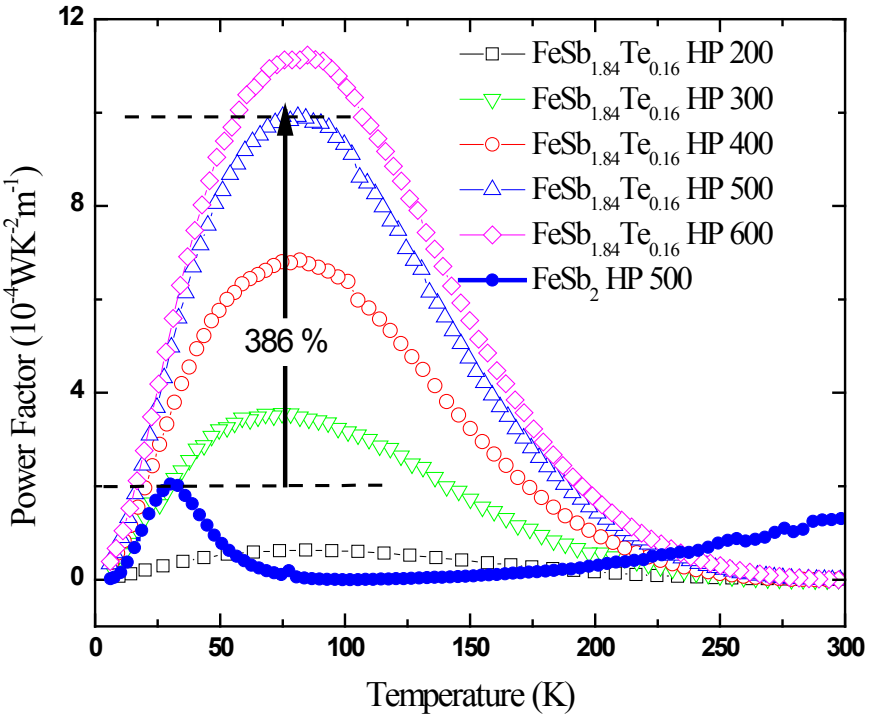

Figure 4.20 Thermoelectric power factor of the nanostructured $FeSb_{1.84}Te_{0.16}$ samples as a function of temperature.

Figure 4.20 shows the temperature dependence of the power factor ($S^2\rho^{-1}$). When compared with the undoped nanostructured samples, the power factors in the Te-doped samples increased significantly. For example, $S^2\rho^{-1} = 9.9 \times 10^{-4}$ W m^{-2} K^{-1} at 80 K for the representative sample $FeSb_{1.84}Te_{0.16}$ HP 500, which is an increase of 386 % from the

corresponding value for the undoped sample $FeSb_2$ HP 500. Among the Te-doped samples, the peak values for the power factor decrease with decreasing the hot-pressing temperature.

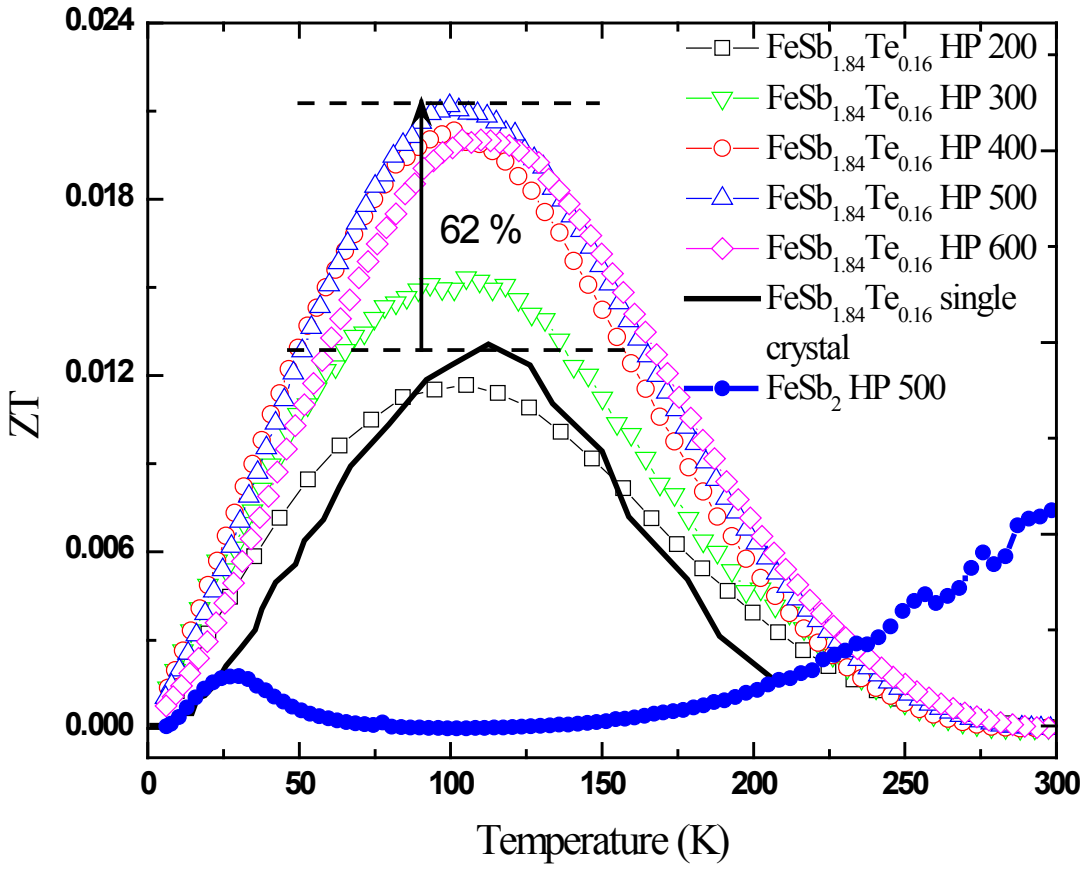

Figure 4.21 ZT of the nanostructured $FeSb_{1.84}Te_{0.16}$ samples as a function of temperature. The data for single crystal is also shown for comparison.

In Figure 4.21, we have presented *ZT* as a function of temperature. For all the doped samples, the curve assumes a peak value (ZT_{max}) at around 100 K. For the optimized sample $FeSb_{1.84}Te_{0.16}$ HP 500, ZT_{max} = 0.022 at 100 K, this is an increase of 62 % compared with the optimized value for the Te-doped single crystal which was 0.012 in

reference [16]. When compared with the *ZT* of $FeSb_2$ HP 500 (ZT_{max} = 0.0017 at 25 K), the *ZT* values for the optimized sample $FeSb_{1.84}Te_{0.16}$ HP 500 is increased by a factor of 11.

In conclusion, nanostructured samples of $FeSb_{1.84}Te_{0.16}$ have been prepared using the hot-press method and their thermoelectric properties have been studied in the range of temperatures 5 – 300 K. Based on our analysis, the grain-boundary scattering and the point-defect scattering are the two dominant phonon scattering mechanisms that contributed to a significantly reduced (by 85% at 100 K) thermal conductivity in Te-doped nanostructured samples. Te-doping in $FeSb_2$ contributed not only to the thermal conductivity reduction but also to enhanced power factor by inducing a semiconductor to metal transition. With a decrease in hot-pressing temperature, both the thermal conductivity and the power factor decreased. The optimal conditions for *ZT* were observed for the doped sample hot pressed at 500 ^{o}C. The *ZT* value of 0.022 at 100 K was observed for the optimized sample $FeSb_{1.84}Te_{0.16}$ HP 500, 62% higher than the corresponding value for the single crystal. Therefore, it has been successfully demonstrated that combining the technique of doping with nanostructuring significantly enhances the thermoelectric performance of $FeSb_2$ at low temperatures. This approach can easily be extended to improve ZT of other phonon dominated thermoelectric systems at low temperatures.

4.5 Effect of Nanoinclusions

Currently developed approaches to optimize thermoelectric properties of materials, such as nanostructures reducing lattice thermal conductivity [21, 31, 39],

resonant doping [40, 41, 42], band engineering [43, 44] at the Fermi level, as well as modulation doping providing additional electrical conductivity channels [45, 46], have been proven to be efficient in a few material systems. In the literature, the metal/semiconductor interface concept was proposed theoretically and testified experimentally in a few cases for their potential application in thermoelectric materials [47-52]. Indeed, modeling shows that, by introducing uniformly distributed metal nanoparticles to the three-dimensional semiconductor structure, either electronic (κ_e) or phononic (κ_{ph}) thermal conductivity, and thus the total thermal conductivity can be suppressed dramatically [49]. Furthermore, due to the energy barrier (V_B) built between metal nanoparticles and the host semiconductor at the interfaces, the lower energy carrier could be scattered, which would result in a reduced electrical conductivity but an enhanced Seebeck coefficient. As a result, the power factor could be enhanced and an enhanced ZT could be expected. However, for a phononic thermal conductivity dominated system, the modeling showed that a much smaller V_B than 0.03 eV is preferred to secure an even slightly enhanced PF [49], and zero energy barriers at the interface would be expected in the real case even though there is no net gain on PF. Overall, for a phononic thermal conductivity dominated system, the enhanced ZT could be expected solely from the reduced thermal conductivity through the metal/semiconductor nanocomposite approach. In reality, due to the difficulty matching the semiconductor with the right metals, there has been no convincing demonstration of this concept. In this section, effect of Ag and Cu nanoinclusions on the thermoelectric properties of $FeSb_2$ will be discussed.

4.5.1 Ag-nanoinclusion

Various numbers of Ag nanoparticles (NPs) (100 nm, Aldrich) were added to the synthesized $FeSb_2$ powders with the targeted final nominal composition $FeSb_2Ag_m$ with m = 0.028, 0.056, 0.11, 0.22, and 0.33. Together with the $FeSb_2$ nanopowder, each individual composition having the weight of 5 g was further mixed via ball milling for 3 hours. The direct current (dc) hot pressing method was used to prepare disk samples from the final powders with different compositions. All disk samples were pressed at 200 ^oC and 80 MPa for 2 min, resulting densities in the range of 5.91– 6.01 g cm^{-3}, about 76.8% –78.1% of the theoretical densities of 7.70 g cm^{-3}.

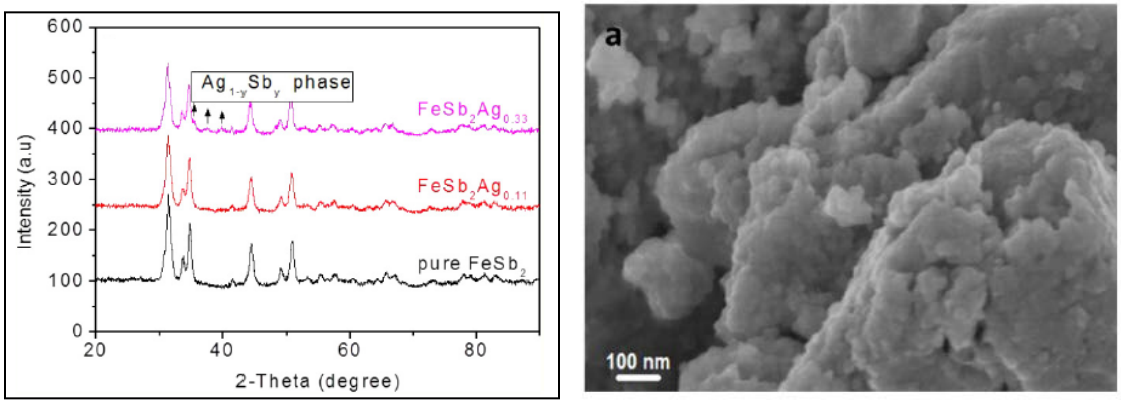

(a) (b)

Figure 4.22 (a) X-ray diffraction pattern of pure $FeSb_2$ and $FeSb_2Ag_m$ (m = 0.11, 0.33). (b) SEM image of representative sample $FeSb_2Ag_{0.11}$.

X–ray diffraction pattern of pure $FeSb_2$ and $FeSb_2Ag_m$ (m = 0.11, 0.33). are shown in Figure 4.22 (a). Some of the Ag replaces Sb of $FeSb_2$ whereas some of it reacts with Sb which is evidenced by the presence of a secondary phase of $Ag_{1-y}Sb_y$ in $FeSb_2Ag_m$ composition. Essentially, nanostructured samples of $FeSb_{2-x}Ag_x$ with $Ag_{1-y}Sb_y$ nanoinclusions are obtained. Because the densities and grain sizes (~30 nm) of all six

samples are very similar, only an SEM image for sample $FeSb_2Ag_{0.11}$ is shown in figure 4.22(b). It can be seen that the sample is composed of micro-sized aggregates consisting of much smaller grains of 30 nm on average, which is consistent with the TEM observation [53]. Figure 4.23(a) is the schematic of phonon scattering due to $Ag_{1-y}Sb_y$ nanoinclusions dispersed in $FeSb_2$ host.

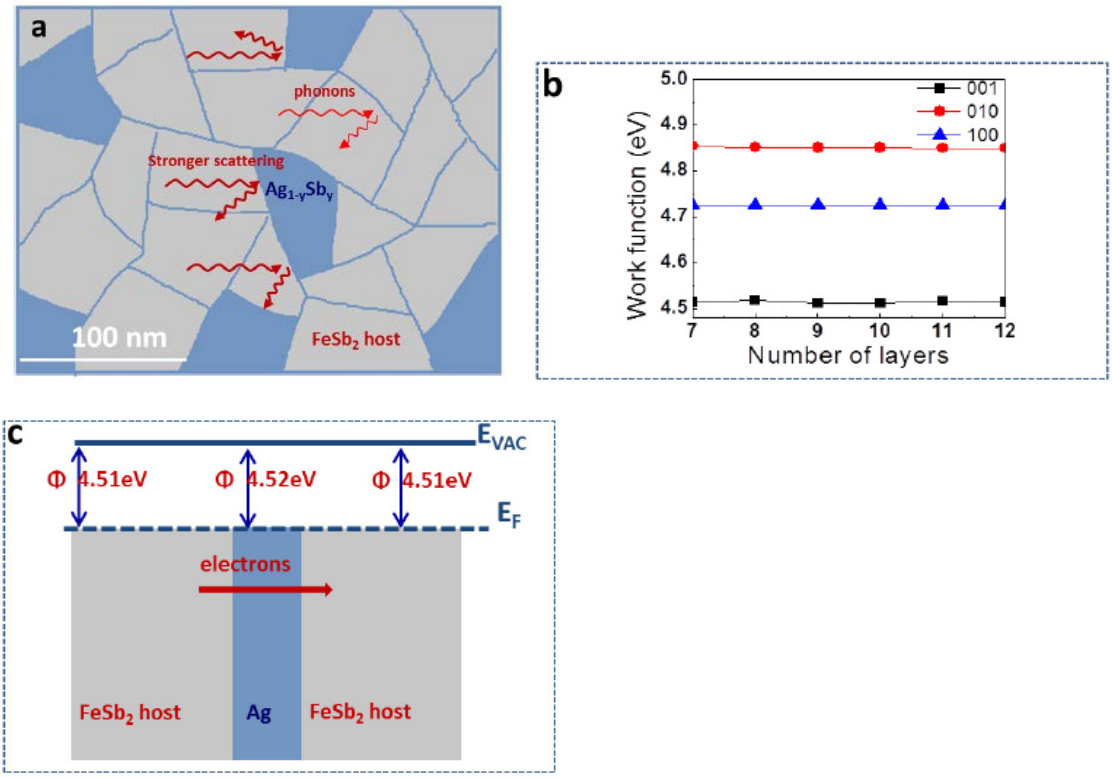

Figure 4.23 (a) Schematic representations of $Ag_{1-y}Sb_y$ nanoinclusions present in $FeSb_2$ host material and scattering of phonons (b) DFT convergence plot on work function of $Fesb_2$. (c) Band alignment and electron diffusion.

In addition to the phonon scattering by nanograins as we have reported [31], the interface shown in Figure 4.23 (a) between FeSb2-xAg_x and $Ag_{1-y}Sb_y$ can also scatter the medium to long wavelength phonons as predicted by theory [48, 49]. The work function of $FeSb_2$ can be simply calculated by subtracting the Fermi level from the vacuum energy

level. The work functions of $FeSb_2$ were calculated to be 4.514 eV for the (001) plane, 4.852 eV for the (010) plane, and 4.723 eV for the (100) plane (as shown in Figure 4.23 (b)). Meanwhile, the reported work functions of silver are 4.52 eV for the (110) plane and 4.74 eV for (111) plane [31]. It is noted that Ag and $FeSb_2$ have similar work functions in at least two crystal planes. Figure 4.23(c) shows the band alignment and the electron transport between the (110) plane of silver and (001) plane of $FeSb_2$. Due to the similarity of work functions between Ag and $FeSb_2$ in these planes, it can be argued that due to band alignment there is no energy barrier at the interface. Based on the model developed by Kim *et al.* [48], it is reasonable to speculate that the electrons transported from $FeSb_2$ to Ag will be minimally scattered and enhanced ZT can be expected solely from thermal conductivity reduction in the nanocomposite.

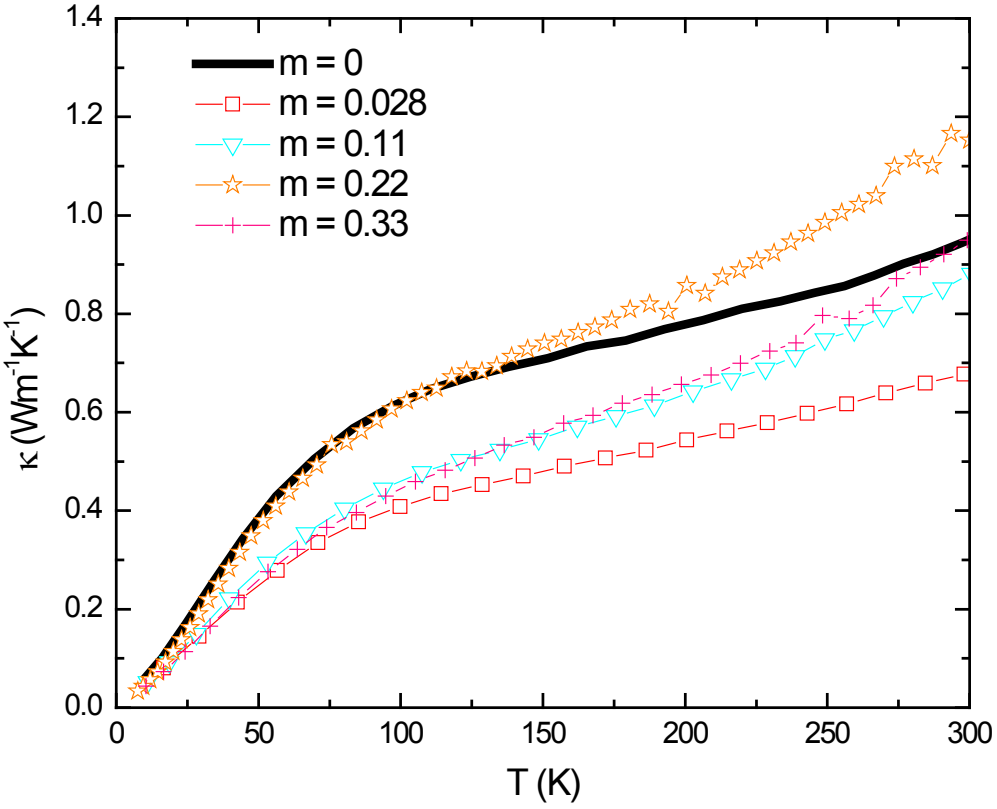

Figure 4.24 Thermal conductivity of the $FeSb_{2-x}Ag_x/Ag_{1-y}Sb_y$ nanocomposite samples as function of temperature.

A significant thermal conductivity reduction for all $FeSb_2Ag_m$ composites is observed as shown in Figure 4.24. At 50 K, with the increase of Ag content, thermal conductivity first decreased to a minimum of 0.24 W m^{-1} K^{-1} for nanocomposite $FeSb_2Ag_{0.028}$ from 0.38 W $^{m-1}$ K^{-1} for pure nanostructured $FeSb_2$. The TEM and EDX investigations [53] for all $FeSb_2Ag_m$ samples revealed uniformly distributed $Ag_{1-y}Sb_y$ nanoparticles in these nanocomposites with an average size of 20 nm. With the increase of Ag content, allargentum, $Ag_{1-y}Sb_y$, emerged as a significant phase in $FeSb_2Ag_m$ nanocomposite. Owing to the high thermal conductivity of $Ag_{1-y}Sb_y$ metal phase, the total

thermal conductivity in the nanocomposite increases with the increase of Ag content, and reaches a maximum at 0.29 W $^{m-1}$ K^{-1} for $FeSb_2Ag_{0.22}$. Meanwhile, with the increase of Ag, the phonon scattering from the interfaces between $FeSb_{2-x}Agx$ and $Ag_{1-y}Sb_y$ became dominant and eventually outweighed the contribution of the $Ag_{1-y}Sb_y$ metal phase, and the total thermal conductivity decreased to another low level at 0.26 W $^{m-1}$ K^{-1} for $FeSb_2Ag_{0.33}$ nanocomposite.

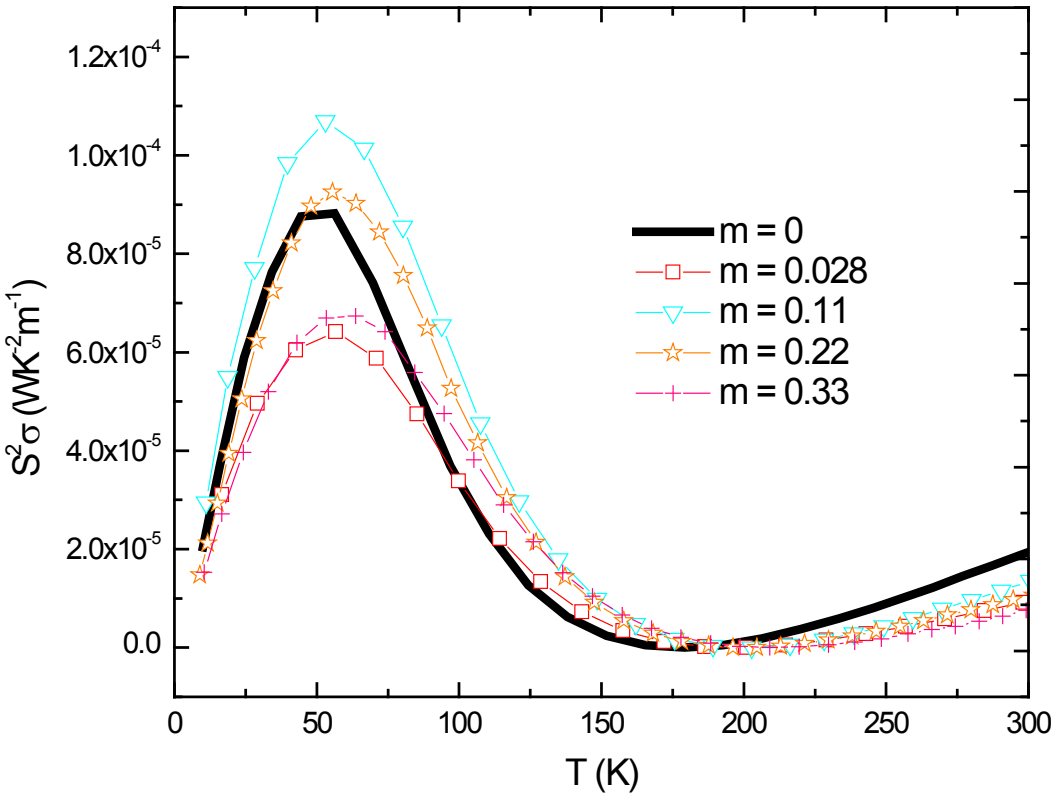

Figure 4.25 Thermoelectric power factor of the $FeSb_{2-x}Ag_x/Ag_{1-y}Sb_y$ nanocomposite samples as function of temperature.

The power factor (PF) in Figure 4.25 shows a trade-off between the Seebeck

coefficient and the electrical resistivity. Due to relatively less affected value of the Seebeck coefficient, the sample $FeSb_2Ag_{0.11}$ exhibits tallest peak in the power factor. The peak value of the power factor increases with the increasing Ag content, assumes maximum for m = 0.11 and decreases on further increasing m values. A further explanation of the Ag-nanoinclusion effect can be found in reference [53].

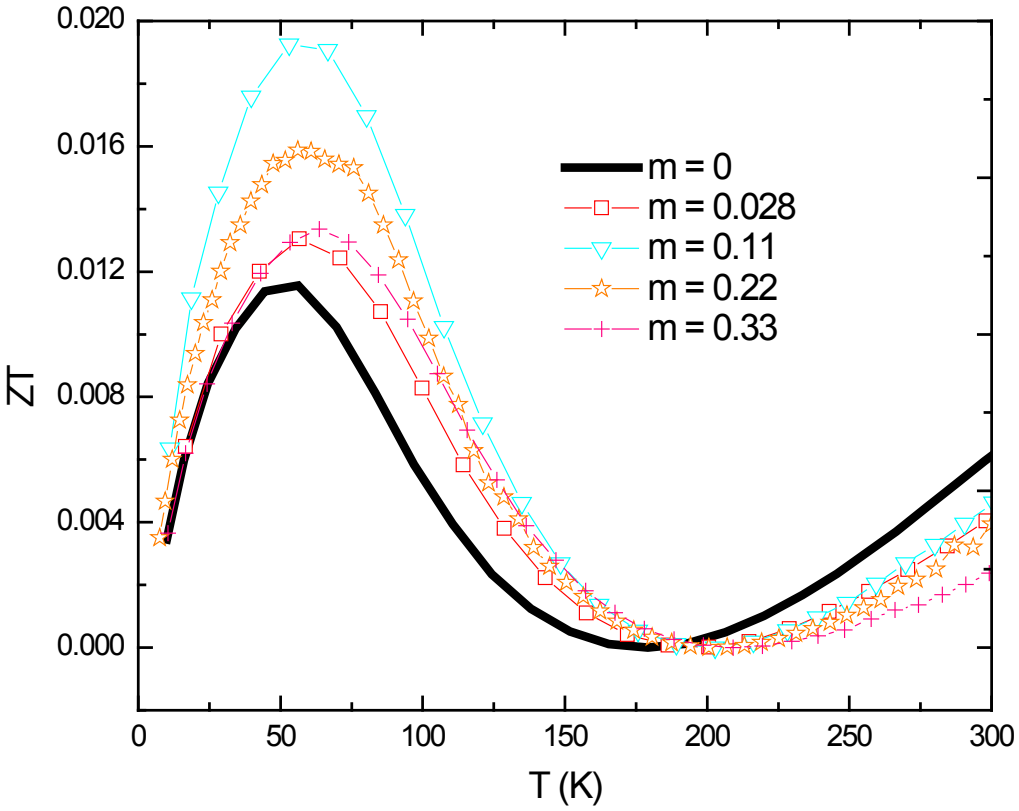

Figure 4.26 ZT of the $FeSb_{2-x}Ag_x/Ag_{1-y}Sb_y$ nanocomposite samples as function of temperature.

Figure 4.26 shows the temperature dependent ZT of the samples with Ag nanoinclusions. By taking advantage of the greatly reduced thermal conductivity for all

$FeSb_2Ag_m$ nanocomposites, the peak ZT are enhanced to 0.02, which is four times higher than the single crystal value [6], and 70% improvement over the best undoped $FeSb_2$ nanocomposite discussed in section 4.3.2.

Being a phonon thermal conductivity dominated system; the thermal conductivity reduction in $FeSb_2Ag_m$ nanocomposites is not too surprising. Inspired by the model proposed by L´eonard [49], the band bending and Fermi level alignment at the interface of $FeSb_2$ and Ag showed there is no significant potential barriers. Reasonably, the electron configuration at the $FeSb_{2-x}Ag_x$ and $Ag_{1-y}Sb_y$ without any need to overcome energy barriers, led to increased electrical conductivity for the composites. From this investigation an improved ZT is shown to be plausible through tuning the nature of metal phase, size, and distribution of the grains in the nanocomposite. These results also provide insight for the application of metal/semiconductor interfaces in other strongly correlated materials or Kondo systems for increasing ZT.

4.5.2 Cu-nanoinclusions

Inspired by the results, achieved with the $FeSb_{2-x}Ag_x/Ag_{1-y}Sb_y$ nanocomposite by adding Ag nanoparticles (NPs) into the $FeSb_2$ system (section 4.5.1), the Cu nanoparticles were introduced. A similar approach was used in the synthesis of a SiGe alloy which showed significant amounts of B or P diffused easily into the parent compound [45, 46]. In the case of Cu nanoparticles in $FeSb_2$ there is no evidence of diffusion. As seen with Ag-nanoinclusion, the work functions of the (100) planes in $FeSb_2$ and Cu are similar and therefore facilitate the electron transfer from Cu to $FeSb_2$ at their interfaces to increase the electrical conductivity.

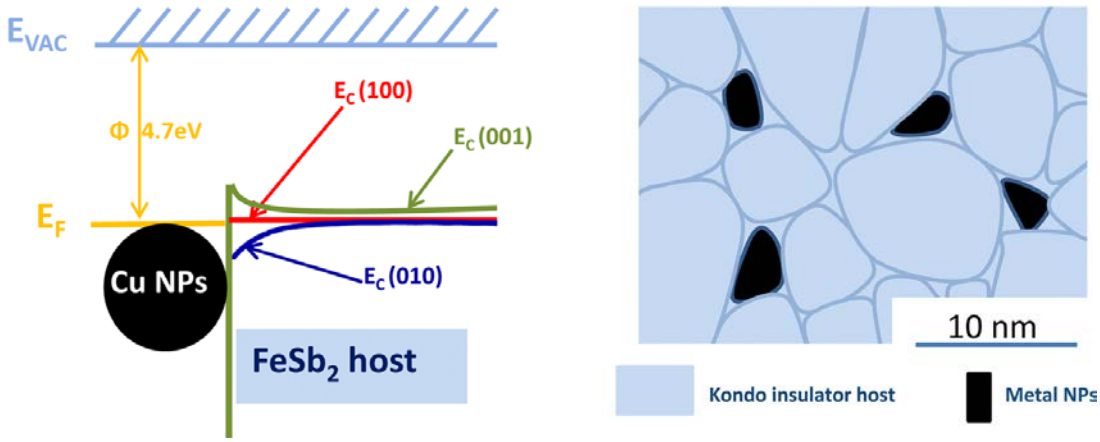

Figure 4.27 Schematics of (a) band aignment between $FeSb_2$ and Cu and (b) distribution of Cu nanoparticles in $FeSb_2$. Scale bar indicates that the grains of FeSb2 are around 50 nm on average and 5 nm for Cu NPs.

Figure 4.27 shows the schematics of (a) band alignment of $FeSb_2$ and Cu and (b) distribution of Cu nanoparticles in host $FeSb_2$.The $FeSb_2/Cu_x$ nanocomposites were synthesized by two procedures. For the synthesis of nanocomposites with 5nm Cu nanoparticle inclusions, a total of 25 grams of Fe, Sb, and Cu with the stoichiometry of $FeSb_2Cu_y$ (y = 0.0225, 0.045, and 0.09) were mixed and sealed in vacuum in a quartz tube. Following a high temperature melt, quenching and 12 h of ball milling, 3 g of the ball milled powders with various amounts of Cu nanoparticles (NPs) were pressed at 200 ^oC and 80 MPa for 2min using direct current (dc) induced hot pressing method. For the synthesis of nanocomposites with 100 nm Cu nanoparticle inclusion, $FeSb_2$ nanopowders were first prepared, then Cu NPs (100 nm, Aldrich) were added into the powder with a final nominal composition of $FeSb_2Cu_{0.045}$. The mixed powders of 5g were further ball milled for 3 h. After this 3 h ball milling, some of the 100 nm Cu particles may be milled to smaller nanoparticles, but should still be larger than 5 nm. Disk samples were prepared

by the same method mentioned above. Details of sample preparation and measurements can also be found in reference [54].

Figure 4.28 shows temperature dependence of thermal conductivity for all $FeSb_2Cu_y$ composites as well as the pure nanostructured $FeSb_2$. First, owing to the interfaces between Cu NPs and $FeSb_2$, reduced thermal conductivity was observed for most samples. For all nanocomposites with 5 nm Cu NPs, it is seen that with the increase of Cu content (inset of Fig. 4.28 (a)), thermal conductivity at 60K decreased slowly to a minimum of $0.39 Wm^{-1}K^{-1}$ for $FeSb_2Cu_{0.045}$ from $0.44 Wm^{-1}K^{-1}$ for the pure nanostructured $FeSb_2$. We believe that this is due to the phonon scattering at the interface of $FeSb_2$ and Cu. When the Cu volume ratio reaches 1.8% for sample $FeSb_2Cu_{0.09}$, thermal conductivity becomes comp arable to the pure nanostructured

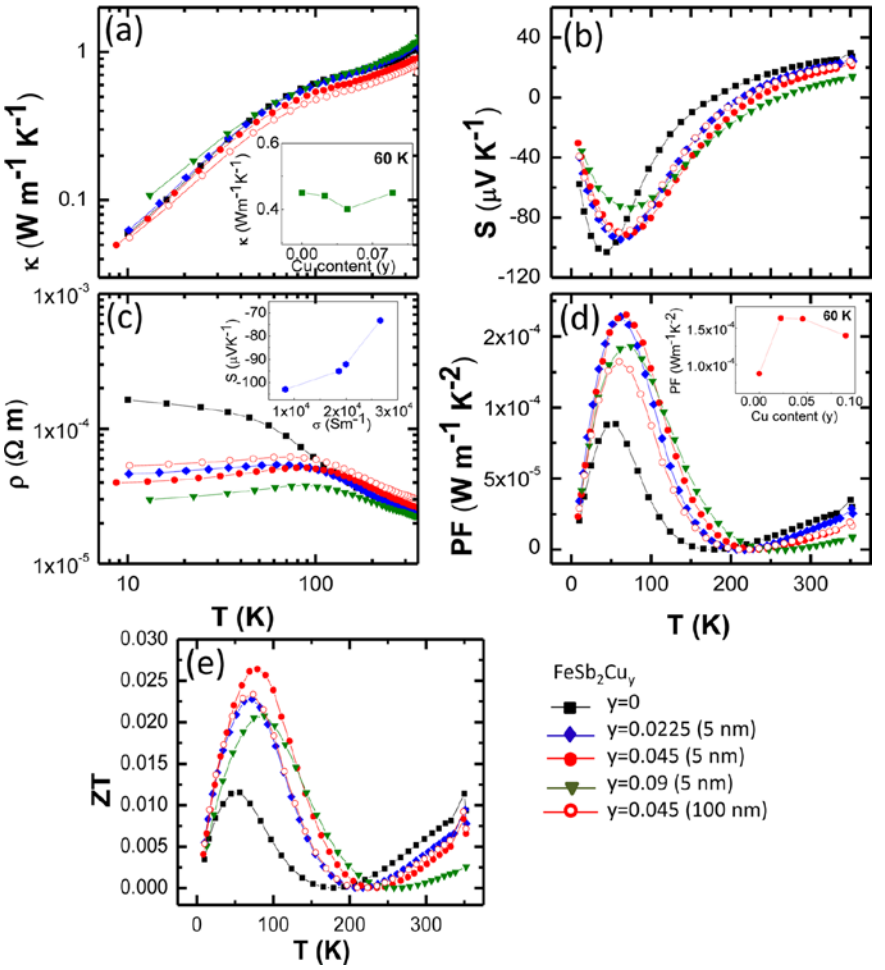

Figure 4.28 Thermoelectric properties of $FeSb_2Cu_y$ (y = 0, 0.0225, 0.045, 0.09) samples: (a) temperature dependence of thermal conductivity, inset shows the measured thermal conductivity versus Cu content at 60 K; (b) temperature dependence of Seebeck coefficients; (c) temperature dependence of electrical resistivity, inset shows the peak Seebeck coefficient versus electrical conductivity at corresponding temperatures; (d) temperature dependence of power factor, inset shows the peak value of power factor at 60K versus Cu content; and (e) temperature dependence of ZT for $FeSb_2$ and $FeSb_2Cu_y$ nanocomposites.

$FeSb_2$ and even larger below 50 K, which shows that the contribution of increased

electron thermal conductivity outweighs the decrease of the lattice thermal conductivity.

Seebeck coefficient results were shown in Fig. 4.28 (b). Interestingly, the Seebeck coefficient only slightly decreases from 102 μVK^{-1} to 93 μVK^{-1} even though the electrical conductivity is increased by a factor of 2 as shown is Figure 4.28 (c) for the $FeSb_2Cu_{0.045}$ sample with 5 nm Cu NPs comparing to pure FeSb2. The relatively high Seebeck coefficients at different concentrations of Cu nanoparticles can be understood as the result of modulation doping since the matrix $FeSb_2$ is not significantly affected.

Regarding the electrical conductivity as shown in Figure 4.28 (c) we have achieved significant improvement by incorporating Cu NPs to the nanostructured $FeSb_2$. Inset in Figure 4.28 (c) shows a peak Seebeck coefficient dependence of electrical conductivity for all nanocomposites with 5 nm Cu NPs inclusion.

Because of the increased electrical conductivity and slightly reduced Seebeck coefficient for the $FeSb_2Cu_y$ nanocomposites, we observe a significant power factor PF improvement below 200 K for all Cu NPs incorporated nanocomposites compared to pure $FeSb_2$. As can be seen from Figure 4.28 (d) a maximum PF $1.64 \times 10^{-4} Wm^{-1}K^{-2}$ at 60K was obtained for $FeSb_2Cu_{0.0225}$ before decreasing to $1.39 \times 10^{-4} Wm^{-1}K^{-2}$ for $FeSb_2Cu_{0.045}$. Combined with the slight decrease of thermal conductivity, ZT of 0.027 has been achieved, that is 110% enhancement over 0.013 achieved in the nanostructured pure $FeSb_2$ at 60 K.

4.6 Phonon-drag Effect in $FeSb_2$

In earlier works explained above, we were able to reduce the thermal conductivity by three orders of magnitude in nanocomposite samples. However the Seebeck coefficient in the nanocomposites is severely degraded at low temperatures when

compared to that of the single crystal counterpart. For optimized sample with $\kappa = 0.40$ $Wm^{-1}K^{-1}$ and $\rho = 1.2 \times 10^{-4}$ Ω-m at 50 K, a Seebeck coefficient of - 970 μVK^{-1} is required to achieve a ZT of 1. But the measured value of the Seebeck coefficient at 50 K was only -109 μVK^{-1}. So it is important to know the origin of the large Seebeck coefficient in this system so that we can further improve the ZT.

The classical theory of thermoelectricity is based on the assumption that the flow of charge carriers and the phonons can be treated independently. Under this assumption, the Seebeck coefficient arises due solely to spontaneous electron diffusion. However when the two flows are linked, the effect of electron-phonon scattering should be taken into account [55]. Hence, in general, the Seebeck coefficient is the sum of two independent contributions from spontaneous electron diffusion and phonon-drag as given by equation 2.39. In phonon-drag picture, the carriers are preferentially scattered or dragged by the phonons toward the cold end of the sample. This dragging gives rise to an additional thermoelectric emf. Generally, such an effect becomes stronger at lower temperature region where the phonon mean free path becomes longer. Since only the long wavelength phonons are involved, the size effect on this phenomenon becomes appreciable even in the large size before other phenomena start to see this effect.

The origin of enormous Seebeck coefficient of $FeSb_2$ at low temperature has not been completely understood. Many authors [15 - 19] suggested a strong electron-electron correlation as a possible cause. However, recently there have been several authors [56, 57] who argue for the electronic origin of the colossal value of the Seebeck coefficient in $FeSb_2$. In this section, analysis of the thermoelectric properties of the $FeSb_2$

nanocomposites showing a substantial phonon-drag contribution to the huge Seebeck coefficient will be presented.

Table 4.2 Sample code, pressing temperature and average grain-size for the four nanostrucruted samples used for phonon-drag analysis.

Sample code	Hot pressing temperature (°C)	Average grain size (nm)
S-300	300	30
S-400	400	100
S-500	500	350
S-600	600	20,000

Four nanostructured $FeSb_2$ samples were synthesized by ball milling and hot-pressing technique as described in chapter 3. Different pressing temperatures yielded different grain sizes in the samples. The average grain-size corresponding to four different pressing temperatures are given in Table 4.2. The thermoelectric properties of the samples were measured in PPMS.

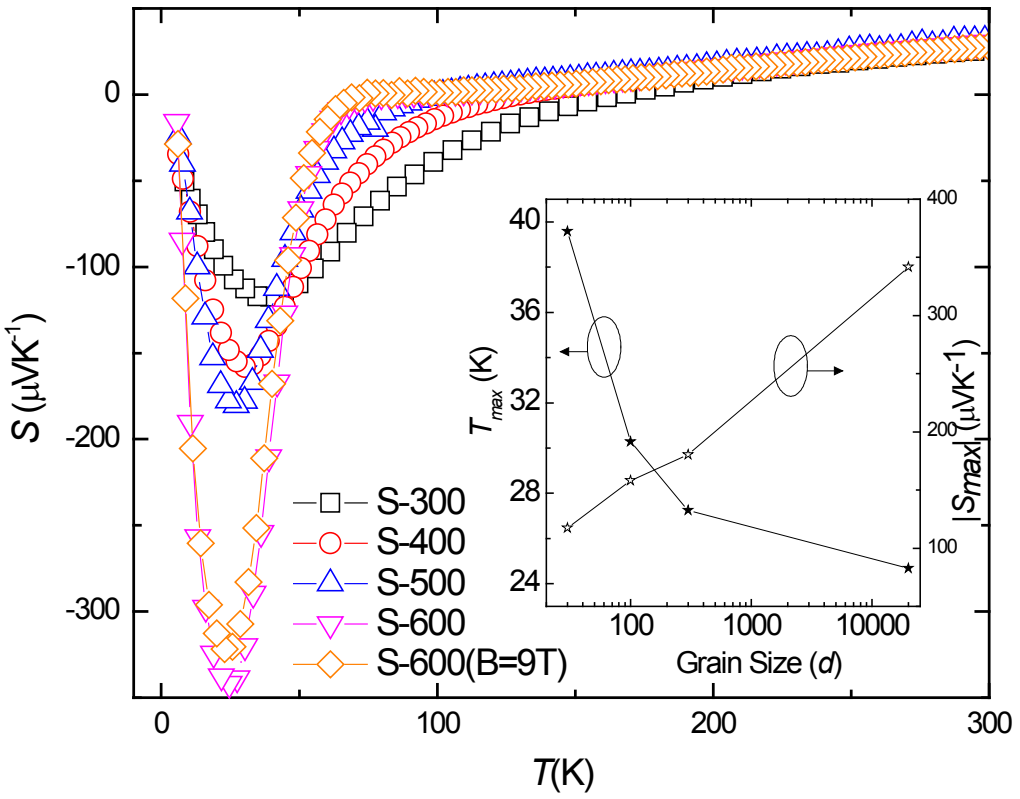

Figure 4.29 Temperature dependence of the Seebeck coefficient of the four samples. Sample S-600 was measured both at 0 and 9 Tesla magnetic fields. Inset: The grain size dependence of the peak value of the Seebeck coefficient (S_{max}) and the peak position (T_{max}).

Figure 4.29 shows the temperature dependence of the Seebeck coefficient for the four nanocomposite samples. Sample S-600 was measured both in magnetic fields of 0 and 9 Tesla. The Seebeck coefficients of all the samples are significantly smaller than that of single crystal at low temperature whereas at high temperature the values are comparable. For single crystal a room temperature value of 31 μVK^{-1} was reported

[58]. For all of our samples it is ~ 26 μVK^{-1}. A decrease in Seebeck coefficient at low temperature in polycrystal [15], arsenic-substituted $FeSb_2$ single crystals [5] and thin films [59] were reported earlier. As shown in the inset of Figure 4.29, the peak value of the Seebeck coefficient (S_{max}) decreases with the decreasing grain size. In phonon-drag picture, this is expected because the nonelectronic scattering (grain boundary scattering in case of nanocomposites) reduces the phonon mean free path which in turn decreases the phonon-drag contribution. A similar conclusion was made by authors in reference [57]. Weber *et al*. [60] showed, using the semiconducting point contacts of silicon that when the contact size becomes comparable to the mean free path of the relevant phonons, the phonon-drag part of the thermopower is suppressed by the boundary scattering. Here we also note that the temperature profile of Seebeck coefficient for the samples with larger grains follow the typical behavior of phonon-drag system as suggested by Blatt [61].

The Seebeck peaks shift to the higher temperature when the grain size decreases (inset of Figure 4.29). This type of size dependent shift in Seebeck peak is one of the characteristics of the phonon- drag dominated systems as pointed out by many authors [62-64].

Usually, a small magnetothermopower is expected for the phonon-drag dominated system. For sample S-600 at 25 K, $\frac{S(9T)-S(0T)}{S(0T)} = 0.059$ was observed. Such a small value supports the non-electronic origin of the large Seebeck coefficient in this sample.

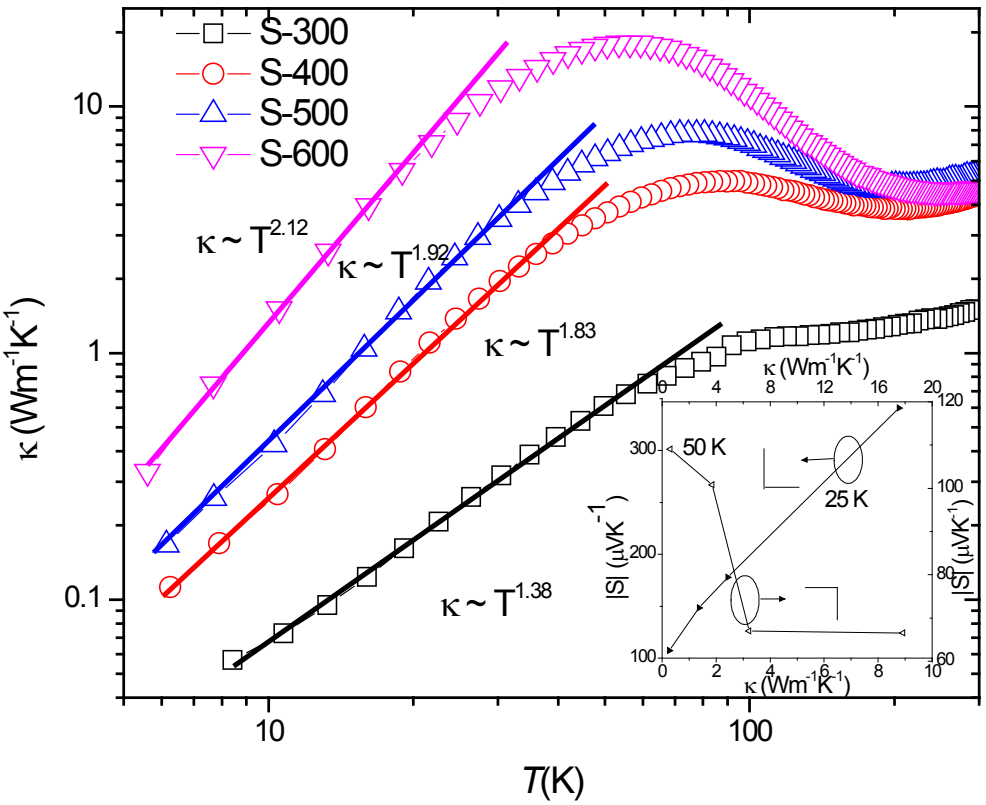

Figure 4.30 Temperature dependence of the thermal conductivity of the four samples. The fitting to the power law was applied for all the samples below 50 K. Inset: Seebeek coefficient as a function of thermal conductivity at 25 K and 50 K.

Figure 4.30 shows the temperature dependence of thermal conductivity (κ). Calculation based on Widemann-Franz law shows that more than 97% of the total thermal conductivity comes from the lattice contribution. For coarse-grained samples $\kappa \sim T^2$ is nearly obeyed at temperature below 50 K. As the grain size goes down, a gradual deviation from the T^2-law occurs. Weber *et al.*[60], reported a similar T^2 behavior in silicon below 20 K which they attributed to the strong electron-phonon scattering. For a coarse-grained sample, the number of available phonons interacting

with the carriers is large and as the grain size decreases this number decreases causing a gradual deviation from the T^2-law. Peruchhi *et al*.[7],through optical spectroscopy, reported a large change in phonon lifetimes across metal-insulator transition indicating the presence of electron-phonon coupling whereas Lazarevic *et al*.[65] suggested the presence of temperature dependent electron-phonon coupling below 40 K in single crystals.

The inset of Figure 4.30 shows the change in Seebeck coefficient with thermal conductivity for temperatures 25 K and 50 K. At 25 K, the Seebeck coefficient increases almost linearly with the thermal conductivity. This clearly indicates that phonons play a significant role in determining Seebeck coefficient values of our samples at around 25 K. At 50 K, however the Seebeck coefficient decreases with increasing thermal conductivity without any obvious trend. At higher temperature, the phonon-mean free path decreases and the phonon-drag effect becomes weak.

Significant phonon drag effect is expected to occur when the dominant phonons acquire sufficient momentum to scatter carriers across Fermi surface. In a rough approximation, $T_{max} \approx \frac{1}{10}\theta_D$, where T_{max} is the temperature at which phonon drag peak occurs and θ_D is the Debye temperature. For rutile TiO_2 [66], θ_D is 450-780 K and the Seebeck peak occurs at 10-30 K. For Bismuth [63], another well-known phonon drag system, θ_D is 119 K whereas Seebeck peak occurs at 2-3 K. For $FeSb_2$ polycrystal, $\theta_D \approx$ 330-350 K was reported in reference [15] and 256 K in reference [13]. The Seebeck peak in single crystal occurs at around 10 K. For our sample S-600, the peak occurs at 25 K. Hence comparing with the other phonon drag systems, scaling between T_{max} and θ_D in $FeSb_2$ is roughly what one would expect in phonon drag picture.

Following Herring [55], the electron-diffusion part of the Seebeck coefficient, in μVK^{-1}, for a semiconductor is given by,

$$S_d = \mp 86.2 \left[ln \frac{4.7\times10^{15}}{n} + \frac{3}{2} ln \frac{m^*}{m} + \frac{|\Delta E|}{kT} + \frac{3}{2} lnT \right] \quad (4.3)$$

For the case of lattice scattering by long wavelength phonons, $\frac{|\Delta E|}{kT}$ can be approximated by,

$$\left|\frac{\Delta E}{kT}\right| = \frac{5}{2} + r \quad (4.4)$$

where the scattering parameter r is taken to be -1/2. S_d was calculated taking $m^* = m$ and using the charge carrier density (n) calculated from the Hall-coefficient measurements. The diffusion part was then subtracted from the total measured Seebeck coefficient to obtain the drag contribution as shown in Figure 4.31. For S-600 at 25 K at which the Seebeck peak occurs, S_d = -110 μVK^{-1} was found.

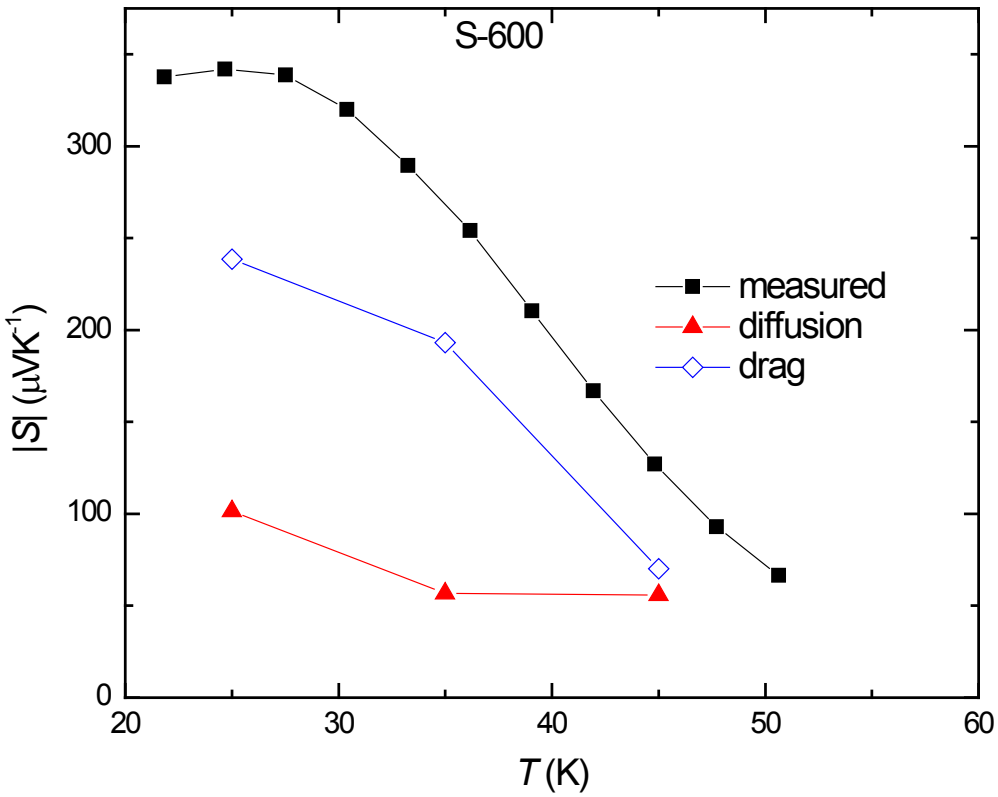

Figure 4.31 Temperature dependence of the calculated value of diffusion and drag part for the sample S-600 based on equation (4.3) and (4.4). The carrier concentration obtained from the Hall coefficient data was used in the calculation. The measured total Seebeck coefficient is also plotted for comparison.

Using equation (4.3), S_p was calculated to be -238 μVK^{-1}. However for S-300 the calculated diffusion contribution turned out to be slightly greater than the measured values. So no significant phonon drag contribution could be expected for this sample. This is understandable because the phonon mean free path for S-300 sample is drastically reduced so that the dominant phonons do not carry sufficient momentum to scatter

carriers. Moreover phonon drag is expected to be weak with increase in carrier concentration and in fact it has been proposed that there occurs the saturation effect at high concentration level. The overestimation of diffusion part of Seebeck coefficient in S-300 could be due, in part, to the approximations made during the calculations.

According to Herring [55], the phonon-drag thermopower for semiconductors, in the first order approximation, can be written as,

$$S_p = \frac{\beta v_s \lambda_p n e}{\sigma T} \tag{4.5}$$

where v_s is the velocity of sound, λ_p the wavelength of the interacting phonons, n the charge carrier density, σ the electrical conductivity, T is the absolute temperature and β the dimensionless parameter with its value ranging from 0 to 1 depending upon the strength of the interaction. This formula can be used to find approximate values of the mean free path of the phonons which interact with the electrons. v_s= 3116 ms^{-1} and e = 1.6×10^{-19} C were used. σ was calculated from the measured resistivity values using $\sigma = \frac{1}{\rho}$. We chose intermediate value of β to be 0.5 because we are interested more in temperature dependence than in magnitude. The mean free path of an average phonon can also be estimated from the lattice thermal conductivity based on kinetic theory,

$$K_l = \frac{1}{3} c_V \widetilde{\lambda_P} v_S \tag{4.6}$$

Where K_l is the lattice thermal conductivity and c_V the phonon contribution to the total specific heat capacity. The lattice portion of the total thermal conductivity was calculated assuming $\kappa_{total} = \kappa_l + \kappa_e$ and $\kappa_e = L\sigma T$, where κ_e is the electronic contribution to the total thermal conductivity. c_V was calculated using $C_P - \gamma T = \beta T^3$ with $\gamma = 3.98 \times 10^{-3}$ $JK^{-2}mol^{-1}$ as reported in reference [15]. C_P values were obtained from the same

reference. Since only the long wavelength phonons interact with electrons, $\lambda_p$is usually greater than $\widetilde{\lambda_P}$.

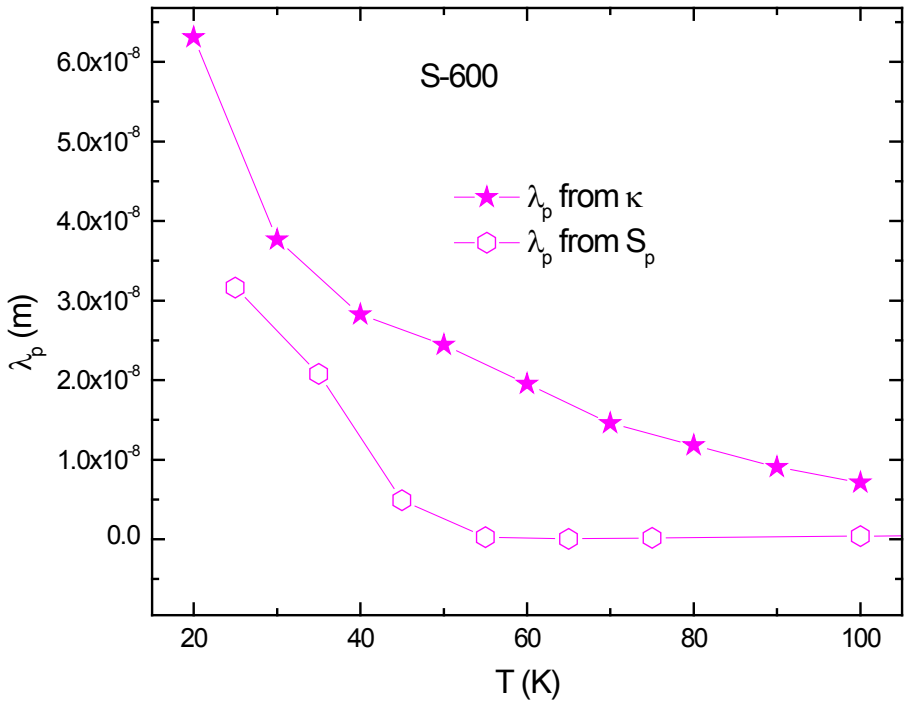

Figure 4.32 Temperature dependence of the phonon mean free paths calculated from two independent calculations using equations (4.5) and (4.6).

Our nanocomposite data and analysis of phonon drag do not support other mechanisms that might explain the large Seebeck effects reported by Bentien *et al.* [15]. Although one cannot preclude the presence of electron-electron correlation effects, their role in this phenomenon may be a minor one. The recent analysis of electron correlations using a hybrid functional approach of Becke [67] and Hegin's *GW* functional approach [68] by Tomczak *et al*. [27] suggest that the high thermopower in $FeSb_2$ should not be understood in the context of local correlations, but rather by utilizing vertex corrections

to the transport coefficients. Such vertex corrections describe the phonon-drag effect. The phonon-drag effects in $FeSb_2$ are similar to those described in p-type Ge by Geballe and Hull [64]. In a similar vein the study of magnetoresistance and Hall effect by Takahashi *et al.* [56] concludes that the large Seebeck coefficient in $FeSb_2$ is unlikely to originate from electron-electron correlations because they have an insignificant effect on the Seebeck coefficient in the low-temperature insulating regime. Our data on $FeSb_2$ nanocomposite supports their conjecture that the phonon-drag effect plays an essential role for enhancing the Seebeck coefficient in the low-temperature regime, as shown in other semiconductor materials *e.g.* InSb [69] and weakly P doped Si [60].

4.7 Kapitza Resistance of $FeSb_2$

It is clear that $FeSb_2$ exhibits a strong grain size dependent thermal conductivity at low temperatures. The model usually proposed to understand the grain size dependence of the thermal conductivity is the relaxation time approach of boundary scattering based on the Klemens-Callaway theory [70, 71]. This is a microscopic model and takes into account various scattering mechanisms involved in the heat conduction. A simpler model for analyzing thermal conductivity of polycrystals, which avoids the microscopic details, is based on the combination of Kapitza resistance [72, 73] and the effective medium approximation (EMA) [74, 75]. In an effective medium approach, the total thermal conductivity of a polycrystal is the sum of the intra-grain and the inter-grain contributions [76]. The inter-grain component arises due to the interfacial resistance, also known as the Kapitza resistance, to the thermal transport. In the presence of thermal gradient, the Kapitza resistance results in a temperature discontinuity across the interface which was

first observed by Kapitza [72]. The overall effect of the Kapitza resistance is to reduce the thermal conductivity and the effect is more pronounced at smaller grain sizes. Based on the Kapitza resistance-EMA model, Nan *et al*. [77] showed that for an isotropic polycrystalline solid made up of spherical grains of equal size, the effective thermal conductivity (κ) is given by,

$$\kappa\,(T,d) = \frac{\kappa_i}{1+\frac{2R_k\kappa_i}{d}} \tag{4.7}$$

where κ_i is the intrinsic (or bulk) thermal conductivity, R_k is the Kapitza resistance and d is the grain size. Here κ_i is grain-size independent but is temperature dependent while $L_k = R_k\kappa_i$ and $G_k = \frac{1}{R_k}$ are called the Kapitza length and Kapitza conductance, respectively. Here L_k represents the distance over which the temperature drop is the same as at the interface and its magnitude measures the relative importance of the Kapitza conductance. When the grain size in nanocomposites becomes comparable to L_k, interfaces will predominantly determine the overall thermal conductance [78]. So, to predict the thermal properties of the nanocomposites it is important to develop an understanding of the interfacial thermal conductance.

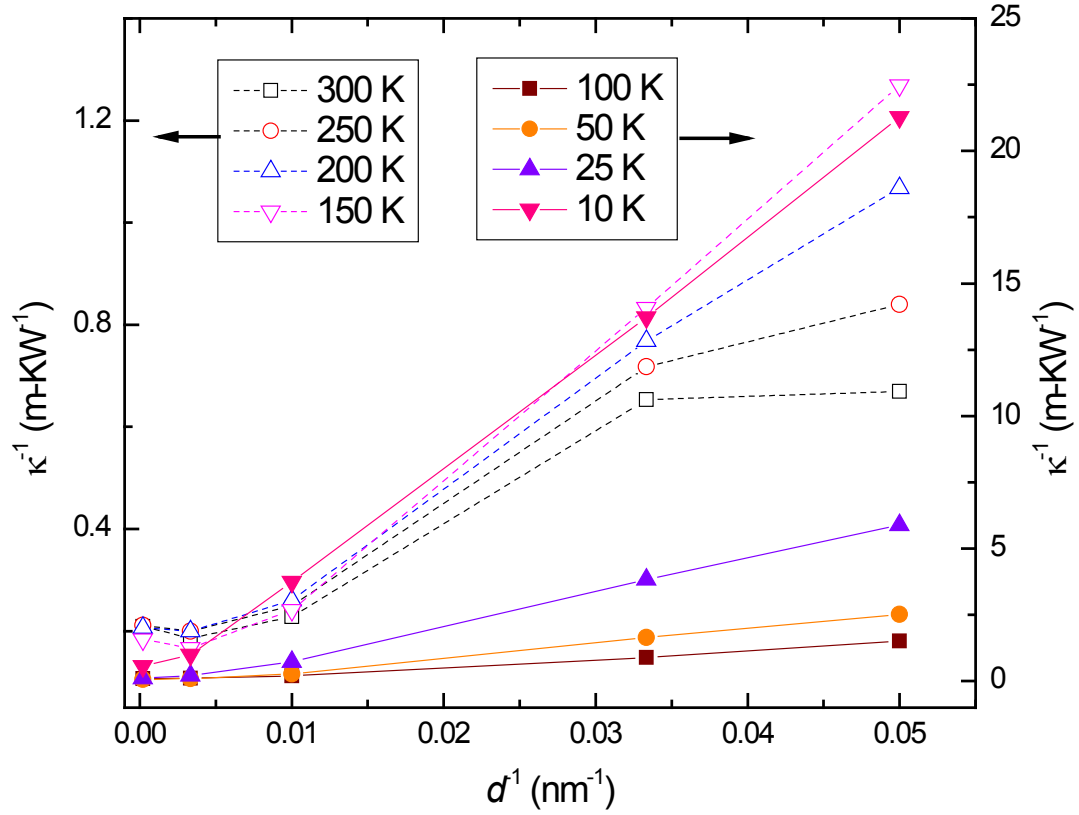

Figure 4.33 κ^{-1} plotted versus d^{-1}. The open symbols with the dashed lines and the closed symbols with solid lines correspond to the left and right Y-axes respectively. The first point from the left was excluded during the fitting process.

From the best-fit lines of the experimental data in κ^{-1} vs. d^{-1} plots predicted by equation 4.7, the values of R_k and G_k for the samples were determined. As seen in the Figure 3, a deviation from the linearity was observed at the largest grain size and those points were excluded during fitting process. As the temperature decreases, the trend becomes more linear. This suggests that the Kapitza resistance-EMA model in $FeSb_2$ system is more valid at low temperatures. With decreasing temperature, the slope of the linear fit increases monotonically. So the Kapitza resistance increases as temperature

decreases.

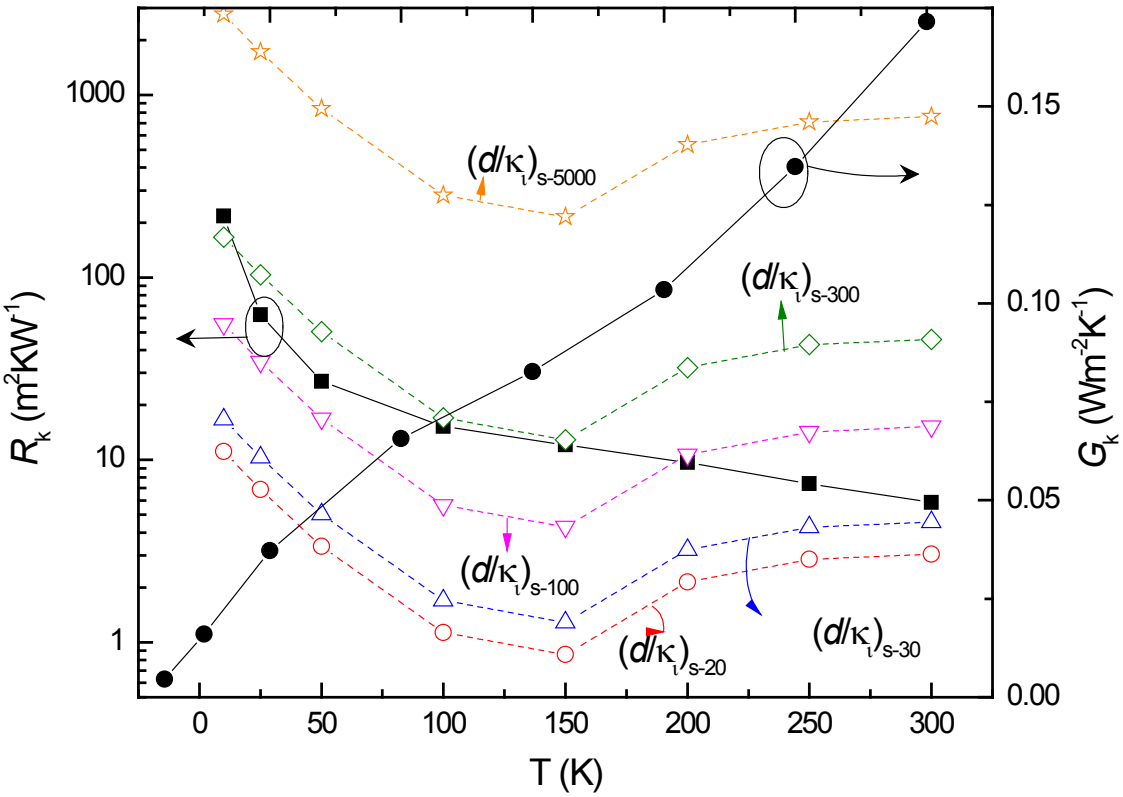

Figure 4.34 Temperature dependence of the Kapitza resistance (R_k) and Kapitza conductance (G_k) obtained from the best fit to Eq (4.7). R_k and G_k values are represented by left and right Y-axes, respectively. The open symbols with dashed lines represent the temperature dependence of the bulk thermal resistance (d/κ_i) as indicated by the left Y-axis for the five samples. (Stars: (d/κ_i) for S-5000, Diamonds: (d/κ_i) for S-300, down-pointed triangles: (d/κ_i) for S-100, up-pointed triangles: (d/κ_i) for S-30, open-circles: (d/κ_i) for S-20, filled circles: G_k as a function of temperature, filled squares: R_k as a function of temperature).

Figure 4.34 represents the temperature dependence of the Kapitza resistance (R_k) and the Kapitza conductance (G_k). The bulk thermal resistances for the five samples are also plotted for comparison. R_k has a weak temperature dependence from 300 K down to 50 K and increases sharply below 50 K. Fitting to the power law shows that $R_k \approx 4.0 \times 10^{-6} T^{-1.27}$. This is consistent with the fact that the *in situ* Kapitza resistance is expected to follow $R_k \sim T^{-\alpha}$, where $\alpha > 0$ [79]. $R_k = 5.83 \times 10^{-9}$ m^2KW^{-1} and 2.68×10^{-8} m^2KW^{-1}, respectively, at 300 K and 50 K were observed whereas at 10 K, R_k reaches a value as high as 2.17×10^{-7} m^2KW^{-1}. From a microscopic point of view this is understandable because at low temperature, the diffusive scattering of phonons off the grain boundary is the dominant scattering mechanism and it becomes weak at higher temperature where other mechanisms like three phonon-phonon process and Umklapp-process become more important. We note the significant value of the Kapitza resistance in this system. For SiGe alloys, Nan. *et al*. [77] reported $R_k = 1.1 \times 10^{-7}$ to 4.98×10^{-8} m^2KW^{-1} values at room temperature. Whereas for nanocrystalline yttria-stabilized zirconia (YSZ), which exhibits a strong grain-size dependence of the thermal conductivity, values for R_k of the order of 10^{-8} m^2KW^{-1} at low temperature was reported by Yang *et al*.[80].

As seen in Figure 4.34, the Kapitza conductance initially increases with increasing temperature and then becomes less sensitive to temperature between 100 and 200 K. Below 200 K, G_k follows roughly the same trend as the specific heat capacity (C_p) does in ref [19]. In fact, G_k is expected to be proportional to C_p [80]. This indicates that despite the sample porosity, the error in estimating the grain size and the other assumptions that are made, calculations based on this simple Kapitza resistance -EMA model for $FeSb_2$ nanocomposite samples are justified. The minimum value of the Kapitza

length was observed at room temperature, where $L_k = R_k \kappa_i \approx 38$ nm. At low temperature, L_k increases reaching a value of 390 nm at 10 K. This large value of L_k at low temperature implies a relatively weak interfacial conductance which is consistent with the observed thermal conductivity.

The calculated values for κ_i were found to be much smaller compared to that of the single crystal. For example, at 50 K, κ_i = 5.94 $Wm^{-1}K^{-1}$. Reduced values of κ_i were also observed by Nan *et al*. [77] in Bi_2Te_3/Sb_2Te_3 alloys and they attributed the reduced values of κ_i to the effect of porosity.

The open symbols in Figure 4.34 represent the bulk thermal resistance (d/κ_i) for these five samples. For samples S-20 and S-30, the Kapitza resistance is dominant over the bulk thermal resistance from 5-300 K, whereas for S-100 a crossover is observed at around 200 K. On the other hand, for S-300 and S-5000, the bulk thermal resistances are dominant throughout. This explains the two important features of the thermal conductivity curves that are seen from Figure 4.8. (i)For the large grain size, the contribution of the bulk is dominant and the thermal conductivity curve mimics its single crystal counterpart with a pronounced peak. As the grain size goes down the Kapitza resistance becomes stronger thereby reducing the bulk nature of the curve and at the smallest grain size, the Kapitza resistance dominates over the bulk part completely. (ii) The crossover between the two resistance curves occurs at higher temperature as the grain size gets smaller. This is why the thermal conductivity peaks shift to higher temperature as the grain size decreases.

In conclusion, calculations based on the Kapitza resistance-EMA model for $FeSb_2$ nanocomposite samples show a strong grain-size dependence of the thermal conductivity

at low temperature with a significantly large value of the Kapitza resistance. The Kapitza resistance was found to be the predominating factor in determining the bulk thermal properties below 50 K. For coarse-grained samples, the bulk thermal resistance dominates over the Kapitza resistance values. As the grain size decreases the Kapitza resistance becomes more important. A large value of the Kapitza length at low temperature is observed. These results suggest that the interfacial thermal resistance across the grain boundaries plays a significant role in determining the thermal transport properties of $FeSb_2$ at low temperature.

4.8 Magnetic Properties of Nanocomposite $FeSb_2$

Single crystal $FeSb_2$ is known to be paramagnetic, having unusual temperature dependence of magnetic susceptibility with a diamagnetic to paramagnetic crossover at ~ 100 K [4,9]. Extensive efforts have been made in the past decade to explain the anomalous temperature dependence of the magnetic susceptibility of $FeSb_2$. A simple analysis based on a free-ion model was shown to explain this behavior in Ref. [58]. It was also demonstrated in reference [13] that a narrow-band picture with two peaks in the density of states at the gap edge explains the observed data well, thereby validating the Kondo insulator description of a spin state transition in $FeSb_2$. Recently, Koyama *et al*. [81] employed the Stoner-Wohlfath theory and the Arrot plot technique to determine the temperature dependence of the inverse of the fourth expansion coefficient γ for the $FeSb_2$ single crystal. The temperature dependence of γ they found was similar to that observed in FeSi reported in reference [82], which can be explained by the spin fluctuation theory.

So far most of the previous studies have been made in single crystal samples; the experimental data on the magnetic properties of polycrystalline $FeSb_2$ samples remains

scarce. Here I report and analyze the magnetic properties of a polycrystalline $FeSb_2$ prepared by hot-press method. For this, sample hot-pressed at 400 ^oC denoted as HP 400 as explained in previous section 4.3.2 was chosen. A vibrating sample magnetometer (VSM) option of the Physical Property Measurement System (PPMS) from Quantum Design was used to measure the magnetic moment. The molar susceptibility was calculated by $\chi = \frac{M}{H}$, where M is the magnetization and H is an applied magnetizing field of 0.1 Tesla during measurement. The Hall coefficient (R_H) was measured using the horizontal rotator option of the PPMS.

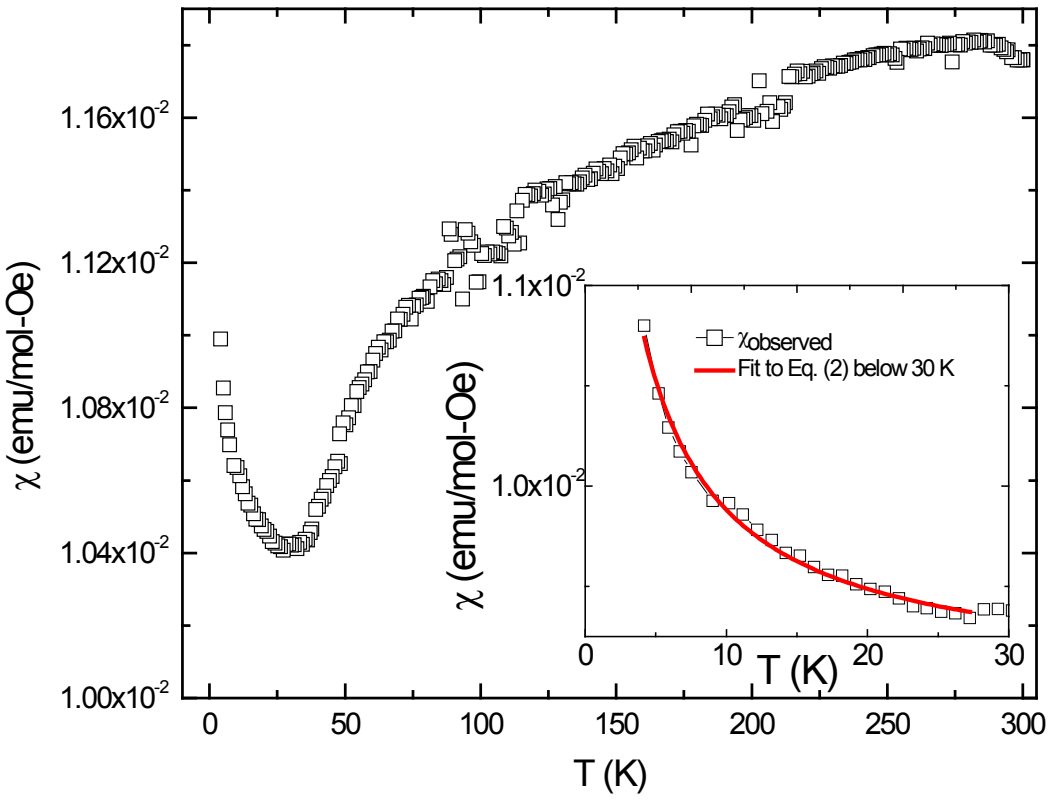

Figure 4.35 Observed magnetic susceptibility of the nanocomposite $FeSb_2$ sample as a function of temperature. Inset shows fitting to the Curie-Weiss law below 30 K.

Figure 4.35 shows the temperature dependence of the molar susceptibility for the $FeSb_2$ sample used in this study. The susceptibility values for the sample are significantly enhanced throughout the temperature range of 2 – 300 K when compared to the single crystal data reported in the literature. For example, at 300 K, $\chi \sim 1.2\times10^{-2}$ emu mol^{-1} is two orders of magnitude higher than the estimated polycrystalline average value of 3×10^{-4} emu mol^{-1} calculated in reference [4] and 6×10^{-4} emu-mol^{-1} reported by Fan *et al*. [2]. Consequently no diamagnetic to paramagnetic crossover is observed for our sample. Such a vertical shift of the χ (T) curve was also reported in the arsenic-substituted single crystals of $FeSb_2$ [5] that they attributed to the substantial Pauli paramagnetism of the increased carrier concentration, which is induced by defects or impurities. We note that while most of the qualitative features of the susceptibility curves are preserved, a more pronounced Curie type of tail compared to that reported in references [2] and [4] is observed at low temperatures.

The observed magnetic susceptibility (χ_{obs}) in a semiconductor is given by [83],

$$\chi_{obs}\,(T) = \chi_0 + \chi_p + \chi_c \tag{4.8}$$

where χ_0 is the temperature independent susceptibility and is the sum of the contributions coming from the lattice, lattice defects and neutral impurities (if any), χ_p is the temperature dependent susceptibility due to paramagnetic impurities and χ_c is the magnetic susceptibility due to the free carriers. The pronounced upturn in the susceptibility below 30 K indicated the presence of a substantial amount of paramagnetic impurities. Data below 30 K was fitted to the equation,

$$\chi(T) = \chi_0 + \chi_p = \chi_0 + \frac{\gamma C}{T-\Theta} \tag{4.9}$$

Here γC is the effective Curie constant, γ being a dimensionless constant and Θ is the

Weiss temperature. A satisfactory fitting (represented by solid line in the inset of Figure 4.35) was found for the parameter values of $\chi_0 = 1.0\times10^{-2}$ emu mol^{-1}, $\gamma C = 3.96\times10^{-3}$ emu-K mol^{-1} and Θ = -1.6 K. Here we note a large value of χ_0 which has the same order of magnitude as χ_{obs}, indicating a significant contribution from the temperature independent term. For single crystals, $\chi_0 \sim -4\times10^{-5}$ emu mol^{-1} was reported in reference [4].

Assuming that the orbital angular momentum is quenched and only the spin angular momentum contributes, the Curie constant C is given by,

$$C = \frac{N_A g^2 \mu_B^2}{3k_B}[s(s+1)] = 0.125g^2[s(s+1)] \text{ emu-K mol}^{-1} \qquad (4.10)$$

where N_A is the Avogadro's number, $\mu_B = 9.27\times10^{-24}$ JT^{-1} is the Bohr magneton, g is the electron Lande g factor, s is the spin and k_B is the Boltzmann constant. Taking s = 2 and g = 2.0023, C = 3.0 emu-K mol^{-1} is expected for Fe^{2+} ion. We conclude that the Curie-like term below 30 K is due to ≈ 0.2 % of the Fe^{2+} impurities per mol. This value is less than the 0.5 % reported for the single crystals in reference [4].

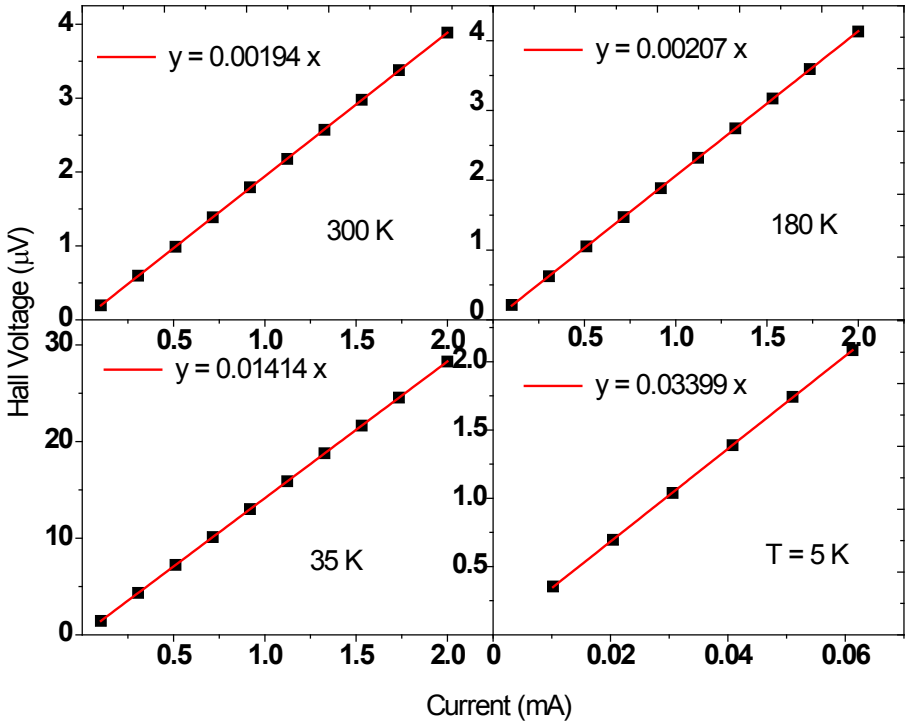

Figure 4.36 Transverse Hall voltages as a function of excitation current for temperatures of 300, 180, 35, and 5 K. A magnetic field of 9T was applied.

The Hall coefficient R_H for a specimen of thickness t is given by, $R_H = V_H\, t/IB$, where V_H is the Hall voltage, B is the applied magnetic field and I is the current. Figure 4.36 shows V_H plotted as a function of I at B = 9 T for some selected temperatures. The Hall coefficients at different temperatures were calculated from the slope of the linear fit.

Values for free carrier density (n) were estimated from the Hall coefficient measurement using the single parabolic band (SPB) model, $n = 1/R_H\, e$ where e is the electronic charge. Inset of Figure 4.38 shows the temperature dependence of the carrier concentration. A thermally activated behavior is observed above 30 K.

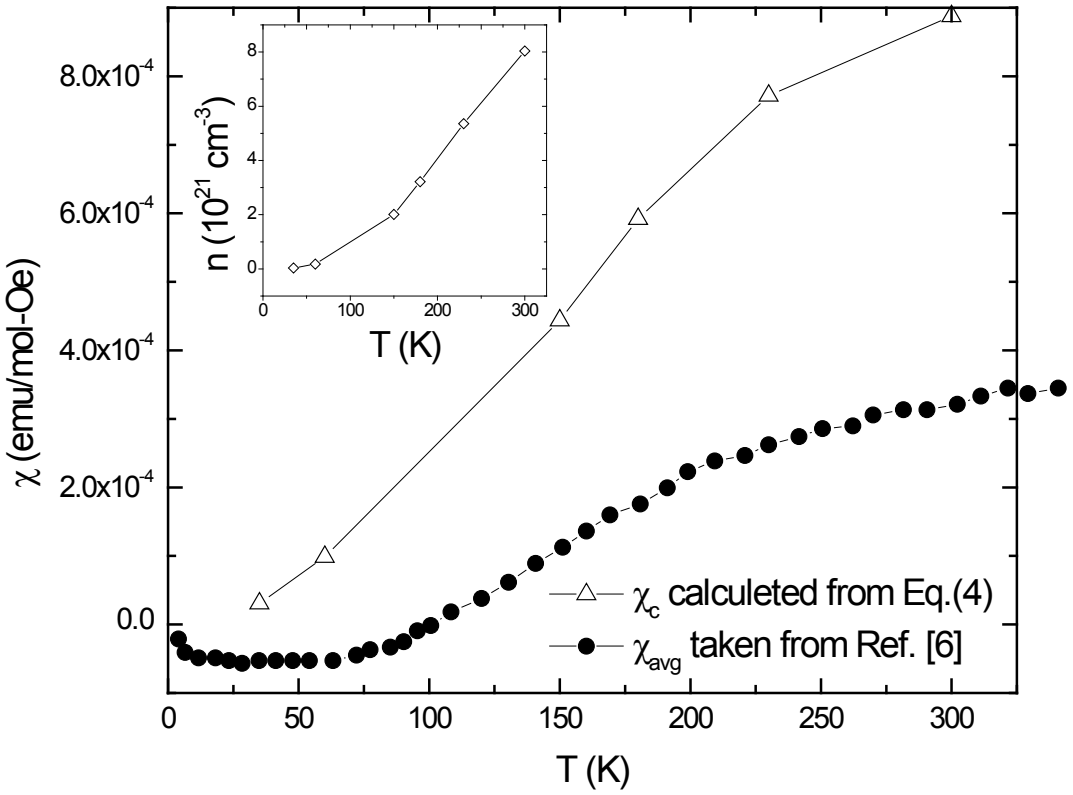

Figure 4.37 The open triangles represent the χ_c values calculated using Eq. (4) for the nanocomposite sample as a function of temperature. The filled circles represent the polycrystalline average data taken from reference [4]. Inset: Temperature dependence of free carrier concentration obtained from Hall coefficient.

In the region of intrinsic conductivity (above 30 K in this case), the magnetic susceptibility due to the free carriers, assuming *g* factor to be 2 for both electron and holes, can be determined as [83],

$$\chi_c = \frac{n\mu_B^2}{3\rho k_B T}[6 - \left(\frac{m}{m_n^*}\right)^2 - \left(\frac{m}{m_p^*}\right)^2 \quad (4.11)$$

where *n* is the free carrier concentration, ρ is the density, *m* is the free electron mass and

m_n^* (m_p^*) are the effective masses for the electrons (holes). An approximate calculation of χ_c was performed using the n values obtained above and taking $m = m_n^* = m_p^*$ and $\rho = 7.5$ g cm^{-3}. Figure 4.38 shows the comparison between χ_c calculated using equation (4.11) and $\chi_{avg} = (\chi_a + \chi_b + \chi_c)/3$ taken from reference [4]. The increased susceptibility for the hot-pressed sample is due possibly to the increased carrier concentration (~ 10^{21} cm^{-3}) due to lattice and strain defects arising from the ball milling process. For the single crystal samples, carrier concentration values of ~ 10^{17} – 10^{20} cm^{-3} were reported [2, 19].

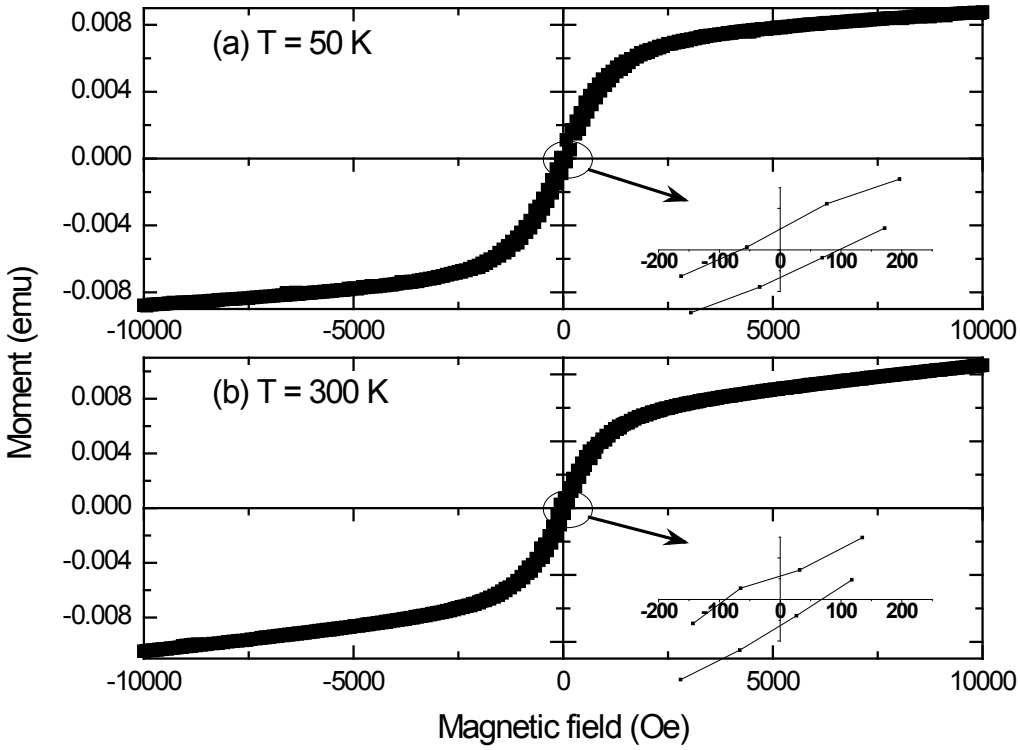

Figure 4.38 Magnetic moment of the nanostrustured $FeSb_2$ as a function of applied magnetic field at (a) 50 K and (b) 300 K. The insets show the region around the origin.

Figure 4.39 shows the field dependence of the magnetization at 50 and 300 K. The magnetization increases with the applied field near the origin, changes slope at a

magnetic field of value around 2 kOe and then increases slowly with the increasing field. Presence of a weak ferromagnetism at both the temperatures (50 and 300 K) is evidenced by a narrow hysteresis loop as seen in Figure 4.39. A small coercivity value of ~ 100 Oe (inset of Figure 4.39) is observed at both the temperatures. Since pure $FeSb_2$ is paramagnetic at 300 K and diamagnetic at 50 K, a narrow hysteresis loop at both the temperatures with nearly equal value of the coercivities indicates the presence of some neutral ferromagnetic phase. It is believed that, a small fraction of unreacted Iron (Fe) exists as a second phase in our sample. As a result the magnetic susceptibility is enhanced by a significant constant value, consistent with the large value of χ_0 as mentioned above. Cullity *et al*. [84] have pointed out the effect of a small amount of ferromagnetic second phase (0.1% of Fe by weight) on the magnetic property of diamagnetic material (Cu). Our data on magnetic moment (m) versus magnetizing field (H) is very consistent with their data. We believe that even small amount of Fe is enough to cause such a dramatic enhancement of the susceptibility and therefore no second phase Fe was detected from the XRD pattern.

A rough estimation of the contribution from ferromagnetic Fe phase (χ_{Fe}) can be made calculating the susceptibility at 0.1 T from m-H curves. $\chi_{Fe} \approx 1.05 \times 10^{-2}$ emu mol^{-1} at both the temperatures (50 and 300 K). This value of χ_{Fe} is in close agreement with the value of χ_0 obtained from fitting of the Curie-Weiss law. Also the similar values of χ_{Fe} at both the temperatures are consistent with the temperature independent nature of χ_0.

Finally, contribution from the impurities varies among samples. Therefore it is understandable that sample dependence of the measured values of the involved physical quantities might have played a role. Also the calculation was made based on one - band

model. Usually, in a narrow gap semiconductor like $FeSb_2$, two types of carriers are involved. Nevertheless this simple model explains the observed magnetic susceptibility reasonably well. This report, in addition to providing data on magnetic properties of polycrystalline $FeSb_2$, also provides a demonstration of how a small amount of neutral ferromagnetic phase masks the true magnetic behavior of a material.

References

1. H. Holseth and A. Kjekshus, Acta Chem. Scand, **23**, 3043 (1969).
2. A. K. L. Fan, G. H. Rosenthal, H. L. McKinzie and A. Wold, J. Solid State Chem. **5**, 136 (1972).
3. J. Steger and E. Kostiner, J. Solid State Chem. **5**, 131(1972).
4. C. Ptrovic, J. W. Kim, S. L. Bud'ko, A. I. Goldman, and P.C. Canfield, Phys Rev B **67**, 155205 (2003).
5. P. Sun, N. Oeschler, S. Johnsen, B. B. Iversen , and F. Steglich, Dalton Trans., **39**,1012-1019 (2010).
6. A. Bentien, S. Johnson, G. K. H. Madsen, B. B. Iversen and F. Steglich, EPL, **80**, 17008 (2007).
7. A. Perucchi, L. Degiorgi, Rongwei Hu, C. Petrovic, and V.F. Mitrovi´c; Eur. Phys. J. B **54**, 175–183 (2006).
8. A. Zaliznyak , A. Savici, V. Garlea, R. Hu, C. Petrovic, Phys Rev B, **83**, 18 (2011)
9. R. Hu, V. F. Mitrovic, and C. Petrovic, Phys. Rev. B., **74** 195130 (2006).
10. R. Hu, Ph. D. Dissertation, Brown University, Providence, Rhode Island (2010).
11. B. Sales, E. Jones, B. Chakoumakos, J. Fernandez-Baca , H. Harmon, J. Sharp, E. Volckmann, Phys Rev B, **50**, 12 (1994).

12. J. Goodenough, Journal of Solid State Chemistry, **5**, 1 (1972).
13. C. Petrovic, Y. Lee, T. Vogt, N. Dj. Lazarov, S. L. Bud'ko and P. C. Canfield, Phys.Rev. B, **72**, 045103 (2005).
14. G. D. Mahan, B. Sales, J. Sharp, J. Phys. Today. **50**, 42-47 (1997).
15. A. Bentien, G. K.H. Madsen, S. Johnson, B.B. Iversen, Phys. Rev. B.**74** (20), 205105 (2006).
16. P. Sun, M. Søndergaard, Y. Sun., S. Johnsen, B.B. Iversen, F. Steglich, Appl. Phys. Lett. **98**, 072105 (2011).
17. K. Wang, R. Hu, J. Warren and C. Petrovic, Journal of Applied Physics **112**, 013703 (2012).
18. A. Sanchela, A. D. Thakur and C.V. Tomy, AIP Conf. Proc. **1447**, 1003 (2012).
19. P. Sun, N. Oeschler, S. Johnsen, B.B. Iversen, F. Steglich, Phys. Rev. B.**79** (15), 153308 (2009).
20. Z. Wang, J. E. Alaniz, W. Jang, J. E. Garay, C. Dames, Nano Lett. **11** (6), 2206-2213 (2011).
21. B. Poudel, Q. Hao, Y. Ma, Y. Lan, A. Minnich, B. Yu, X.Yan, D. Wang, A. Muto, D. Vashaee, X. Chen, J. Liu, M. S. Dresselhaus, G. Chen, Z. Ren, Science **320** (5876), 634-638 (2008).
22. Y. C. Lan, A. J. Minnich, G. Chen, Z. Ren, Adv. Func. Mater. **20**, 357 (2010).
23. X. Yan, G. Joshi, W. S. Liu, Y. C. Lan, H. Wang, S. Lee, J. W. Simonson, S. J. Poon, T. M. Tritt, G. Chen, Z. Ren, Nano Lett. **11**, 556 – 560 (2011).

24. B. C. Sales, E. C. Jones, B. C. Chakoumakos, J. A. Fernandez-Baca, H. E. Harmon, J. W. Sharp, E. H. Volckmann, Phys. Rev. B: Condens. Matter. **50** (12), 8207-8213 (1994).

25. P. Sun, N. Oeschler, S. Johnsen, B. B. Iversen, F. Steglich, J. Phys.: Conf. Ser. **150**, 012049 (2009).

26. S. R. Harutyunyan, V. H. Vardanyan, A. S. Kuzanyan, V. R. Nikoghosyan, S. Kunii, K. S. Wood, A. M. Gulian, Appl. Phys. Lett. **83** (11), 2142-2144 (2003).

27. J. M. Tomczak, K. Haule, T. Miyake, A. Georges, G. Kotliar, Phys. Rev. B. **82** (8), 085104 (2010).

28. C. Kittel, Introduction to Solid State Physics, 8th ed. (John Willey & Sons, Berkeley, CA), pp. 112-114 (2005).

29. S. Zhu, W. Xie, D. Thompson, T. Holgate, M. Zhou, Y. Yan, T. M. Tritt, J. Mater. Res., DIO: 10.1557/jmr.2011.86 (2011).

30. G. D. Cahill, S. K. Watson, R. O. Pohl, Phys. Rev. B **46** (10), 6131-6140 (1992).

31. H. Zhao, M. Pokharel, G. Zhu, S. Chen, K. Lukas, Q. Jie, C. Opeil, G. Chen , and Z. Ren, Appl. Phys. Lett. **99**, 163101 (2011).

32. G. Joshi, H. Lee, Y. Lan, X. Wang, G. Zhu, D. Wang, R. W. Gould, D. C. Cuff, M. Y. Tang, M. S. Dresselhaus, G. Chen, Z. Ren, Nano Lett. **8** (12), 4670-4674 (2008).

33. M. Pokharel, H. Zhao, Z. Ren, C. Opeil, International Journal of Thermal Sciences **71** 32-35 (2013).

34. M. Pokharel, H. Zhao, K. Lukas, B. Mihaila, Z. Ren, and C. Opeil, MRS Communications **3**, 31–36 (2013).

35. Q. Jie, Correlation between structure and thermoelectric properties: Searching for better thermoelectric materials. (Dissertation, Dec 2010, Stony Brook University), pp. 71-83.
36. A. Sanchela, A. D. Thakur, and C. V. Tomy, AIP Conf. Proc. 1447, 1003 (2012).
37. K. Wang, R. Hu, J. Warren, and C. Petrovic, Journal of Applied Physics **112**, 013703 (2012).
38. M. Pokharel, M. Koirala, H. Zhao, Z. Ren, and C. Opeil, J. Low Temp. Phys. **176**, 122-130 (2014).
39. K. F. Hsu, S. Loo, F. Guo, W. Chen, J. S. Dyck, C. Uher, T. Hogan, E. K. Polychroniadis and M. G. Kanatzidis, Science **303** 818–21 (2004).
40. J. P. Heremans, V. Jovovic, E. S. Toberer, A. Saramat, K. Kurosaki, A. Charoenphakdee , S. Yamanaka and J. G. Snyder, Science **321** 554–8 (2008).
41. Q. Y. Zhang *et al*., Energy Environ. Sci. **5**, 5246–51 (2012).
42. J. P. Heremans, B. Wiendlocha and A. M. Chamoire, Energ Environ. Sci. **5**, 5510–30 (2012).
43. Y. Z. Pei, X. Y. Shi, A. LaLonde, H. Wang, L. D. Chen and J. G. Snyder, Nature **473** 66–9 (2011).
44. Q. Zhang, F. Cao, W. S. Liu, K. Lukas, B. Yu , S. Chen, C. Opeil, D. Broido, G. Chen and Z. F. Ren, J. Am. Chem. Soc. **134**, 10031–8 (2012).
45. Zebarjadi M, Joshi G, Zhu G H, Yu B, Minnich A, Lan Y C, Wang X W, Dresselhaus M, Ren Z F and Chen G 2011 Nano Lett. 11 2225–30.
46. B. Yu, M. Zebarjadi, H. Wang, K. Lukas, H. Z. Wang, D. Z. Wang, C. Opeil, M. Dresselhaus, G. Chen and Z. F. Ren, Nano Lett. **12**, 2077–82 (2012).

47. J. P. Heremans, C. M. Thrush and D. T. Morelli, J. Appl. Phys. **98**, 063703 (2005).

48. W. Kim, J. Zide, A. Gossard, D. Klenov, S. Stemmer, A. Shakouri and A. Majumdar Phys. Rev. Lett. **96**, 045901 (2006).

49. S. V. Faleev and F. L´eonard, Phys. Rev. B **77**, 214304 (2008).

50. M. Zebarjadi, K. Esfarjani, A. Shakouri, J. H. Bahk and Z. X. Bian, Appl. Phys. Lett. **94**, 202105 (2009).

51. S. Sumithra, N. J. Takas, D. K. Misra, W. M. Nolting, P. F. P. Poudeu and K. L. Stokes, Adv. Energy Mater. **1**, 1141–7 (2011).

52. D. K. Ko, Y. J. Kang and C. B. Murray, Nano Lett. **11**, 2841–4 (2011).

53. H. Zhao, M. Pokharel, S. Chen, B. Liao, K. Lukas, C. Opeil, G. Chen, and Z. Ren, Nanotechnology **23**, 505402 (2012).

54. M. Koirala, H. Zhao, M. Pokharel, S. Chen, T. Dahal, C. Opeil, G. Chen, and Z. Ren, Appl. Phys. Lett. **102**, 213111 (2013).

55. C. Herring, Phys Rev **96**, 5 (1954).

56. H. Takahashi, R. Okazaki, Y. Yasui, and I. Terasaki, Phys. Rev. B **84**, 205215 (2011).

57. J. M. Tomczak, K. Haule, T. Miyake, A. Georges and G. Kotliar, Phys. Rev. B **82**, 085104 (2010).

58. N. H. Abrikosov, L. I. Pterova, Inorg. Materials **25**, 8 (1989).

59. Y. Sun, S. Johnsen, P. Eklund, M. Sillassen, J. Bøttiger, N. Oeschler, P. Sun, F. Steglich, and B. B. Iversen; Journal of Applied Physics **106**, 033710 (2009).

60. L. Weber, M. Lehr, and E. Gmelin , Phys. Rev. B **46** (1992).

61. F. J. Blatt, Physics of Electronic Conduction in Solids, McGraw-Hill; 1st Ed. edition (1968) Page 214.

62. Q. R. Hou, B. F. Gu, Y. B. Chen, and Y. He, Modern Physics Letters B **25**, 22, 1829-1838 (2011).

63. J. P. Issi, and J. Boxus, Cryogenics **19**, 517 (1979).

64. T. H. Geballe, and G. W. Hull, Phys. Rev. **94**, 5 (1954).

65. N. Lazarević , Z. V. Popović, N. Lazarević, Rongwei Hu, and C. Petrovic; Phys. Rev. B **81**,144302(2010).

66. J. Tang, W. Wang, G. Zhao, and Q. Li, J. Phys. Condens. Matter **21**, 205703 (2009).

67. A. D. Becke, J. Chem. Phys. **98**, 1372 (1993).

68. L. Hedin, Phys. Rev. **139**, A796 (1965).

69. H. P. R. Frederikse, E. V. Mielczarek, Phys. Rev. **99**, 1889 (1995).

70. P. G. Klemens, Proc. Phys. Soc. London, Sect. A **68**, 1113 (1955).

71. J. Callaway, Phys. Rev. **113**, 1046 (1959).

72. P. L. Kapitza, J. Phys. (Moscow) **4**, 181 (1941).

73. E. T. Swartz, and R. O. Pohl, Rev. Mod. Phys. **61**, 605 (1989).

74. D. A. G. Bruggeman, Ann. Phys. (Leipzig) **24**, 636 (1935).

75. R. Landauer, J. Appl. Phys. **23**, 779 (1952).

76. T. S. English, J. L. Smoyer, J. C. Duda , P. M. Norris, T. E. Beechem, and P. E. Hopkins , Proceedings of the ASME/JSME Thermal Engineering Joint Conference AJTEC2011, March 13-17, 2011, Honolulu, Hawaii, USA.

77. C. Nan, and R. Barringer, Phys. Rev. B, **57**, 8263 (1998).

78. M. Hu, P. Keblinski, and P. K. Schelling, Phys. Rev. B **79**, 104305 (2009).

79. J. Amrit, J. Phys D: Appl. Phys. **39** 4472 (2006).

80. H. Yang, G. R. Bai, L. J. Thompson, and J. A. Eastman , Acta Materialia **50** 2309-2317 (2002).

81. T. Koyama, H. Nakamura, T. Kohara, and Y. Takahashi, J. Phys. Soc. Jpn. **79**, 093704-1 (2010).

82. K. Koyama, T. Goto, T. Konomata, R. Note, and Y. Takahashi, J. Phys. Soc. Jpn. **69**, 219 (2009).

83. E. Arushanov, M. Respaud, J. M. Broto , J. Leotin, S. Askenazy, Ch. Kloc, E. Bucher, and K. Lisunov, Phys. Rev. B **55**, 13 (1997).

84. B. D. Cullity, and C. D. Graham, Introduction to Magnetic Materials, John Wiley and Sons Inc. (2009) 2nd edition, Chap. 3 p.112.

Chapter 5

Thermoelectric Properties of Heavy Fermion Compounds $CeCu_6$, $CeAl_3$ and $YbAgCu_4$

5.1 Introduction

Materials with strong electron correlation behavior are the focus of increasing scientific and technological interest in search of a new generation of thermoelectric materials with higher performance and efficiency [1]. These materials exhibit a variety of highly enhanced electronic and magnetic properties at low temperatures which are of considerable interest in many technological applications. Among strongly correlated materials, heavy electron materials have long been the subject of extensive investigation. For reviews of these compounds see references [2–8]. Measurement of thermoelectric properties usually offers an informative approach to investigating quasiparticle excitation in this class of materials [9, 10]. Many heavy Fermion [65] compounds (HFCs) (for example $CeCu_6$, $CeCu_2Si_2$, $CeAl_3$) have been shown to exhibit large Seebeck coefficient values at low temperatures [11, 12]. Assuming one band model, the Seebeck coefficient is related to the effective mass by he relation $S = \frac{8\pi^2 \kappa_B^2 T}{3e\hbar^2} m^* \left(\frac{\pi}{3n}\right)^{2/3}$. Here $k_B = 1.38 \times 10^{-23}$ J K^{-1} is the Boltzmann constant, $\hbar = 1.05 \times 10^{-34}$ J S is the reduced Planck constant, T is the absolute temperature and n is the carrier density. One can expect an enhanced Seebeck coefficient in these systems due to large effective mass at low temperature. Among them, a number of Ce-based compounds ($CeCu_6$ and $CeAl_3$) have been reported to exhibit two well separated maxima (minima) in the temperature dependent Seebeck coefficient plot [13-15]. Usually, the low-T extremum occurs around the characteristic temperature T_K and is attributed to the Kondo scattering on the ground state doublet. The

high temperature peak ($T > T_K$), results from Kondo scattering on higher multiplets which are split by crystal electric field (CEF) effects [11]. In addition to large Seebeck coefficients, many compounds of this class exhibit reasonably high electrical conductivity values which make them promising candidates for thermoelectric cooling applications. Ironically, this class of material has not yet been thoroughly investigated as potential thermoelectric materials. In this chapter, the thermoelectric properties of the polycrystalline samples of the heavy fermion compounds $CeCu_6$, $CeAl_3$ and $YbAgCu_4$ will be presented. The effect of mechanical nanostructuring on the thermoelectric properties was studied for the first time and will be discussed in detail.

5.2 Thermoelectric properties of $CeCu_6$

5.2.1 Introduction to $CeCu_6$

$CeCu_6$ is a conventional heavy fermion compound with enormously enhanced value of γ coefficient at low temperatures ($\gamma = 1600$ mJ mol^{-1}K^{-2}) in the relation,

$$C = \gamma T + \beta T^3 \tag{5.1}$$

This compound was first investigated by Stewart *et al*. [16] in 1984. Since then, it has been one of the widely studied HFCs. A great deal of interest was focused on transport properties of this system in the following years [17-22], owing to the Fermi liquid (FL) behavior at low temperature. Subsequent studies on this compound were focused on non-fermi liquid (NFL) behavior [23, 24] and its anomalous thermopower [25-27]. In the recent years this compound with a small substitution of Au on the Cu site ($CeCu_{6-x}Au_x$ for $0.1 \leq x \leq 0.3$) has been a platform to study quantum critical point (QCP) behavior [28]. Although there appear several reports on temperature dependence of the Seebeck

coefficient and electrical resistivity of this compound below room temperature, the thermal conductivity has not been thoroughly investigated. In this work, a complete data set for all the thermoelectric properties of $CeCu_6$ was obtained. The results were published and can be found in reference [29].

5.2.2 Experimental

Stoichiometric amounts of Ce (99.9%, Alfa Aesar) and Cu (99.999 %, Alfa Aesar) were melted in an argon environment using an arc-melter (MRF Inc.). To improve chemical homogeneity, the melted sample was flipped over and re-melted three times. The resulting ingot was etched in dilute nitric acid then ball milled for five hours to create a nanopowder of $CeCu_6$. The nanopowder was then hot pressed for two minutes at 450, 600 and 800 ^{o}C under a uniaxial pressure of 80 MPa. Mass density of the pressed samples was determined using the Archimedes' method (see Table 1). The mass densities for the ingot and the sample HP 800 are comparable. However, the densities decrease as the hot-pressing temperature decreases. X-ray diffraction (XRD, Bruker, AXS) was performed on the freshly fractured surface of the samples. Scanning Electron Microscopy (SEM, JEOL 6340F) was used to investigate the grain-size distribution of the samples. The Seebeck Coefficient (S)

Table 5.1 IDs and densities of the four $CeCu_6$ samples used in this study.

Sample name	**Hot-pressing temperature (^oC)**	**Mass density** **(% of theoretical density)**
Ingot		90.8
HP 800	800	91.3
HP 600	600	80.4
HP 450	450	79.1

, electrical resistivity (ρ), and thermal conductivity (κ) from 5 to 300 K were measured on samples of typical dimensions of a 3x3x4 mm^3. A 2-point method in thermal transport option (TTO) of the Physical Property Measurement System (PPMS) was used to measure the thermoelectric properties. The horizontal rotator option of PPMS was used to measure Hall coefficient (R_H) of the samples with typical dimensions of $1\times2\times10$ mm^3.

5.2.3 Results and Discussion

The X-ray diffraction patterns are shown in Figure 5.1. The peak positions can be indexed confirming the orthorhombic crystal structure which also indicates that the ingot was alloyed in a single phase form. We note the X-ray pattern peaks are broadened only slightly by the ball-milling process, while the crystal structure is retained by all the hot pressed samples.

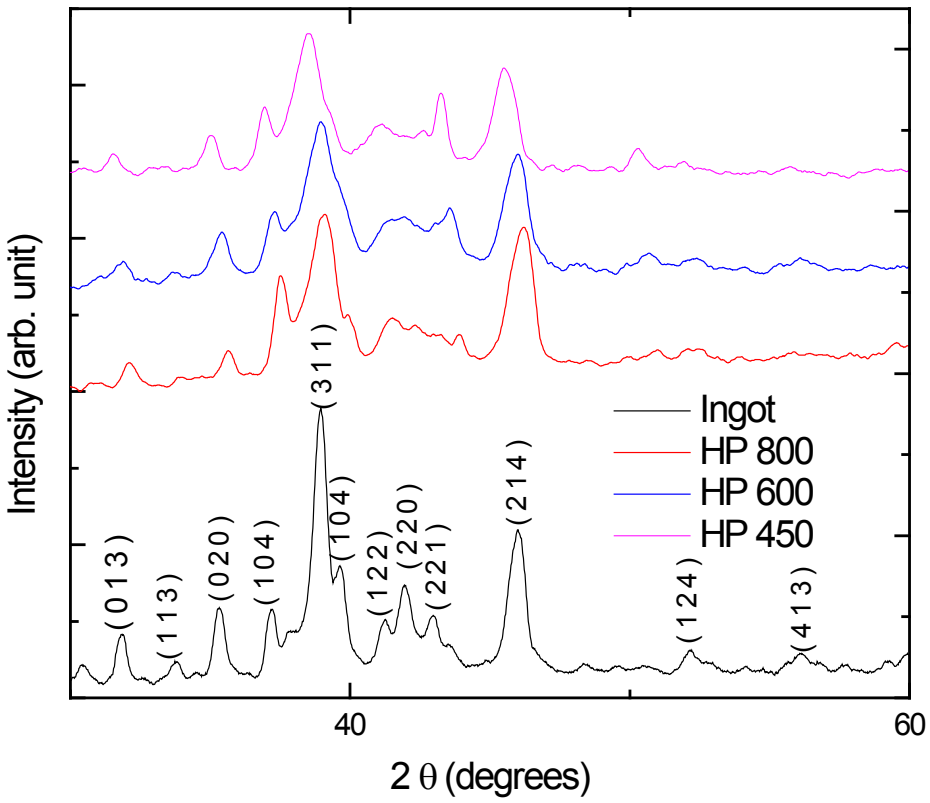

Figure 5.1 X-ray diffraction pattern for the arc melted ingot and the three hot pressed samples of $CeCu_6$.

Figure 5.2 shows the SEM images of the samples. No voids, within the resolution of the equipment, are seen for the ingot and the sample HP 800 ^{o}C. The comparable density values for the ingot and the sample HP 800 (Table 1) are consistent with the similar texture seen in the SEM images. The samples hot pressed at 450 and 600 °C show a distinctly different microstructure from the HP 800 sample. Sample porosity increases and surface texture becomes rough at the lower hot pressing temperatures. Degraded density with a smaller grain-size distribution at lower hot pressing temperature is typical trend in mechanical nanostructuring.

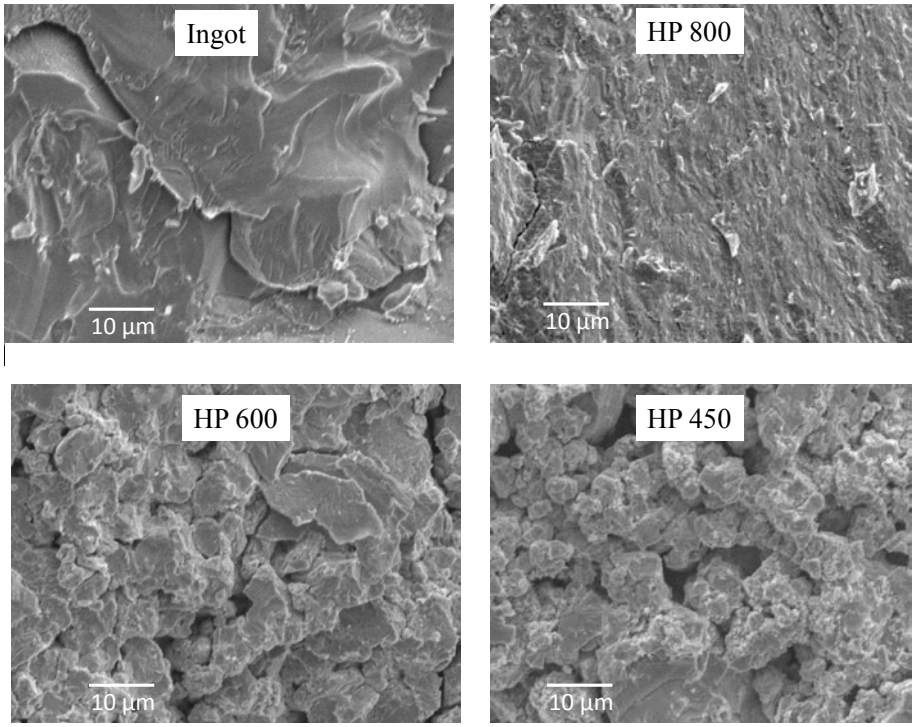

Figure 5.2 SEM images of the freshly fractured surface of $CeCu_6$ samples.

The electrical resistivity □□of the samples as a function of temperature are shown in Figure 5.3. All the samples exhibit a similar resistivity profile, typical of single crystal $CeCu_6$. Below 300 K, the resistivity decreases as the temperature is lowered until it reaches a flat minimum. At approximately 75 K a Kondo-like behavior emerges with a negative value for the temperature-derivative ($\partial\rho/\partial T$). The resistivity then reaches a maximum at around 15 K before declining sharply with decreasing temperature, an indication of Kondo coherence development. Electrical resistivity of the 800 ^{o}C hot-pressed sample is slightly increased when compared to the ingot; this is expected due to the increased scattering from the nanocomposite grains. A comparison among the hot-pressed samples shows that the electrical properties of $CeCu_6$ are greatly affected by

varying HP temperature. With decreasing HP temperature the electrical resistivity increases significantly. When comparing HP 800 and 450 ^{o}C samples, we note at 60 K an increase in resistivity by a factor of ~ 3.4. Such a drastic increase in the electrical resistivity is attributed to the reduced grain size and the increased porosity.

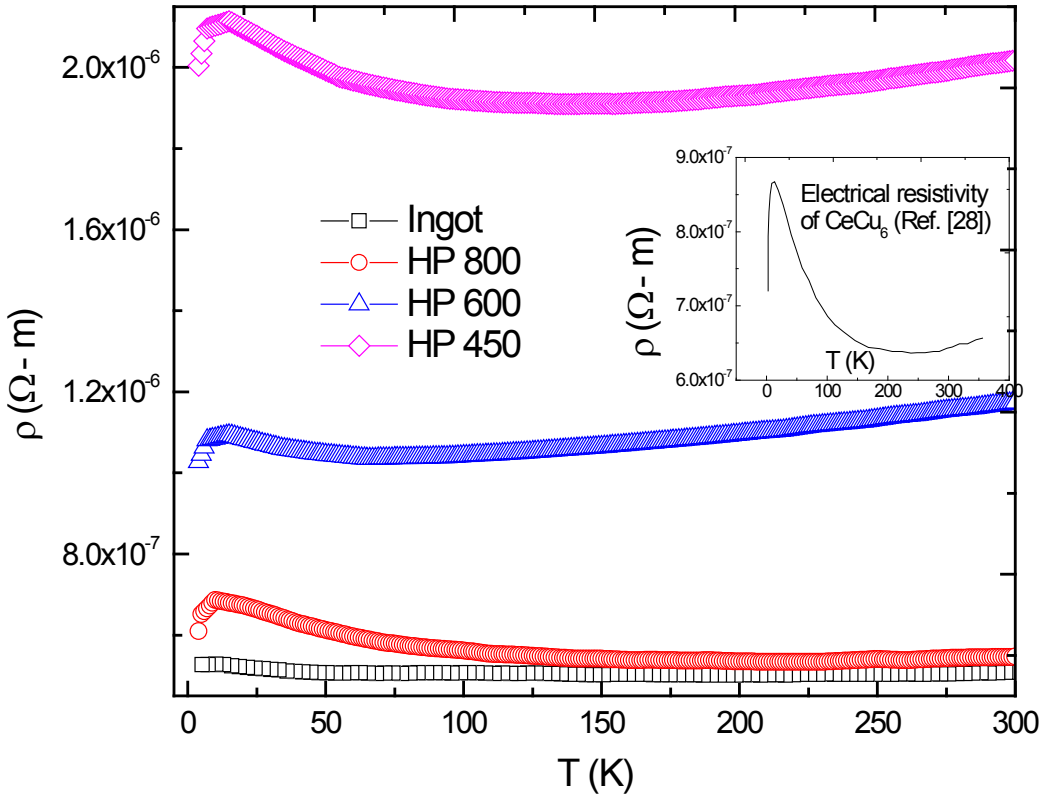

Figure 5.3 Electrical resistivity as a function of temperature for the $CeCu_6$ samples. The inset shows a typical resistivity profile for $CeCu_6$ [25].

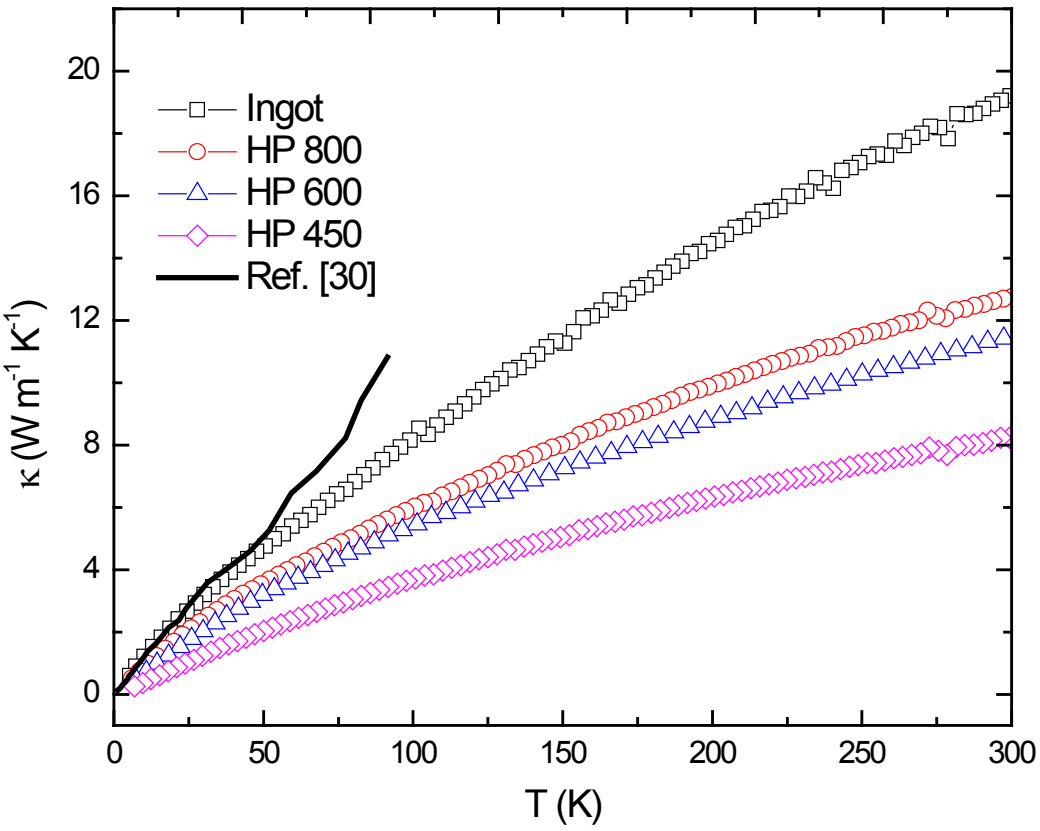

Figure 5.4 Thermal conductivity as a function of temperature for the three nanostructured $CeCu_6$ samples. The data for the polycrystalline sample was drawn from Ref. [30] and replotted for comparison.

Figure 5.4 shows the total thermal conductivity (κ) for the samples as a function of temperature. For comparison the thermal conductivity for polycrystalline samples of $CeCu_6$ was taken from reference [30] and plotted. The thermal conductivity follows temperature dependence similar to that reported for another HFC, $CeCu_4Al$ [31]. The total thermal conductivity decreases as the HP temperature decreases. At 60 K, κ was reduced from ~ 5 W m^{-1} K^{-1} (for ingot) to ~ 2 W m^{-1} K^{-1} (for sample HP 450), a reduction

by 60 %. In general, $\kappa = \kappa_l + \kappa_e$, where κ_l and κ_e are the lattice and electronic contributions to the total thermal conductivity, respectively. Generally, phonon scattering by grain boundary reduces the phonon contribution (κ_l) whereas macroscale porosity is shown to reduce the electronic contribution (κ_e) [32, 33]. The SEM images (Figure 5.2) suggest that the reduction of the thermal conductivity with decreasing HP temperature might be attributed to the combined effect of both the contributions from grain boundary scattering and the porosity effect.

In Figure 5.5, the temperature dependence of the Seebeck coefficient for the CeCu6 samples are shown. All the samples exhibit a positive Seebeck coefficient (p-type) below 300 K with a maximum at $T_{max} \approx 50$ K. This value for T_{max} is in agreement with the previously reported data [32, 33]. In the context of heavy-fermions, such a peak in S at higher T ($T > T_K$) is usually attributed to the Kondo scattering on higher multiplets (as opposed ground state doublet) which are split by crystal field effects (CEF). For $T > T_{max}$, S follows an unusual temperature dependence of the form: $S \propto -lnT$, whereas for $T < T_{max}$, S follows the typical behavior of metals ($S \propto T$). The Seebeck coefficient decreases as the HP temperature is reduced.

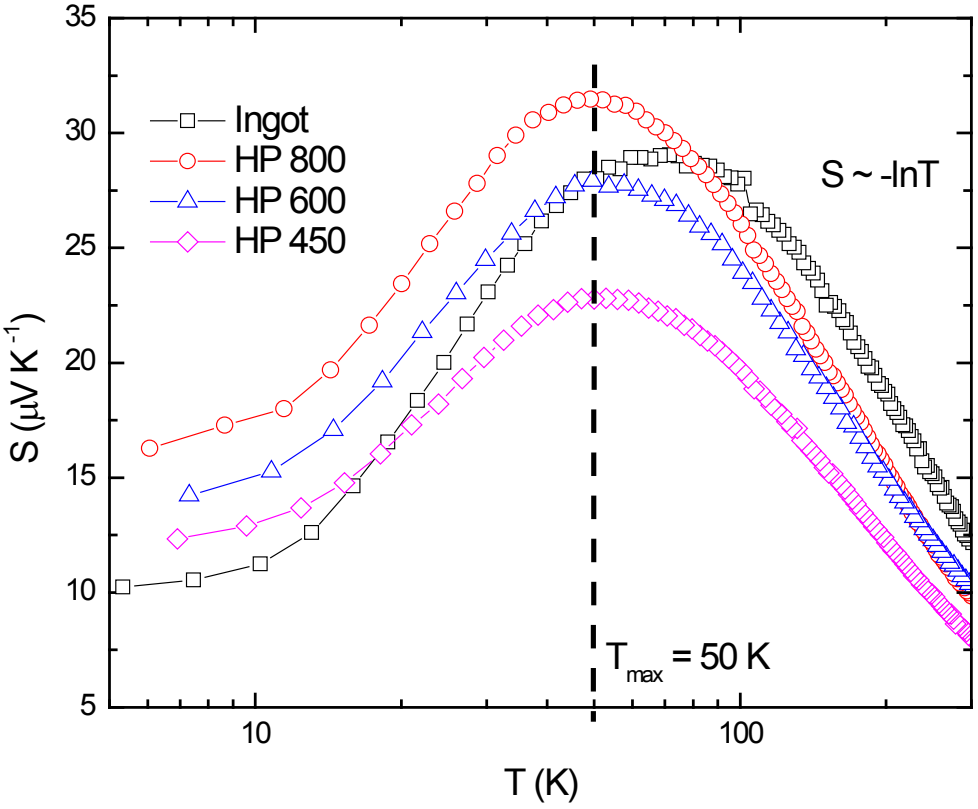

Figure 5.5: Seebeck coefficient as a function of temperature for the $CeCu_6$ samples.

The Hall coefficients (R_H) of the samples as a function of temperature below 100 K (temperature range at which the *ZT* curve peaks) were also measured. Under the assumption of one band model, the effective carrier density (n) and the Hall mobility (μ) were calculated using the formulas, $n = {}^{1}/_{|R_H|e}$ and $\mu_H = {}^{|R_H|}/_{\rho}$, respectively, where e = 1.6 $\times 10^{-19}$ C is the electronic charge. R_H, and μ_H of the samples as a function of temperature are shown in Figure 5.6. Our data is consistent with the previous report [34] with R_H staying positive in the whole range of 5 – 100 K. At high temperature, $R_H \approx 0$

indicates that the electron and hole contributions to R_H cancel the effect of each other. As the temperature decreases, the contribution from holes increases leading to a prominent peak at low temperature. This is taken as an indication of coherent state development, usually observed in heavy Fermion metals. The Hall coefficient for the ingot sample (5.26×10^{-4} cm^3 C^{-1}) is of the same order as reported in literature [34]. R_H, and μ_H decrease by two orders of magnitude going from the ingot to the hot-pressed samples. This indicates increased carrier concentration in the nanostructured samples when compared to the ingot. The defects induced during ball-milling process might have contributed to such a drastic increase in carrier concentration.

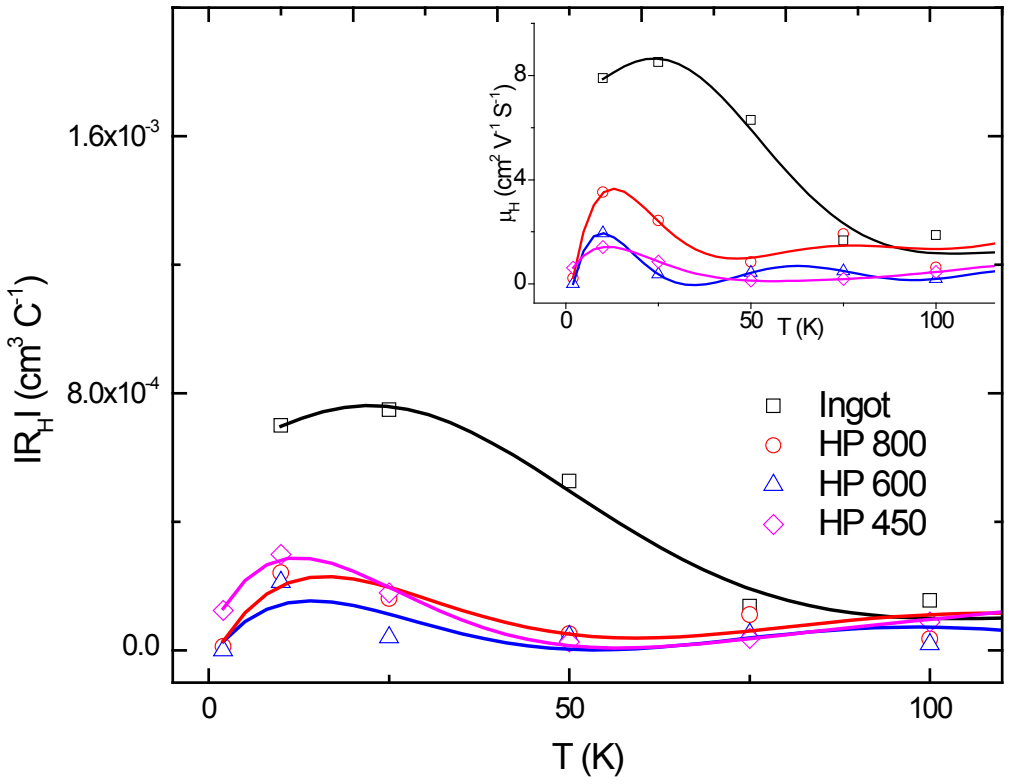

Figure 5.6 Hall coefficient of $CeCu_6$ samples as a function of temperature in the temperature range 2 – 100 K. Solid lines are just guide to eyes. Inset: Hall mobility as a

function of temperature. Solid lines are drawn to guide eyes.

When compared among the hot-pressed samples, R_H does not change much. However there is clear trend in mobility data indicating that decrease in hot-pressing temperature decreases the carrier mobility.

The calculated temperature dependent dimensionless thermoelectric figure-of-merit (*ZT*) is shown in Figure 5.7. The *ZT* values reach a peak at around 60 K for all the samples. The peak value of *ZT* for the optimized sample HP 800 is 0.024 at 60 K. Since the ingot and the sample HP 800 have comparable values of power factor at 60 K (Inset of Fig 5.7), the improved *ZT* is derived from the reduction in thermal conductivity. This ZT at this low temperature is significant when compared with other materials [35,36,37].

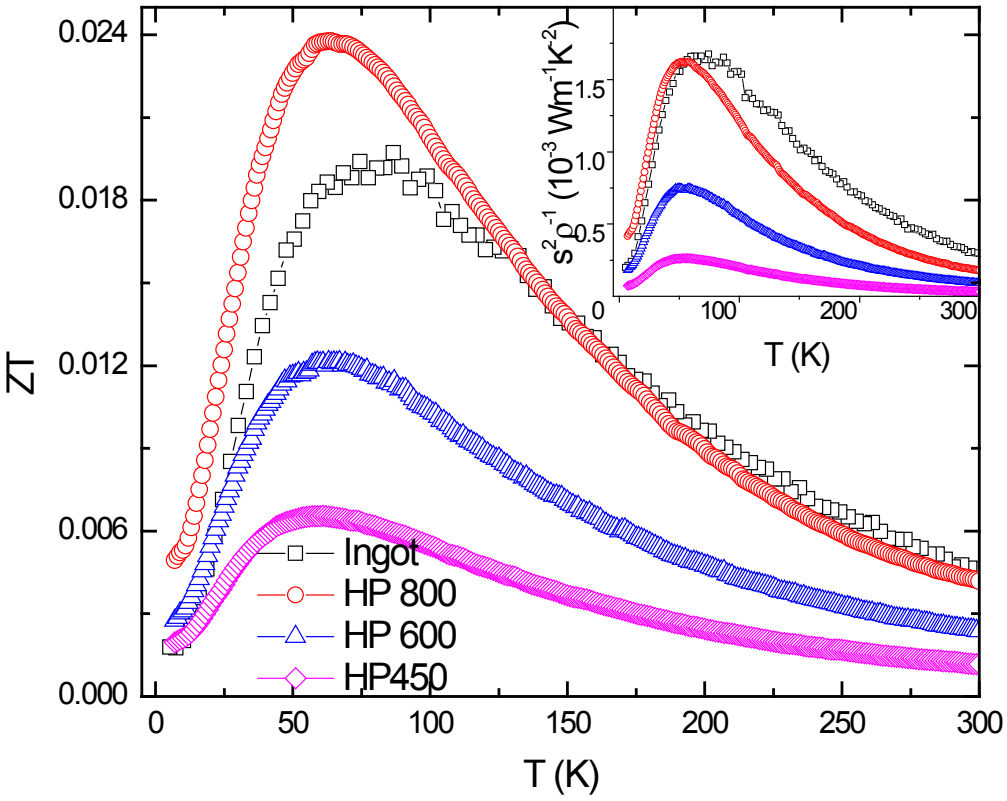

Figure 5.7 *ZT* as a function of temperature for the $CeCu_6$ samples. Inset shows the power factor as a function of temperature.

While the original goal for nanostructuring was to increase the power factor (*PF*) by employing quantum confinement of carriers [38, 39], experiments [40-42] have shown that the key reason for improved *ZT* was the reduction of thermal conductivity. Therefore, in recent years researchers on nanostructured thermoelectric material have focused on reducing the thermal conductivity, while producing minimal adverse effects on the Seebeck coefficient and the electrical conductivity. This approach seems to work most effectively in systems where the thermal transport is phonon-dominated (as opposed to electron-dominated).

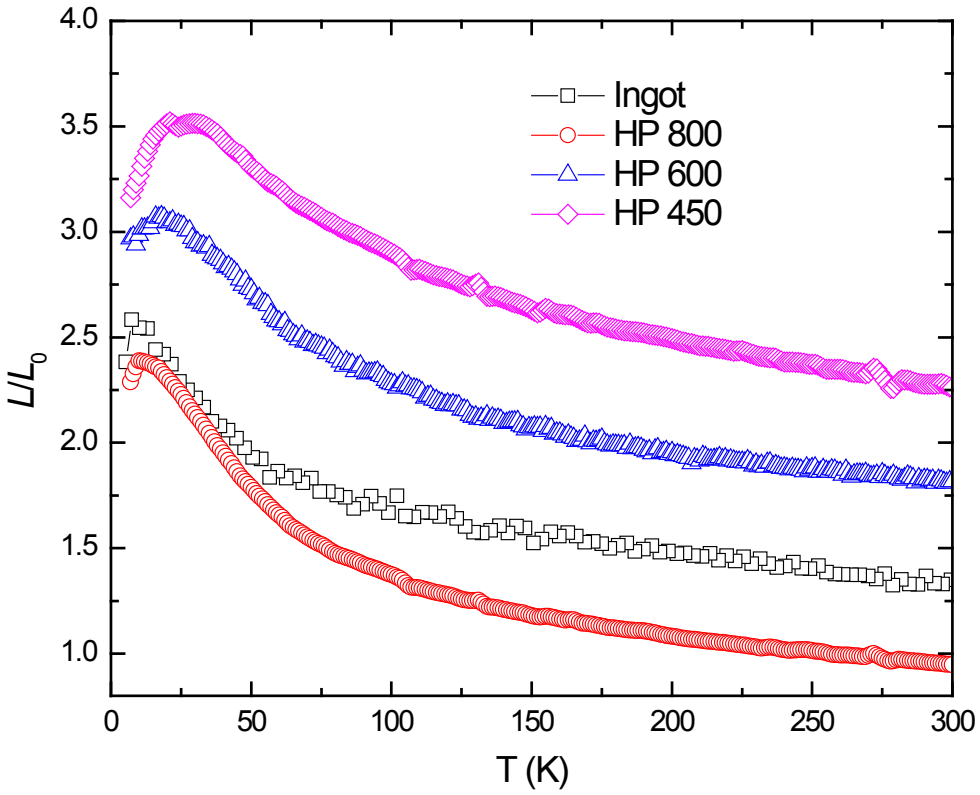

Figure 5.8 Reduce Lorenz number as a function of temperature for the $CeCu_6$ samples. L is defined as $L = \kappa\rho T^{-1}$ and L_0 = 2.45 $\times 10^{-8}$ W Ω K^{-2} for free electron was used in calculation.

One of the ways to analyze the effectiveness of nanostructuring is to look at the values of the reduced Lorenz number (L/L_0). Here L is defined as $L = \kappa\rho T^{-1}$ and L_0 = 2.45 $\times 10^{-8}$ W Ω K^{-2} is the free-electron value. In general a value of L/L_0 much greater than 1 implies that the phonons are the dominant mode of thermal transport. In Figure 5.8, the temperature dependence of L/L_0 is illustrated. The shape of the $L/L_0\,(T)$ curve for all of the samples is typical of heavy fermions, generally there is a slow monotonic rise in L/L_0 as temperature decreases until a maximum is reached at low tempertures. The L/L_0

ratio decreases in the sample HP 800 when compared to the ingot showing that the lattice contribution to the total thermal conductivity was effectively reduced in the HP 800 sample. However, with a further decrease in the HP temperature, L/L_0 increases significantly. At lower HP temperatures, the thermoelectric properties are affected in such a way that the electronic contribution to the total thermal conductivity decreases more rapidly than the phononic contribution does. As a result no net gain in *ZT* was achieved by lowering the hot-pressing temperature.

5.3 Thermoelectric Properties of $CeAl_3$

5.3.1 Introduction

Since the first study by Andres *et al*. [43] in 1975, $CeAl_3$ has been the subject of extensive research. Like $CeCu_6$, this compound also exhibits an extremely large Sommerfeld coefficient γ = 1620 mJ/(K^2-mol) and A = 35 μΩ cm /K^2 where A is associated with the Fermi liquid relation of the electrical resistivity $\rho = \rho_0 + AT^2$ [43]. Originally, $CeAl_3$ was considered to be a heavy fermion without any magnetic ordering. However, later, it was revealed by μSR and NMR experiments [44, 45] that $CeAl_3$ orders antiferromagnetically below T_N = 1.2 K. Initially, many researchers paid attention to its electrical transport properties [46, 47] and their pressure dependence [15]. Later, Ott *et al*. [48] reported the thermal conductivity in the temperature range of 0.06 – 50 K thereby demonstrating the validity of Wiedemann-Franz law in heavy electron systems.

5.3.2 Experimental

The synthesis procedure for $CeAl_3$ is similar to that used for $CeCu_6$. Stoichiometric amounts of Ce (99.9%) and Al (99.999 %) were mixed and arc melted

together on a water-cooled copper hearth in an argon atmosphere. To attain chemical homogeneity, the melted sample was flipped on the hearth plate and re-melted twice. Nanopowders of $CeAl_3$ were prepared by ball milling the ingot for 5 hours. The nanopowder was then hot pressed for 2 minutes at 400, 600 and 800 ^oC while a uniaxial pressure of 80 MPa was applied. X-ray diffraction (XRD) was performed on the fresh fracture surfaces of the samples. The Seebeck Coefficient (S), electrical resistivity (ρ), and thermal conductivity (κ) from 5 to 330 K were measured simultaneously on a sample of typical dimensions of 2x2x8 mm^3. The four-point method of thermal transport option (TTO) of the Physical Property Measurement System (PPMS) was used. The horizontal rotator option of PPMS was used to measure Hall coefficient (R_H) on a sample with typical dimensions of $1\times2\times10$ mm^3.

5.3.3 Results and Discussion

Figure 5.9 shows the X-ray diffraction patterns for the samples. Some impurity phases associated with $CeAl_2$, Ce, and Al can be seen for the ingot. However, these impurity phases disappear in the X-ray diffraction patterns for the hot-pressed samples at 800 ^oC and the peaks can be indexed to the hexagonal Ni_3Sn-type crystal structure. The samples become more homogeneous and show an enhanced single phase behavior after the ball-milling and hot-pressing process.

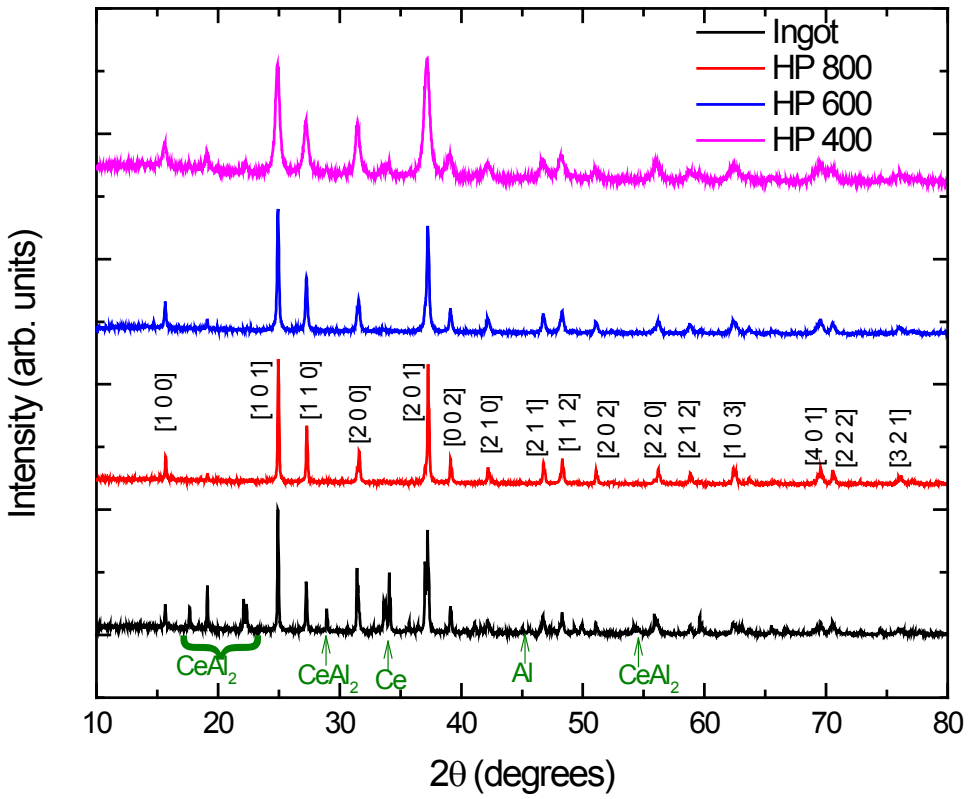

Figure 5.9 X-ray diffraction patterns of the $CeAl_3$ samples used in this work.

The results of the measurements of the temperature dependence of the total thermal conductivity are shown in Figure 5.10. The temperature dependence for all the samples are typical of heavy fermion systems and closely resemble the dependence reported for other HFCs such as CeB_6 [49] and $CeCu_4Al$ [31]. The thermal conductivity values for the ingot sample are consistent with the values for the polycrystalline sample reported by Ott *et al*. [48]. Within the 5-330 K range, the thermal conductivity decreases significantly as the HP temperature decreases. As a reference, at 55 K, $\kappa = 2.5$ W m^{-1} K^{-1} and 0.4 W m^{-1} K^{-1} for the samples HP 800 and HP 400 respectively, this represents a

reduction in the thermal conductivity by ~85 %. In nanostructured samples, such a decrease in thermal conductivity is mainly attributed to the increased scattering of phonons off the grain boundaries.

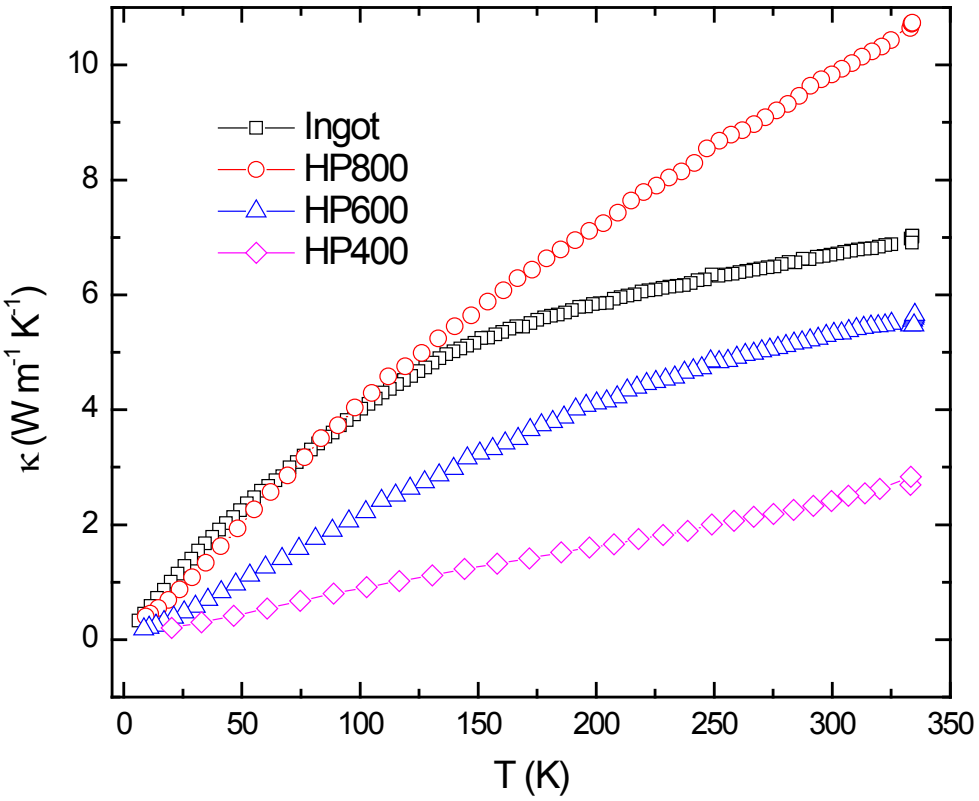

Figure 5.10 Thermal conductivity of the $CeAl_3$ samples as a function of temperature.

In general, the total thermal conductivity is the sum of two independent contributions from the lattice and the carriers. The relationship is described by the following equation: $\kappa = \kappa_{carrier} + \kappa_{lattice}$ where κ is the total effective thermal conductivity of the system, and $\kappa_{carrier}$ and $\kappa_{lattice}$ are the carrier and lattice contributions respectively. A rough estimation of $\kappa_{carrier}$ can be made using the Wiedemann-Franz law,

$\kappa_{carrier} = L_0\rho^{-1}T$ where L_0 = 2.45 $\times 10^{-8}$ W Ω K^{-2} is the Lorenz number, ρ is the electrical resistivity, and T is the temperature in K. The $\kappa_{carrier}$ for all the samples was calculated using the experimentally determined values of ρ. In Figure 5.11, we show the temperature dependence of $\kappa_{lattice}$ in a log-log plot in the 6-50 K temperature range. At 55 K, 65 % of the total thermal conductivity of the sample HP 800 comes from the lattice contribution. For the HP 600 and HP 400 samples, these contributions are 74 % and 78 %, respectively. Fitting data to the power law, $\kappa = \beta T^{\alpha}$, shows the almost linear dependence of κ on T with the α values ranging from 0.83 to 1.11. Such a linear dependence is consistent with previous reports and is related to the fact that relevant phonon wavelengths are comparable to or larger than the electronic mean free paths [48].

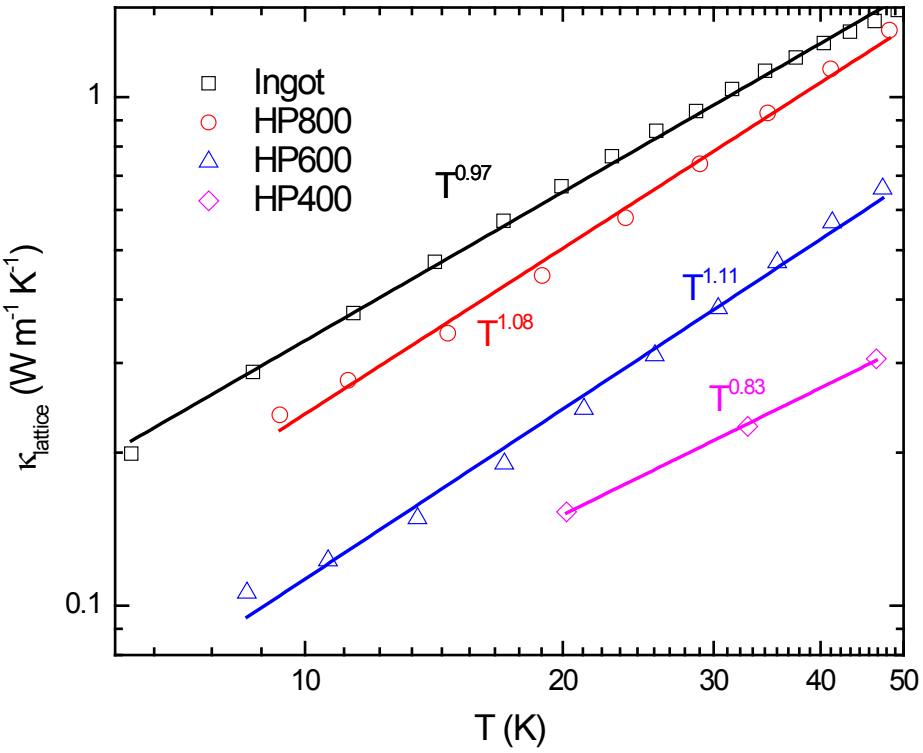

Figure 5.11 Lattice thermal conductivity as a function of temperature in the range of 6 –

50 K.

The experimental data on the electrical resistivity is shown in Figure 5.12. $\rho(T)$ curves for all the samples follow the classic shape for a strongly correlated HF metal, with a coherence peak at ~35 K. While the coherence peak has been consistently reported to occur at around 35 K, the resistivity values for our nanostructured samples hot pressed at 400 and 600 ^{o}C are considerably larger than their single crystal counterparts. This is expected due to the increased porosity and number of defects in the nanostructured samples. Among the hot-pressed samples, the electrical resistivity varies significantly with HP temperature. At 35 K, the resistivity increases by a factor of 1.9 from the HP 800 sample to the HP 600 sample, and from HP 600 to HP 400, it increases by a factor of 2.6. A similar behavior in resistivity at lower HP temperature was observed in the HFC $CeCu_6$ [29].

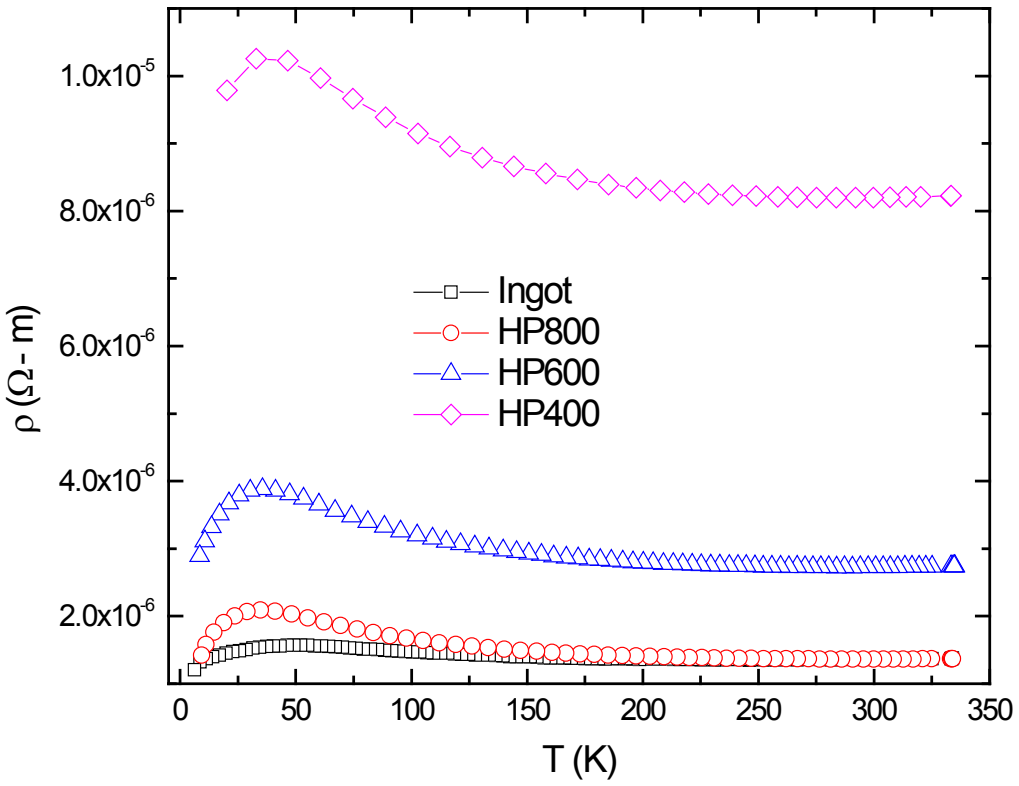

Figure 5.12 Electrical resistivity of the $CeAl_3$ samples as a function of temperature.

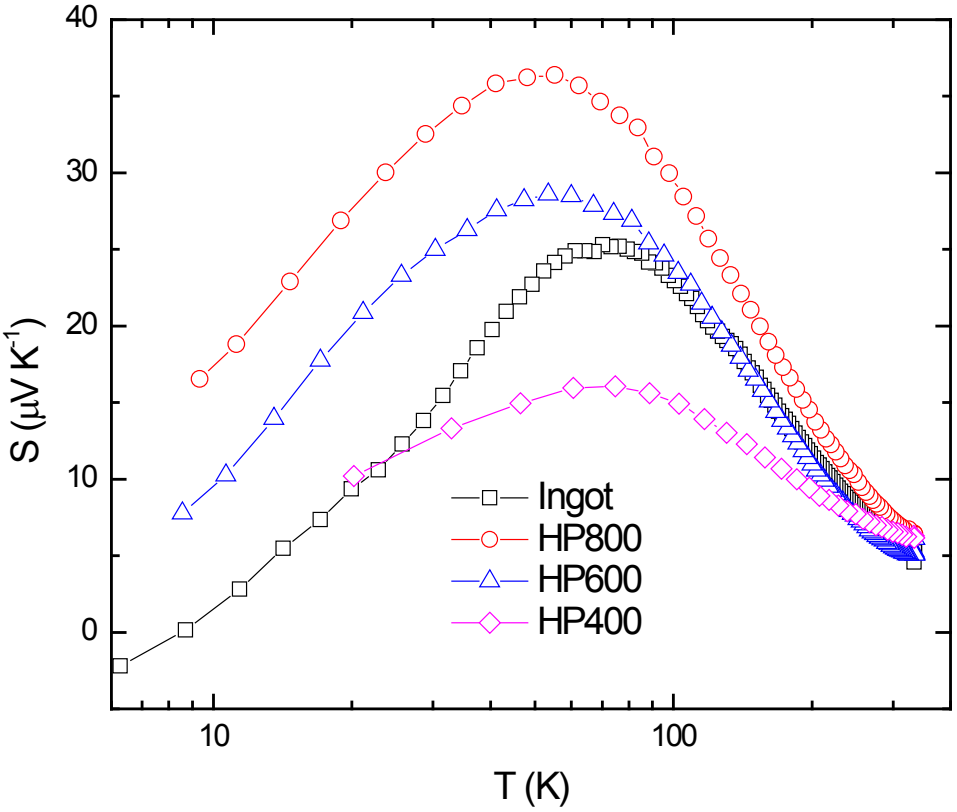

Figure 5.13 Seebeck coefficient of the $CeAl_3$ samples as a function of temperature.

Figure 5.13 shows the Seebeck coefficient as a function of temperature. For all the samples, the Seebeck coefficient is positive in the temperature range of 5-330 K, implying that the majority charge carriers are holes (p-type). The peak in Seebeck coefficient, which is thought to result from Kondo scattering of higher energy multiplets, occurs at ~55 K. The negative peak due to the Kondo scattering of ground state doublet has been shown to occur at 3.5 K for $CeAl_3$ [15] that is out of the temperature range of this experiment. Above 55 K, a logarithmic dependence $S \propto -(lnT)$ is followed. This trend is consistent with the data previously reported and is usually associated with the

formation of heavy charge carriers (also called the spin polarons) as a result of the DOS renormalization in the vicinity of the Fermi energy [27]. The maximum value of S = 36 μV K^{-1} was observed for the HP 800 sample. The peaks are suppressed as Hot-Pressing temperature decreases.

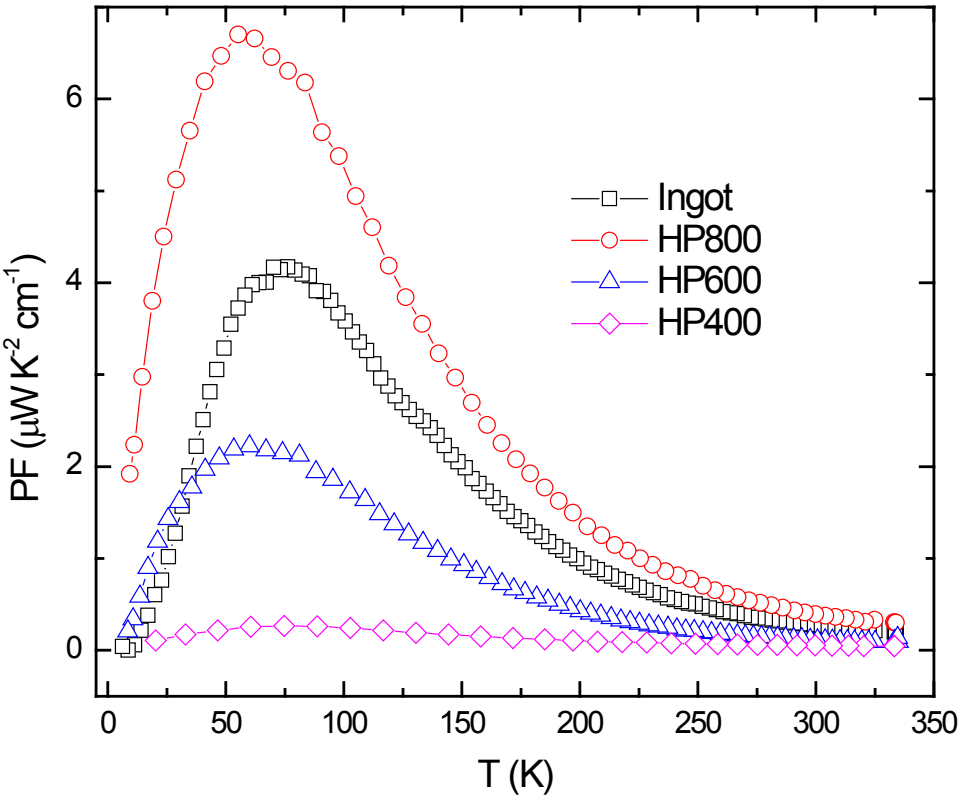

Figure 5. 14 Power factor of the $CeAl_3$ samples as a function of temperature.

In Figure 5.14, we plot the power factor ($PF = S^2\rho^{-1}$) as a function of temperature. The HP 800 sample produces the highest value of PF (6.6 $\mu WK^{-2}cm^{-1}$) at 55 K that is less than the value of 15 μW K^{-2} cm^{-1} at 50 K reported by Mahan *et al*. [50]. The smaller PF value in our samples is due to decreased Seebeck coefficient and increased resistivity

brought on by the nanostructuring process. As the HP temperature decreases, *PF* decreases dramatically.

Although reducing the HP temperature decreases the thermal conductivity of $CeAl_3$, it also lowers the Seebeck Coeffient and electrical conductivity, which ultimately results in a decrease in ZT with decreasing HP temperature (see Figure 5.15). The highest *ZT* reported is 0.016 at 55 K in the HP 800 sample. Since at 55 K the ingot and the sample HP 800 have nearly the same thermal conductivity value, the improved *ZT* value for the latter comes from the improved Seebeck coefficient.

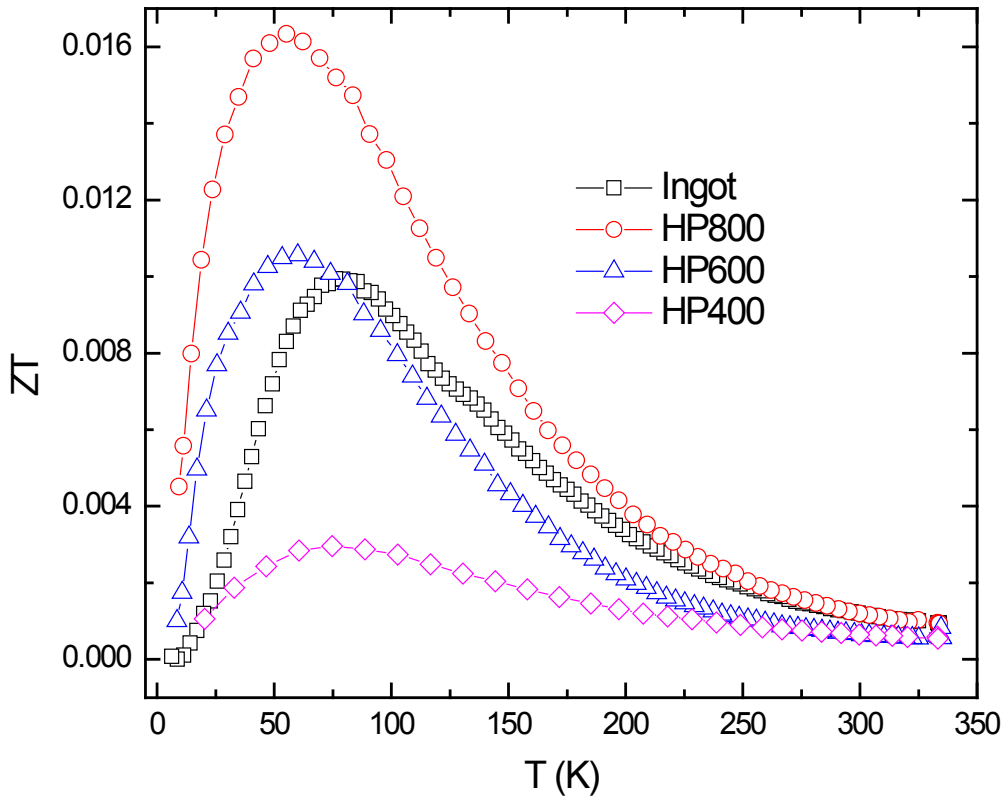

Figure 5.15 Thermoelectric figure-of-merit (*ZT*) of the $CeAl_3$ samples as a function of temperature.

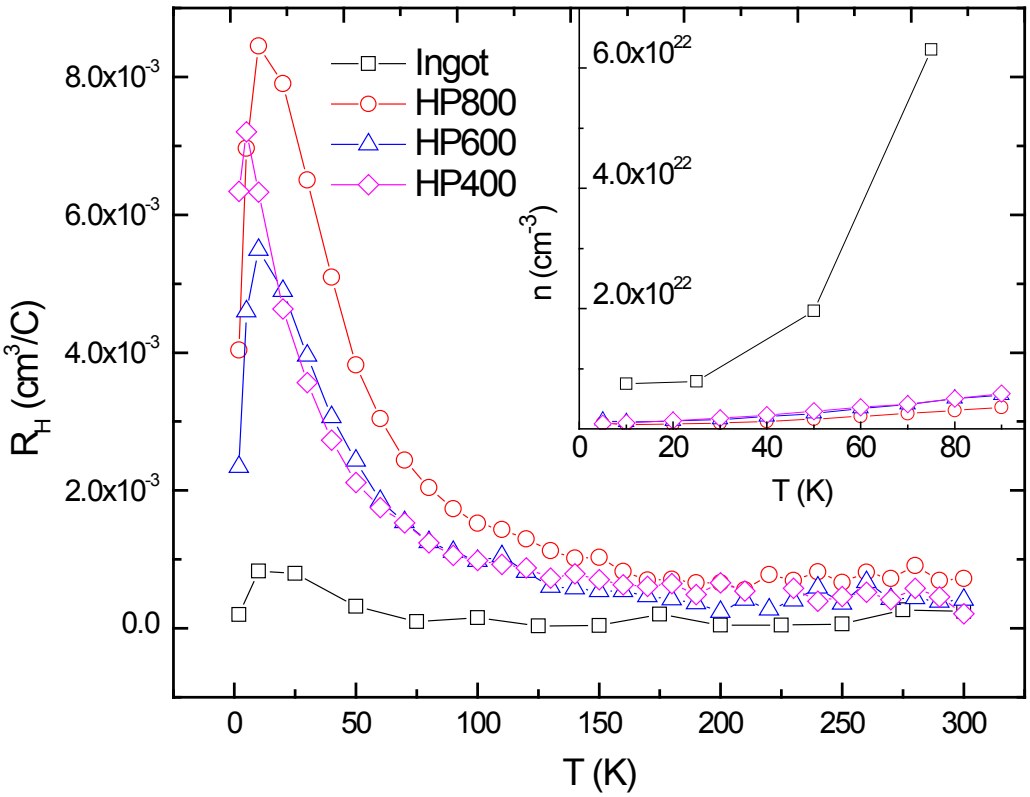

Figure 5.16 Hall Coefficient of the $CeAl_3$ samples as a function of temperature. Inset shows the temperature dependent carrier concentration.

Figure 5.16 shows the temperature dependence of the Hall coefficient (R_H). A magnetic field of 9 T was applied during Hall measurements. Our data is consistent with previous reports [51, 52] with R_H staying positive in the whole range of 5 – 330 K. At high temperatures, R_H is small indicating that the electron and hole contributions to R_H cancel each other. As the temperature decreases, the hole-contribution increases leading to a well-defined peak at T ≈ 10 K. A rapid increase in the Hall coefficient above the residual value at low temperatures is typical feature of heavy fermion metals and is associated with the development of skew scattering by fluctuation about the coherent

state [47]. The Hall coefficient of the ingot sample remains significantly smaller than that of the hot-pressed samples throughout the temperature range of the experiment. Since $R_H = {}^{1}/_{n\,e}$, where n is the carrier density and e is the electronic charge; this is indicative of a reduced carrier density in the hot-pressed as shown in the inset of Figure 8. Among the hot-pressed samples, amplitude of R_H decreases with decrease in HP temperature. In general, increases in carrier concentration decrease the absolute value of the Seebeck coefficient [53]. Therefore the decrease in S with decreasing HP temperature in our samples can be attributed, in part, to the increase in carrier density.

A rough calculation of effective mass (m^*) can be done using the relation $S = \frac{8\pi^2 \kappa_B^2 T}{3e\hbar^2} m^* \left(\frac{\pi}{3n}\right)^{2/3}$. Here $k_B = 1.38 \times 10^{-23}$ J K^{-1} is the Boltzmann constant, $\hbar = 1.05 \times 10^{-34}$ J S is the reduced Planck constant, T is the absolute temperature and n is the carrier density. Using experimentally determined Hall coefficient (Figure 5.16) and the Seebeck coefficient (Figure 5.13), calculations give $m^* \approx 33\ m_o$, $25\ m_o$ and $23\ m_o$ for samples HP 800, 600 and 400 respectively at 20 K (shown in inset of Figure 15.17). These values are slightly less than previously reported values ($\approx 45\ m_o$) in reference [10]. Hall mobility (μ_H) for the samples was calculated under the assumption of one band model using relation $\mu_H = {}^{R_H}/_{\rho}$. Figure 9 shows the temperature dependence of the Hall mobility, these results were derived from resistivity measurement shown in Figure 3. Quantitatively, the Hall mobility values are of the same order as reported earlier [28].

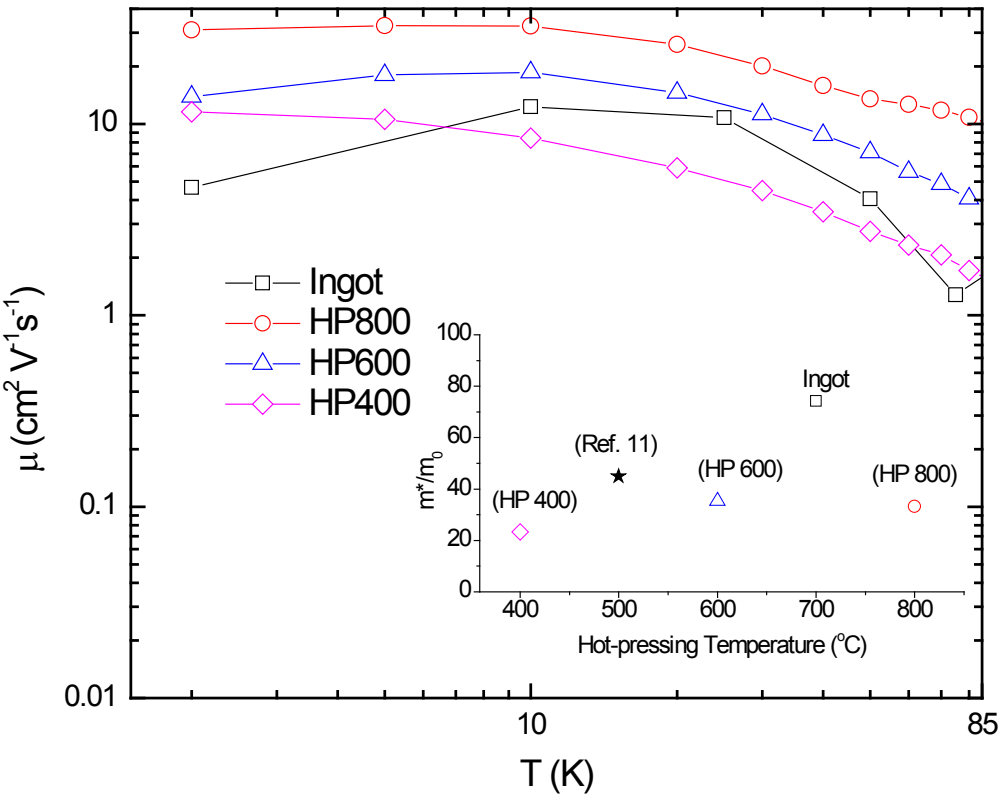

Figure 5.17 Hall mobility of the $CeAl_3$ samples as a function of temperature. Inset shows the effective mass at 20 K for all the samples.

In conclusion, samples of the heavy fermion compound $CeAl_3$ have been successfully synthesized by ball-milling of arc-melted ingot followed by hot-pressing. The thermoelectric properties of the samples have been measured and it has been shown that the temperature dependences of the properties are typical of the heavy fermion metal. The results show that variation of hot-pressing temperature results in significant changes in the thermal and the electronic transport properties. Mechanical nanostructuring was shown to be effective at decreasing the thermal conductivity of the system. The highest

ZT value measured was 0.016 at 55 K in the sample that was hot-pressed at 800 ℃. The results from the Hall coefficient measurements provide evidence for the differences in the carrier density and mobility among the samples. Further optimization of the thermoelectric properties of the heavy fermion compound $CeAl_3$ may also be achievable by doping.

5.4 Thermoelectric Properties of $YbAgCu_4$

5.4.1 Introduction

$YbAgCu_4$ comes from the family of parent compound $YbCu_5$ which hexagonal cr ystal structure [54-56]. Replacing of one Cu atom by Ag changes the crystal structure int o fcc structure [57]. $YbAgCu_4$ has been classified as moderate heavy Fermion with a Su mmerfield coefficient γ of ~250 mJ $mol^{-1}K^{-2}$, γ =C/T where C is the electronic specific h eat and T absolute temperature [58]. Mahan [59] mentioned a high power factor of ~ 235 $\mu W\ cm^{-1}\ K^{-2}$ on this compound. Such an attractive value for power factor makes this com pound worth investigation. The ground state of $YbAgCu_4$ is intermediate valence compou nd with 8 fold degeneracy [60]. There is presence of giant Seebeck peak at 45 K that is d ue to Kondo scattering of conduction electron from almost the full f band [61]. The therm al conductivity of $YbAgCu_4$ is mysteriously low below 50 K in comparison to other heav y fermion systems that are good thermoelectric materials [62].

5.4.2 Experimental

Nanostructured samples of $YbAgCu_4$ were prepared by arc melting followed by mechanical alloying process. The stoichiometric ratio of 99.9% pure Ag and 99.9% Cu g- ranular from Alfa Aesar was kept in arc melting hearth and melted to make the single pie- ce. 99.9% pure Yb pieces with 10 % extra Yb is kept in arc melting hearth with Ag-Cu pi

ece and melted together. The main idea for this melting approach is to avoid the direct co ntact of arc with Yb, which is volatile in nature. The melting process is repeated for 8 tim es by monitoring the total weight loss at each step. The ingot is polished with metal brush and ball milled for 6 hours in high energy ball mill machine. The powder is DC hot press ed at 550, 650, and 750 ^{o}C at a pressure 100 MPa for five minutes to see the effect of hot pressing temperature on the structures and properties.

5.4.3 Results and Discussion

The results on thermoelectric properties are shown in Figure 5.18 below. The ther mal conductivity of these samples decrease with temperature. The thermal conductivity o f the samples hot pressed at 550 ^{o}C is smaller than the other two because of probably the smaller grain size.

The electrical resistivity of the samples exhibits a strong metallic behavior below 75 K, and a weak semiconductor above 75 K. This phenomenon is well understood in ter ms of dilute Kondo scattering of conduction electron by Yb atoms. When the temperature decreases from 200 K to lower temperature, Kondo scattering is more prominent and hen ce the electrical resistivity increases with decreasing temperature. When the temperature goes below 75 K, the dilute Kondo system transformed to Kondo lattice system with peri odic localization of f- ion arrangement. Such a localized state forms a coherent f band wh ere all the elastic scattering of conduction electron get vanished with sharp decrease in ele ctrical resistivity. The electrical resistivity of the sample hot pressed at 550 ^{o}C is higher c ompared to the other two samples. This can be understood as the result of higher defect d ensity present in the samples, which scatters the charged carrier. Since the defects and ch arged carrier affects the density of states, it is reasonable to have higher density of states f

or the sample hot pressed at 550 ^{o}C. For the other two samples, the lines are nearly parall el showing nearly the same density of states.

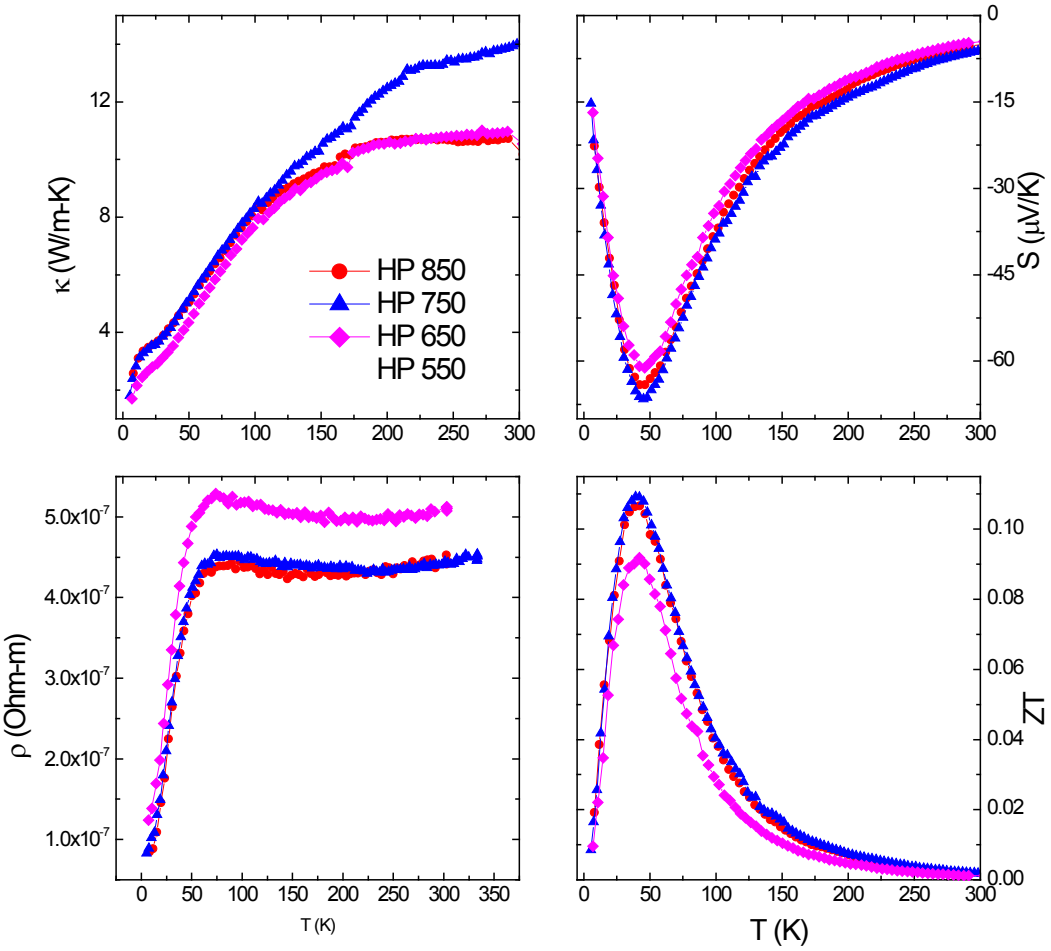

Figure 5.18 Temperature dependence of the thermoelectric properties of the $YbAgCu_4$ samples.

The Seebeck coefficient for all the samples is negative from 5 K to 200 K and has maximum value at 45 K. The Seebeck coefficient data was analyzed to obtain the value of the energy gap between the Kondo peak and Fermi level to be ~3 meV [63] which matches well with the gap obtained by optical measurement reported [64]. The sample hot p-

ressed at 550 ^{o}C has larger number of defects giving larger contribution to positive Seebeck which in fact decreases our negative Seebeck coefficient.

With the high power factor, a peak *ZT* of 0.11 for the sample hot-pressed at 550 ^{o} C has been achieved at 42 K, which is notably high at this low temperature. We believe even higher *ZT* can be achieved with further effort on this material.

References

1. N. Oeschler, S. Hartmann, U. Koehler, M. Deppe, Sun P, Steglich F. Thermoelectric power of correlated compounds. NATO Science for Peace and Security Series B: Physics and Biophysics (2009).
2. N. Grewe and F. Steglich, Handbook on the Physics and Chemistry of Rare Earths vol 14, ed K A Gschneider Jr and L L Eyring (Amsterdam: Elsevier) p 343 (1993).
3. A. C. Hewson, The Kondo Problem to Heavy Fermions (Cambridge: Cambridge University Press) (1993).
4. G. Aeppli and Z. Fisk, Comments Condens. Matter Phys. **16** 155 (1992).
5. Z. Fisk *et al*, Physica B **223/224** 409 (1996).
6. T. Takabatake et al, J. Magn. Magn. Mater. **177–181** 277 (1998).
7. L. Degiorgi, Rev. Mod. Phys. **71** 687 (1999).
8. P. S. Riseborough, Adv. Phys. **49** 257 (2000).
9. P. M. Chaikin, Organic Superconductivity, Edited By V. Z. Kresin, and W. A. Little (Plenum, New York), p. 101 (1991).
10. M. I. Ignatov, A. V. Bogach, G. S. Burkhanov, V. V. Glushkov, S. V. Demishev, A. V. Kuznetsov, O. D. Chistyakov, N. Yu. Shitsevalova, and N. E. Sluchanko, Journal of Experimental and Theoretical Physics, **105**, 58–61 (2007).

11. V. Zlatić, A. C. Hewson, Properties and Applications of Thermoelectric Materials: The Search for New Materials for Thermoelectric Devices, Springer, (2009).
12. P. Paschen: Thermoelectric Handbook, Edited by D. M. Rowe, CRC Press, Taylor and Francis, Boca Raton, FL (2006).
13. G. Sparn, W. Lieke, U. Gottwick, F. Steglich, and N. Grewe, J. Magn. Magn. Mater. **47**, **48**, 521-523 (1985).
14. A. Amato, D. Jaccard, J. Sierro, F. Steglich, and N. Grewe, J. Magn. Magn. Mater. **76**, **77**, 263-264 (1988).
15. Ch. Fierz, D. Jaccard, J. Sierro, and J. Flouquet, J. Appl. Phys. **63**, 3899
16. G. R. Stewart, Z. Fisk, M. S. Wire, Phys. Rev. B **30**, 482 (1984).
17. A. Amato, D. Jaccard, E. Walker, J. Flouquet, Sol. State Commun. **55**, 1131 (1985).
18. Y. Onuki, Y. Shimizu, T. Komatsubara, J. Phys. Soc. Japan **54**, 304 (1985).
19. Y. Onuki and T. Komatsubara, J. Magn.Magn. Mater., **63** and **64**, 281 (1987).
20. F. P. Milliken, T. Penney, F. Holtzberg, Z. Fisk, J. Magn. Magn. Mater. **76**, 201(1988).
21. A. Amato, D. Jaccard, J. Flouquet, F. Lapierre, J. L. Tholence, R. A. Fisher, S. E. Lacy, J. A. Olsen, N. E. Phillips, J. Low Temp. Phys. **68**, 371 (1987).
22. H. R. Ott, H. Rudigier, Z. Fisk, J.O. Willis, and G. R. Stewart, Solid State Commun. **53**, 235 (1985).
23. H. V. Lohneysen, T. Portisch, H. G. Schlager, A. Schroder, M. Sieck, and T. Trappmann, Phys. Rev. Lett. **72**, 20 (1994).

24. A. Rosch, A. Schroder, O. Stockert, and H. v. Lohneysen, Phys. Rev. Lett. **79**, 1 (1997).

25. J. Sakurai, F. Taniguchi, K. Nishimura, K. Sumiyama, H. Amano, and K. Suzuki, Physica B **186-188** (1993).

26. M. Ocko, M. Miljak, I Kost, J-G Park, and S. B. Roy, J. Phys. Condens. Matter **7,** 2979-2986 (1995).

27. M. I. Ignatov, A. V. Bogach, G. S. Burkhanov, V. V. Glushkov, S. V. Demishev, A. V. Kuznetsov, O. D. Chistyakov, N. Yu. Shitsevalova, and N. E. Sluchanko, Journal of Experimental and Theoretical Physics, **105** 58-61 (2007).

28. N. E. Sluchanko, D. N. Sluchanko, N. A. Samarin, V.V. Gluskhov, S. V. Demishev, A. V. Kuznestov, G. S. Burkhanov, and O. D. Chistyakov, Low Temperature Physics **35**, 7 (2009).

29. M. Pokharel, T. Dahal, Z. Ren and C. Opeil, Journal of Alloys and Compounds, **609**,228–232 (2014).

30. Y. Peysson, B. Salce, and C. Ayche, J. magn. Magn. Mater, **54-57**, 423-424 (1986).

31. M. Falkowski, and A. Kowalczyk, Proceedings of the European Conference Physics of Magnetism (PM'11), Pozman, June 27-July 1 (2011).

32. H. Lee, D. Vashaee, D. Z. Wang, M. S. Dresselhaus, Z. F. Ren and G. Chen, J. Appl.Phys. **107**, 094308 (2010).

33. J.M. Montes, F.G. Cuevas and J. Cintas, Appl. Phys. A **92**, 375–380 (2008).

34. A. S. Krivoshchekov, B. N. Goshchitskii, V. I. Voroin, I. F. Berger, Yu. N. Akshentsev, and A. E. Earkin, Physica B **359-361**, 178-180 (2005).

35. A. Bentien, S. Johnsen, G. K. H. Madsen, B. B. Iversen, F. Steglich, Europhys. Lett., **80**, 17008 (2007).

36. H. Zhao, M. Pokharel, S. Chen, B. Liao, K. Lukas, C. Opeil, G. Chen, and Z. Ren, Nanotechnology **23**, 505402 (2012).

37. B. C. Sales, E. C. Jones, B. C. Chakoumakos, J. A. Fernandez-Baca, H. E. Harmon, J. W. Sharp, E. H. Volckmann, Phys. Rev. B: Condens. Matter., **50** , 8207-8213 (1994).

38. L. D. Hicks and M. S. Dresselhaus, Phys. Rev. B, **47**, 12727 (1993).

39. L. D. Hicks and M. S. Dresselhaus, Phys. Rev. B, **47**, 16631 (1993).

40. R. Venkatasubramanian, E. Silvola, T. Colpitts, and B. O'Quinn, Nature, **413**, 597-602 (2001).

41. T. C. Harman, P. J. Taylor, M. P. Walsh, and B. E. LaForge, Science, **297**, 2229-2232 (2002).

42. K. F. Hsu, S. Loo, F. Guo, W. Chen, J. S. Dyck, C. Uher, T. Hogan, E. K. Polychroniadis, and M. G. Kanatzidis, Science, **303**, 818-821 (2004).

43. K. Andres, J. E. Graebner, and H. R. Ott, Phys. Rev. Lett. **35**, 1779-1782 (1975).

44. S. Barth, H. R. Ott, F. N. Gygax, B. Hitti, E. Lippelt, A. Schenck, C. Baines, B. van den Brandt, T. Konter and S. Mango, Phys. Rev. Lett. **59**, 26 (1987).

45. H. Nakamura, Y. Kitaoka, K. Asayama, and J. Flouquet, Journal of Magnetism and Magnetic Materials. **76** and **77**, 465-466 (1988).

46. J. Flouquet, J. C. Lasjaunias, J. Peyrard and M. Ribault, J. Appl. Phys. **53** (1982).

47. M. Hadzic Leroux, A. Hamzic, A. Fert, P. Haen, F. Lapierre and O. Laborde, Europhys. Lett. **1** (1986).

48. H. R. Ott, O. Marti, and F. Hulliger, Solid State Communications, **49** (1984).

49. E. Matsuoka, K. Umeo, S. Tsuji, M. Sera, F. Iga and T. Takabatake, Journal of the Physical Society of Japan **72**, 9 (2003).

50. G. D Mahan, Solid State Physics, **51** (Academic Press, Boston) (1998).

51. N. B. Brandt, V.V.Moshchalkov, N.E.Sluchanko et. al., Sol. St. Commun., **53**, 645 (1985).

52. P. Haen, J. Flouquet, F. Lapierre, P. Lejay and G. Re- menyi, J. Low Temp. Phys., **67**, 391 (1987).

53. A. F. Ioffe, Physics of Semiconductors, Academic Press, New York, 1960 (translated from Russian, Fizika Poluprovodnikov, Russian Academy of Sciences, Moscow, 1957).

54. H. Yamaoka, I. Jarrige, N. Tsujii, N. Hiraoka, H. Ishii, K. D. Tuesi, Phys. Rev. B, **80**, 035120 (2009).

55. N. Tsujii, J. He, F. Amita, K. Yoshimura, K. Kosuge, H. Michor, G. Hilscher, T. Goto, Phys. Rev. B, **56**, 8103 (1997).

56. A. Mitsuda, K. Yamauchi, N. Tsujii, K. Yoshimura, Y. Isikawa, Y. J. Yamada, Phys. Soc. Jpn., **76**, 78 (2007).

57. N. Tsujii, J. He, K. Yoshimura, K. Kosuge, H. Michor, K. Kreiner, G. Hilscher, Phys. Rev. B, **55**, 1032 (1997).

58. A. Yoshimori, H. Kasai, Journal of Magnetism and Magnetic Materials, **31 – 34**, 475 (1983).

59. G. D. Mahan, Solid State Physics, **51**, 81 (1998).

60. T. Graf, R. Movshovich, J. D. Thompson, Z. Fisk, P. C. Canfield, Phys. Rev. B, **52**, 3009 (1995).

61. R. Casanova, D. Jaccard, C. Marcenat, C. Hamdaoui, M. J. Besnus, Journal of Magnetism and Magnetic Materials, **90 & 91**, 587 (1990).

62. A. V. Golubkov, L. S. Parfen'eva, I. A. Smirnov, H. Misiorek, J. Mucha, A. Jezowski, Physics of Solid State, **43** (2001).

63. M. Koirala, M. Pokharel, H. Wang, Y. Lan, C. Guo, C. Opeil, and Z. F. Ren; Nano Letter **14** (9), 5016–5020 (2014).

64. M. Galli, F. Marabelli, E. Bauer, Physica B, **206** and **207**, 355 (1995).

65. Heavy-Fermions (HF) are a class of intermetallic compound, containing elements with 4f or 5f electrons, where the electrons appear to be "heavy" due to electron-electron correlations or interactions in the material. The effective electron mass, m*, in a HF is calculated to be greater than the rest mass, m_o, of a typical electron, such that $m^* = \square\, m_o$, where $\square > 1$. In this thesis the term heavy-Fermion is used, because the materials under consideration $CeCu_6$ and $CeAl_3$, exhibit evidence of electron-electron correlation behaviors and give rise to a peak in Seebeck coefficient below 50 K. Additionally, calculations on $CeAl_3$ data show $m^* \sim 33\ m_o$, $25\ m_o$ and $23\ m_o$ for samples prepared at different pressing temperatures and evaluated at ~ 20 K (see Ref: Pokharel, *et al., Energ. Convers. and Manage.* **87**, 584 (2014).). Although the $\square\square$values may be considered modest here for $CeAl_3$ as compared to the much larger values calculated for other heavy-Fermion compounds at lower temperatures, the term heavy-Fermion applies here simply because $\square > 1$.

Chapter 6

Conclusion

6.1 Overview

To sum up, samples of the n-type compounds $FeSb_2$ and $YbAgCu_4$ and p-type compounds $CeCu_6$ and $CeAl_3$ are prepared and characterized using the laboratory facilities of both Prof. Ren and Prof. Opeil. In some cases, the data represented the first attempt to explore the underlined physics behind thermoelectric phenomena in these compounds in the nanocomposite state. Several publications came out as a result of this work and can be found in Appendix B.

Chapter 1 introduces the basics of the thermoelectric phenomena and their application in practical life as the energy conversion technology.

In chapter 2, a brief description of the theory of thermoelectricity is presented. Different types of phonon scattering mechanisms which play key role in the thermoelectric properties of a material are discussed. Also some possible routes to achieve high *ZT* in cryogenic temperature are presented.

Several techniques of material synthesis, spectroscopic characterization and measurement are involved in this work. Chapter 3 presents on the description of these techniques. Calibration and benchmarking of a home-built AC susceptometer are discussed in Appendix A.

Significant improvements in the thermoelectric figure-of-merit (*ZT*) of the compound $FeSb_2$ is achieved in this work via different routes: nanostructuring, doping and semiconductor/metal interface approach. Chapter 4 is the result of several systematic studies made to improve ZT of $FeSb_2$. The phonon mean free path in $FeSb_2$ (~ 40 μm)

being almost two orders of magnitude larger than the electron mean free path (~ 10 nm) at low temperature (~ 15 K), mechanical nanostructuring is shown to be very effective to reduce the thermal conductivity. With a dramatic reduction in thermal conductivity by three orders of magnitude, the *ZT* in nanstructured $FeSb_2$ is increased by 160% from single crystal value of 0.005 to 0.013 at ~ 50 K. The concept of semiconductor/metal interface to improve thermoelectric properties is employed by incorporating Ag- and Cu-nanoparticles in the host nanostructured samples of $FeSb_2$. Ag-inclusion introduces the interfaces between $FeSb_{2-y}Ag_y$ and $Ag_{1-x}Sb_x$ phases in the samples. Due to the high electrical conductivity of the $Ag_{1-x}Sb_x$ phase, both thermal conductivity and electrical resistivity of the nanocomposite sample were reduced significantly in the lower temperature regime. This process enhanced the peak *ZT* to 0.020 at 60 ~ K, which is a 70% improvement over the best value (0.013), obtained through nanostructuring alone. Among the several dopants including In, Cr, Co, Ru and Sn, tellurium (Te) further decreases the thermal conductivity of nanostructured sample by introducing the point-defect scattering and improve the *ZT* value to 0.022 at 100 K. The largest value of peak *ZT* for $FeSb_2$ achieved in this work is 0.027 at ~ 65 K which was obtained through Cu-nanoinclusion. Calculations suggest the $FeSb_2$ and Cu have comparable values of the work functions. The highly conductive Cu helps suppress the insulating behavior of $FeSb_2$ at low temperature thereby resulting improved thermoelectric power factor.

Our study shows that the mechanical nanostructuring in $FeSb_2$, along with a drastic thermal conductivity reduction, also brings on a severe suppression of the Seebeck coefficient values at low temperatures. Furthermore, the suppression in the Seebeck coefficient was found strongly associated with the reduction in the thermal conductivity.

Both quantitative and qualitative analysis of the data clearly indicates a presence of phonon-drag mechanism at low temperature. We conclude that despite having the record value for the thermoelectric power factor, $FeSb_2$ does not offer much promise to be a good thermoelectric material at low temperature.

The Kapitza resistance analysis based on the effective medium approach (EMA) turns out to be a simple macroscopic model explaining several key features seen in the temperature dependent thermal conductivity of nanostructured $FeSb_2$ surprisingly well. Specifically, a large value of the Kapitza length (~ 390 nm at 10 K) implies the importance of interfacial thermal resistance over the bulk thermal properties of $FeSb_2$.

Chapter 5 presents a complete set of data for the thermoelectric properties for the heavy-fermion compounds $CeCu_6$, $CeAl_3$ and $YbAgCu_4$ and their *ZT* values are reported. The temperature dependent *ZT* values for these compounds are reported for the first time. The ZT values of 0.024 at 60 K, 0.016 at 55 K and 0.11 at 42 K are achieved for the compounds $CeCu_6$, $CeAl_3$ and $YbAgCu_4$ respectively. The positive values for the Seebeck coefficient (p-type) and a peaked nature of the *ZT* (*T*) curve in the temperature range of interest (5 -5300 K) for the compounds $CeCu_6$ and $CeAl_3$ are significantly important. This study shows that the thermoelectric properties of these heavy-fermion compounds exhibit strong dependence on sample processing temperature. The results indicate that mechanical nanostruturing deteriorates the electronic properties rapidly upon reducing grain-size thereby negating the gain obtained through the reduction of the thermal conductivity.

6.2 Future Work

While a great deal has been achieved carrying out this research, further

improvement in the thermoelectric performance of n-type $FeSb_2$, and $YbAgCu_4$ and p-type $CeCu_6$ and $CeAl_3$ are possible.

In case of $FeSb_2$, doping is promising direction to further improve thermoelectric performance. Effect of hot-pressing temperature variation on thermoelectric properties of $FeSb_{1.84}Te_{0.16}$ is carried out in this study. However the optimal composition for nanostructured sample may be different. An interesting future experiment would vary the Te content for to improve thermoelectric performance of Te-doped $FeSb_2$. Also Se-doping on Sb-site has shown to be promising but has not been studied extensively. Using nanostructuring in $FeSb_{2-x}Se_x$ samples could lead to improved *ZT*.

The study thermoelectric properties of undoped $CeCu_6$, $CeAl_3$ and $YbAgCu_4$ have been carried out in this thesis. Substituting Ce and Yb with other lanthanides like Ho, Yb etc. may be useful in reducing the thermal conductivity of these compounds by introducing point-defect scattering. Effect of doping on Cu and Al-sites is also worth investigation.

Appendix A

AC Susceptometer

A.1 Set up

The AC susceptometer was comprised of two coaxial coils: a primary coil and a secondary coil. The secondary coil consisted of a pair of counter-wound coils. The sample to be investigated goes inside of one of the secondary coils. The counter-winding ensures the cancelation of any signal arising from oter than the sample itself. An AC signal of particular frequency generated by a frequency generator (HP 3325A) is driven through the primary which induces an oscillating magnetic field inside it. In the presence of the sample inside one of the secondary coils, a voltage is detected which is proportional to the effective magnteic moment of the sample. Details on the design and working principle of an AC susceptometer can be found in references [1-4]. A lock in amplifier (SR 830) was used to detect the induced voltge across the secondary. A high resistance of the order of 10 KΩ was used to stabilize the current through the primary circuit. Figure A1 shows a block diagram showing different components of the set up. The primary and secondary coils were made by winding an insulated copper wire around a core frame made up of G10. The numbers of primary turns was 3000 whereas each coil in secondary contained 1100 turns. Digital multimeters (Agilent 34410A) were used to measure current through primary circuit and resistance of the cernox thermometer. Grounding loops were avoided by grounding devices properly. The open conducting parts of the wires and connectors were shielded with aluminum foil to minimize the noise from surroundings.

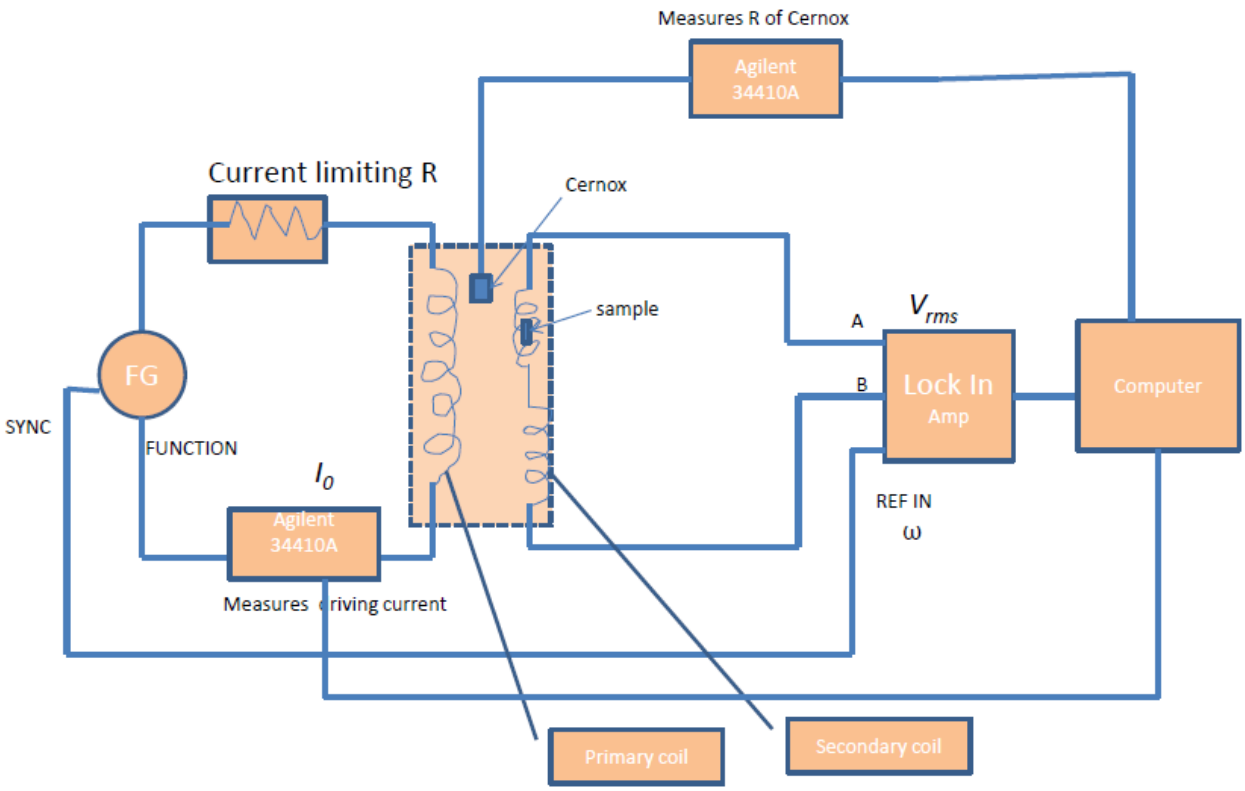

Figure A1 Block diagram representation of ac susceptometer set up. The rectangular box with dotted boarder line represents the coil assembly with sample mount that goes inside the commercial closed system cryostat (PPMS).

The applied frequency (f), current through the primary (I_{rms}) and the voltage signal detected by lock in amplifier (V_{rms}) are properly recorded in a datafile using labview software. Both the real (χ') and imaginary (χ") part of the ac magnetic susceptibility can be calculated using the relation,

$$\chi = \frac{\alpha}{\nu f I_{rms}} V_{rms} \qquad \text{(A1)}$$

Where υ is the fraction of volume occupied by the sample and is determined as volume of the sample divided by volume of the sensing coil. Here α is the calibration constant to be determined using a sample of known magnetic susceptibility. A spherical sample of niobium in the superconducting state (at 5 K) was used for calibration. Calculations were made based on the assumption that $\chi' = -1$ and $\chi'' = 0$ in the superconducting state.

A.2 Calibrating Cernox Thermometer

The susceptometer coil assembly (shown in Figure 3.14 (b)) is mounted in a multipurpose probe and inserted inside the sample chamber of the closed system cryostat (PPMS). The temperature of the sample chamber is essentially controlled by the thermometers of cryostat itself. However, the cryostat thermometers are placed at the bottom of the probe which is at a distance of few centimeters from the sample. This could lead to a significant offset in the temperature reading of the sample. Therefore, to obtain a more accurate temperature of the sample, a cernox thermometer was mounted in the copper holder just below the sample as shown in Figure A2. Note that copper is a good thermal conductor and is weakly magnetic (weak diamagnetic).

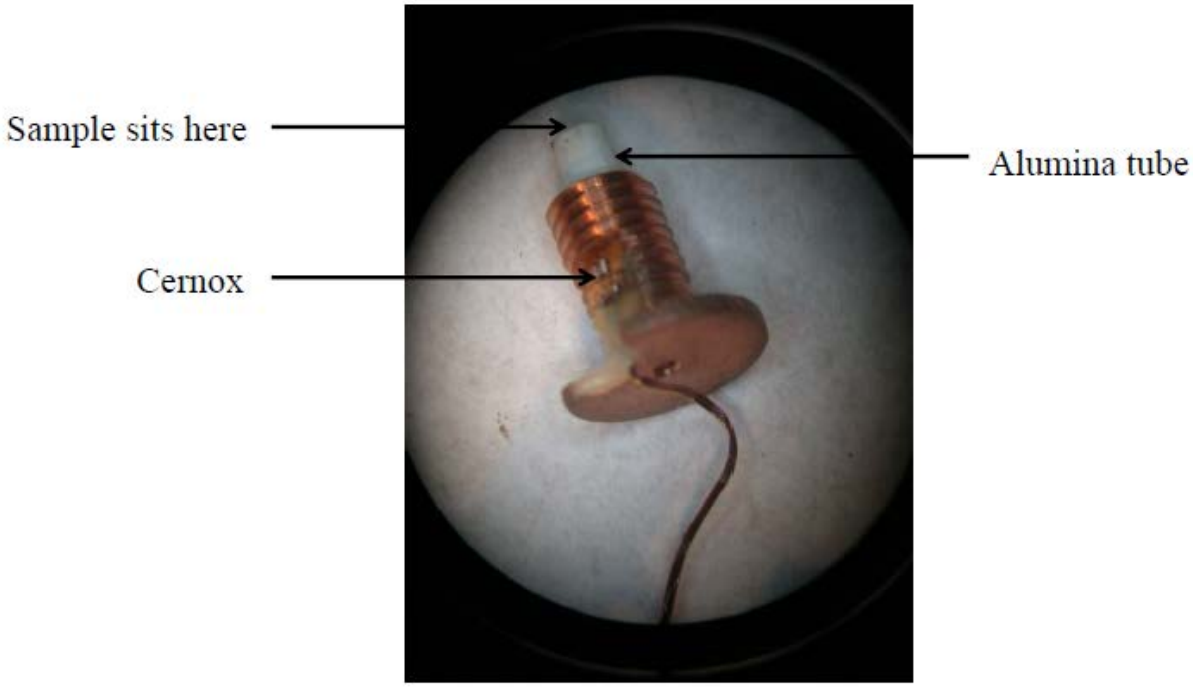

Figure A2 Picture of copper sample holder screw with a cernox thermometer securely mounted on it. An alumina rod on top facilitates as a sample platform.

To calibrate the cernox, its resistance was first determined from 350 K down to 2 K in steps of 10 K. The temperature of PPMS was well stabilized by waiting 30 minutes at every step. The data was then fitted using polynomial equation based on Chebychev polynomials of the from [5],

$$T(X) = \sum a_n t_n(X) \tag{A2}$$

Here T (X) is the temperature in Kelvin, $t_n(X)$ is the Chebychev polynomial and a_n represents the Chebychev coefficient. The summation over n goes from 0 to the order of the fit. The parameter X is defined as [5],

$$X = \frac{(Z-Z_L)-(Z_U-Z)}{(Z_U-Z_L)} \tag{A3}$$

Here Z = $\log_{10}$(R). The superscripts L and U stand for the lower and upper limit. In this study, $Z_L = 1.87842$ and $Z_U = 3.70079$. t_n (X) can be generated from the recursion relation [5],

$$t_n(X) = cos[n * cos^{-1}(X)] \quad \text{(A4)}$$

Fitting polynomials for three different temperature ranges are given in the table A1. The calculated values of the resistances fit well with the measured values as shown in Figure A3.

Table A1 Fitting polynomials at three different temperature regions.

Temperature range	X range	Fitting equation
350 K > T >150 K	-1 < X <-0.58721	$T=256.0478-15.2331t_2-127.8612t_3+27.9605t_5-12.6821t_7-3.3961t_8$
150 K ≥ T >30 K	-0.5871 ≤ X < 0.34584	$T=109-141.4399t_1+73.4477t_2-14.1981t_3+8.5683t_4+6.7318t_5+1.2127t_6$
30 K ≥ T ≥ 5 K	0.34584 ≤ X ≤ 1	$T=14.0027-2.5473t_4-6.7123t_8$

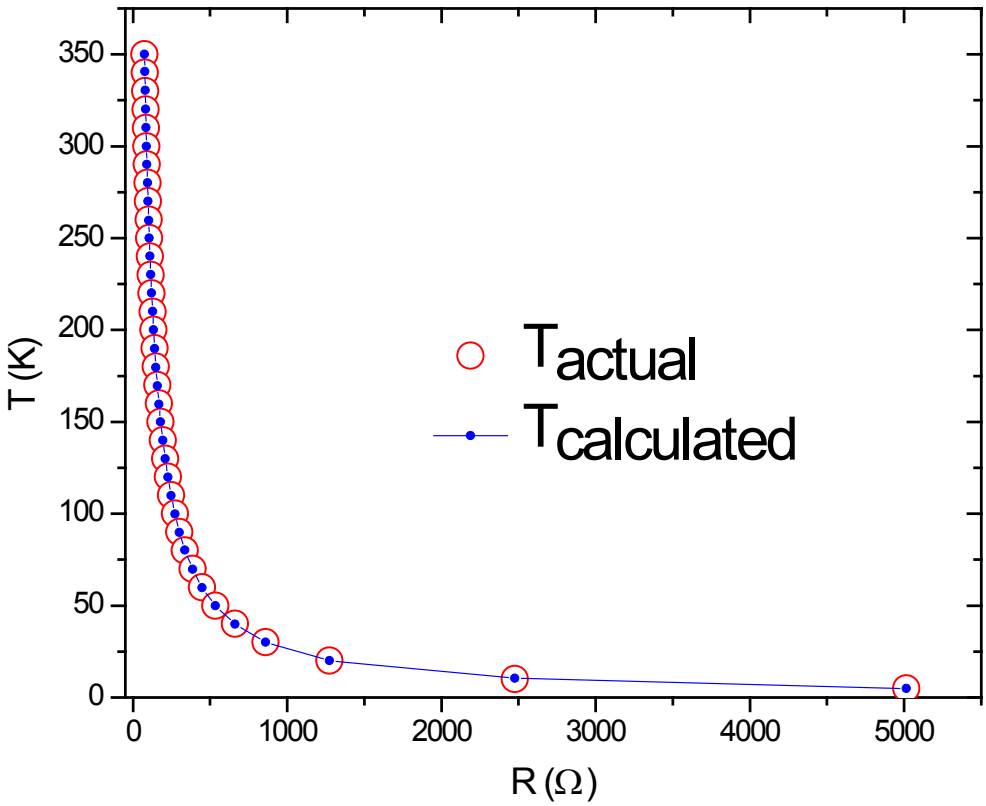

Figure A3 Temperature as a function of resistance for the cernox thermometer. The red open circles represent actual temperature measured by calibrated thermometer already installed in the cryostat. The blue dots represent the calculated temperatures using polynomials listed in Table A1.

A.3 Determination of α and ϕ

When expressed in terms of real and imaginary parts, Eq. A1 is written in a more general form by taking into account of the demagnetization factor (D) associated with the sample geometry and the phase angle (ϕ) as given below.

$$\begin{bmatrix} \frac{\chi'}{1-D\chi'} \\ \frac{\chi''}{1-D\chi''} \end{bmatrix} = \frac{\alpha}{\nu f I_{rms}} \begin{bmatrix} cos\phi & -sin\phi \\ sin\phi & cos\phi \end{bmatrix} \begin{bmatrix} \frac{V_s'}{I_s} - \frac{V_e'}{I_e} \\ \frac{V_s''}{I_s} - \frac{V_e''}{I_e} \end{bmatrix} \quad \text{(A5)}$$

Here subscripts s and e stand for sample and empty respectively. For a given frequency, there corresponds a phase angle (ϕ) that separates the voltages in absolute real (Channel 1) and imaginary (Channel 2) parts. A niobium sphere (D = 1/3) was installed in the sample holder and the temperature of the sample was maintained at 5 K during calibration. The applied frequency of the AC signal through the primary was varied and the real and imaginary part of the voltages was measured in channel 1 and 2 respectively of the lock in amplifier. Figure A4 - A5 show the frequency dependence at 5 K of the voltages detected in Ch1 and Ch2 of the lock in amplifier. The blue triangles represent the data points with no sample (e) whereas the red rectangles are the data points with Nb sample inside the susceptometer. In Figure A6, the background is subtracted.

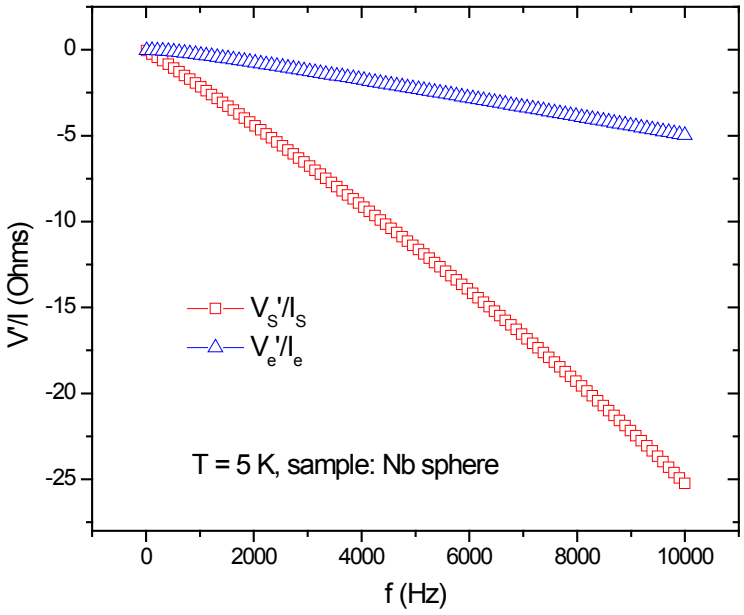

Figure A4 V'/I as a function of frequency for niobium sample at 5 K.

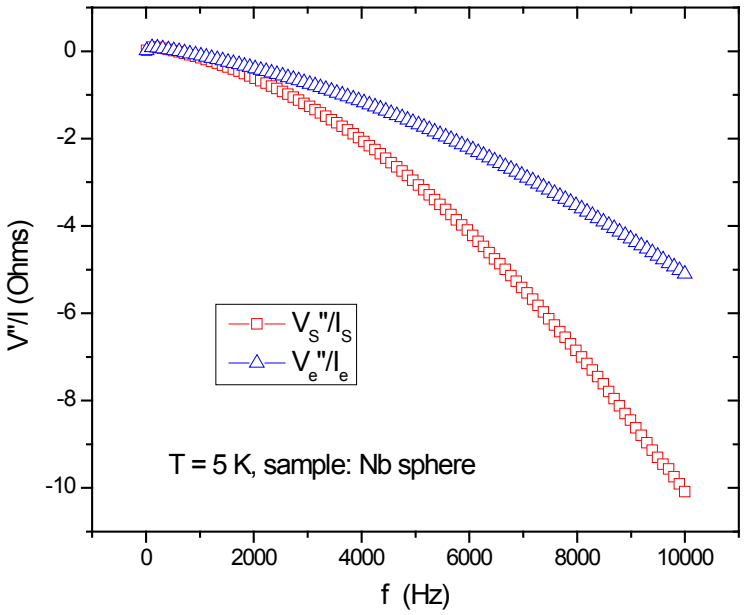

Figure A5 V"/I as a function of frequency for niobium sample at 5 K.

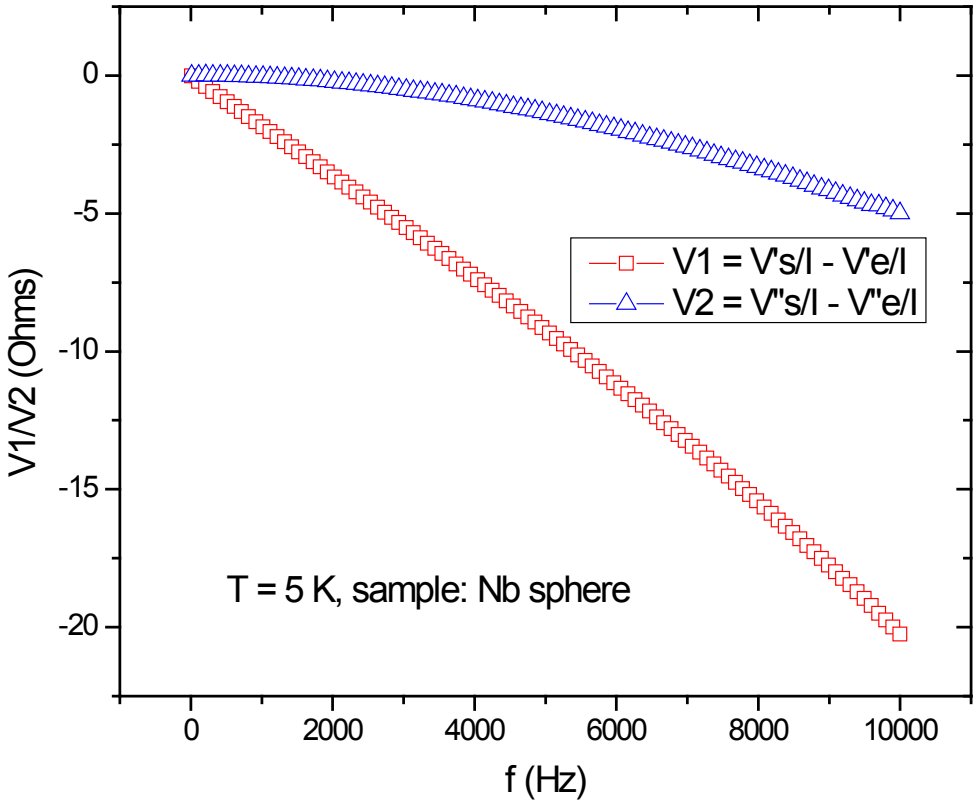

Figure A6 Background subtracted V/I as a function of frequency for niobium sample at 5 K.

Frequency dependence (at 5 K) of α and ϕ obtained from the calculation using above data are shown in the Figure A7 below.

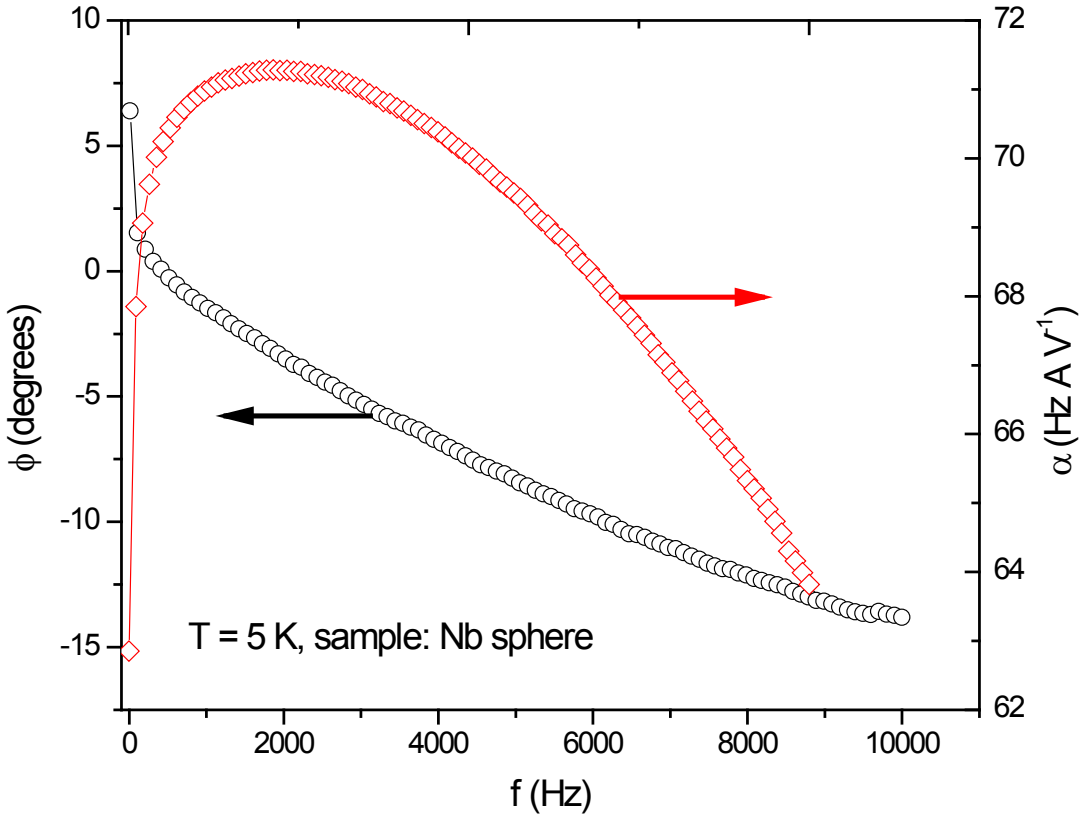

Figure A7 Multiplication factor (α) and the phase angle (ϕ) as function of frequency.

A.4 Benchmarking

AC magnetic susceptibility measurement is often taken as a nondestructive technique to determine and characterize the inter-grain component in high Tc superconductors [6]. $Bi_2Sr_2Ca_2Cu_3O_y$ (BSCCO) is one of the high Tc superconductors which have been widely studied using this technique. Once the susceptometer was calibrated using the niobium sample at the superconducting state (5 K), BSCCO was run for the benchmarking purpose. Figure A8 was taken from the work of Salamati *et al*. [8] which shows temperature dependent real and imaginary parts of the susceptibility of BSCCO for different magnitude of the magnetic field induced inside the primary coil.

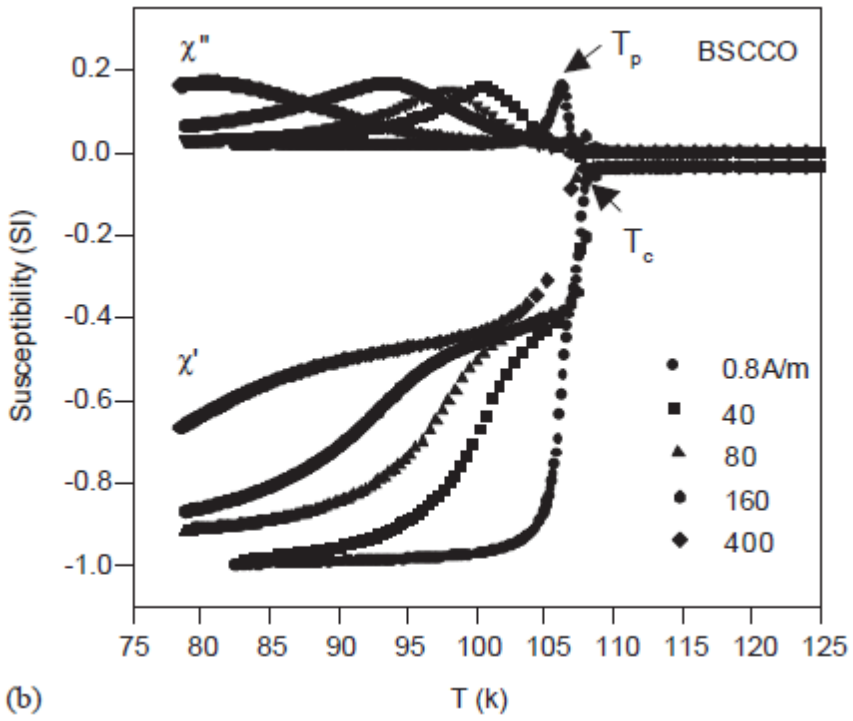

Figure A8 AC magnetic susceptibilities of BSCCO sample as function of temperature for different amplitudes of AC magnetic field. The figure was taken from reference [6].

In Figure A9, we have plotted the temperature dependent susceptibilities obtained by using homebuilt susceptometer for two different magnetic field strengths 0.8 A/m and 40 A/m. Qualitatively, the real and imaginary part of the susceptibilities obtained from the homebuilt system follow a similar temperature profile as observed in reference [6]. Quantitatively, the real part of the susceptibility does not drop down to -1 as it does in reference [6]. The system was further benchmarked by measuring the susceptibility of a gadolinium polycrystalline sample to reproduce data from the work of Fukuda *et al*. [7] as discussed in section 3.6 of chapter 3.

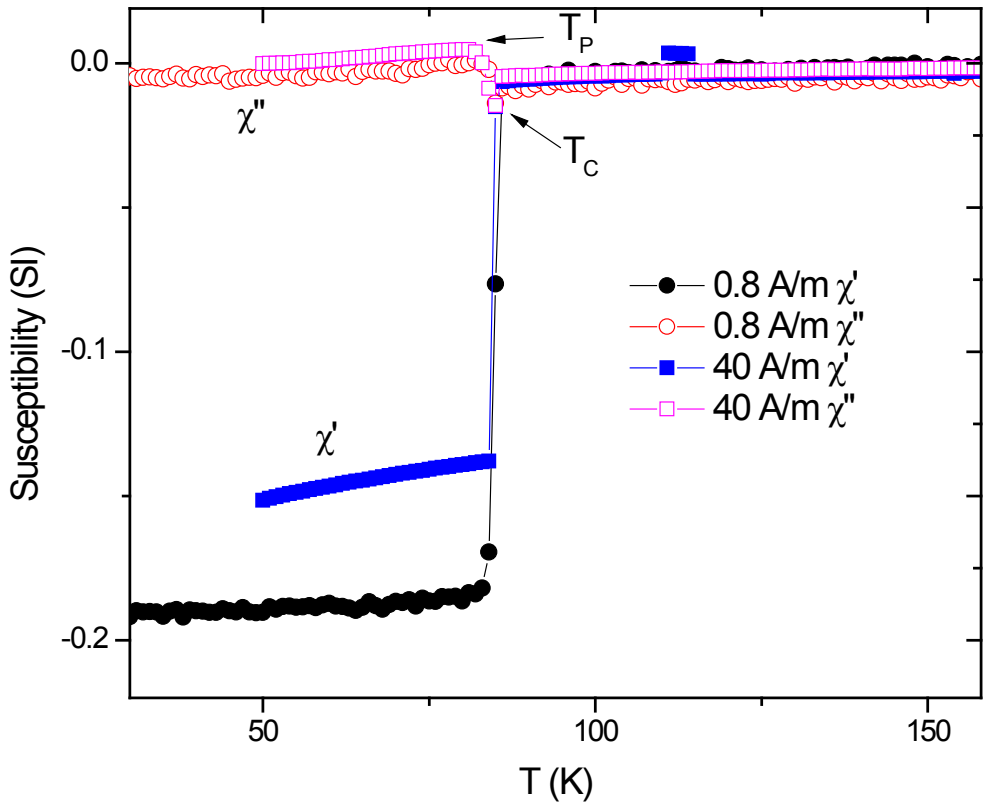

Figure A9 Temperature dependent susceptibilities, for two chosen amplitudes of magnetic fields 0.8 A/m and 40 A/m, of BSCCO sample measured in homebuilt susceptometer.

The goal was to measure, quantitatively, the real and imaginary parts of the AC magnetic susceptibility. However, the data were reproduced only qualitatively. We came to the conclusion that so many factors (including noise) make it difficult to achieve a quantitatively precise measurement using an AC susceptometer in its simplest design. Construction of a very sensitive AC susceptometer requires much more effort to take into account of different circumtances. For example, one of the difficulties is related to the

field dependent background due to magnetic asymmetries in the coil assembly materials. Also, a high resolution method of voltage compensation and detection is required to improve the accuracy of the susceptometer. Also it is assumed that the calibration factor α and the phase angle for a given frequency do not change with temperature. Temperature dependence of α and ϕ, if present; may cause significant offset in the calculated value of susceptibility. Nevertheless, our AC susceptometer is low cost and is very sensitive to magnetic transitions giving accurate information of the transition temperature.

References

1. J. K. Krause, IEEE Transactions on Magnetics, **28**, 5 (1992).
2. C. P. Bindinosti, and W. N. Hardy, Review of Scientific Instruments, **71**, 10 (2000).
3. M. Nikolo, American Journal of Physics, **63**, 1 (1995).
4. R. C. Johnson, Doctoral Thesis, Boston College, Page 36 (2012).
5. Temperature Measurement and Control Catalog, Lake Shore Cryotronics Inc. , Appendix D (2013).
6. H. Salamati, P. Kameli, Journal of Magnetism and Magnetic Materials, **278**, 237–243 (2004).
7. R. H. Fukuda, S. Sunny, Proceedings on the National Conference on Undergraduate Research (NCUR) 2012.

Energy Conversion and Management 87 (2014) 584–588

Contents lists available at ScienceDirect

Energy Conversion and Management

journal homepage: www.elsevier.com/locate/enconman

Thermoelectric properties of $CeAl_3$ prepared by hot-press method

Mani Pokharel [a,*], Tulashi Dahal [b], Zhensong Ren [a], Peter Czajka [a], Stephen Wilson [a], Zhifeng Ren [b], Cyril Opeil [a,*]

[a] Department of Physics, Boston College, Chestnut Hill, MA 02467, USA
[b] Department of Physics and TcSUH, University of Houston, Houston, TX 77204, USA

ARTICLE INFO

Article history:
Received 10 June 2014
Accepted 17 July 2014

Keywords:
Cerium–aluminum
Thermoelectricity
Hot-pressing
Thermoelectric figure-of-merit

ABSTRACT

We present data on the heavy fermion compound $CeAl_3$ as a potential *p*-type thermoelectric material at cryogenic temperatures. Samples of $CeAl_3$ were synthesized by arc-melting, ball milling and hot pressing the nano-powder at different temperatures. Thermal conductivity (κ), Seebeck coefficient (S), electrical resistivity (ρ) and Hall coefficient (R_H) of the samples were measured at temperatures ranging from 5 to 330 K. The thermoelectric properties of this compound are highly dependent on the hot-pressing (HP) temperature. The thermal conductivity increases with increase in HP temperature which is compensated by increased power factor ($S^2\rho^{-1}$). As a result the samples with higher HP temperatures exhibit higher ZT values. The highest ZT value of 0.016 at 55 K was observed for the sample hot-pressed at 800 °C. The Hall coefficient data reflects an increase in carrier concentration and a decrease in carrier mobility with decreasing hot pressing temperature.

1. Introduction

Thermoelectricity is the reversible conversion between thermal and electrical energy. For a given material, the efficiency of this process is quantified by the dimensionless figure of merit, $ZT = \frac{S^2}{\rho\kappa}T$ where S is the Seebeck coefficient, ρ is the electrical resistivity, κ is the thermal conductivity, and T is the absolute temperature [1]. Thermoelectric materials currently available for high temperature applications typically exhibit a $ZT \approx 2$ at their peak operating temperature. A material as this efficient below ambient temperature has not yet been observed. There are several materials which possess promising thermoelectric properties at cryogenic temperatures [2]. One class of materials that we feel has been overlooked is a class of materials called Heavy Fermion Compounds (HFCs). While many materials included in this category have been the subject of extensive study [3–9], as correlated electron materials and quantum behavior, they have not yet been thoroughly investigated as thermoelectric materials. Many materials that belong to this class are known to exhibit unique correlated electron properties at low temperatures which make them potential candidates for thermoelectric cooling applications.

Measurement of thermoelectric properties usually offers an excellent approach to investigate quasiparticle excitation in heavy fermion materials [10,11]. Many HFCs have been shown to exhibit large Seebeck coefficient values at low temperatures [12,13]. Among them, many Ce-based compounds have been reported to exhibit two well separated maxima (minima) in the temperature dependent Seebeck coefficient [14–16]. Usually, the low-T extremum occurs around the characteristic temperature T_K and is attributed to the Kondo scattering on the ground state doublet. The high temperature peak ($T > T_K$) on the other hand, results from Kondo scattering on higher multiplets which are split by crystal electric field (CEF) effects [12]. In addition to large Seebeck coefficients, many compounds of this class exhibit relatively high electrical conductivity values which make them promising thermoelectric materials.

In this work, we studied the thermoelectric properties of the heavy fermion compound $CeAl_3$. Since the first study by Andres et al. [17] in 1975, $CeAl_3$ has been the subject of extensive research. This compound exhibits an extremely large Sommerfeld coefficient $\gamma = 1620$ mJ/(K^2-mol) and $A = 35$ μΩ cm/K^2 where A is associated with the Fermi liquid relation of the electrical resistivity $\rho = \rho_0 + AT^2$ [17]. Originally, $CeAl_3$ was considered to be a heavy fermion without any magnetic ordering. Later, it was revealed by μSR and NMR experiments [18,19] that $CeAl_3$ orders antiferromagnetically below $T_N = 1.2$ K. Initially, many researchers paid attention to its electrical transport properties [20,21] and their pressure dependence [16]. Later Ott et al. [22] reported the thermal conductivity in the temperature range of 0.06–50 K thereby demonstrating the validity of Wiedemann-Franz law in heavy electron systems. We focus on determining ZT of $CeAl_3$ as a potential material for Peltier cooling applications.

* Corresponding authors. Tel.: +1 617 552 3589; fax: +1 617 552 8478.
E-mail address: pokharem@bc.edu (M. Pokharel).

http://dx.doi.org/10.1016/j.enconman.2014.07.050
0196-8904/

In general, an increase in ZT can be achieved through either power factor ($S^2\rho^{-1}$) enhancement or thermal conductivity reduction or by both. For strongly correlated systems like HFCs, the electronic transport properties (S and ρ) are usually found to be very sensitive to the carrier density. Therefore it is plausible to assert that the power factor of these systems can be effectively optimized by tuning carrier density. In an earlier study on another strongly correlated system, $FeSb_2$, we showed that mechanical nanostructuring (ball-milling of ingot into powder and hot pressing of the powder into bulk pellets) not only reduces the thermal conductivity but also induces modification of the electronic band structure which in turn changes the carrier density [23]. In this study we employ the technique of nanostructuring in $CeAl_3$ and investigate the effects of varying hot-pressing (HP) temperature on its thermoelectric properties.

2. Experimental

Stoichiometric amounts of Ce (99.9%) and Al (99.99%) were mixed and arc melted together on a water-cooled copper hearth in an argon atmosphere. To attain chemical homogeneity, the melted sample was flipped on the hearth plate and re-melted twice. Nanopowders of $CeAl_3$ were prepared by ball milling the ingot for 5 h. The nanopowder was then hot pressed for 2 min at 400, 600 and 800 °C while a uniaxial pressure of 80 MPa was applied. X-ray diffraction (XRD) and scanning electron microscopy (SEM) were performed on the fresh fracture surfaces of the samples. The Seebeck Coefficient (S), electrical resistivity (ρ), and thermal conductivity (κ) from 5 to 330 K were measured simultaneously on a sample of typical dimensions of $2 \times 2 \times 8$ mm^3. The four-point method of thermal transport option (TTO) of the Physical Property Measurement System (PPMS) was used. The horizontal rotator option of PPMS was used to measure Hall coefficient (R_H) on a sample with typical dimensions of $1 \times 2 \times 10$ mm^3.

3. Results and discussion

Fig. 1(a) shows the X-ray diffraction patterns for the samples. Some impurity phases associated with $CeAl_2$, Ce, and Al can be seen for the ingot. However, these impurity phases disappear in the X-ray diffraction patterns for the hot-pressed samples at 800 °C and the peaks can be indexed to the hexagonal Ni_3Sn-type crystal structure. The samples become more homogeneous and show an enhanced single phase behavior after the ball-milling and hot-pressing process. The SEM images of the freshly fractured surface of the four samples are presented in Fig. 1(b). Clearly, texture of the hot-pressed samples differs drastically from that of the ingot sample with porosity increasing with decreasing pressing temperature. As the hot-pressing temperature decreases, the grains tend to agglomerate. Approximate grain-size in the hot-pressed samples is in the order of ~1 μm.

The results on the temperature dependence of the total thermal conductivity are shown in Fig. 2. The temperature dependence for all the samples are typical of heavy fermion systems and closely resemble the dependence reported for other HFCs such as CeB_6 [24] and $CeCu_4Al$ [25]. The thermal conductivity values for the ingot sample are consistent with the values for the polycrystalline sample reported by Ott et al. [22]. Within the 5–330 K range, the thermal conductivity decreases significantly as the HP temperature decreases. As a reference, at 55 K, $\kappa = 2.5$ W m^{-1} K^{-1} and 0.4 W m^{-1} K^{-1} for the samples HP 800 and HP 400 respectively, this represents a reduction in the thermal conductivity by ~85%. In ball-milled and then hot-pressed samples, such a decrease in thermal conductivity is mainly attributed to the increased scattering of phonons off the grain boundaries.

In general, the total thermal conductivity is the sum of two independent contributions from the lattice and the carriers. The relationship is described by the following equation: $k = k_{carrier} + k_{lattice}$ where k is the total effective thermal conductivity of the system, and $\kappa_{carrier}$ and $\kappa_{lattice}$ are the carrier and lattice contributions respectively. A rough estimation of $\kappa_{carrier}$ can be made using the Wiedemann-Franz law, $k_{carrier} = L_0\rho^{-1}T$ where $L_0 = 2.45 \times 10^{-8}$ W Ω K^{-2} is the Lorenz number, ρ is the electrical resistivity, and T is the temperature in K. The $\kappa_{carrier}$ for all the samples was calculated using the experimentally determined values of ρ. In Fig 3, we show the temperature dependence of $k_{lattice}$ ($= k - k_{carrier}$) in a log-log plot in the 6–50 K temperature range. At 55 K, 65% of the total thermal conductivity of the sample HP 800 comes from the lattice contribution. For the HP 600 and HP 400 samples, these

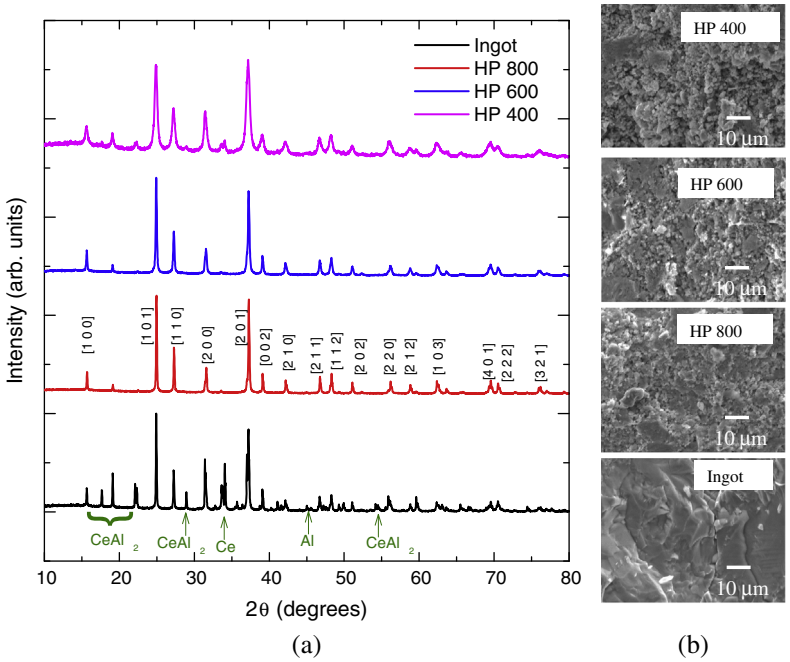

Fig. 1. X-ray diffraction pattern (a) and the SEM images (b) of the samples.

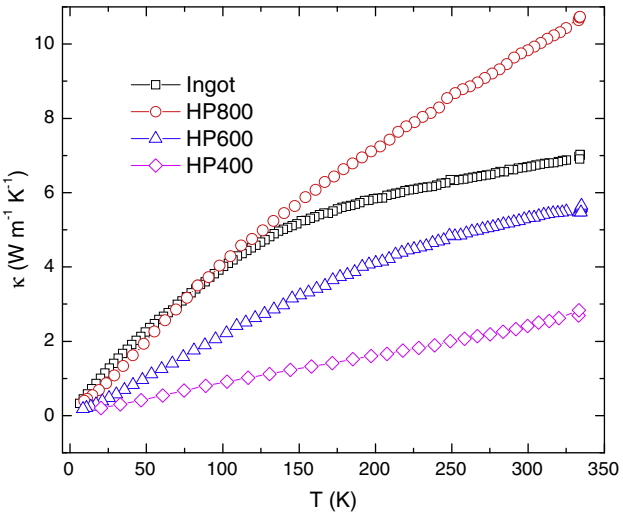

Fig. 2. Thermal conductivity of the samples as a function of temperature.

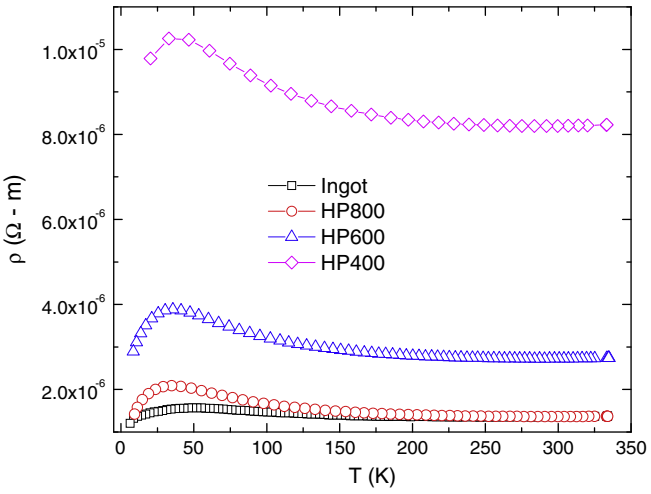

Fig. 4. Electrical resistivity of the samples as a function of temperature.

contributions are 74% and 78%, respectively. Fitting data to the power law, $k = \beta T^{\alpha}$, shows the almost linear dependence of κ on T with the α values ranging from 0.83 to 1.11. Such a linear dependence is consistent with previous reports and is related to the fact that relevant phonon wavelengths are comparable to or larger than the electronic mean free paths [22].

The experimental data on the electrical resistivity is shown in Fig. 4. $\rho(T)$ curves for all the samples follow the classic shape for a strongly correlated HF metal, with a coherence peak at ~35 K. While the coherence peak has been consistently reported to occur at around 35 K, the resistivity values for our samples hot pressed at 400 and 600 °C are considerably larger than previously reported values for their single crystal counterparts. This is expected due to the increased porosity and number of defects in the hot-pressed samples. Among the hot-pressed samples, the electrical resistivity varies significantly with HP temperature. At 35 K, the resistivity increases by a factor of 1.9 from the HP 800 sample to the HP 600 sample, and from HP 600 to HP 400, it increases by a factor of 2.6. A similar behavior in resistivity at lower HP temperature was observed in the HFC $CeCu_6$ [26].

Fig. 5 shows the Seebeck coefficient as a function of temperature. For all the samples, the Seebeck coefficient is positive in the temperature range of 5–330 K, implying that the majority charge carriers are holes (p-type). The peak in Seebeck coefficient, which is thought to result from Kondo scattering of higher energy multiplets, occurs at ~55 K. The negative peak due to the Kondo scattering of ground state doublet has been shown to occur at 3.5 K for $CeAl_3$ [16] which is out of the temperature range of this experiment. Above 55 K, a logarithmic dependence $S \propto -(\ln T)$ is followed. This trend is consistent with the data previously reported and is usually associated with the formation of heavy charge carriers (also called the spin polarons) as a result of the density of states (DOS) renormalization in the vicinity of the Fermi energy [11]. The maximum value of $S = 36\ \mu V\ K^{-1}$ was observed for the HP 800 sample. The peaks are suppressed as hot-pressing temperature decreases.

In Fig. 6, we plot the power factor ($PF = S^2\rho^{-1}$) as a function of temperature. The HP 800 sample produces the highest value of PF ($6.6\ \mu W\ K^{-2}\ cm^{-1}$) at 55 K that is less than the value of $15\ \mu W\ K^{-2}\ cm^{-1}$ at 50 K reported by Mahan et al. [27]. The smaller PF value in our samples is due to decreased Seebeck coefficient and increased resistivity. As the HP temperature decreases, PF decreases dramatically.

The original goal of nanostructuring was to increase the power factor (PF) by employing quantum confinement of carriers [28,29],

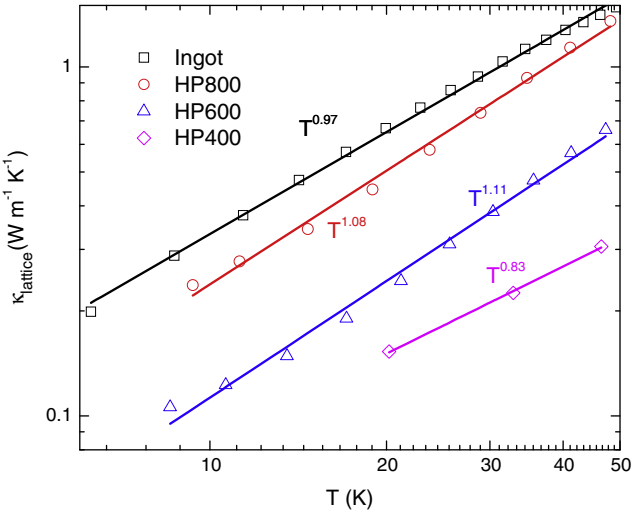

Fig. 3. Lattice thermal conductivity as a function of temperature in the range of 6–50 K.

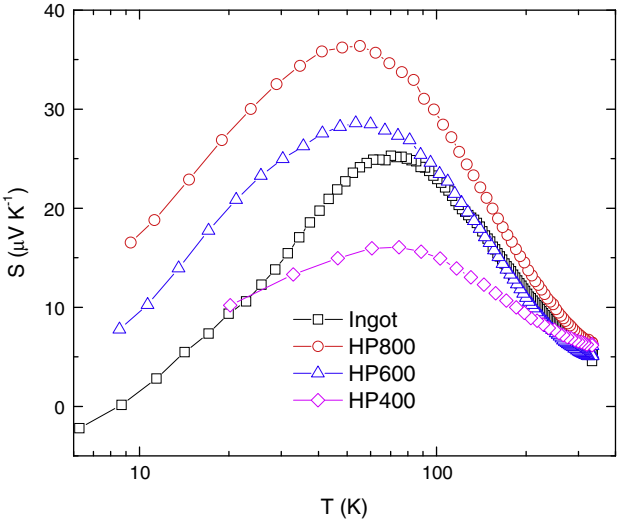

Fig. 5. Seebeck coefficient of the samples as a function of temperature.

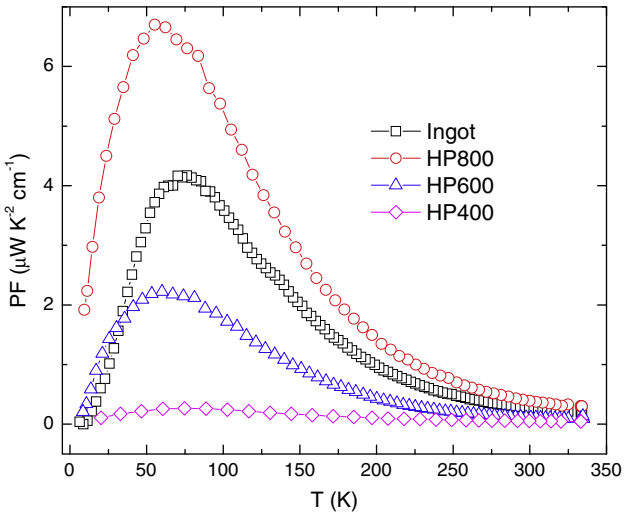

Fig. 6. Power factor of the samples as a function of temperature.

but the experiments [30–32] have shown that the main reason for the *ZT* improvement was the reduction of thermal conductivity. Therefore in the recent years, research on nanostructured thermoelectric materials have mainly focused on reducing the thermal conductivity while producing only minimal adverse effects on the Seebeck coefficient and electrical conductivity. In case of $CeAl_3$, although reducing the HP temperature decreases thermal conductivity of $CeAl_3$, it also lowers the Seebeck Coeffient and electrical conductivity, which ultimately results in a decrease in *ZT* with decreasing HP temperature (see Fig. 7). The highest *ZT* reported is 0.016 at 55 K in the HP 800 sample. Since at 55 K the ingot and the sample HP 800 have nearly the same thermal conductivity value, the improved *ZT* value for the latter comes from the improved Seebeck coefficient.

Fig. 8 shows the temperature dependence of the Hall coefficient (R_H). A magnetic field of 9 T was applied during Hall measurements. Our data is consistent with previous reports [33,34] with R_H staying positive in the whole range of 5–330 K. At high temperatures, R_H is small indicating that the electron and hole contributions to R_H cancel each other. As the temperature decreases, the hole-contribution increases leading to a well-defined peak at $T \approx 10$ K. A rapid increase in the Hall coefficient above the residual value at low temperatures is typical feature of heavy fermion metals and is associated with the development of skew scattering by fluctuation about the coherent state [21]. The Hall coefficient of the ingot sample remains significantly smaller than that of the hot-pressed samples throughout the temperature range of the experiment. Under one band model, the Hall coefficient (R_H) and the carrier density (n) are related as, $R_H = 1/ne$, where n is the carrier density and e is the electronic charge. Carrier density calculated based on this simplified model as a function of temperature is shown in the inset of Fig. 8. The carrier density decreases in hot-pressed samples when compared with carrier density of the ingot sample. Among the hot-pressed samples, amplitude of R_H (or n) decreases (or increases) with decrease in HP temperature. In general, increases in carrier concentration decrease the absolute value of the Seebeck coefficient [35]. Therefore the decrease in *S* with decreasing HP temperature in our samples can be attributed, in part, to the increase in carrier density.

A rough calculation of effective mass (m^*) can be done using the relation $s = \frac{8\pi^2 k_B^2 T}{3eh^2} m^* \left(\frac{\pi}{3n}\right)^{2/3}$. Here $k_B = 1.38 \times 10^{-23}$ J K^{-1} is the Boltzmann constant, $\hbar = 1.05 \times 10^{-34}$ J S is the reduced Planck constant, T is the absolute temperature and n is the carrier density. Using experimentally determined Hall coefficient (Fig. 8) and the Seebeck coefficient (Fig. 5), calculations give $m^* \approx 33\ m_o$, $25\ m_o$ and $23\ m_o$ (m_o is bare mass of electron) for samples HP 800, 600 and 400 respectively at 20 K (shown in inset of Fig. 9). These values are slightly less than previously reported values ($\approx 45\ m_o$) in reference [11]. Hall mobility (μ_H) for the samples were calculated under the assumption of one band model using relation $\mu_H = R_H/\rho$. Fig. 9 shows the temperature dependence of the Hall mobility, these results were derived from resistivity measurement shown in Fig. 3. Quantitatively, the Hall mobility values are of the same order as reported earlier [36]. Despite lower carrier concentration and enhanced effective mass, the sample HP 800 has significantly small resistivity compared to the resistivity of samples HP 600 and HP 400. This is due possibly to the decreased defect concentration at higher pressing temperature.

In conclusion, samples of the heavy fermion compound $CeAl_3$ have been successfully synthesized by ball-milling of arc-melted ingot followed by hot-pressing. The thermoelectric properties of the samples have been measured and it has been shown that the temperature dependences of the properties are typical of the heavy fermion metal. The results show that variation of hot-pressing

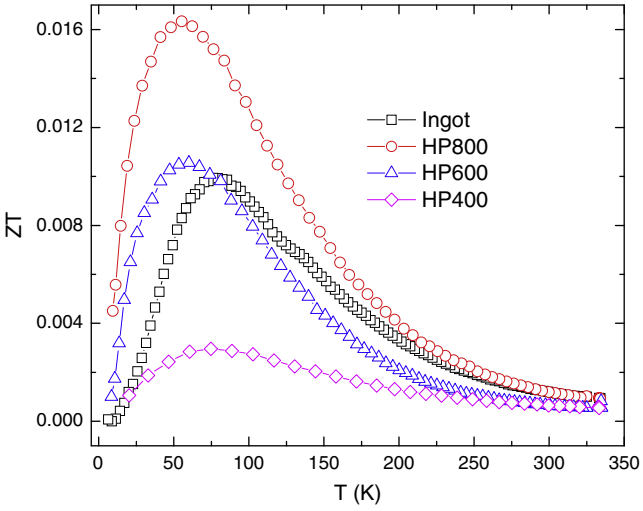

Fig. 7. Thermoelectric figure-of-merit (*ZT*) of the samples as a function of temperature.

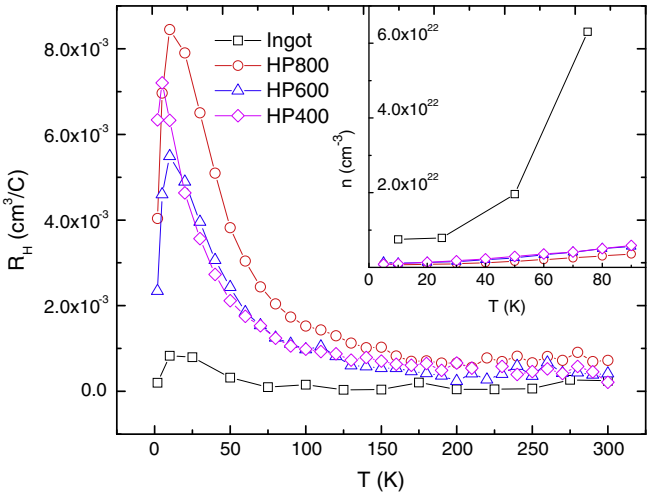

Fig. 8. Hall coefficient of the samples as a function of temperature. Inset shows temperature dependent carrier concentration.

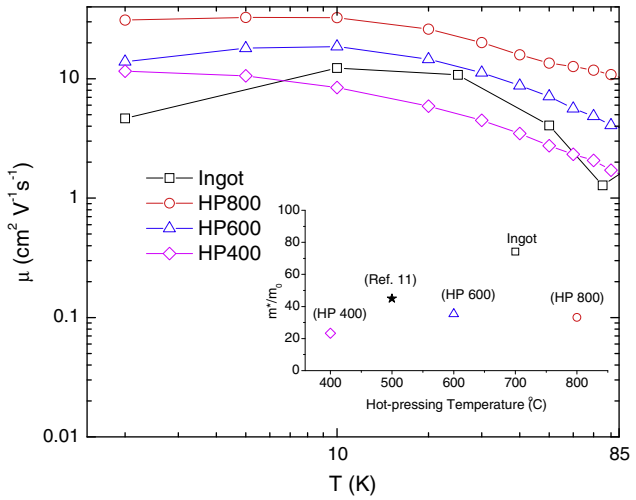

Fig. 9. Hall mobility of the samples as a function of temperature. Inset shows the effective mass to bare mass ratio at 20 K for the samples.

temperature results in significant changes in the thermal and the electronic transport properties. Mechanical nanostructuring was shown to be effective at decreasing the thermal conductivity of the system. The highest *ZT* value measured was 0.016 at 55 K in the sample that was hot-pressed at 800 °C. The results from the Hall coefficient measurements provide evidence for the differences in the carrier density and mobility among the samples. Further optimization of the thermoelectric properties of the heavy fermion compound $CeAl_3$ may also be achievable by doping.

Acknowledgment

We gratefully acknowledge funding for this work by the Department of Defense, United States Air Force Office of Scientific Research's MURI program under contract FA9550-10-1-0533. CO is grateful to the Trustees of Boston College for their support.

References

[1] Nolas GS, Sharp J, Goldsmid HJ. Thermoelectrics. Berlin: Springer-Verlag; 2001.
[2] Mahan GD, Sales BC, Sharp J. Phys Today 1997;50:42.
[3] Gschneider Jr KA, Eyring LL. Handbook on the physics and chemistry of rare earths 1991;14.
[4] Hewson AC. The Kondo Problem to Heavy Fermions. Cambridge: Cambridge University Press); 1993.
[5] Aeppli G, Fisk Z. Comments Condens Matter Phys 1992;16:155.
[6] Fisk Z, Sarrao JL, Cooper SL, Nyhus P, Boebinger GS, Passner A, et al. Physica B 1996;223–224:409.
[7] Takabatake T, Iga F, Yoshino TY, Echizen Y, Katoh K, Kobayashi K, et al. J Magn Magn Mater 1998;177–181:277–82.
[8] Degiorgi L. Rev Mod Phys 1999;71:687.
[9] Riseborough PS. Adv Phys 2000;49:257.
[10] Chaikin PM. Organic superconductivity. In: Kresin VZ, Little WA, Plenum, New York; 1991. p. 101.
[11] Ignatov MI, Bogach AV, Burkhanov GS, Glushkov VV, Demishev SV, Kuznetsov AV, et al. J Exp Theor Phys 2007;105:58–61.
[12] Zlatić V, Hewson AC. Properties and applications of thermoelectric materials: the search for new materials for thermoelectric devices. Springer; 2009.
[13] Paschen P. Thermoelectric handbook. In: Rowe DM. Boca Raton (FL): CRC Press, Taylor and Francis; 2006.
[14] Sparn G, Lieke W, Gottwick U, Steglich F, Grewe N. J Magn Magn Mater 1985;47(48):521–3.
[15] Amato A, Jaccard D, Sierro J, Steglich F, Grewe N. J Magn Magn Mater 1988;76(77):263–4.
[16] Fierz Ch, Jaccard D, Sierro J, Flouquet J. J Appl Phys 1988;63:3899.
[17] Andres K, Graebner JE, Ott H. Phys Rev Lett 1975;35:26.
[18] Barth S, Ott HR, Gygax FN, Hitti B, Lippelt E, Schenck A, et al. Phys Rev Lett 1987;59:26.
[19] Nakamura H, Kitaoka Y, Asayama K, Flouquet J. J Mag Mag Mater 1988; 76 and 77: 465–6.
[20] Flouquet J, Lasjaunias JC, Peyrard J, Ribault M. J Appl Phys 1982;53:2127.
[21] Hadzic Leroux M, Hamzic A, Fert A, Haen P, Lapierre F, Laborde O. Europhys Lett 1986;1(11):579–84.
[22] Ott HR, Marti O, Hulliger F. Solid State Commun 1984;49(12):1129–31.
[23] Zhao H, Pokharel M, Zhu G, Chen S, Lukas K, Jie Q, et al. Appl Phys Lett 2011;99:163101.
[24] Matsuoka E, Umeo K, Tsuji S, Sera M, Iga F, Takabatake T. J Phys Soc Jpn 2003;72:9.
[25] Falkowski M, Kowalczyk A. In: Proceedings of the European conference physics of magnetism (PM'11), Pozman, June 27–July 1, 2011.
[26] Pokharel M, Dahal T, Ren Z, Opeil C. J Alloy Compd 2014;609:228–32.
[27] Mahan GD. Solid State Phys 1997;51:81–157.
[28] Hicks LD, Dresselhaus MS. Phys Rev B 1993;47:12727.
[29] Hicks LD, Dresselhaus MS. Phys Rev B 1993;47:16631.
[30] Venkatasubramanian R, Silvola E, Colpitts T, O'Quinn B. Nature 2001;413:597–602.
[31] Harman TC, Taylor PJ, Walsh MP, LaForge BE. Science 2002;297:2229–32.
[32] Hsu KF, Loo S, Guo F, Chen W, Dyck JS, Uher C, et al. Science 2004;303:818–21.
[33] Brandt NB, Moshchalkov VV, Sluchanko NE, et al. Sol St Commun 1985;53:645.
[34] Haen P, Flouquet J, Lapierre F, Lejay P, Remenyi G. J Low Temp Phys 1987;67:391.
[35] Ioffe AF. Physics of semiconductors, Academic Press, New York; 1960 [translated from Russian, Fizika Poluprovodnikov, Russian Academy of Sciences, Moscow, 1957].
[36] Sluchanko NE, Sluchanko DN, Samarin NA, Gluskhov VV, Demishev SV, Kuznestov AV, et al. Low Temp Phys 2009;35:7.

Journal of Alloys and Compounds 609 (2014) 228–232

Contents lists available at ScienceDirect

Journal of Alloys and Compounds

journal homepage: www.elsevier.com/locate/jalcom

Thermoelectric properties of nanocomposite heavy fermion $CeCu_6$

Mani Pokharel [a,*], Tulashi Dahal [b], Zhifeng Ren [b], Cyril Opeil [a,*]

[a] Department of Physics, Boston College, Chestnut Hill, MA 02467, USA
[b] Department of Physics and TcSUH, University of Houston, Houston, TX 77204, USA

ARTICLE INFO

Article history:
Received 13 March 2014
Received in revised form 16 April 2014
Accepted 19 April 2014
Available online 29 April 2014

Keywords:
Cerium–copper
Thermoelectricity
Peltier cooling
Heavy fermion
Nanostructuring

ABSTRACT

We report on the thermoelectric performance of the heavy fermion compound $CeCu_6$ nanocomposite samples. Measurements of Seebeck coefficient, electrical resistivity and thermal conductivity are presented over the temperature range $5 < T < 350$ K. The dimensionless figure-of-merit (ZT) was optimized by varying the sample hot-pressing temperature. Thermal conductivity measurements show that the lowest hot pressing temperature (450 °C) produces the lowest thermal conductivity. Electrical resistivity is strongly influenced by hot pressing temperature and drops by a factor of ~3.4 as the hot pressing temperature is lowered from 800 to 450 °C. Seebeck coefficient shows a slight increase over other samples when hot pressed at 800 °C. Our ZT calculations show a broad peak with a maximum value of 0.024 at ~60 K for the sample hot pressed at 800 °C.

1. Introduction

In recent years, solid-state cooling based on the Peltier effect has gained increased attention. Coefficient of performance (Φ) for a Peltier cooler is given as [1,2],

$$\text{ø}_{\max} = \frac{T_1\left[(1+ZT)^{1/2} - T_2/T_1\right]}{(T_2 - T_1)[(1+ZT)^{1/2} + 1]} \quad (1)$$

where T_1 and T_2 are the temperature of heat source and sink respectively and $T = (T_1 + T_2)/2$. The quantity ZT is dimensionless thermoelectric figure-of-merit and is defined as $ZT = S^2\rho^{-1}\kappa^{-1}T$. Here S is the Seebeck coefficient, ρ is the electrical resistivity, κ is the total thermal conductivity, and T is the absolute temperature. It is essential that high ZT materials and process methods be discovered to build efficient Peltier coolers particularly when operating at low temperatures. Optimizing the ZT of a material has been challenging due to the complex and interrelated quantities: S, ρ and κ. Current state of-the-art materials typically possess a peak ZT in the range of 1–1.8 for different materials [3,4]. Such a system has yet to be discovered for temperatures below 200 K. Correlated electron systems are considered one of the materials which might be useful for Peltier coolers below 77 K. Among the correlated systems, heavy-fermion compounds (HFCs) show promising thermoelectric properties at low temperatures, with a large S and small ρ [5]. In these compounds, below some characteristic temperature T_k a sharp peak of the density of states develops at the Fermi level (E_F) which results in highly enhanced values for both the Sommerfeld (γ) and Seebeck coefficient (S) [6].

Since the discovery by Stewart et al. [7] in 1984, $CeCu_6$ has been one of the widely studied HFCs. A great deal of interest was focused on transport properties of this system in the following years [8–13], owing to the Fermi liquid (FL) behavior at low temperature, similar to that of $CeAl_3$ [14]. Subsequent studies on this compound were focused on non-Fermi liquid (NFL) behavior [15,16] and anomalous thermopower [17–19]. In the recent years this compound has been a platform for studying the quantum critical point (QCP) behavior [20]. Although measurement of its transport properties has long been taken as an approach to investigate quasiparticle excitation, $CeCu_6$ has not been heavily studied as a thermoelectric material. In this work we studied the thermoelectric properties of $CeCu_6$ and applied the technique of mechanical nanostructuring approach to the synthesis of the materials to improve their ZTs.

Nanostructuring has been proven to be very effective at reducing the thermal conductivity without harming the electronic properties [3]. There have been many studies which attempted to employ this technique to increase ZT near or above room temperature. Since the phonon contribution, in general, increases with a decrease in temperature; it is possible that nanostructuring could lead to a reduction in the thermal conductivity of thermoelectric material at low temperatures. In our previous work, we successfully enhanced the ZT of strongly correlated narrow-gap semiconductor $FeSb_2$ using nanostructuring approach [21–23]. This paper

* Corresponding author. Tel.: +1 6175523589.
E-mail address: pokharem@bc.edu (M. Pokharel).

http://dx.doi.org/10.1016/j.jallcom.2014.04.139
0925-8388/

is a result of our continued investigation of the effectiveness of nanostructuring at improving ZT at low temperatures (below 77 K).

2. Experimental

Stoichiometric amounts of Ce (99.9%, Alfa Aesar) and Cu (99.99%, Alfa Aesar) were melted in an argon environment using an arc-melter. To improve chemical homogeneity, the melted sample was flipped over and re-melted three times. The resulting ingot was etched in dilute nitric acid then ball milled for five hours to create a nanopowder of $CeCu_6$. The nanopowder was then hot pressed for two minutes at 450, 600 and 800 °C under a uniaxial pressure of 80 MPa. For simplicity, the samples are given short names. For instance, the name "HP 800" stands for the sample hot-pressed at 800 °C. X-ray diffraction (XRD, Bruker, AXS) was performed on the freshly fractured surface of the samples. Scanning Electron Microscopy (SEM, JEOL 6340F) was used to investigate the grain-size distribution of the samples. The Seebeck coefficient (S), electrical resistivity (ρ), and thermal conductivity (κ) from 5 to 300 K were measured on samples of typical dimensions of $3 \times 3 \times 4$ mm^3. A 2-point method in thermal transport option (TTO) of the Physical Property Measurement System (PPMS) was used to measure the thermoelectric properties. The horizontal rotator option of the PPMS was used to measure Hall coefficient (R_H) of the samples with typical dimensions of $1 \times 2 \times 10$ mm^3.

3. Results and discussion

The X-ray diffraction patterns are shown in Fig. 1 for the ingot and ball milled/hot pressed samples. The peak positions confirm the orthorhombic crystal structure and indicate that the ingot was alloyed in a single phase form. We note the X-ray peaks are broadened only slightly by the ball-milling process, while the crystal structure is retained.

Fig. 2 shows the SEM images of the samples. No voids are seen for ingot and the sample HP 800 °C. The nearly equal values for the densities of the ingot and the sample HP 800 are consistent with the SEM images. The samples hot pressed at 450 and 600 °C show a distinctly different microstructure from the HP 800 sample. Sample porosity increases and surface texture becomes rough at the lower hot pressing temperatures

The electrical resistivity ρ of the samples are shown in Fig. 3 as a function of temperature. All the samples exhibit a similar resistivity profile, typical of single crystal $CeCu_6$. Below 300 K, the resistivity decreases as the temperature is lowered until it reaches a flat minimum. At approximately 75 K, a Kondo-like behavior emerges with a negative value for $\partial\rho/\partial T$. The resistivity then reaches a maximum at around 15 K before declining sharply with decreasing temperature, an indication of coherence development. Electrical resistivity of the 800 °C hot-pressed sample is slightly increased

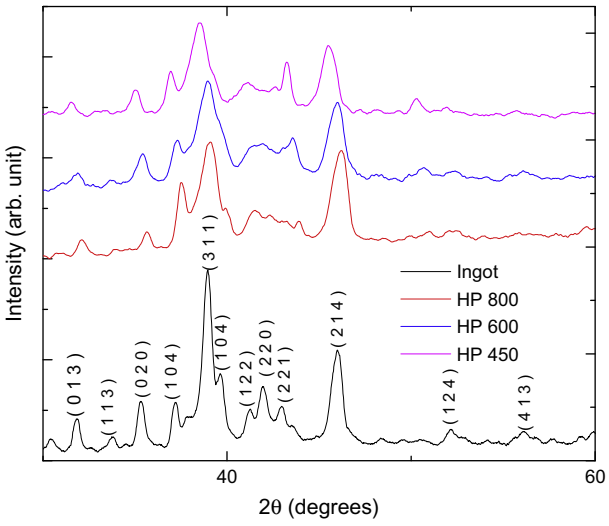

Fig. 1. X-ray diffraction pattern for the arc melted ingot and the three hot pressed samples of $CeCu_6$.

when compared to the ingot; this is expected due to the increased scattering from the nanocomposite grains. A comparison among the hot-pressed samples shows that the electrical properties of $CeCu_6$ are greatly affected by varying HP temperature. With decreasing HP temperature the electrical resistivity increases significantly. When comparing HP 800 and 450 °C samples, we note at 60 K an increase in resistivity by a factor of ~3.4. Such a drastic increase in the electrical resistivity is attributed to the reduced grain size and the increased porosity.

Fig. 4 shows the total thermal conductivity (κ) for the samples as a function of temperature. For comparison the thermal conductivity for polycrystalline samples of $CeCu_6$ was taken from Ref. [24]. The thermal conductivity follows temperature dependence similar to that reported for another HFC $CeCu_4Al$ [25]. The total thermal conductivity decreases as the HP temperature decreases. At 60 K, κ was reduced from ~5 W m^{-1} K^{-1} (for ingot) to ~2 W m^{-1} K^{-1} (for sample HP 450), a reduction by 60%. In general, $\kappa = \kappa_l + \kappa_e$, where κ_l and κ_e are the lattice and electronic contributions to the total thermal conductivity, respectively. Generally, phonon scattering by grain boundary reduces the phonon contribution (κ_l) whereas macroscale porosity is shown to reduce the electronic contribution (κ_e) [26,27]. The SEM images (Fig. 2) suggest that the reduction of the thermal conductivity with decreasing HP temperature might be attributed to both the contributions from grain boundary scattering and the porosity effect.

In Fig. 5 we present the temperature dependence of the Seebeck coefficient. All the samples exhibit a positive Seebeck coefficient below 300 K with a maximum at $T_{max} \approx 50$ K. This value for T_{max} is in agreement with the previously reported data [18,19]. In the context of heavy-fermions, such a peak in S at higher T ($T > T_K$) is usually attributed to the Kondo scattering on higher multiplets (as opposed ground state doublet) which are split by crystal effect field (CEF). For $T > T_{max}$, S follows an unusual temperature dependence of the form: $S \propto -\ln T$, whereas for $T < T_{max}$, S follows the typical behavior of metals. The Seebeck coefficient decreases as the HP temperature decreases.

We also measured temperature dependent Hall coefficient (R_H) of the samples. Under the assumption of single band (SB) model, the effective carrier density (n) and the Hall mobility (μ_H) were calculated using the formulas, $n = 1/|R_H|e$ and $\mu_H = |R_H|/\rho$, respectively, where $e = 1.6 \times 10^{-19}$ C is the electronic charge. R_H, and μ_H of the samples as a function of temperature are shown in Fig. 6. Our data is consistent with the previous report [28] with R_H staying positive in the whole range of 2–100 K. At high temperature, $R_H \approx 0$ indicates that the electron and hole contributions to R_H cancel the effect of each other. As the temperature decreases, the hole contribution increases leading to a prominent peak at low temperature. This is an indication of coherent state development and is usually observed in heavy fermion metals. The Hall coefficient for the ingot sample (5.26×10^{-4} cm^3 C^{-1} at 50 K) is of the same order as reported in literature [28]. R_H, and μ_H decrease by two orders of magnitude going from the ingot to the hot-pressed samples. This indicates increased carrier concentration in the nanostructured samples when compared to the ingot. The defects induced during ball-milling process might have contributed to such a drastic increase in carrier concentration. When compared among the hot-pressed samples, R_H does not change much. However there is clear trend in mobility data indicating that decrease in hot-pressing temperature decreases the carrier mobility.

The calculated temperature dependent ZT is shown in Fig. 7. The ZT values reach a peak at around 60 K for all the samples. The peak value of ZT for the optimized sample HP 800 is 0.024 at 60 K. Since the ingot and the sample HP 800 have comparable values of power factor at 60 K (Inset of Fig 7), the improved ZT is derived from the reduction in thermal conductivity. Here we note that ZT greater than 0.1 at cryogenic temperatures (<77 K) has rarely been

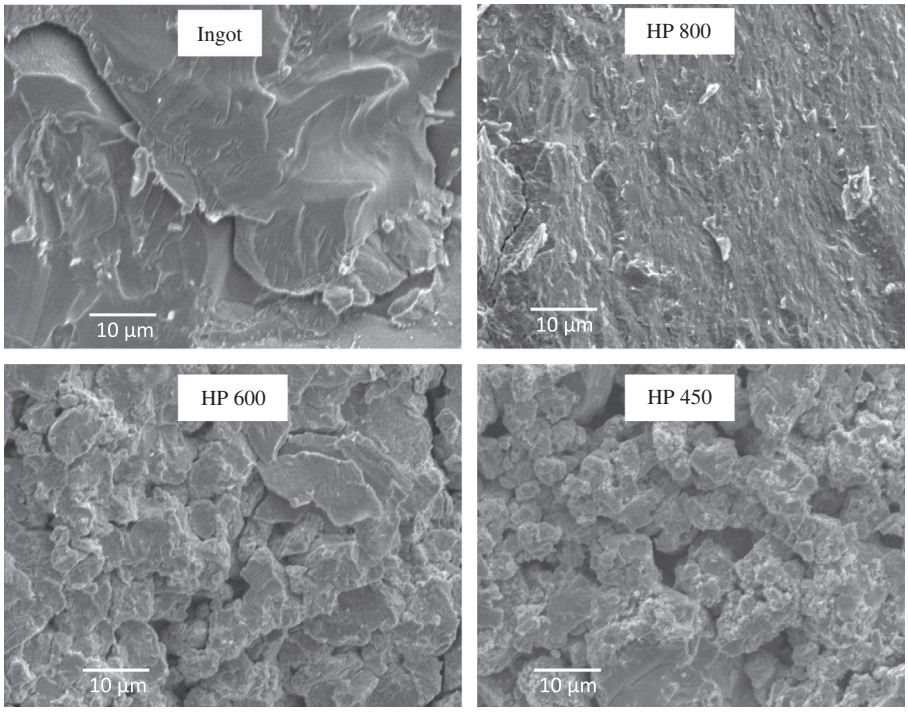

Fig. 2. SEM images of the freshly fractured surface of ingot and hot pressed samples.

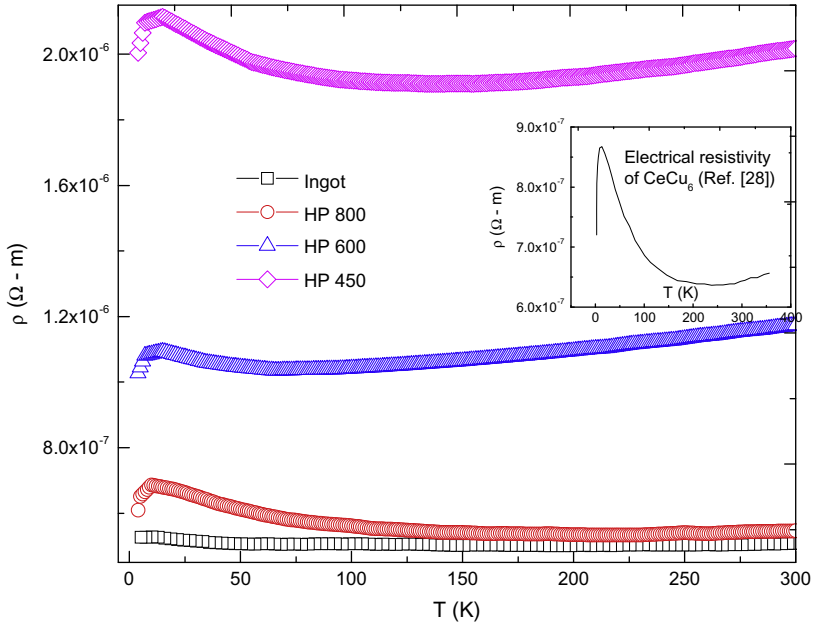

Fig. 3. Electrical resistivity as a function of temperature for the $CeCu_6$ samples. The inset shows a typical resistivity profile for $CeCu_6$ [25].

reported. $FeSb_2$ single crystal exhibits a peak *ZT* value of ~0.005 at ~10 K [29] which was increased to 0.013 at 50 K in nanostructured samples [23]. Single crystal FeSi has *ZT* of 0.01 at 50 K, which can be slightly raised to 0.07 at 100 K by 5% Ir doping [30].

While the original goal for nanostructuring was to increase the power factor (*PF*) by employing quantum confinement of carriers [31,32], experiments [33–35] have shown that the key reason for improved *ZT* was the reduction of thermal conductivity. Therefore, in recent years research on nanostructured thermoelectric material has focused on reducing the thermal conductivity, while producing minimal adverse effects on the Seebeck coefficient and the electrical conductivity. This approach seems to work most effectively in systems where the thermal transport is phonon-dominated (as opposed to electron-dominated). One of the ways to analyze the effectiveness of nanostructuring is to look at the values of the reduced Lorenz number (L/L_0). Here L is defined as $L = k\rho T^{-1}$ and $L_0 = 2.45 \times 10^{-8}\ \mathrm{W\,\Omega\,K^{-2}}$ is the free-electron value. In general a value of L/L_0 much greater than 1 implies that the phonons are the dominant mode of thermal transport. In Fig. 8, we present the temperature dependence of L/L_0. The shape of the $L/L_0\,(T)$ curve for all of the samples is typical of heavy fermions. The L/L_0 ratio decreases in the sample HP 800 when compared to the ingot

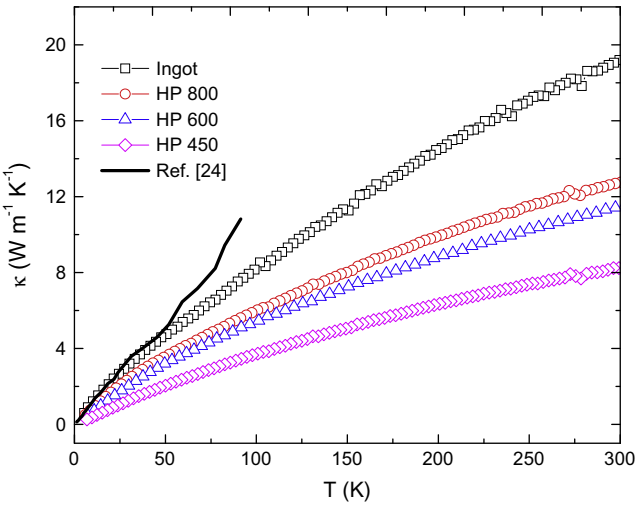

Fig. 4. Thermal conductivity as a function of temperature for the three nanostructured $CeCu_6$ samples. The data for the polycrystalline sample was drawn from Ref. [21] and replotted for comparison.

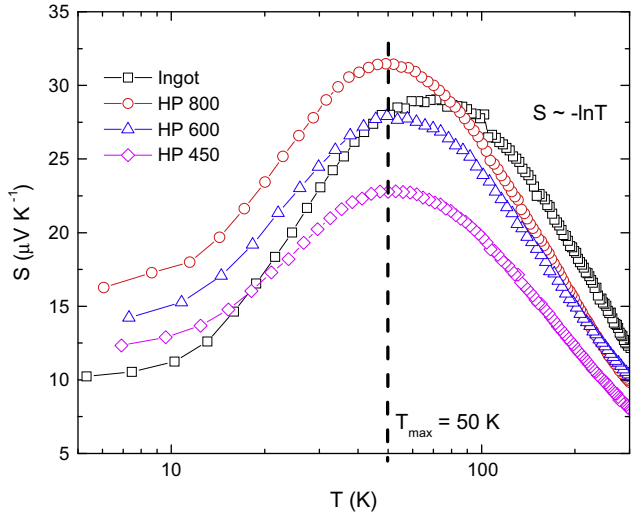

Fig. 5. Seebeck coefficient as a function of temperature for the $CeCu_6$ samples.

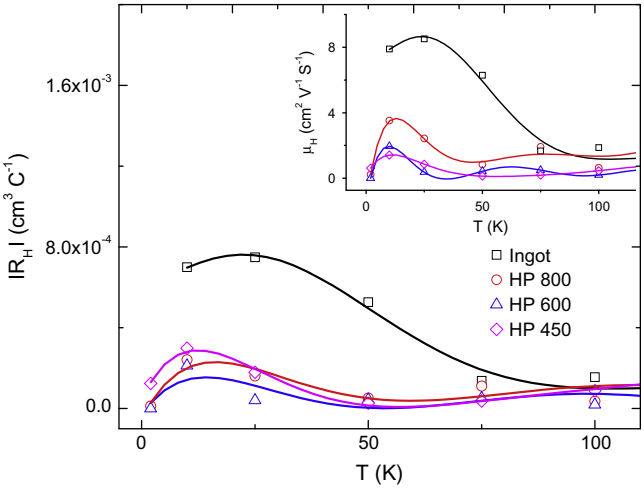

Fig. 6. Hall coefficient as a function of temperature in the temperature range 2–100 K. Solid lines are guide to eyes. Inset: Hall mobility as a function of temperature. Solid lines are guide to eyes.

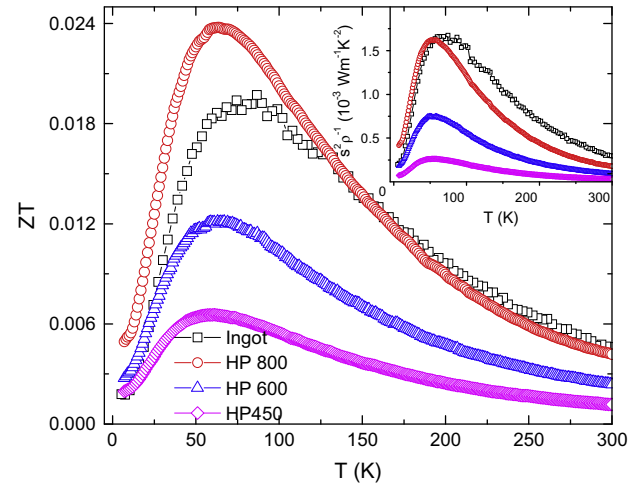

Fig. 7. *ZT* as a function of temperature for the $CeCu_6$ samples. Inset shows the power factor as a function of temperature.

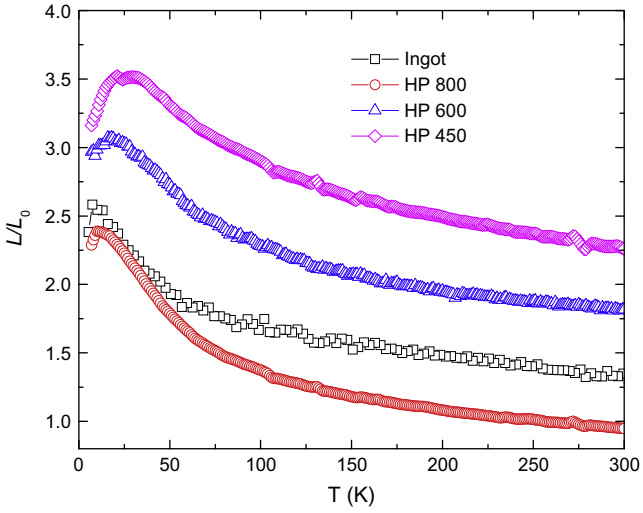

Fig. 8. Reduced Lorenz number as a function of temperature for the $CeCu_6$ samples. L is defined as $L = \kappa\rho T^{-1}$ and $L_0 = 2.45 \times 10^{-8}$ W Ω K^{-2} for free electron was used in the calculation.

showing that the lattice contribution to the total thermal conductivity was effectively reduced in the HP 800 sample. However, with a further decrease in the HP temperature, L/L_0 increases significantly. At lower HP temperatures, the thermoelectric properties are affected in such a way that the electronic contribution to the total thermal conductivity decreases more rapidly than the phononic contribution does. As a result no net gain in *ZT* was achieved by lowering the hot-pressing temperature.

4. Conclusion

In conclusion, nanostructured samples of $CeCu_6$ were prepared by arc melting and ball milling the arc-melted ingot followed by hot pressing at different temperatures. The thermoelectric properties were optimized by varying the hot pressing temperature. The thermal conductivity decreased as the hot pressing temperature was lowered showing that nanostructuring is an effective approach to reduce thermal conductivity of this system. However, the electrical resistivity increased and the Seebeck coefficient decreased to decrease the power factor. Overall the *ZT* values improved with

an increase in hot pressing temperature. A significant value for the *ZT* of 0.024 at 60 K was observed for the optimized sample HP 800. The broad and pronounced peak in *ZT* highlights its potential as a *p*-type thermoelectric material at low-temperature. Further *ZT* improvement of this HF compound could be achieved by combining doping with a nanostructuring approach.

Acknowledgment

We gratefully acknowledge funding for this work by the Department of Defense, United States Air Force Office of Scientific Research's MURI program under contract FA9550-10-1-0533. C. O. and M. P. would like to thank P. Czajka, R. Farrell, S.J. and K. Gofryk for helpful discussions and comments on the manuscript.

References

[1] H.J. Goldsmid, Thermoelectric Refrigeration, Plenum Press, New York, 1964.
[2] D.M. Rowe (Ed.), CRC Handbook of Thermoelectrics, CRC Press, Raton, FL, 1995.
[3] B. Poudel, Q. Hao, Y.C. Ma, Y. Lan, A. Minnich, B. Yu, X. Yan, D.Z. Wang, A. Muto, D. Vashaee, X. Chen, J. Liu, M.S. Dresselhaus, G. Chen, Z.F. Ren, Science 320 (2008) 634.
[4] J.P. Heremans, V. Jovovic, E.S. Toberer, A. Saramat, K. Kurosaki, A. Charoenphakdee, S. Yamanaka, G.J. Snyder, Science 321 (2008) 554.
[5] G.D. Mahan, Solid State Phys. 51 (1998) 81.
[6] V. Zlatić, A.C Hewson, Properties and Applications of Thermoelectric Materials: The Search for New Materials for Thermoelectric Devices, Springer, 2009. Jan 1.
[7] G.R. Stewart, Z. Fisk, M.S. Wire, Phys. Rev. B 30 (1984) 482.
[8] Y. Onuki, Y. Shimizu, T. Komatsubara, J. Phys. Soc. Jpn. 53 (1984) 1210.
[9] A. Amato, D. Jaccard, E. Walker, J. Flouquet, Solid State Commun. 55 (1985) 1131.
[10] Y. Onuki, Y. Shimizu, T. Komatsubara, J. Phys. Soc. Jpn. 54 (1985) 304.
[11] Y. Onuki, T. Komatsubara, J. Magn. Magn. Mater. 63 and 64 (1987) 281.
[12] F.P. Milliken, T. Penney, F. Holtzberg, Z. Fisk, J. Magn. Magn. Mater. 76 (1988) 201.
[13] A. Amato, D. Jaccard, J. Flouquet, F. Lapierre, J.L. Tholence, R.A. Fisher, S.E. Lacy, J.A. Olsen, N.E. Phillips, J. Low Temp. Phys. 68 (1987) 371.
[14] H.R. Ott, H. Rudigier, Z. Fisk, J.O. Willis, G.R. Stewart, Solid State Commun. 53 (1985) 235.
[15] H.V. Lohneysen, T. Portisch, H.G. Schlager, A. Schroder, M. Sieck, T. Trappmann, Phys. Rev. Lett. 72 (1994) 20.
[16] A. Rosch, A. Schroder, O. Stockert, H.V. Lohneysen, Phys. Rev. Lett. 79 (1) (1997).
[17] J. Sakurai, F. Taniguchi, K. Nishimura, K. Sumiyama, H. Amano, K. Suzuki, Physica B 186–188 (1993).
[18] M. Ocko, M. Miljak, I Kost, J-G Park, S.B. Roy, J. Phys. Condens. Matter. 7 (1995) 2979–2986.
[19] M.I. Ignatov, A.V. Bogach, G.S. Burkhanov, V.V. Glushkov, S.V. Demishev, A.V. Kuznetsov, O.D. Chistyakov, N.Yu. Shitsevalova, N.E. Sluchanko, J. Experiment. Theoret. Phys. 105 (2007) 58–61.
[20] N.E. Sluchanko, D.N. Sluchanko, N.A. Samarin, V.V. Gluskhov, S.V. Demishev, A.V. Kuznestov, G.S. Burkhanov, O.D. Chistyakov, Low Temp. Phys. 35 (2009) 7.
[21] H. Zhao, M. Pokharel, G. Zhu, S. Chen, K. Lukas, Q. Jie, C. Opeil, G. Chen, Z. Ren, Appl. Phys. Lett. 99 (2011) 163101.
[22] M. Pokharel, H. Zhao, R. Lukas Z, and C. and Opeil, Mater. Res. Soc. Symp. Proc. vol. 1 ©, 2012.
[23] H. Zhao, M. Pokharel, S. Chen, B. Liao, K. Lukas, C. Opeil, G. Chen, Z. Ren, Nanotechnology 23 (2012) 505402.
[24] Y. Peysson, B. Salce, C. Ayche, J. Magn. Magn. Mater. 54–57 (1986) 423–424.
[25] M. Falkowski, A. Kowalczyk, in: Proceedings of the European Conference Physics of Magnetism (PM'11), Pozman, June 27-July 1, 2011.
[26] H. Lee, D. Vashaee, D.Z. Wang, M.S. Dresselhaus, Z.F. Ren, G. Chen, J. Appl. Phys. 107 (2010) 094308.
[27] J.M. Montes, F.G. Cuevas, J. Cintas, Appl. Phys. A 92 (2008) 375–380.
[28] A.S. Krivoshchekov, B.N. Goshchitskii, V.I. Voroin, I.F. Berger, Yu.N. Akshentsev, A.E. Earkin, Physica B 359–361 (2005) 178–180.
[29] A. Bentien, S. Johnsen, G.K.H. Madsen, B.B. Iversen, F. Steglich, Europhys. Lett. 80 (2007) 17008.
[30] B.C. Sales, E.C. Jones, B.C. Chakoumakos, J.A. Fernandez-Baca, H.E. Harmon, J.W. Sharp, E.H. Volckmann, Phys. Rev. B: Condens. Matter. 50 (12) (1994) 8207–8213.
[31] L.D. Hicks, M.S. Dresselhaus, Phys. Rev. B 47 (1993) 12727.
[32] L.D. Hicks, M.S. Dresselhaus, Phys. Rev. B 47 (1993) 16631.
[33] R. Venkatasubramanian, E. Silvola, T. Colpitts, B. O'Quinn, Nature 413 (2001) 597–602.
[34] T.C. Harman, P.J. Taylor, M.P. Walsh, B.E. LaForge, Science 297 (2002) 2229–2232.
[35] K.F. Hsu, S. Loo, F. Guo, W. Chen, J.S. Dyck, C. Uher, T. Hogan, E.K. Polychroniadis, M.G. Kanatzidis, Science 303 (2004) 818–821.

J Low Temp Phys (2014) 176:122–130
DOI 10.1007/s10909-014-1148-y

Enhanced Thermoelectric Performance of Te-doped $FeSb_2$ Nanocomposite

M. Pokharel · H. Z. Zhao · M. Koirala · Z. F. Ren · C. Opeil

Received: 30 December 2013 / Accepted: 22 February 2014 / Published online: 6 March 2014

Abstract Nanostructured samples of $FeSb_{1.84}Te_{0.16}$ were prepared using a hot-press method and thermoelectric properties were studied. Nanostructured samples exhibited significantly reduced values for the thermal conductivity. Te-doping, in addition to enhancing point-defect scattering, also induced a semiconductor-to-metal transition which increased the power factor value at low temperatures. Both the power factor and the thermal conductivity were shown to decrease with a decrease in hot-pressing temperature. The combined effect resulted in a figure-of-merit *ZT* of 0.022 at 100 K for the optimized sample, a 62 % increase over the single crystal counterpart. Within nanostructured samples, *ZT* increases by as much as 11 times.

Keywords Iron diantimonide · Thermal conductivity · Point-defect scattering

1 Introduction

In the past few decades, the narrow-gap semiconductor $FeSb_2$ has been extensively studied due to its unusual magnetic and electronic transport properties [1–3]. In more recent years, $FeSb_2$ has attracted considerable attention as a thermoelectric material. Efficiency (for thermoelectric power generation) or coefficient of performance (for Peltier cooling) of a thermoelectric material is directly related to a dimensionless

M. Pokharel (✉) · C. Opeil (✉)
Department of Physics, Boston College, Chestnut Hill, MA02467-3800, USA
e-mail: pokharem@bc.edu

C. Opeil
e-mail: cyril.opeil@bc.edu

H. Z. Zhao · M. Koirala · Z. F. Ren
Department of Physics and TcSUH, University of Houston, Houston, TX 77204-5005, USA

figure-of-merit (ZT) defined by, $ZT = \frac{S^2 T}{\rho\kappa}$ where S is the Seebeck coefficient, ρ is the electrical resistivity, κ is the thermal conductivity, and T is the absolute temperature. A ZT value of at least 1 is required for a thermoelectric material to be practically useful. Since $ZT \sim S^2$, a high Seebeck coefficient is necessary for a good thermoelectric material. Narrow-gap semiconductors are considered to be one of the best classes of thermoelectric material and for most of these materials the value of the Seebeck coefficient is on the order of 100 μVK^{-1}. For $FeSb_2$, an unusually large Seebeck coefficient of ~45,000 μVK^{-1} has been reported at ~10 K [4] with a moderate value for the electrical conductivity at that temperature. As a result, a record high value for the power factor ($S^2\rho^{-1}$) of 0.23 W m^{-1} K^{-2} at 10 K was observed [4]. Despite the large power factor value, the ZT values for single crystal $FeSb_2$ are rather low due to the high thermal conductivity. For undoped $FeSb_2$ single crystals, the reported ZT values are around 0.005 at ~10 K [4].

Recently there has been a large amount of interest in reducing the thermal conductivity of $FeSb_2$ while maintaining a high Seebeck coefficient. Specifically, efforts have been made to improve the thermoelectric performance of $FeSb_2$ using the techniques of doping[5–8], nanoinclusions [9,10], nanostructuring [11,12] and stoichiometric adjustment [13]. In our earlier work [11], we were able to reduce the thermal conductivity of $FeSb_2$ by three orders of magnitude using the technique of nanostructuring. Unfortunately, the values of the Seebeck coefficient were drastically reduced in these nanostructured samples possibly indicating a significant phonon-drag contribution[14]. As a result, ZT was increased by only one order of magnitude. Data from our earlier work clearly showed that a significant increase in ZT of $FeSb_2$ through nanostructuring alone cannot be expected. On the other hand, studies have shown tellurium to be an effective dopant for improving ZT of single crystal $FeSb_2$ by reducing the thermal conductivity via point defect scattering. Sun et al. [6] reported a ZT value of ~0.013 at around 100 K in $FeSb_{2-x}Te_x$ single crystal samples for their optimized doping concentration of x = 0.16. In this report, we present the combined effect of nanostructuring and Te-doping on the thermoelectric properties of $FeSb_2$. To conduct our research, we used the previously reported optimized Te-doped stoichiometric composition ($FeSb_{1.84}Te_{0.16}$) and tuned the thermoelectric properties by changing the hot-pressing (HP) temperature. Our results showed a significant drop in thermal conductivity and an enhanced power factor value which lead to improved ZT values.

2 Experimental

Stoichiometric amounts of Fe, Sb and Te were mixed and melted at 1,000 °C inside an evacuated and sealed quartz tube. The tube was quenched in cooling water for rapid cooling and solidification. The resulting polycrystalline ingot was ball milled for 15 hours and obtained nanopowder was DC hot pressed under a pressure of 80 MPa for 2 min at several different temperatures (200, 300, 400, 500 and 600 °C). The sample disks were sputtered with gold to optimize electrical and thermal contacts and then cut into rectangular shapes of typical dimension 2 × 2 × 8 mm^3. The Seebeck Coefficient (S), electrical resistivity (ρ), and thermal conductivity (κ) were measured using thermal transport option (TTO) of the Physical Property Measurement System (PPMS).

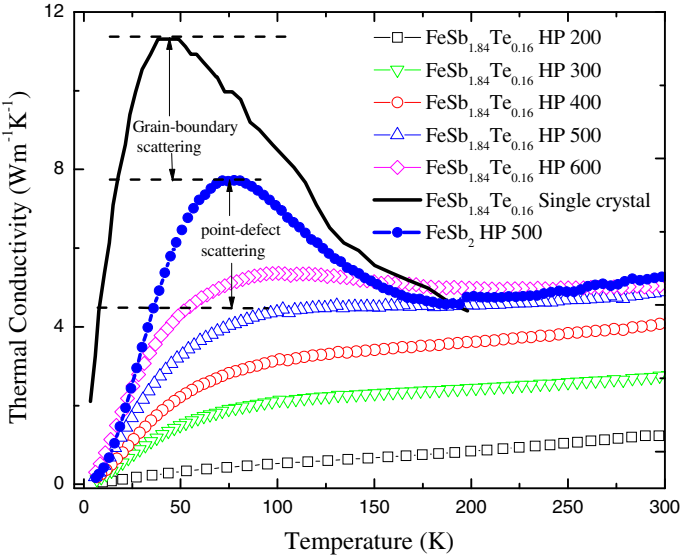

Fig. 1 Thermal conductivity of the samples as a function of temperature (Color figure online)

The Hall coefficient (R_H) was measured using samples with typical dimensions of $1\times2\times10$ mm^3 employing a five-point configuration on the horizontal rotator option of the PPMS.

3 Results and Discussion

Figure (1) shows the temperature dependence of the thermal conductivity for the samples. The thermal conductivity values of all the nanostructured samples are significantly lower than the values reported for single crystals [4]. For the sample $FeSb_2$ HP 500, κ = 7.08 W m^{-1} K^{-1} at 100 K which is 76 % lower than the value reported for single crystal $FeSb_2$ (∼30 W m^{-1} K^{-1}). By doping with Te, the thermal conductivity was further reduced to 4.38 W m^{-1} K^{-1} in the representative sample $FeSb_{1.84}Te_{0.16}$ HP 500; a reduction by 38 %. In this way an overall reduction in thermal conductivity by 85 % was achieved.

In general, $\kappa = \kappa_{carrier} + \kappa_{lattice}$. Here $\kappa_{carrier}$ and $\kappa_{lattice}$ are the carrier and lattice contributions respectively. Calculations based on the Wiedemann-Franz law ($\kappa_{carrier} = L_0\rho^{-1}T$) show that more than 99 % of the total thermal conductivity of $FeSb_2$ comes from lattice vibrations (phonons). Therefore any reduction in the total thermal conductivity of this system is due to reduction in lattice contribution. The physics of the lattice thermal conductivity is commonly interpreted using the Debye approximation [15,16],

$$\kappa_{lattice} = \frac{k_B}{2\pi^2 v}\left(\frac{k_B}{\hbar}\right)^3 T^3 \int_0^{\frac{\theta_D}{T}} \frac{\tau_c x^4 e^x}{(e^x-1)^2} dx \quad (1)$$

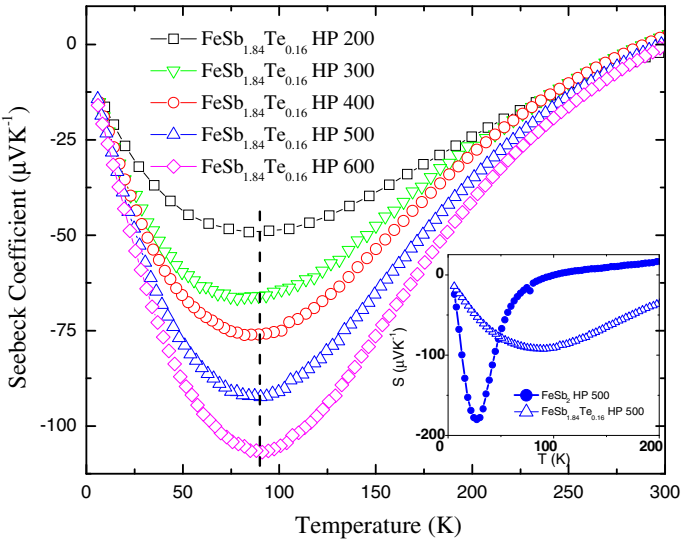

Fig. 2 Seebeck coefficient of the samples as a function of temperature. The *inset* shows the comparison between the temperature dependence of the representative sample $FeSb_{1.84}Te_{0.16}$ HP 500 and an undoped counterpart $FeSb_2$ HP 500 (Color figure online)

where $x = \frac{\hbar w}{k_B T}$, w is the frequency, k_B is the Boltzmann constant, $\hbar$ is the Planck constant, v is the speed of sound, θ_D is the Debye temperature and τ_c is the relaxation time. The overall time constant (τ_c) is given by the Matthiessen's rule,

$$\tau_c^{-1} = \tau_{defect}^{-1} + \tau_{umklapp}^{-1} + \tau_{boundary}^{-1} \tag{2}$$

Here τ_{defect}, $\tau_{umklapp}$ and $\tau_{boundary}$ are the relaxation times associated with the three scattering mechanisms: phonon-defect scattering, umklapp process and phonon-boundary scattering respectively. The reduced (by 76 %) thermal conductivity in our nanostructured samples is due primarily to scattering of the phonons off the grain boundaries. On the other hand, since addition of a small amount of Te should not change the Umklapp process and grain-boundary scattering that much, the additional reduction (by 38 %) comes mainly from the point-defect scattering. Now the mass difference between Sb (121.75) and Te (127.60) is considerably small; therefore the difference in interatomic coupling force constants probably plays a dominant role in scattering of phonons in doped samples. The contributions of nanostructuring and defect scattering are depicted in Fig (1). A significant reduction of thermal conductivity in Te-doped $FeSb_2$ single crystals has been previously discussed in detail by Sun et al. [6] They attributed the thermal conductivity reduction to the introduced charge carriers rather than chemical disorder whereas Wang et al. [7] attributed the reduction to the enhanced point defect scattering caused by both the different bonding tendency and different thermal conductivities of Sb and Te.

Figure 2 shows the temperature dependence of the Seebeck coefficient. At 300 K, the Seebeck coefficient has a small positive value (p-type) ~ 2 μV K^{-1} for all the

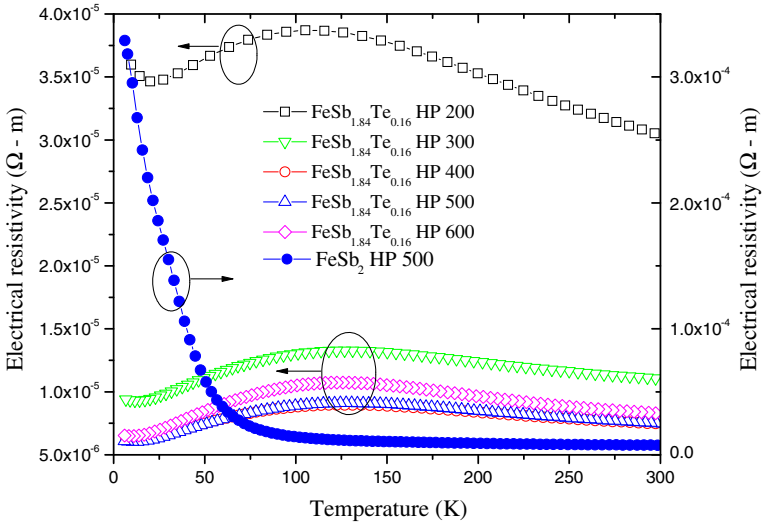

Fig. 3 Electrical resistivity (left *y*-axis) as a function of temperature for the four Te-doped samples. The right *y*-axis corresponds to the electrical resistivity for the undoped sample $FeSb_2$ HP 500 (Color figure online)

Te-doped samples. This value of Seebeck coefficient is significantly less than 31 μV K^{-1} observed for undoped samples. As the temperature decreases, the Seebeck coefficient decreases and changes to a negative (n-type) value at ∼290 K. The Seebeck coefficient assumes a peak value at 90 K for all the samples. The largest peak value for the Seebeck coefficient among our samples is ∼ -107 μV K^{-1}for sample $FeSb_{1.84}Te_{0.16}$ HP 600 which is two orders of magnitude less than the reported value for undoped $FeSb_2$single crystals [4] and is one-fourth of the value (∼ - 400 μV K^{-1}) for $FeSb_{1.84}Te_{0.16}$ single crystals [6]. The peak value of the Seebeck coefficient decreases with decreasing HP temperature. This decrease, based on our analysis, comes from two factors: increased carrier density [11] and suppression of the phonon-drag contribution due to increased grain boundary scattering at lower HP temperatures[14]. The inset of Fig. 2 shows the temperature-dependent Seebeck coefficient for the representative sample $FeSb_{1.84}Te_{0.16}$ HP 500 and its undoped counterpart $FeSb_2$ HP 500. Upon Te-doping, the peak value of the Seebeck coefficient decreases and shifts to a higher temperature. A similar shifting of the Seebeck peak with increasing Te-content has been reported also in ref. [6].

Figure 3 shows the temperature dependence of the electrical resistivity for the samples. The electrical resistivity of the sample $FeSb_2$ HP 500 is represented by the right *y*-axis. The undoped sample exhibits semiconducting behavior throughout the temperature range 5–300 K with increasing resistivity as temperature decreases. A sharp increase in resistivity below 70 K indicates an insulating ground state. In contrast to the undoped $FeSb_2$, the Te doped samples exhibit suppressed electrical resistivity with a metallic ground state. The electrical resistivity decreases by one order of magnitude at 100 K. The semiconductor to metal transition temperature for the different samples falls within the range of 100–130 K.

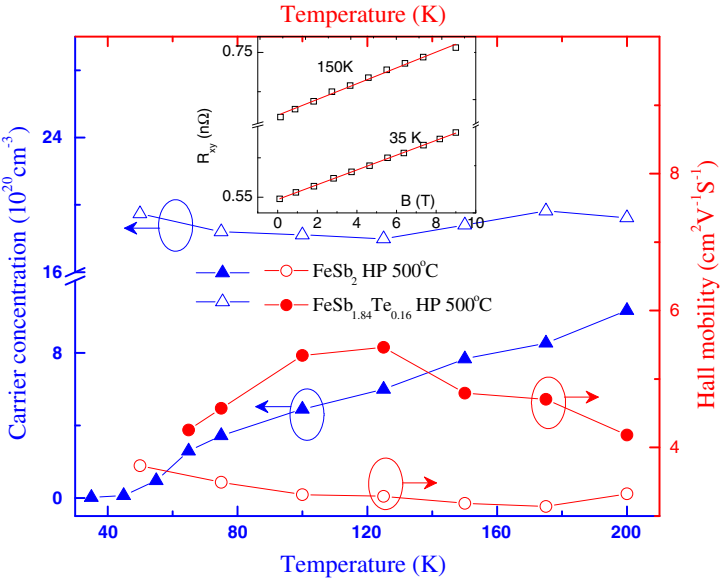

Fig. 4 Carrier concentration (left *y*-axis) and Hall mobility (right *y*-axis) as a function of temperature in the temperature range of 60–200 K. *Inset* shows the magnetic field dependence of Hall resistivity for representative sample $FeSb_{1.84}Te_{0.16}$ HP 500 at 35 and 150 K (Color figure online)

Figure 4 shows the temperature dependence of the carrier concentration (n) and the Hall mobility (μ) for the undoped and doped nanostructured samples pressed at 500 °C. In the inset of the Fig. 4, we have plotted the magnetic field dependence of the Hall resistivity (R_{xy}) for the samples $FeSb_{1.84}Te_{0.16}$ HP 500 both below (35 K) and above (150 K) the semiconductor to metal transition temperature. A linear relationship as expected in single band model is observed.n and μ were estimated from the Hall coefficient (R_H) and electrical resistivity (ρ) measurements using $n = 1/|R_H|e$ and $\mu = |R_H|/\rho$, under the single band model. Here $e = 1.6 \times 10^{-19}$ C is the electronic charge. At 100 K, the carrier concentration of the doped sample is increased by one order of magnitude when compared with that of undoped sample. Also, the carrier concentration is less temperature sensitive for doped samples, a result consistent with the metallic nature seen in the electrical resistivity data at lower temperatures. The Hall mobility is reduced in the doped sample. For example, $\mu = 5.3$ and 3.3 cm^2 V^{-1} S^{-1} for samples $FeSb_2$ HP 500 and $FeSb_{1.84}Te_{0.16}$ HP 500, respectively at 100 K.

Figure 5 shows the temperature dependence of the power factor ($S^2\rho^{-1}$). When compared with the undoped nanostructured samples, the power factors in the Te-doped samples increased significantly. For example, $S^2\rho^{-1} = 9.9 \times 10^{-4}$ W m^{-2} K^{-1} at 80 K for the representative sample $FeSb_{1.84}Te_{0.16}$ HP 500, which is an increase of 386 % from the corresponding value for the undoped sample $FeSb_2$ HP 500. Among the Te-doped samples, the peak values for the power factor decrease with decreasing the HP temperature.

In Figure 6, we have presented *ZT* as a function of temperature. For all the doped samples, the curve assumes a peak value (ZT_{max}) at around 100 K. For the optimized

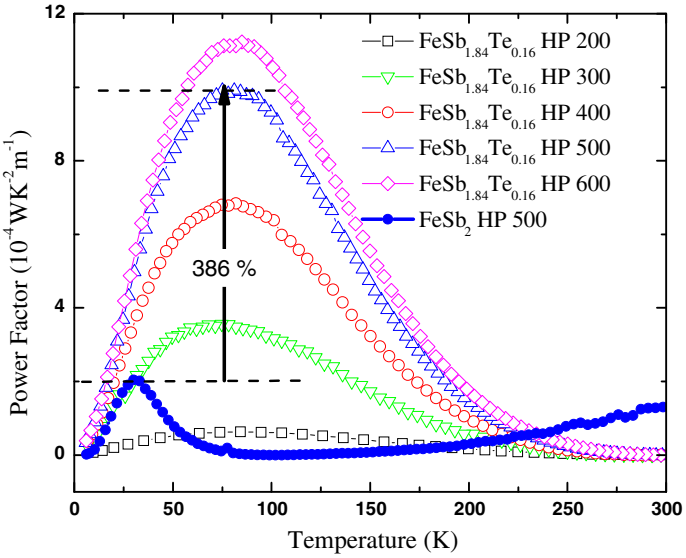

Fig. 5 Power factor as a function of temperature (Color figure online)

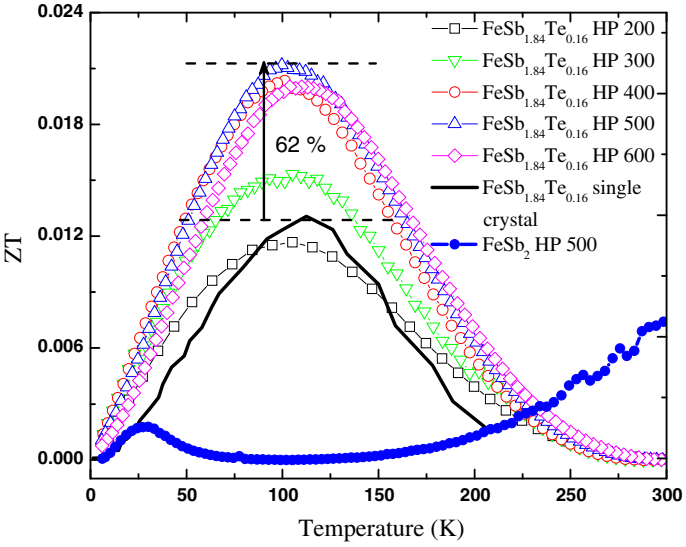

Fig. 6 *ZT* as a function of temperature. Data for $FeSb_{1.84}Te_{0.16}$ single crystal (taken from ref. [6]) are also included for comparison (Color figure online)

sample $FeSb_{1.84}Te_{0.16}$ HP 500, ZT_{max} = 0.022 at 100 K, this is an increase of 62 % compared with the optimized value for the Te-doped single crystal which was 0.012 in ref. [6]. When compared with the *ZT* of $FeSb_2$ HP 500 (ZT_{max} = 0.0017 at 25 K), the *ZT* values for the optimized sample $FeSb_{1.84}Te_{0.16}$ HP 500 is increased by a factor of 11.

4 Conclusion

In conclusion, nanostructured samples of $FeSb_{1.84}Te_{0.16}$ have been prepared using the hot-press method and their thermoelectric properties have been studied in the range of temperatures 5–300 K. Based on our analysis, the grain-boundary scattering and the point-defect scattering are the two dominant phonon scattering mechanisms that contributed to a significantly reduced (by 85 % at 100 K) thermal conductivity in Te-doped nanostructured samples. Te-doping in $FeSb_2$ contributed not only to the thermal conductivity reduction but also to an enhanced power factor by inducing a semiconductor to metal transition. With a decrease in HP temperature, both the thermal conductivity and the power factor decreased. The optimal conditions for *ZT* were observed for the doped sample hot pressed at 500 °C. The *ZT* value of 0.022 at 100 K was observed for the optimized sample $FeSb_{1.84}Te_{0.16}$ HP 500, 62 % higher than the corresponding value for the single crystal. Therefore, it has been successfully demonstrated that combining the technique of doping with nanostructuring significantly enhances the thermoelectric performance of $FeSb_2$ at low temperatures. This approach can easily be extended to improve ZT of other phonon dominated thermoelectric systems at low temperatures.

Acknowledgments We gratefully acknowledge funding for this work by the Department of Defense, United States Air Force Office of Scientific Research's MURI program under contract FA9550-10-1-0533. C.O. wishes to thank B. Mihaila, T. Hoeler, and Peter Czajka for their helpful comments on the manuscript.

References

1. H. Holseth, A. Kjekshus, Compounds with marcasite type of structure IV. The crystal structure of $FeSb_2$. Acta Chem. Scand. **23**, 3043 (1969)
2. A.K.L. Fan, G.H. Rosentha, A. Wold, H.L. Mckinzie, Preparation and Properties of $FeAs_2$ and $FeSb_2$. J. Solid State Chem. **5**, 136 (1972)
3. J. Steger, E. Kostiner, Mossbauer effect study of $FeSb_2$. J. Solid State Chem. **5**, 131 (1972)
4. A. Bentien, S. Johnsen, G.K.H. Madsen, B.B. Iversen, F. Steglich, Colossal Seebeck coefficient in strongly correlated semiconductor $FeSb_2$. Europhys. Lett. **80**, 17008 (2007)
5. A. Bentien, G.K.H. Madsen, S. Johnsen, B.B. Iversen, Experimental and theoretical investigations of strongly correlated $FeSb_{2-x}Sn_x$. Phys. Rev. B **74**, 205105 (2006)
6. P. Sun, M. Sondergaard, Y. Sun, S. Johnsen, B.B. Iversen, F. Steglich, Unchanged thermopower enhancement at the semiconductor-metal transition in correlated $FeSb_{2-x}Te_x$. Appl. Phys. Lett. **98**, 072105 (2011)
7. K. Wang, R. Hu, J. Warren, C. Petrovic, Enhancement of the thermoelectric properties in doped $FeSb_2$ bulk crystals. J. Appl. Phys. **112**, 013703 (2012)
8. A. Sanchela, A.D. Thakur, C.V. Tomy, Room temperature thermoelectric material $Fe(Sb_{1-x}Se_x)_2$. AIP Conf. Proc. **1447**, 1003 (2012)
9. S. Zhu, W. Xie, D. Thompson, T. Holgate, M. Zhou, Y. Yan, T.M. Tritt, Tuning the thermoelectric properties of polycrystalline $FeSb_2$ by the in situ formation of Sb/InSb nanoinclusions. J. Mater. Res. **26**, 1894 (2011)
10. H. Zhao, M. Pokharel, S. Chen, B. Liao, K. Lukas, C. Opeil, G. Chen, Z. Ren, Figure-of-merit enhancement in nanostructured $FeSb_{2-x}Ag_x$ with $Ag_{1-y}Sb_y$ nanoinclusions. Nanotechnology **23**, 505402 (2012)
11. H. Zhao, M. Pokharel, G. Zhu, S. Chen, K. Lukas, Q. Jie, C. Opeil, G. Chen, Z. Ren, Dramatic thermal conductivity reduction by nanostructures for large increase in thermoelectric figure-of-merit of $FeSb_2$. Appl. Phys. Lett. **100**, 059902 (2012)

12. A. Datta, Synthesis and characterization of nanocrystalline $FeSb_2$ for thermoelectric applications. Eur. J. Inorg. Chem. **2012**, 55 (2012)
13. M. Pokharel, H. Zhao, R. Lukas Z., and C. and Opeil: Enhanced thermoelectric properties of FeSbx nanocomposites through stoichiometric adjustment. Mater. Res. Soc. Symp. Proc. 1, San Francisco, 2012).
14. M. Pokharel, H. Zhao, K. Lukas, B. Mihaila, Z. Ren, C. Opeil, honon drag effect in nanocomposite $FeSb_2$. MRS Commun. **3**, 31–36 (2013)
15. J. Callaway, Model for lattice thermal conductivity at low temperatures. Phys. Rev. **113**, 1046 (1959)
16. C. Kittel, *Introduction to Solid State Physics*, 8th edn. (Wiley, Hoboken, 2004)

Magnetic Properties of Hot-Pressed $FeSb_2$

Mani Pokharel[1], Huaizhou Zhao[2], Kimberly A. Modic[3], Zhifeng Ren[2], and Cyril Opeil[1]

[1]Department of Physics, Boston College, Chestnut Hill, MA 02467 USA
[2]Department of Physics and TcSUH, University of Houston, Houston, TX 77204 USA
[3]Los Alamos National Laboratory, Los Alamos, NM 87545 USA

We report on the magnetic properties of a hot-pressed $FeSb_2$ sample. We find a significant increase in the magnetic susceptibility in our sample when compared with the values previously reported for the polycrystalline sample. The pronounced Curie tail at low temperature corresponds to 0.2% of Fe^{2+} impurities per mole. In the intrinsic conductivity region, the susceptibility due to free carriers shows thermally activated behavior and is consistent with the data reported for single crystal $FeSb_2$. Based on our data and analysis, while the enhanced magnetic susceptibility in our sample comes mainly from a small amount of unreacted Fe, the contribution from the enhanced carrier density due to lattice and strain defects arising from the ball milling process is also significant. Existence of an unreacted Fe phase is evidenced by small coercivity values of ~100 Oe observed at 50 and 300 K.

Index Terms—**Hall effect, hysterisis, iron doantimonide, magnetization.**

I. Introduction

$FeSb_2$ has drawn considerable research efforts because of its unusual electronic and magnetic properties [1]–[5]. Single crystal $FeSb_2$ is known to be paramagnetic, having unusual temperature dependence of magnetic susceptibility with a diamagnetic to paramagnetic crossover at ~100 K. Petrovic *et al*. [6] reported such a crossover for the magnetic field applied along all the three crystallographic axes whereas Hu *et al*. [7] reported the crossover only along the *c*-axis. It has also been demonstrated that the magnetic properties exhibit weaker anisotropy when compared with the electronic properties [6]. Extensive efforts have been made in the past decade to explain the anomalous temperature dependence of the magnetic susceptibility of $FeSb_2$. A simple analysis based on a free-ion model was shown to explain this behavior in [6]. It was also demonstrated in [8] that a narrowband picture with two peaks in the density of states at the gap edge explains the observed data well, thereby validating the Kondo insulator description of a spin state transition in $FeSb_2$. Recently, Koyama *et al*. [9] employed the Stoner–Wohlfath theory and the Arrot plot technique to determine the temperature dependence of the inverse of the fourth expansion coefficient γ for the $FeSb_2$ single crystal. The temperature dependence of γ they found was similar to that observed in FeSi reported in [10], which can be explained by the spin fluctuation theory.

So far most of the studies have been made in single crystal samples; the experimental data on the magnetic properties of polycrystalline $FeSb_2$ samples remains scarce. In this paper, we report and analyze the magnetic properties of a polycrystalline $FeSb_2$ prepared by hot-press method. We report a significant enhancement in the magnetic susceptibility of the hot-pressed polycrystalline sample when compared with the polycrystalline average predicted from the single crystal data. Based on our analysis, this enhancement is possibly due to a significant temperature-independent contribution coming from the unreacted iron (Fe) and also from lattice and strain defects arising from the ball milling process. Thus, diamagnetic to paramagnetic crossover, reported for the single crystals, disappeared in our sample. A pronounced upturn in susceptibility below 30 K can be attributed to Curie type of behavior coming from paramagnetic impurities. A weak ferromagnetism is also evidenced by a small value of coercivity at 50 and 300 K.

Manuscript received October 4, 2013; accepted November 16, 2013. Date of publication November 26, 2013; date of current version May 1, 2014. Corresponding author: M. Pokharel (e-mail: pokharem@bc.edu).

Color versions of one or more of the figures in this paper are available online at http://ieeexplore.ieee.org.

Digital Object Identifier 10.1109/TMAG.2013.2292607

II. Experiment

Stoichiometric amounts of Fe and Sb were mixed and melted at 1000 °C inside an evacuated and sealed quartz tube. The tube was quenched in water for rapid cooling and solidification. After solidification the ingot was ball milled for 15 h. The resulting nanopowder was densified in a dc hot press under 80 MPa for 2 min at 400 °C to obtain the disk of nanocomposite sample, as described in [11]. The sample disk was then characterized using X-ray diffraction (XRD) and scanning electron microscopy (SEM). Using Archimedes' method, the sample density was measured to be 97.7% of the theoretical density. A vibrating sample magnetometer option of the physical property measurement system (PPMS) from quantum design was used to measure the magnetic moment. The molar susceptibility was calculated by $\chi = (M/H)$, where M is the magnetization and H is an applied magnetizing field of 0.1 T during measurement. The Hall coefficient (R_H) was measured using the horizontal rotator option of the PPMS.

III. Results and Discussion

Fig. 1 shows the XRD pattern of the as-prepared $FeSb_2$ sample disk. Leaving a few small peaks coming from background, the peak positions are consistent with the orthorhombic crystal structure and can be indexed as shown.

Fig. 2 shows the SEM images of a fractured surface of the sample. An estimated value of the average grain size is ~200 nm.

Fig. 3 shows the temperature dependence of the molar susceptibility for the $FeSb_2$ sample used in this paper. The susceptibility values for the sample are significantly enhanced

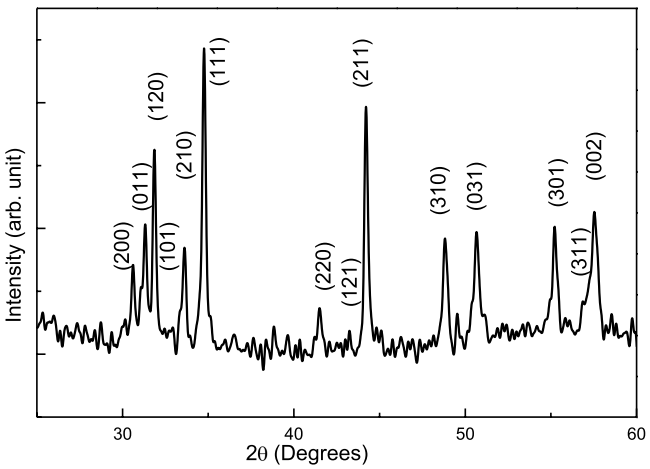

Fig. 1. XRD pattern of hot-pressed $FeSb_2$ sample.

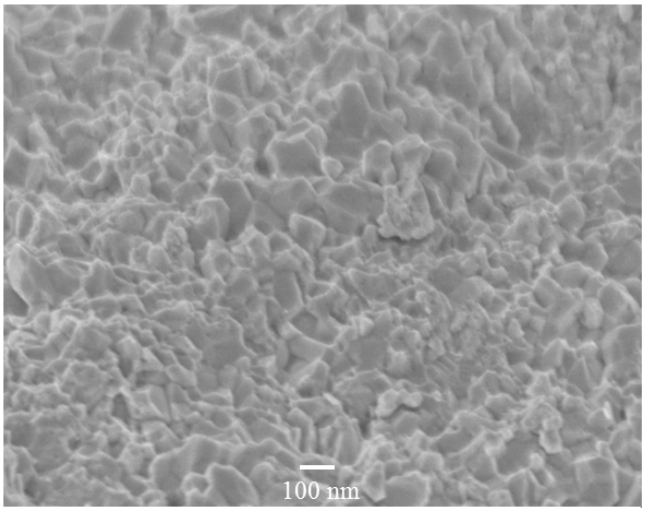

Fig. 2. SEM images of the hot-pressed $FeSb_2$ sample.

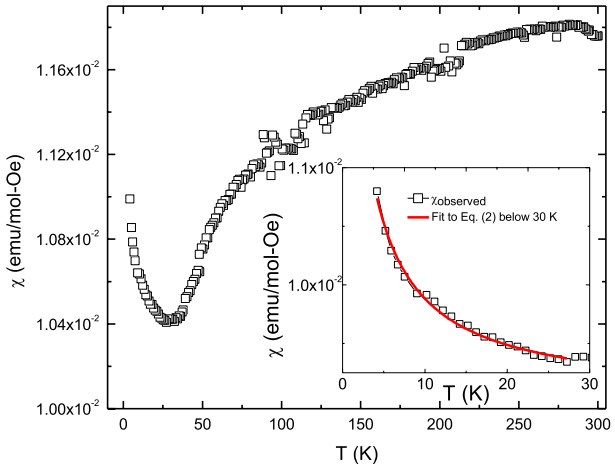

Fig. 3. Observed magnetic susceptibility of the $FeSb_2$ sample as a function of temperature. Inset: fitting to the Curie–Weiss law below 30 K.

throughout the temperature range 2–300 K when compared with the single crystal data reported in the literature. For example, at 300 K, $\chi \sim 1.2 \times 10^{-2}$ emu/mol^{-1} is two orders of magnitude higher than the estimated polycrystalline average value of 3×10^{-4} emu/mol^{-1} calculated in [6] and 6×10^{-4} emu/mol^{-1} reported in [2]. Therefore no diamagnetic to paramagnetic crossover is observed for our sample. Such a vertical shift of the $\chi(T)$ curve was also reported in the arsenic-substituted single crystals of $FeSb_2$ [12] that they attributed to the substantial Pauli paramagnetism of the increased carrier concentration, which is induced by defects or impurities. We note that while most of the qualitative features of the susceptibility curves are preserved, a more pronounced Curie type of tail compared with that reported in [2] and [6] is observed at low temperatures.

The observed magnetic susceptibility (χ_{obs}) in a semiconductor is given by [13]

$$\chi_{\text{obs}}(T) = \chi_0 + \chi_{\text{p}} + \chi_{\text{c}} \tag{1}$$

where χ_0 is the temperature-independent susceptibility and is the sum of the contributions coming from the lattice, lattice defects and neutral impurities (if any), χ_{p} is the temperature dependent susceptibility due to paramagnetic impurities and χ_{c} is the magnetic susceptibility due to the free carriers. The pronounced upturn in the susceptibility below 30 K indicated the presence of a substantial amount of paramagnetic impurities. Data below 30 K were fitted to

$$\chi(T) = \chi_0 + \gamma C/T - \theta \tag{2}$$

where γC is the effective Curie constant, γ being a dimensionless constant and θ is the Weiss temperature. A satisfactory fitting (represented by solid line in the inset of Fig. 3) was found for the parameter values of $\chi_0 = 1.0 \times 10^{-2}$ emu/mol^{-1}, $\gamma C = 3.96 \times 10^{-3}$ emu/Kmol^{-1}, and $\theta = -1.6$ K. Here we note a large value of χ_0, which has the same order of magnitude as χ_{obs}, indicating a significant contribution from the temperature-independent term. For single crystals, $\chi_0 \sim -4 \times 10^{-5}$ emu/mol^{-1} was reported in [6].

Assuming that the orbital angular momentum is quenched and only the spin angular momentum contributes, the Curie constant C is given by

$$\begin{aligned} \text{C} &= (\text{N}_\text{A} g^2 \mu_B^2 / 3k_B)[s(s+1)] \\ &= 0.125 g^2 [s(s+1)] \text{ emu/Kmol}^{-1} \end{aligned} \tag{3}$$

where N_A is the Avogadro's number, $\mu_B = 9.27 \times 10^{-24}$ JT^{-1} is the Bohr magneton, g is the electron Lande g factor, s is spin and k_B is the Boltzmann's constant. Taking $s = 2$ and $g = 2.0023$, $C = 3.0$ emu/Kmol^{-1} is expected for Fe^{2+} ion. We conclude that the Curie-like term below 30 K is due to $\approx$0.2% of the Fe^{2+} impurities per mol. This value is less than the 0.5% reported for the single crystals in [6].

The Hall coefficient R_H for a specimen of thickness t is given by $R_H = V_H t/IB$, where V_H is the Hall voltage, B is the applied magnetic field and I is the current. Fig. 4 shows V_H plotted as a function of I at B = 9 T for some selected temperatures. The Hall coefficients at different temperatures were calculated from the slope of the linear fit.

Values for free carrier density (n) were estimated from the Hall coefficient measurement using the single band model, $n = 1/R_H\, e$, where e is the electronic charge. Inset of Fig. 5 shows the temperature dependence of the carrier concentration. A thermally activated behavior is observed above 30 K.

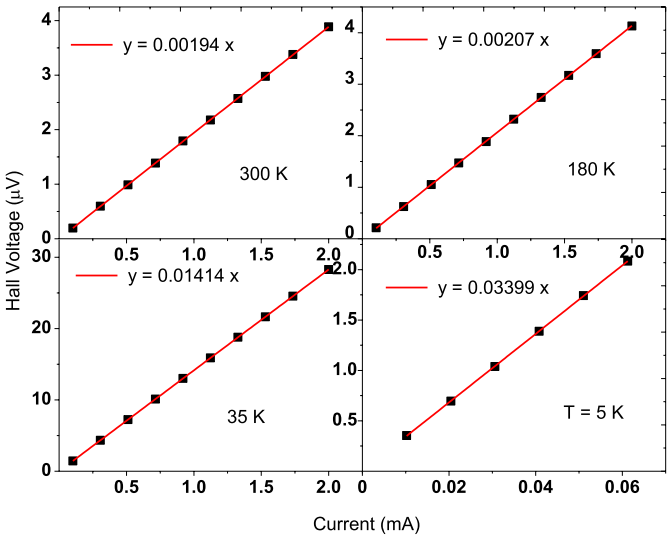

Fig. 4. Transverse Hall voltage as a function of excitation current for temperatures of 300, 180, 35, and 5 K. A magnetic field of 9 T was applied.

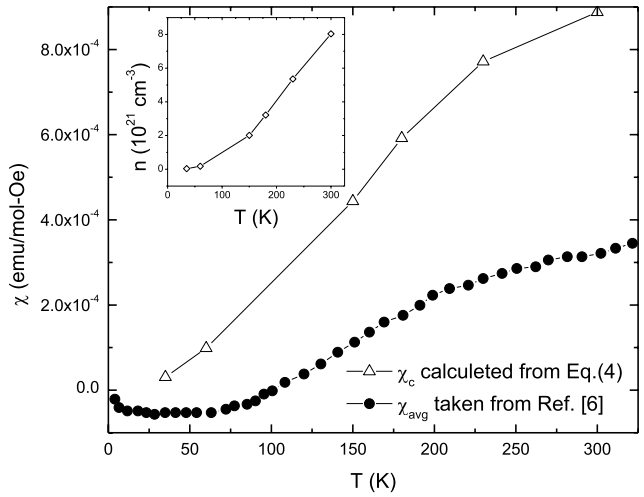

Fig. 5. Magnetic susceptibility as a function of temperature. Open triangles (△) represent the χ_c values calculated using (4) for the nanocomposite sample as a function of temperature. The filled circles (•) represent the polycrystalline average data taken from [6]. Inset: temperature dependence of free carrier concentration obtained from Hall coefficient.

In the region of intrinsic conductivity (>30 K in this case), the magnetic susceptibility due to the free carriers, assuming g factor to be 2 for both electron and holes, can be determined as [13]

$$\chi_c = (n\mu_B^2/3\rho k_B T)[6 - (m/m_n^*)^2 - (m/m_p^*)^2] \qquad (4)$$

where n is the free carrier concentration, ρ is the density, m is the free electron mass and m_n^* (m_p^*) are the effective masses for the electrons (holes). An approximate calculation of χ_c was performed using the n values obtained above and taking $m = m_n^* = m_p^*$ and $\rho = 7.5$ g cm^{-3}. Fig. 5 shows the comparison between χ_c calculated using (4) and $\chi_{avg} = (\chi_a+\chi_b+\chi_c)/3$ taken from [6]. The increased susceptibility for the hot-pressed sample is due possibly to the increased carrier concentration ($\sim 10^{21}$ cm^{-3}) due to lattice and strain defects arising from the ball milling process. For the single crystal

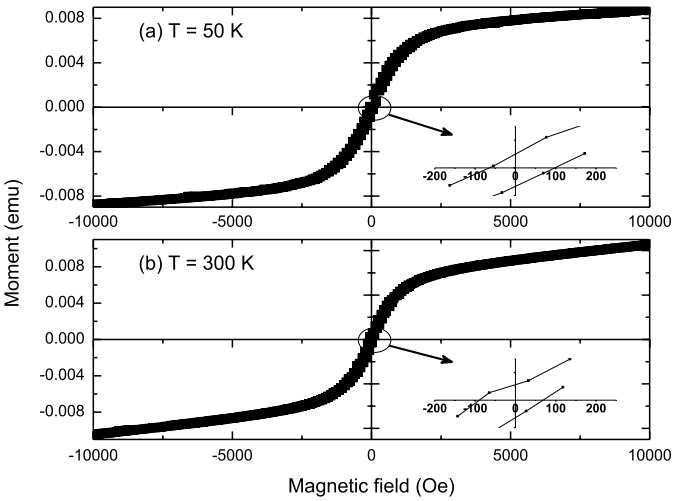

Fig. 6. Magnetic moment of the $FeSb_2$ sample as a function of applied magnetic field at (a) 50 and (b) 300 K. Insets: region around the origin.

samples, carrier concentration values of $\sim 10^{17} - 10^{20}$ cm^{-3} were reported [2], [14].

Fig. 6 shows the field dependence of the magnetization at 50 and 300 K. The magnetization increases with the applied field near the origin, changes slope at a magnetic field of value ~2 kOe and then increases slowly with the increasing field. Presence of a weak ferromagnetism at both the temperatures (50 and 300 K) is evidenced by a narrow hysteresis loop, as observed in Fig. 6. A small coercivity value of ~100 Oe (inset of Fig. 6) is observed at both temperatures. Since pure $FeSb_2$ is paramagnetic at 300 K and diamagnetic at 50 K, a narrow hysteresis loop at both the temperatures with nearly equal value of the coercivities indicates the presence of some neutral ferromagnetic phase. We believe that a small fraction of unreacted iron (Fe) exists as a second phase in our sample. Thus, the magnetic susceptibility is enhanced by a significant constant value, consistent with the large value of χ_0 as mentioned previously. Cullity *et al.* [15] have pointed out the effect of a small amount of ferromagnetic second phase (0.1% of Fe by weight) on the magnetic property of diamagnetic material (Cu). Our data on magnetic moment (m) versus magnetizing field (H) are very consistent with their data. We believe that even small amount of Fe is enough to cause such a dramatic enhancement of the susceptibility. Such a small amount of Fe was not detected from the XRD pattern.

A rough estimation of the contribution from ferromagnetic Fe phase (χ_{Fe}) can be made calculating the susceptibility at 0.1 T from m–H curves. $\chi_{Fe} \approx 1.05 \times 10^{-2}$ emu/mol^{-1} at both temperatures (50 and 300 K). This value of χ_{Fe} is in close agreement with the value of χ_0 obtained from fitting of the Curie–Weiss law. Also the similar values of χ_{Fe} at both the temperatures are consistent with the temperature independent nature of χ_0.

Finally, we emphasize that contribution from the impurities varies among the samples. Therefore, it is understandable that sample dependence of the measured values of the involved physical quantities might have played a role. Also, the

calculation was made based on one-band model. Usually, in a narrow gap semiconductor like $FeSb_2$, two types of carriers are involved. Nevertheless, this simple model explains the observed magnetic susceptibility reasonably well. This paper, in addition to providing data on magnetic properties of polycrystalline $FeSb_2$, also provides a demonstration of how a small amount of neutral ferromagnetic phase masks the true magnetic behavior of a material. We believe that this paper will help researchers to further understand the magnetic behavior of $FeSb_2$. More specifically, combining magnetic properties with thermoelectric transport properties of nanostructured $FeSb_2$ might help understand the origin of large Seebeck coefficient, which will eventually help setup future direction to improve thermoelectric performance of this system.

IV. Conclusion

To summarize, we studied the magnetization in the $FeSb_2$ hot-pressed sample. A significant value of $\sim 10^{-2}$ emu/mol^{-1} for the temperature-independent magnetic susceptibility is observed. A Curie type of behavior below 30 K corresponded to 0.2% Fe^{2+} impurities per mole. The susceptibility above 30 K can be understood as a consequence of the thermally activated behavior of the free carrier concentration. The presence of a weak ferromagnetic interaction is evidenced by the small value of coercivity of $\sim$100 Oe. While the enhanced magnetic susceptibility comes mainly from the moment of unreacted Fe, contribution from the enhanced carrier density due to lattice and strain defects arising from ball milling process is also significant.

Acknowledgment

This work was supported by the Department of Defense, U.S. Air Force Office of Scientific Research MURI Program under Contract FA9550-10-1-0533. C. Opeil would like to thank J. C. Lashley for technical assistance and T. Hoeler for a careful review of the manuscript.

References

[1] H. Holseth, A. Kjekshus, S. E. Harnung, H. Lundström, G. Borch, and J. Cymerman Craig, "Compounds with the marcasite type crystal structure. IV. The crystal structure of $FeSb_2$," *Acta Chem. Scandinavica*, vol. 23, no. 1, pp. 3043–3050, 1969.

[2] A. K. L. Fan, G. H. Rosenthal, H. L. McKinzie, and A. J. Wold, "Preparation and properties of $FeAs_2$ and $FeSb_2$," *J. Solid State Chem.*, vol. 5, no. 1, pp. 136–143, 1972.

[3] J. Steger and E. Kostiner, "Mössbauer effect study of $FeSb_2$," *J. Solid State Chem.*, vol. 5, no. 1, pp. 131–135, 1972.

[4] N. H. Abrikosov and L. I. Pterova, "The polythermal cross section $FeSb_2$-$FeTe_2$ of the Fe-Sb-Te system," *Inorg. Mater.*, vol. 25, no. 8, pp. 1–13, 1989.

[5] C. E. T. Gonçalves da Silva, "Magnetic susceptibility of $FeSb_2$: A quasi-magnetic semiconductor," *Solid State Commun.*, vol. 33, no. 1, pp. 63–68, 1980.

[6] C. Petrovic, J. W. Kim, S. L. Bud'ko, A. I. Goldman, and P. C. Canfield, "Anisotropy and large magnetoresistance in the narrow-gap semiconductor $FeSb_2$," *Phys. Rev. B*, vol. 67, no. 15, pp. 155205-1–155205-4, 2003.

[7] R. Hu, V. F. Mitrovic, and C. Petrovic, "Anisotropy in the magnetic and transport properties of $Fe_{1-x}Co_xSb_2$," *Phys. Rev. B*, vol. 74, no. 19, pp. 195130-1–195130-6, 2006.

[8] C. Petrovic, Y. Lee, T. Vogt, N. D. Lazarov, S. L. Bud'ko, and P. C. Canfield, "Prediction of anomalous diffusion and algebraic relaxations for long-range interacting systems, using classical statistical mechanics," *Phys. Rev. B*, vol. 72, no. 4, pp. 045103-1–045103-4, 2005.

[9] T. Koyama, H. Nakamura, T. Kohara, and Y. Takahashi, "Magnetization process of narrow-gap semiconductor $FeSb_2$," *J. Phys. Soc. Jpn.*, vol. 79, no. 9, pp. 093704-1–093704-4, 2010.

[10] K. Koyama, T. Goto, T. Konomata, R. Note, and Y. Takahashi, "Nonlinear magnetization process of single-crystalline FeSi," *J. Phys. Soc. Jpn.*, vol. 69, pp. 219–224, Feb. 2009.

[11] H. Zhao, M. Pokharel, G. Zhu, S. Chen, K. Lukas, Q. Jie, *et al.*, "Dramatic thermal conductivity reduction by nanostructures for large increase in thermoelectric figure-of-merit of $FeSb_2$," *Appl. Phys. Lett.*, vol. 99, no. 16, pp. 163101-1–163101-4, 2011.

[12] P. Sun, N. Oeschler, S. Johnsen, B. B. Iversen, and F. Steglich, "Narrow band gap and enhanced thermoelectricity in $FeSb_2$," *Dalton Trans.*, vol. 39, pp. 1012–1019, Dec. 2010.

[13] E. Arushanov, M. Respaud, J. M. Broto, J. Leotin, S. Askenazy, C. Kloc, E. Bucher, and K. Lisunov, "Band parameters of FeSi single crystals determined by magnetic measurements," *Phys. Rev. B*, vol. 55, no. 9, pp. 1–13 1997.

[14] R. Hu, V. F. Mitrovic, and C. Petrovic, *Appl. Phys. Lett.* vol. 92, no. 1, pp. 182108-1–182108-3, 2008.

[15] B. D. Cullity, and C. D. Graham, "Chapter 3: Diamagnetism and paramagnetism," *Introduction to Magnetic Materials*, 2nd ed. New York, NY, USA: Wiley, pp. 1–112, 1972.

International Journal of Thermal Sciences 71 (2013) 32–35

Contents lists available at SciVerse ScienceDirect

International Journal of Thermal Sciences

journal homepage: www.elsevier.com/locate/ijts

Grain boundary Kapitza resistance analysis of nanostructured $FeSb_2$

Mani Pokharel [a,*], Huaizhou Zhao [b], Zhifeng Ren [b], Cyril Opeil [a,*]

[a] Department of Physics, Boston College, Chestnut Hill, MA 02467, USA
[b] Department of Physics and TcSUH, University of Houston, Houston, TX 77204 ,USA

ARTICLE INFO

Article history:
Received 23 August 2012
Received in revised form
23 January 2013
Accepted 17 March 2013
Available online 24 April 2013

Keywords:
Kapitza resistance
Iron diantimonide
Thermal conductivity

ABSTRACT

We apply the effective medium approach model to determine the Kapitza resistance across the grain boundaries of nanostructured $FeSb_2$ samples. A Kapitza resistance of 2.17×10^{-7} $m^2K\ W^{-1}$ at 10 K is observed. The results suggest a competition between the bulk thermal resistance and the Kapitza resistance. The suppression and peak shifting of the thermal conductivity to a higher temperature are caused by the large Kapitza resistance due to the decreasing grain-size in the nanocomposite. A large value of Kapitza length (L_k) of 390 nm at 10 K is also observed. Based on the results, it is proposed that nanostructuring could be a viable approach to improve thermoelectric properties of $FeSb_2$.

1. Introduction

$FeSb_2$ had been one of the well-studied compounds in the past few decades because of its unusual electronic and magnetic properties [2–7]. In the past few years, this compound has gained considerable interest as a promising candidate for Peltier cooling applications at cryogenic temperatures. The renewed interest on this compound comes after Bentien et al. [8] reported a colossal value of Seebeck coefficient at ~10 K for single crystal samples. The authors therein suggested that the huge Seebeck coefficient is a consequence of the strong electronic correlations. This explanation was further supported by Sun et al. [9]. There have also been extensive studies on thermoelectric properties of doped $FeSb_2$ single crystal samples [10–14]. Undoped single crystal of $FeSb_2$ exhibits a very high thermal conductivity at low temperature which reaches as high as 500 $Wm^{-1}\ K^{-1}$ at ~10 K [7]. Such a huge thermal conductivity limits the thermoelectric efficiency far below the value required for practical applications. A better understanding of thermal properties of $FeSb_2$ would help to find a more effective technique to reduce the thermal conductivity so that the thermoelectric performance can be improved.

Our earlier work [1] showed that $FeSb_2$ exhibits a strong grain size dependent thermal conductivity at low temperatures. The model usually proposed to understand the grain size dependence of the thermal conductivity is the relaxation time approach of boundary scattering based on the Klemens–Callaway theory [15,16]. This is a microscopic model and takes into account various scattering mechanisms involved in the heat conduction. Another simple model for thermal conductivity of polycrystals without going into the microscopic details is based on the combination of Kapitza resistance [17,18] and the effective medium approximation (EMA) [19,20]. In an effective medium approach, the total thermal conductivity of a polycrystal is the sum of the intra-grain and the inter-grain contributions [21]. The inter-grain component arises due to the interfacial resistance, also known as the Kapitza resistance, to the thermal transport. In the presence of thermal gradient, the Kapitza resistance results in a temperature discontinuity across the interface which was first observed by Kapitza [17]. The overall effect of the Kapitza resistance is to reduce the thermal conductivity and the effect is more pronounced at smaller grain sizes. Based on the Kapitza resistance-EMA model, Nan et al. [22] showed that for an isotropic polycrystalline solid made up of spherical grains of equal size, the effective thermal conductivity (κ) is given by,

$$\kappa(T,d) = \kappa_i/[1 + (2R_k\kappa_i/d)] \quad (1)$$

where κ_i is the intrinsic (or bulk) thermal conductivity, R_k is the Kapitza resistance and d is the grain size. Here κ_i is grain-size independent but is temperature dependent while $L_k = R_k\kappa_i$ and $G_k = 1/R_k$ are called the Kapitza length and Kapitza conductance, respectively. Here L_k represents the distance over which the temperature drop is the same as at the interface and its magnitude measures the relative importance of the Kapitza conductance.

* Corresponding authors.
E-mail addresses: pokharem@bc.edu (M. Pokharel), opeil@bc.edu (C. Opeil).

1290-0729/$ – see front matter © 2013 Elsevier Masson SAS. All rights reserved.
http://dx.doi.org/10.1016/j.ijthermalsci.2013.03.009

When the grain size in nanocomposites becomes comparable to L_k, interfaces will predominantly determine the overall thermal conductance [23]. So, to predict the thermal properties of the nanocomposites it is important to develop an understanding of the interfacial thermal conductance.

The systematic study of Kapitza-resistance for a nanostructured samples is rarely found in the literature. On the other hand, thermal conductivity of nanostructured samples is of quite general interest because of their practical applications both in thermoelectric power generation and thermoelectric refrigeration. In this paper, we apply the Kapitza resistance-EMA model to the $FeSb_2$ nanocomposites. By calculating the Kapitza resistance from the grain size-dependence of the total thermal conductivity, we show that the grain boundary scattering is the dominant scattering mechanism at low temperature. We also show that the change in the temperature profile of the thermal conductivity with the grain size can be interpreted as a consequence of the competition between the bulk thermal resistance and Kapitza resistance.

2. Experimental

Nanostructured $FeSb_2$ samples were synthesized as reported in Ref. [1]. The stoichiometric amounts of Fe and Sb were taken inside an evacuated quartz tube. The mixture was then melted at 1050 °C and then quenched in water. The ingot was ball milled to obtain $FeSb_2$ nanopowder. The powder was then hot pressed at 80 MPa for 2 min to obtain the nanocomposite (NC) samples. Different grain sizes were introduced by varying the ball-milling time and pressing temperature. The disk samples were then characterized by X-ray diffraction (XRD, BrukerAXS) for the phase identification. An average grain size was estimated from the scanning electron microscopy (SEM, JEOL 6340F) images. Density of the samples was determined using the Archimedes method. The codes, average grain sizes and the corresponding processing parameters for five different samples are given in Table 1.

To ensure better contacts, the sample disks were sputtered with the three consecutive layers of Ti, Ni and Au. The sputtered disks were then cut to obtain a bar-shaped sample. The typical dimension of the sample was $3 \times 3 \times 4$ mm^3. The gold plated copper-disks were soldered at the sputtered ends of the sample. The thermal conductivity (κ) from 5 to 300 K was measured on a Physical Property Measurement System (PPMS) from Quantum Design. The normal 2-point method of the thermal transport option (TTO) was used.

3. Results and discussions

Fig. 1 shows the SEM images of the five samples. The average grain size ranges from 20 nm to 5000 nm.

Fig. 2 shows the temperature dependence of the thermal conductivity for the five samples. Assuming that the Wiedemann–Franz law, $\kappa_e = L_0\sigma T$, holds, the lattice contribution (κ_l) to κ was calculated based on the independent approximation, $\kappa = \kappa_e + \kappa_l$. Here σ is the electrical conductivity and T is the absolute temperature. $\sigma = 1/\rho$ was used to calculate σ. The resistivity for all the samples was of the order of 10^{-4} Ω-m below 50 K [1]. The value of the Lorenz number for the free electron gas, $L_0 = 2.45 \times 10^{-8}$ WΩ K^{-2}, was taken in the calculation. For all the samples, more than 97% of the total thermal conductivity comes from the lattice portion below 50 K. As the grain size decreases, the peak in the thermal conductivity curve, which is characteristic of the crystalline solid, becomes less pronounced. For the sample S-20 the peak disappears completely. This is an indication that the crystallinity of the sample degrades as the system becomes more and more disordered with decreasing grain size. Another important feature of the thermal conductivity curves is the shift of the peaks to higher temperature with decreasing grain size. For example κ_{max} occurs at 50 K, 69 K and 95 K for samples S-5000, S-300 and S-100, respectively.

The inset of Fig. 2 shows the thermal conductivity at different temperatures as a function of grain size. From 10 K to 50 K, the grain-size dependence becomes increasingly strong and at 100 K, it becomes weaker. This suggests that the grain-boundary scattering is appreciable below 50 K in this system and becomes small as the temperature increases. For a given temperature, the grain size-dependence is stronger below 300 nm whereas it is weaker above that size. Here we note that these curves roughly follow the trend predicted by Volckmann et al. [24].

From the best-fit lines of the experimental data in κ^{-1} vs. d^{-1} plots predicted by Eq. (1), the values of R_k and G_k for the samples were determined. As seen in Fig. 3, the data fits reasonably well for smaller grain sizes. A deviation from the linearity was observed in the data at the largest grain size as one might expect for the Kapitza resistance-EMA model since it is optimized for application at small grain sizes. Those points corresponding to the largest grain size were excluded during fitting process. At this point we also note that the sample porosity may also affect the linearity. As the temperature decreases, the trend becomes more linear. This suggests that the Kapitza resistance-EMA model in $FeSb_2$ system is more valid at low temperatures. With decreasing temperature, the slope of the linear fit increases monotonically. So the Kapitza resistance increases as temperature decreases.

Fig. 4 represents the temperature dependence of the Kapitza resistance (R_k) and the Kapitza conductance (G_k). The bulk thermal resistances for the five samples are also plotted for comparison. R_k has a weak temperature dependence from 300 K down to 50 K and increases sharply below 50 K. Fitting to the power law shows that $R_k \approx 4.0 \times 10^{-6} T^{-1.27}$. This is consistent with the fact that the *in situ* Kapitza resistance is expected to follow $R_k \sim T^{-\alpha}$, where $\alpha > 0$ [25]. $R_k = 5.83 \times 10^{-9}$ m^{2}K W^{-1} and 2.68×10^{-8} m^{2}K W^{-1}, respectively, at 300 K and 50 K were observed whereas at 10 K, R_k reaches a value as high as 2.17×10^{-7} m^{2}K W^{-1}. From a microscopic point of view this is understandable because at low temperature, the diffusive scattering of phonons off the grain boundary is the dominant scattering mechanism and it becomes weak at higher temperature where other mechanisms like three phonon–phonon process and Umklapp-process become more important. We note the significant value of the Kapitza resistance in this system. For SiGe alloys, Nan. et al. [22] reported $R_k = 1.1 \times 10^{-7}$ to 4.98×10^{-8} m^{2}K W^{-1} values at room temperature. Whereas for nanocrystalline yttria-stabilized zirconia (YSZ), which exhibits a strong grain-size dependence of the thermal conductivity, values for R_k of the order of 10^{-8} m^{2}K W^{-1} at low temperature was reported by Yang et al. [26].

As seen in Fig. 4, the Kapitza conductance initially increases with increasing temperature and then becomes less sensitive to temperature between 100 and 200 K. Below 200 K, G_k follows roughly the same trend as the specific heat capacity (C_p) does in Ref. [10]. In fact, G_k is expected to be proportional to C_p [26]. This indicates that despite the sample porosity, the error in estimating the grain size

Table 1
Assigned codes, processing parameters, average grain-size and density for the five samples.

Sample codes	Ball milling time (hours)	Press temperature (°C)	Average grain size (nm)	Density (% of single crystal)
S-5000	1/6	400	5000	95.2
S-300	1	400	300	96.3
S-100	15	400	100	97.7
S-30	15	300	30	85.6
S-20	15	200	20	77.2

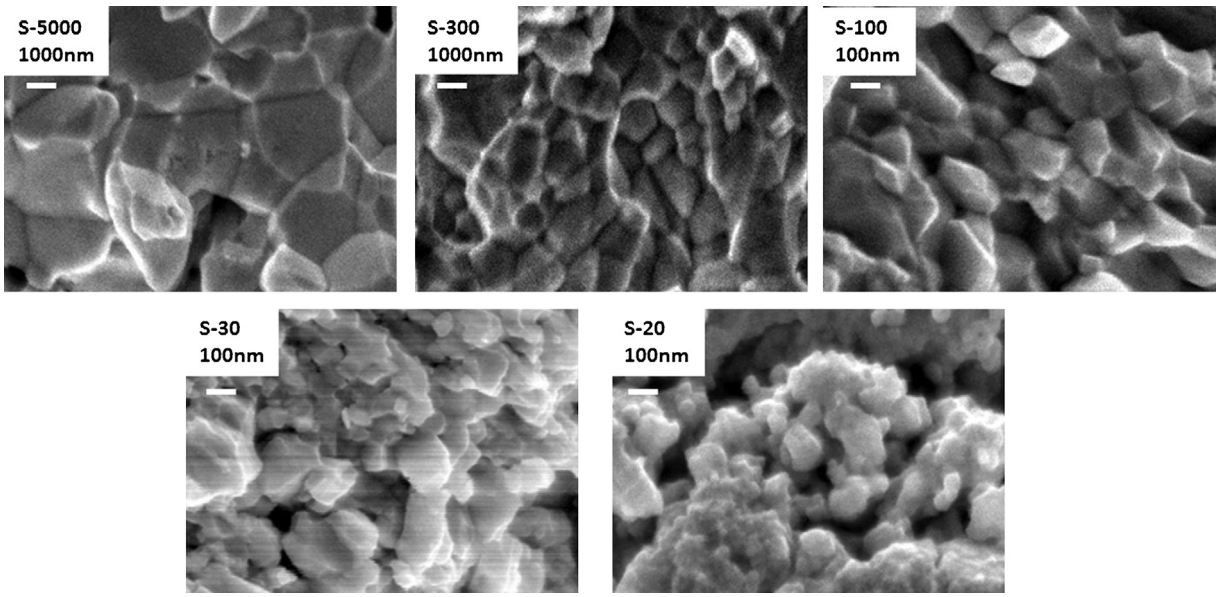

Fig. 1. SEM micrographs of the five nanocomposite samples used in this study. The images for the samples S-5000 and S-300 are taken with a magnification of 30,000 whereas the magnification for images for the samples S-100, S-30 and S-20 is 60,000.

and the other assumptions that are made, calculations based on this simple Kapitza resistance-EMA model for $FeSb_2$ nanocomposite samples are justified. The minimum value of the Kapitza length was observed at room temperature, where $L_k = R_k\kappa_i \approx 38$ nm. At low temperature, L_k increases reaching a value of 390 nm at 10 K. This large value of L_k at low temperature implies a relatively weak interfacial conductance which is consistent with the observed thermal conductivity.

The calculated values for κ_i were found to be much smaller compared to that of the single crystal. For example, at 50 K, $\kappa_i = 5.94\ Wm^{-1}\ K^{-1}$. Reduced values of κ_i were also observed by Nan et al. [22] in Bi_2Te_3/Sb_2Te_3 alloys and they attributed the reduced values of κ_i to the effect of porosity.

The open symbols in Fig. 4 represent the bulk thermal resistance (d/κ_i) for these five samples. For samples S-20 and S-30, the Kapitza resistance is dominant over the bulk thermal resistance from 5 to 300 K, whereas for S-100 a crossover is observed at around 200 K. On the other hand, for S-300 and S-5000, the bulk thermal resistances are dominant throughout. This explains the two important features of the thermal conductivity curves that are seen from Fig. 2. (i)For the large grain size, the contribution of the bulk is dominant and the thermal conductivity curve is similar to its single crystal counterpart with a pronounced peak. As the grain size goes down the Kapitza resistance becomes stronger thereby reducing the bulk nature of the curve and at the smallest grain size, the Kapitza resistance dominates over the bulk part completely. (ii) The crossover between the two resistance curves occurs at higher temperature as the grain size gets smaller. This is why the thermal conductivity peaks shift to higher temperature as the grain size decreases.

For $FeSb_2$, an electron mean free path on the order of few nm is reported in the literature [9]. Using that assumption for electron mean free path, one does not expect much change in electronic properties (Seebeck coefficient and electrical conductivity) as crystal size is altered. However our previous work [1] showed that

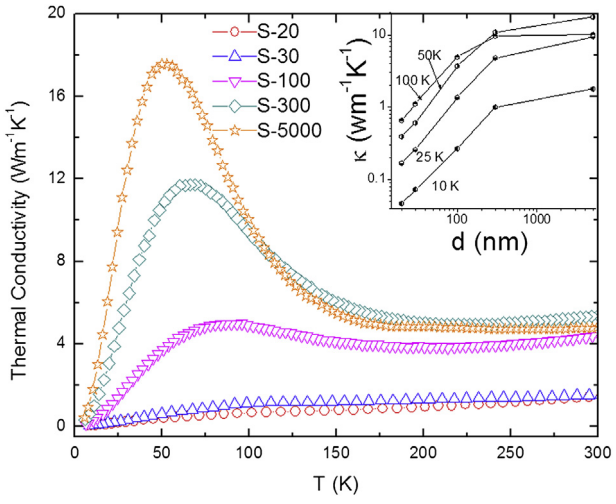

Fig. 2. Temperature dependence of the thermal conductivity of the samples. Inset: Grain-size dependence of the thermal conductivity at 10, 25, 50 and 100 K.

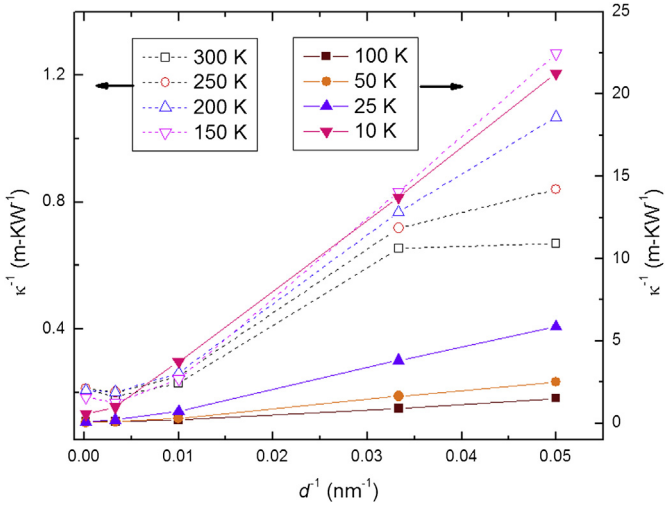

Fig. 3. κ^{-1} plotted versus d^{-1}. The open symbols with the dashed lines and the closed symbols with solid lines correspond to the left and right *Y*-axes respectively. The first point from the left was excluded during the fitting process.

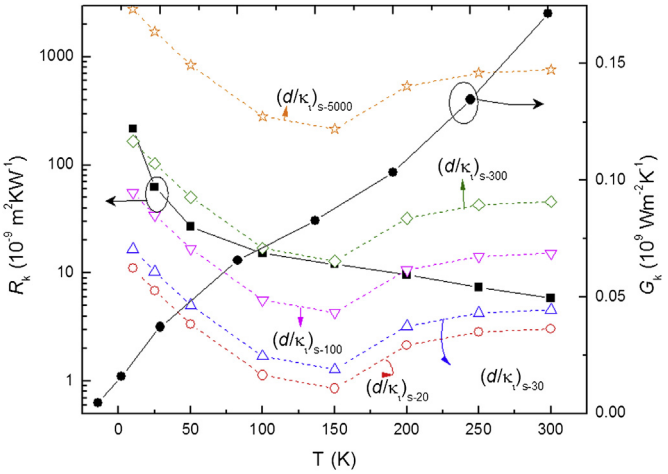

Fig. 4. Temperature dependence of the Kapitza resistance (R_k) and Kapitza conductance (G_k) obtained from the best fit to Eq. (1). R_k and G_k values are represented by left and right *Y*-axes, respectively. The open symbols with dashed lines represent the temperature dependence of the bulk thermal resistance (d/κ_i) as indicated by the left *Y*-axis for the five samples. (Stars: (d/κ_i) for S-5000, Diamonds: (d/κ_i) for S-300, down-pointed triangles: (d/κ_i) for S-100, up-pointed triangles: (d/κ_i) for S-30, open-circles: (d/κ_i) for S-20, filled circles: G_k as a function of temperature, filled squares: R_k as a function of temperature).

the absolute value of Seebeck coefficient decreased significantly with decreasing grain size whereas the electrical conductivity was not affected that much. Therefore, the thermoelectric figure of merit (*ZT*) enhancement was solely attributed to the thermal conductivity reduction.

Finally, mechanical nanostructuring is very effective to reduce thermal conductivity, as indicated by a large value of Kapitza length (L_k), of $FeSb_2$. On the other hand doping has been shown to be able to reduce thermal conductivity keeping relatively large value of Seebeck coefficient [12]. However, the thermal conductivity reduction through nanostructuring looks to be much more effective than point defect scattering approach used in doped samples. Based on this, we suggest that nanostructuring combined with some other technique like doping at the intermediate grain size level could be the viable approach to improve *ZT* of this material.

4. Conclusions

Calculations based on the Kapitza resistance-EMA model for $FeSb_2$ nanocomposite samples show a strong grain-size dependence of the thermal conductivity at low temperature with a significantly large value of the Kapitza resistance. The Kapitza resistance was found to be the predominating factor in determining the bulk thermal properties below 50 K. For coarse-grained samples, the bulk thermal resistance dominates over the Kapitza resistance values. As the grain size decreases the Kapitza resistance becomes more important. A large value of the Kapitza length at low temperature is observed. Our results suggest that the interfacial thermal resistance across the grain boundaries plays a significant role in determining the thermal transport properties of $FeSb_2$ at low temperature. It can also be inferred that nanostructuring could be a viable approach to improve thermoelectric performance of this system taking advantage of an increased Seebeck coefficient at low temperature.

Acknowledgments

The authors would like to thank M. S. Dresselhaus and P. S. Riseborough for helpful discussions and comments on the manuscript. C.O. acknowledges financial support from the Trustees of Boston College. We gratefully acknowledge funding for this work by the Department of Defense, United States Air Force Office of Scientific Research, Multi-University Research Initiative (MURI) Program under Contract # FA9550-10-1-0533.

References

[1] H. Zhao, M. Pokharel, G. Zhu, S. Chen, K. Lukas, Q. Jie, C. Opeil, G. Chen, Z. Ren, Appl. Phys. Lett. 99 (2011) 163101.
[2] H. Holseth, A. Kjekshus, Acta Chem. Scand. 23 (1969) 3043.
[3] A.K.L. Fan, G.H. Rosenthal, H.L. McKinzie, A. Wold, J. Solid State Chem. 5 (1972) 136.
[4] J. Steger, E. Kostiner, J. Solid State Chem. 5 (1972) 131.
[5] C. Petrovic, J.W. Kim, S.L. Bud'ko, A.I. Goldman, P.C. Canfield, Phys. Rev. B 67 (2003) 155205.
[6] N.H. Abrikosov, L.I. Pterova, Inorg. Mater. 25 (1989) 8.
[7] C.E.T. Gonçalves da Silva, Solid State Commun. 33 (1980) 63–68.
[8] A. Bentien, S. Johnson, G.K.H. Madsen, B.B. Iversen, F. Steglich, Europhys. Lett. 80 (2007) 17008.
[9] P. Sun, N. Oeschler, S. Johnsen, B.B. Iversen, F. Steglich, Phys. Rev. B 79 (15) (2009) 153308.
[10] P. Sun, N. Oeschler, S. Johnsen, B.B. Iversen, F. Steglich, Dalton Trans. 39 (2010) 1012–1019.
[11] A. Bentien, G.K.H. Madsen, S. Johnson, B.B. Iversen, Phys. Rev. B 74 (20) (2006) 205105.
[12] P. Sun, M. Søndergaard, Y. Sun, S. Johnsen, B.B. Iversen, F. Steglich, Appl. Phys. Lett. 98 (2011) 072105.
[13] H. Takahashi, R. Okazaki, Y. Yasui, I. Terasaki, Phys. Rev. B 84 (2011) 205215.
[14] J.M. Tomczak, K. Haule, T. Miyake, A. Georges, G. Kotliar1, Phys. Rev. B 82 (2010) 085104.
[15] P.G. Klemens, Proc. Phys. Soc. London, Sect. A 68 (1955) 1113.
[16] J. Callaway, Phys. Rev. 113 (1959) 1046.
[17] P.L. Kapitza, J. Phys. (Moscow) 4 (1941) 181.
[18] E.T. Swartz, R.O. Pohl, Rev. Mod. Phys. 61 (1989) 605.
[19] D.A.G. Bruggeman, Ann. Phys. (Leipzig) 24 (1935) 636.
[20] R. Landauer, J. Appl. Phys. 23 (1952) 779.
[21] T.S. English, J.L. Smoyer, J.C. Duda, P.M. Norris, T.E. Beechem, P.E. Hopkins, Proceedings of the ASME/JSME Thermal Engineering Joint Conference AJTEC2011, March 13–17, 2011. Honolulu, Hawaii, USA.
[22] C. Nan, R. Barringer, Phys. Rev. B 57 (1998) 8263.
[23] M. Hu, P. Keblinski, P.K. Schelling, Phys. Rev. B 79 (2009) 104305.
[24] E.H. Volckmann, H.J. Goldsmid, J. Sharp, 15th International Conference on Thermoelectrics (1996).
[25] J. Amrit, J. Phys. D Appl. Phys. 39 (2006) 4472.
[26] H. Yang, G.R. Bai, L.J. Thompson, J.A. Eastman, Acta Mater. 50 (2002) 2309–2317.

Figure-of-merit enhancement in nanostructured $FeSb_{2-x}Ag_x$ with $Ag_{1-y}Sb_y$ nanoinclusions

2012 Nanotechnology 23 505402

(http://iopscience.iop.org/0957-4484/23/50/505402)

Nanotechnology **23** (2012) 505402 (7pp) doi:10.1088/0957-4484/23/50/505402

Figure-of-merit enhancement in nanostructured $FeSb_{2-x}Ag_x$ with $Ag_{1-y}Sb_y$ nanoinclusions

Huaizhou Zhao[1,3], Mani Pokharel[1,3], Shuo Chen[1], Bolin Liao[2], Kevin Lukas[1], Cyril Opeil[1], Gang Chen[2] and Zhifeng Ren[1]

[1] Department of Physics, Boston College, Chestnut Hill, MA 02467, USA
[2] Department of Mechanical Engineering, Massachusetts Institute of Technology, Cambridge, MA 02139, USA

E-mail: zhifeng.ren@bc.edu

Received 27 August 2012, in final form 28 October 2012
Published 29 November 2012
Online at stacks.iop.org/Nano/23/505402

Abstract

We present the figure-of-merit (ZT) improvement in nanostructured $FeSb_{2-x}Ag_x$ with $Ag_{1-y}Sb_y$ nanoinclusions through a metal/semiconductor interface engineering approach. Owing to the interfaces between $FeSb_{2-x}Ag_x$ and $Ag_{1-y}Sb_y$ phases, as well as the identical work functions, both thermal conductivity and electrical resistivity of the nanocomposites were significantly reduced in the lower temperature regime compared with pure $FeSb_2$. Overall, an improvement of 70% in ZT was achieved for the optimized nanocomposite $FeSb_{1.975}Ag_{0.025}/Ag_{0.77}Sb_{0.23}$ sample, in which $Ag_{0.77}Sb_{0.23}$ is about 10% by molar ratio. The results of this approach clearly demonstrated the metal/semiconductor interface concept and confirmed the potential of strongly correlated material systems as promising thermoelectric materials.

(Some figures may appear in colour only in the online journal)

1. Introduction

As one of the promising technologies in waste-heat recovery and cooling applications, solid-state conversion between heat and electrical power using thermoelectric materials has stimulated enormous efforts and enthusiasm in the last decade. The figure of merit (ZT) of thermoelectric materials, determining the conversion efficiency, has almost been doubled in the last couple of years in a few traditional materials. It is well known that $ZT = (s^2\sigma/\kappa)T$, where S, σ, κ, and T are the Seebeck coefficient, electrical conductivity, thermal conductivity, and absolute temperature, respectively. The competitive nature of these components makes it difficult to enhance the ZT by adjusting any of the individual properties without affecting others. The currently developed approaches, such as nanostructures reducing lattice thermal conductivity [1–4], resonant doping [5–7], band engineering [8, 9] at the Fermi level, as well as modulation doping providing additional electrical conductivity channels [10, 11], have been proved to be efficient in a few material systems. In the literature, the metal/semiconductor interface concept was proposed theoretically and testified experimentally in a few cases for their potential application in thermoelectric materials [12–17]. Indeed, modeling shows that, by introducing uniformly distributed metal nanoparticles to the three-dimensional semiconductor structure, either electronic (κ_e) or phononic (κ_{ph}) thermal conductivity, and thus $\kappa_{total} = \kappa_e + \kappa_{ph}$, can be suppressed dramatically [14]. Furthermore, due to the energy barrier (V_B) built between metal nanoparticles and the host semiconductor at the interfaces, the lower energy carrier could be scattered, which would result in a reduced electrical conductivity but an enhanced Seebeck coefficient. As a result, the power factor ($PF = s^2\sigma$) could be enhanced and an enhanced ZT could be expected. However, for a phononic (κ_{ph}) thermal conductivity dominated system, the modeling showed that a much smaller V_B than 0.03 eV is preferred to secure an even slightly enhanced PF [14], and zero energy barriers at the interface would be expected in the real case

[3] These authors contributed equally to this work.

even though there is no net gain on *PF*. Overall, for a phononic (κ_{ph}) thermal conductivity dominated system, the enhanced *ZT* could be expected solely from the reduced thermal conductivity through the metal/semiconductor nanocomposite approach. In reality, due to the difficulty matching the semiconductor with the right metals, there has been no convincing demonstration of this concept.

Low temperature thermoelectric materials are usually semimetals or narrow bandgap semiconductors [18]. Correlated material and Kondo systems, such as CeB_6 [19], $YbAl_3$ [20], FeSi [21], and $FeSb_2$ [22–28], are promising thermoelectric materials for cryogenic cooling applications, although their *ZT* values are still too low to be considered for real use at this point. Among them, $FeSb_2$ shows extraordinary large *S* and *PF* despite the variations in its magnitude reported and the arguments of the physical origin of such a high *S* [22, 26, 28]. Doping and nanostructures have been adopted in efforts to reduce its phonon dominated thermal conductivity while trying to maintain the high *S* [4, 24, 25]. Although improvements have been achieved in $FeSb_2$ nanocomposite and Te-doped single crystals, further progress seems elusive because of the extreme sensitivity of the Seebeck coefficient to its electron carrier concentrations and the difficulty in further suppressing the thermal conductivity.

In this report, based on the identical work functions at certain crystal faces for $FeSb_2$ and Ag, we have found that Ag might be the matched metal phase to fabricate the metal/semiconductor interface for $FeSb_2$. We designed three-dimensional metal/semiconductor interfaces by adding Ag nanoparticles to form $Ag_{1-y}Sb_y$ nanoparticles in nanostructured $FeSb_{2-x}Ag_x$. Resulting from the chemical reaction between Ag and Sb, a nanocomposite of $FeSb_{1.975}Ag_{0.025}$ with 10% $Ag_{0.77}Sb_{0.23}$ by molar ratio was created and demonstrated to have much enhanced *ZT*, a 70% improvement, in comparison with the pure nanostructured $FeSb_2$. This result exemplified the possible demonstration of the concept of a metal/semiconductor interface in thermoelectric material systems. The same approach can also be extended to other strongly correlated materials or Kondo systems for thermoelectric properties enhancement.

2. Experiments and methods

The $FeSb_{2-x}Ag_x/Ag_{1-y}Sb_y$ nanocomposites were synthesized by the following procedure. First, $FeSb_2$ nanopowder was synthesized through high temperature melting and quenching, followed by 12 h ball milling as we reported before [4]. Then various numbers of Ag nanoparticles (NPs) (100 nm, Aldrich) were added to the synthesized $FeSb_2$ powders with the targeted final nominal composition $FeSb_2Ag_m$ with $m = 0.028, 0.056, 0.11, 0.22$, and 0.33. Together with the $FeSb_2$ nanopowder, each individual composition having the weight of 5 g was further mixed via ball milling for 3 h. The direct current (dc) hot pressing method was used to prepare disk samples from the final powders with different compositions. All disk samples were pressed at 200 °C and 80 MPa for 2 min, resulting densities in the range of 5.91–6.01 g cm^{-3}, about 76.8%–78.1% of the theoretical densities of 7.70 g cm^{-3}.

The final hot pressed products were characterized by x-ray diffraction (XRD, Bruker AXS) for phase identification, scanning electron microscopy (SEM, JEOL 6340F) for texturing and grain size distributions, and transmission electron microscopy (TEM) and scanning transmission electron microscopy (STEM) (JEOL 2010F, which is equipped with both TEM and STEM mode) for detailed structures of the optimized nanocomposite sample with nominal composition $FeSb_2Ag_{0.11}$. The STEM samples were prepared as follows: a small piece of disk sample was gently hand ground, and the obtained suspension was dipped onto a typical carbon-coated Cu grid, which can be used for STEM observation after drying. The edge area of the grains was selected for observations.

The temperature dependent electrical resistivity (ρ), Seebeck coefficient (*S*), thermal conductivity (κ), and Hall coefficient (R_H) were measured on a Physical Property Measurement System (PPMS) from Quantum Design using the thermal transport option (TTO). Gold leads were soldered onto samples with dimensions $3 \times 3 \times 5$ mm^3. The Seebeck coefficient, thermal conductivity and electrical resistivity were measured on a bar sample of dimensions $3 \times 3 \times 5$ mm^3. The normal two-point TTO option of the PPMS was used. As a check, the thermal and electrical conductivities for the sample $FeSb_2$ were measured in both two-point and four-point configurations. The values from the two configurations agreed well within the experimental error, showing negligible effect of the contact resistances. A piece with dimensions $1 \times 3 \times 10$ mm^3 was cut out of the same disk for Hall coefficient measurement. All the properties were measured in the direction perpendicular to the hot pressing direction.

The Hall coefficient $R_H(T)$ was determined under a magnetic field 9 T and a current of 20 mA. Five platinum wires were spark welded onto the Hall sample, and for the four-point resistivity measurement one of the wires was left unconnected. Within the one-band model, the charge carrier concentration was determined by $n = 1/(e|R_H|)$. The Hall mobility was determined by $\mu_H = |R_H|/\rho$. The Hall effect $R_H(T)$ measurements were performed on all samples.

To investigate the property of the metal/semiconductor interfaces between $FeSb_{2-x}Ag_x$ and $Ag_{1-y}Sb_y$ nanoparticles, it is necessary to know the work functions of both materials. Since it is not trivial to extract the work function value of $FeSb_2$ experimentally, here we adopt an alternative approach to roughly estimate the work function of $FeSb_2$ via first-principles calculation based on the density functional theory (DFT). A standard 'slab-supercell method' is used [29]. Slab-supercells are constructed by stacking layers of atoms for (001), (010), and (100) planes with 16 Å vacuum between each two slabs. The DFT calculation is implemented using the Quantum ESPRESSO package [30]. The Perdew–Zunger pseudopotentials with the local density approximation (LDA) are used, which we believe is sufficient to give a reasonable estimation. The plane wave cut-off energy is chosen as 80 Ryd to guarantee the convergence of the total energy and charge density distribution, and the convergence with the *k*-mesh

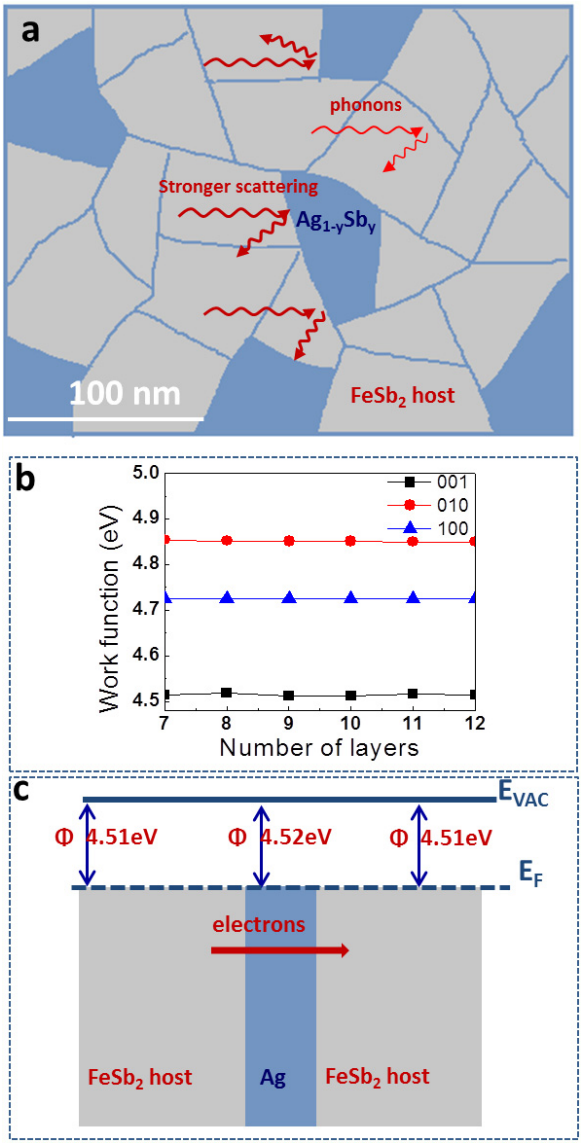

Figure 1. Schematics of the phonon scattering (a), DFT convergence plot on work function for $FeSb_2$ (b), band alignment and electron diffusion (c) at the interface between $FeSb_2$ and Ag in the nanocomposites; the scale bar indicates that the grains inside the sample are around 30 nm on average.

density is also checked. The work functions are calculated as the difference between the vacuum level and the Fermi level inside the slab.

3. Results and discussion

The schematic diagrams of the phonon scattering, the calculated work functions for $FeSb_2$, and the band alignment and electron transport between Ag and $FeSb_2$ in the nanocomposite are shown in figures 1(a)–(c), respectively. In addition to the phonon scattering by nanograins as we have reported [4], the interface shown in figure 1(a) between $FeSb_{2-x}Ag_x$ and $Ag_{1-y}Sb_y$ can also scatter the medium to long wavelength phonons as predicted by theory [13, 14]. The work function of $FeSb_2$ can be simply calculated by subtracting the Fermi level from the vacuum energy level. The

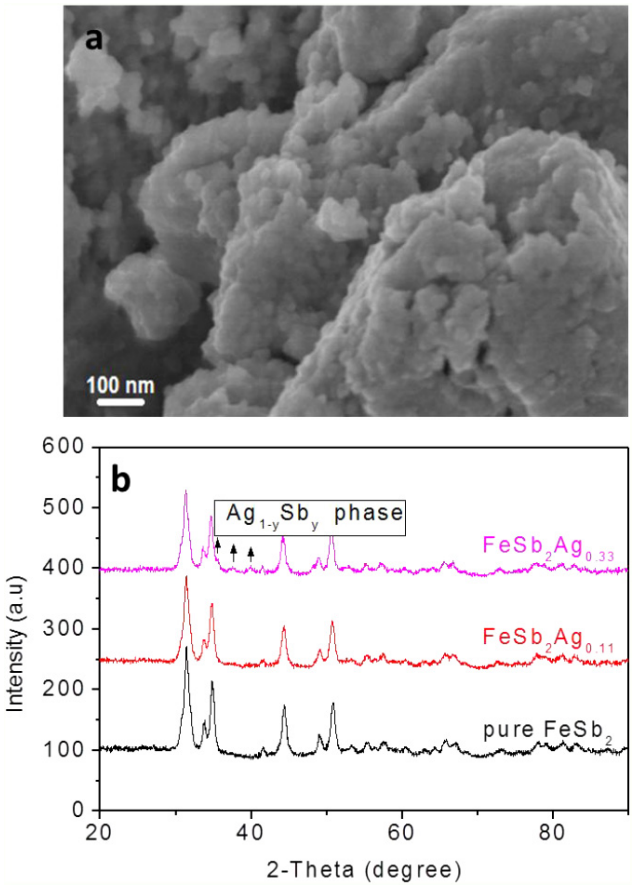

Figure 2. SEM image (a) for $FeSb_2Ag_{0.11}$ nanocomposite, and XRD patterns (b) for pure $FeSb_2$ and nanocomposites $FeSb_2Ag_{0.11}$ and $FeSb_2Ag_{0.33}$.

work functions of $FeSb_2$ were calculated to be 4.514 eV for the (001) plane, 4.852 eV for the (010) plane, and 4.723 eV for the (100) plane (as shown in figure 1(b)). Meanwhile, the reported work functions of silver are 4.52 eV for the (110) plane and 4.74 eV for (111) plane [31]. It is noticed that Ag and $FeSb_2$ have rather close work functions in at least two crystal planes. Therefore, as representative of the band alignment at the interface between Ag and $FeSb_2$ in the designed nanocomposite, figure 1(c) shows the band alignment and the electron transport between the (110) plane of silver and (001) plane of $FeSb_2$. Due to the roughly identical work functions between Ag and $FeSb_2$ in these planes, band alignment showed there is no energy barrier at the interface. Based on the model [13], it is reasonable to speculate that the electron transported from $FeSb_2$ to Ag will not be scattered, and enhanced *ZT* can be expected solely from thermal conductivity reduction in the nanocomposite.

Because the densities 6.23 g cm^{-3} (about 77% of the theoretical value 8.09 g cm^{-3}) and grain sizes (~30 nm) of all six samples are very similar, only an SEM image for sample $FeSb_2Ag_{0.11}$ is shown in figure 2(a). It can be seen that the sample is composed of micro-sized aggregates consisting of much smaller grains of ~30 nm on average, which is consistent with the TEM observation in figure 3(a). The porous structure is also a typical feature of the low-density sample and is consistent with our previous report on

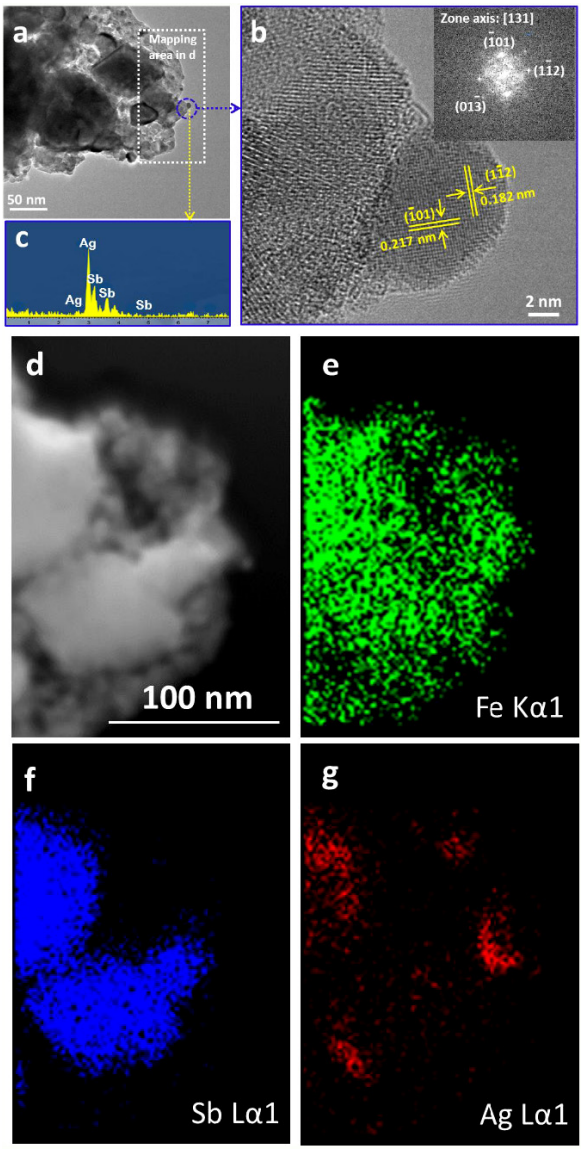

Figure 3. TEM images and STEM mappings of the selected area of $FeSb_2Ag_{0.11}$ nanocomposite: (a) low magnification TEM image of a typical area of the sample; (b) expanded view of a selected area shown in (a), with the IFFT for the nanoinclusion as the inset; (c) EDX showing the targeted nanoparticle in (b) is composed of Ag and Sb with the chemical formula of $Ag_{0.77}Sb_{0.23}$; (d) image of the STEM mapping area selected from (a); (e) mapping of Fe K_{α_1}; (f) mapping of Sb L_{α_1}; (g) mapping of Ag L_{α_1}.

$FeSb_2$ [4]. The small grain size and porous structure in the samples lead to a significant thermal conductivity reduction and enhanced figure of merit ZT in $FeSb_2$ nanocomposite. XRD patterns in figure 2(b) show that, with the addition of Ag NPs, a second phase becomes visible when Ag NPs are higher than a certain amount and can be indexed to allargentum, $Ag_{1-y}Sb_y$ ($P63/mmc$) [32]. Allargentum, $Ag_{1-y}Sb_y$ (with $y = 0.009$–0.16), is a metallic compound, which formed by the reaction between Ag and $FeSb_2$ during the ball milling and hot pressing process. Increasing the hot pressing temperature of the composite would lead to the formation of another impurity phase, Ag_3Sb [33].

Figure 3 shows the STEM results on the composition and structures of the optimized nanocomposite sample with nominal composition $FeSb_2Ag_{0.11}$. The low magnification image in figure 3(a) shows nanograins with abundant grain boundaries, and the grain size varies from ∼10 to ∼100 nm, favorable for phonon scattering. The enlarged image (figure 3(b)) of the selected small area shown in figure 3(a) reveals an impurity phase; combined with its composition ($Ag_{0.77}Sb_{0.23}$) shown in figure 3(c), the impurity phase can be indexed to allargentum $Ag_{1-y}Sb_y$ ($P63/mmc$) structure by indexing its two lattice faces to (1$\bar{1}$2) and (1$\bar{0}$1), which are parallel to the zone axis [131] as shown by the inverse Fast Fourier transform (IFFT) as the inset of figure 3(b). The phase indexing is consistent with our XRD results. Figure 3(d) is the expanded image of the dotted box area shown in figure 3(a). Figures 3(e)–(g) show the elemental mapping results for the selected area in figure 3(d). The total Ag content in the area of figure 3(d) is 3.2% by weight, compared with 3.8% of the initial nominal composition. It is noted that Ag is not uniform, suggesting that Ag is in the form of $Ag_{1-x}Sb_x$ as a second phase in the composite. This is very different from the scenario that Ag alloyed into the $FeSb_2$ lattice forming uniform Ag distribution in the mapping, although there could be a minor concentration in the lattice as we discussed in the following. The second phase as nanoinclusions can be indexed to allargentum $Ag_{0.77}Sb_{0.23}$. The size of each $Ag_{0.77}Sb_{0.23}$ grain is less than 100 nm, which is smaller than the initial 100 nm Ag NPs. Those $Ag_{0.77}Sb_{0.23}$ nanoinclusions in the nanocomposite with nominal composition $FeSb_2Ag_{0.11}$ will behave as phonon scattering centers to reduce thermal conductivity. Here we notice that a possible Ag doping in $FeSb_2$ might happen while Ag reacted with $FeSb_2$ to form $Ag_{0.77}Sb_{0.23}$. A solid chemical reaction can be depicted as the following: $FeSb_2 + 0.11Ag \rightarrow FeSb_{2-x}Ag_x + zAg_{0.77}Sb_{0.23}$. Based on the phase diagram, x is 0.025, and z is 0.11. Thus, the host $FeSb_2$ could be $FeSb_{1.975}Ag_{0.025}$. To be accurate, the as-formed nanocomposite for nominal composition $FeSb_2Ag_{0.11}$ can be presented as $FeSb_{1.975}Ag_{0.025}/Ag_{0.77}Sb_{0.23}$ with $Ag_{0.77}Sb_{0.23}$ of ∼10% in molar ratio.

The measured TE properties are shown in figure 4. We observed a significant thermal conductivity reduction for all $FeSb_2Ag_m$ composites as shown in figure 4(a). The inset in figure 4(a) shows the thermal conductivity versus Ag content for all samples measured at 50 K. It can be seen that, with the increase of Ag content, thermal conductivity first decreased to a minimum of 0.24 W m^{-1} K^{-1} for nanocomposite $FeSb_2Ag_{0.028}$ from 0.38 W m^{-1} K^{-1} for pure nanostructured $FeSb_2$. The TEM and EDX investigations for all $FeSb_2Ag_m$ samples revealed uniformly distributed $Ag_{1-y}Sb_y$ nanoparticles in these nanocomposites with an average size of 20 nm. With the increase of Ag content, allargentum, $Ag_{1-y}Sb_y$, emerged as a significant phase in $FeSb_2Ag_m$ nanocomposite. Owing to the high thermal conductivity of $Ag_{1-y}Sb_y$ metal phase, the total thermal conductivity in the nanocomposite increases with the increase of Ag content, and reaches a maximum at 0.29 W m^{-1} K^{-1} for $FeSb_2Ag_{0.22}$. Meanwhile, with the increase of Ag, the

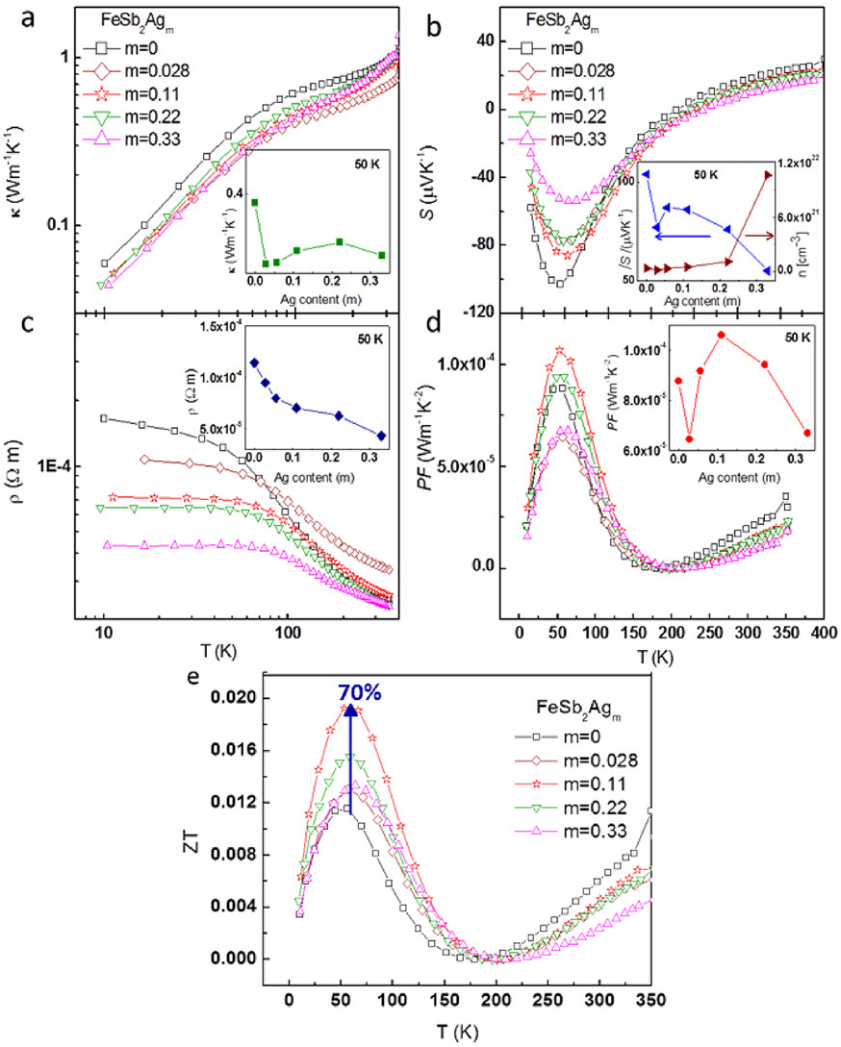

Figure 4. Thermoelectric properties of $FeSb_2Ag_m$ ($m = 0, 0.028, 0.11, 0.22$, and 0.33) samples: (a) temperature dependence of thermal conductivity (the inset shows the measured thermal conductivity at 50 K versus Ag content); (b) temperature dependence of Seebeck Coefficients (the inset shows the measured electron carrier concentrations versus Ag content, as well as the peak Seebeck coefficient at 50 K versus Ag content); (c) temperature dependence of electrical resistivity; (d) temperature dependence of power factor (the inset shows the peak value of power factor at 50 K versus Ag content); (e) temperature dependence of ZT for $FeSb_2$ and $FeSb_{2-x}Ag_x/Ag_{1-y}Sb_y$ nanocomposites.

phonon scattering from the interfaces between $FeSb_{2-x}Ag_x$ and $Ag_{1-y}Sb_y$ became dominant and eventually outweighed the contribution of the $Ag_{1-y}Sb_y$ metal phase, and the total thermal conductivity decreased to another low level at 0.26 W m^{-1} K^{-1} for $FeSb_2Ag_{0.33}$ nanocomposite.

An ideal metal/semiconductor interface in three-dimensional structures has been theoretically predicted to scatter phonons for reducing thermal conductivity [14]. $FeSb_2$ has a very large lattice thermal conductivity in the total thermal conductivity: 99.9% below 75 K [25], and ∼80% at room temperature. Data in figure 4(a) shows the reduced thermal conductivity for all $FeSb_2Ag_m$ composites compared to pure $FeSb_2$ in the whole temperature range. Considering the very low electrical conductivity shown in figure 4(c), the lattice thermal conductivity in the nanocomposite $FeSb_2Ag_m$ is still dominant.

Figure 4(b) indicates the temperature dependence of the Seebeck coefficient. Overall, the peak values are all significantly reduced in comparison with that of single crystals [23, 25, 26], and also lower than those of samples with larger grain sizes [4]. We have ascribed this to the increased carrier concentrations due to defects in $FeSb_2$ nanocomposites [4]. The inset in figure 4(b) indicates the Ag content dependent Seebeck coefficient and carrier concentration for all samples at 50 K. A deep valley of Seebeck coefficient at -77 μV K^{-1} was first observed for $FeSb_2Ag_{0.028}$. With the emergence and increase of allargentum ($Ag_{1-y}Sb_y$) phase, the Seebeck coefficient at 50 K became higher for $FeSb_2Ag_{0.056}$ and then decreased to -55 μV K^{-1} for nanocomposite $FeSb_2Ag_{0.33}$. Meanwhile, we observed that, with the increase of Ag content, the electron carrier concentration at 50 K rose from 0.36×10^{21} cm^{-3} for pure $FeSb_2$ to 10.6×10^{21} cm^{-3} for $FeSb_2Ag_{0.33}$. However, the Seebeck coefficients for the corresponding temperature upon Ag addition in those nanocomposites did not decrease as much as expected, even though they did decrease to some

extent. Based on the parabolic band approximation, $S(T)$ of a degenerate electron system with dominant scattering by acoustic phonons is given by $S(T) = \frac{2m^*Tk_B^2\pi^2}{3eh^2}(\frac{8\pi}{3n})^{\frac{2}{3}}$. By assuming $m^* = m_0$, the free electron mass, the above equation has to be multiplied by a factor of 5.5 in order to reproduce the peak S value for the $FeSb_2Ag_{0.33}$ nanocomposite. This enhancement has been observed in Te-doped $FeSb_2$ single crystal samples reported by Sun *et al* [26], wherein they proposed an enhancement factor of 10–30.

The electrical resistivity shown in figure 4(c) has a similar feature as that of the Te-doped $FeSb_2$ single crystal [26]. Above 100 K, the electrical conductivity is dominated by holes, which means that increasing the electron carrier concentration through n-type Te doping or electron diffusions in our $FeSb_2Ag_m$ composites would not lead to significant improvement in the electrical conductivity. However, below 100 K, the contributions of added electrons from Ag addition and non-scattering transport for electrons between Ag and $FeSb_2$ nanograins became significant. As can be seen in figure 4(c), the electrical conductivity was improved in a linear relationship with the Ag content (inset in figure 4(c)), as happened in Te-doped $FeSb_2$. It is noted that the p-type doping can also increase the electrical conductivity in poly-crystal $FeSb_2$ but with a different mechanism [22]. Upon Sn doping, $FeSb_2$ behaved like a fermion metal and the system became hole dominated, and with the increase of Sn, the electrical resistivity in the whole temperature range decreased dramatically. However, a large reduction on the Seebeck coefficient through Sn doping caused no gain in the power factor of the materials. Certainly, increasing the Seebeck coefficient of $FeSb_2$ nanocomposite by reducing the electron carrier concentration seems very attractive. However, the high sensitivity of the Seebeck coefficient in $FeSb_2$ to doping makes this elusive so far.

The power factor (PF) in figure 4(d) shows a trade-off between Seebeck coefficient and electrical resistivity. The inset in figure 4(d) indicates there is a maximum value at the composition of $FeSb_2Ag_{0.11}$ among all the samples at 50 K. Moreover, a similar valley as that for Seebeck coefficient for the sample $FeSb_2Ag_{0.028}$ is also observed. By taking advantage of the greatly reduced thermal conductivity for all $FeSb_2Ag_m$ nanocomposites, we enhanced the peak ZT to ~0.02, which is four times higher than the single crystal value [23], and ~70% improvement over the best $FeSb_2$ nanocomposite in our previous report [4].

Enhancement of ZT of semiconductor thermoelectric materials through the metal/semiconductor interface approach has been theoretically investigated and predicted by the Léonard group [14]. Typically, for either a κ_e or κ_{ph} dominated system, as a sum, the electron and phonon scatterings at the metal/semiconductor interface would lead to concrete thermal conductivity reductions. In a phonon thermal conductivity dominated system, the thermal conductivity reduction in $FeSb_2Ag_m$ nanocomposites is not too surprising. However, inspired by the model proposed by Léonard [14], the band bending and Fermi level alignment at the interface of $FeSb_2$ and Ag showed there is no significant potential barriers. Reasonably, the electron configuration at the $FeSb_2$/Ag interfaces can be extended to all $FeSb_2Ag_m$ nanocomposites. Under this situation, electrons can transport into the lightly doped $FeSb_{2-x}Ag_x$ and $Ag_{1-y}Sb_y$ without any need to overcome energy barriers, leading to increased electrical conductivity for the composites.

We believe that further ZT enhancement can be realized through tuning the nature of metal phase, size, and distribution of the grains in the nanocomposite. The results also provide inspiring hints for the application of metal/semiconductor interface in other strongly correlated materials or Kondo systems for possible enhancement in ZT.

4. Conclusion

In summary, we present the substantial figure-of-merit ZT improvement in $FeSb_{2-x}Ag_x/Ag_{1-y}Sb_y$ nanocomposite through a metal/semiconductor interface engineering approach by mixing nanopowders of $FeSb_2$ and Ag using ball milling, followed by a dc hot pressing process. Owing to the interfaces between $FeSb_{2-x}Ag_x$ and $Ag_{1-y}Sb_y$ phases, as well as the roughly identical work functions among them, both thermal conductivity and electrical resistivity of the nanocomposite were reduced significantly in the lower temperature regime compared with the pure $FeSb_2$ nanocomposite. Overall, an improvement of 70% in ZT for the optimized sample $FeSb_{1.975}Ag_{0.025}/Ag_{0.77}Sb_{0.23}$ (10% in molar ratio) nanocomposite was achieved. It seems we have evidence to show the metal/semiconductor interface does provide benefits to thermoelectric materials, which may potentially be useful for other strongly correlated material systems.

Acknowledgments

The work is sponsored by the Air Force MURI program under contract FA9550-10-1-0533. The authors would like to thank Dr Mona Zebarjadi for insightful discussion.

References

[1] Hsu K F, Loo S, Guo F, Chen W, Dyck J S, Uher C, Hogan T, Polychroniadis E K and Kanatzidis M G 2004 *Science* **303** 818–21
[2] Poudel B *et al* 2008 *Science* **320** 634–8
[3] Yan X *et al* 2011 *Nano Lett.* **11** 556–60
[4] Zhao H Z, Pokharel M, Zhu G H, Chen S, Lukas K, Jie Q, Opeil C, Chen G and Ren Z F 2011 *Appl. Phys. Lett.* **99** 163101
[5] Heremans J P, Jovovic V, Toberer E S, Saramat A, Kurosaki K, Charoenphakdee A, Yamanaka S and Snyder G J 2008 *Science* **321** 554–8
[6] Zhang Q Y *et al* 2012 *Energy Environ. Sci.* **5** 5246–51
[7] Heremans J P, Wiendlocha B and Chamoire A M 2012 *Energy Environ. Sci.* **5** 5510–30
[8] Pei Y Z, Shi X Y, LaLonde A, Wang H, Chen L D and Snyder G J 2011 *Nature* **473** 66–9
[9] Zhang Q, Cao F, Liu W S, Lukas K, Yu B, Chen S, Opeil C, Broido D, Chen G and Ren Z F 2012 *J. Am. Chem. Soc.* **134** 10031–8
[10] Zebarjadi M, Joshi G, Zhu G H, Yu B, Minnich A, Lan Y C, Wang X W, Dresselhaus M, Ren Z F and Chen G 2011 *Nano Lett.* **11** 2225–30

[11] Yu B, Zebarjadi M, Wang H, Lukas K, Wang H Z, Wang D Z, Opeil C, Dresselhaus M, Chen G and Ren Z F 2012 *Nano Lett.* **12** 2077–82
[12] Heremans J P, Thrush C M and Morelli D T 2005 *J. Appl. Phys.* **98** 063703
[13] Kim W, Zide J, Gossard A, Klenov D, Stemmer S, Shakouri A and Majumdar A 2006 *Phys. Rev. Lett.* **96** 045901
[14] Faleev S V and Léonard F 2008 *Phys. Rev.* B **77** 214304
[15] Zebarjadi M, Esfarjani K, Shakouri A, Bahk J-H and Bian Z X 2009 *Appl. Phys. Lett.* **94** 202105
[16] Sumithra S, Takas N J, Misra D K, Nolting W M, Poudeu P F P and Stokes K L 2011 *Adv. Energy Mater.* **1** 1141–7
[17] Ko D K, Kang Y J and Murray C B 2011 *Nano Lett.* **11** 2841–4
[18] Smith G E and Wolfe R 1962 *J. Appl. Phys.* **33** 841–6
[19] Harutyunyan S R, Vardanyan V H, Kuzanyan A S, Nikoghosyan V R, Kunii S, Wood K S and Gulian A M 2003 *Appl. Phys. Lett.* **83** 2142
[20] Rowe D M, Gao M and Kuznestsov V L 1998 *Phil. Mag. Lett.* **77** 105–8
[21] Sales B C, Delaire O, McGuire M A and May A F 2011 *Phys. Rev.* B **83** 125209
[22] Bentien A, Madsen G K H, Johnson S and Iversen B B 2006 *Phys. Rev.* B **74** 205105
[23] Bentien A, Johnsen S, Madsen G K H, Iversen B B and Steglich F 2007 *Europhys. Lett.* **80** 17008
[24] Sun P, Oeschler N, Johnsen S, Iversen B B and Steglich F 2009 *Phys. Rev.* B **79** 153308
[25] Sun P, Oeschler N, Johnsen S, Iversen B B and Steglich F 2010 *Dalton Trans.* **39** 1012–9
[26] Sun P, Søndergaard M, Sun Y, Johnsen S, Iversen B B and Steglich F 2011 *Appl. Phys. Lett.* **98** 072105
[27] Diakhate M S, Hermann R P, Möchel A, Sergueev I, Søndergaard M, Christensen M and Verstraete M J 2011 *Phys. Rev.* B **84** 125210
[28] Mani A, Janaki J, Satya A T, Kumary T G and Bharathi A 2012 *J. Phys.: Condens. Matter* **24** 075601
[29] Singh-Miller N E and Marzari N 2009 *Phys. Rev.* B **80** 235407
[30] Giannozzi P *et al* 2009 *J. Phys.: Condens. Matter* **21** 395502
[31] *CRC Handbook of Chemistry and Physics* 2008 89th edn, (Boca Raton, FL: CRC Press) pp 12–114
[32] Petruk W, Cabri L J, Harris D C, Stewart J M and Clark L A 1970 *Can. Mineral.* **10** 163–72
[33] Scott J D 1976 *Can. Mineral.* **14** 139–42

MRS Communications (2013), *3*, 31–36

doi:10.1557/mrc.2013.7

MRS Communications

Research Letters

Phonon drag effect in nanocomposite $FeSb_2$

Mani Pokharel, Huaizhou Zhao, Kevin Lukas, Zhifeng Ren, and **Cyril Opeil,** Department of Physics, Boston College, Chestnut Hill, Massachusetts 02467
Bogdan Mihaila, Los Alamos National Laboratory, Los Alamos, New Mexico 87545
Address all correspondence to Mani Pokharel at **pokharem@bc.edu**

(Received 15 November 2012; accepted 1 February 2013)

Abstract

We study the temperature dependence of thermoelectric transport properties of four $FeSb_2$ nanocomposite samples with different grain sizes. The comparison of the single crystals and nanocomposites of varying grain sizes indicates the presence of substantial phonon drag effects in this system contributing to a large Seebeck coefficient at low temperature. As the grain size decreases, the increased phonon scattering at the grain boundaries leads to a suppression of the phonon-drag effect, resulting in a much smaller peak value of the Seebeck coefficient in the nanostructured bulk materials. As a consequence, the ZT values are not improved significantly even though the thermal conductivity is drastically reduced.

Introduction

Owing to its unusual magnetic and electronic transport properties, the narrow-gap semiconductor $FeSb_2$ has been one of the extensively studied compounds in the past few decades.[1–4] The renewed interest in this compound came after Bentien et al.[5] reported a colossal value of the Seebeck coefficient of –45,000 μV/K with a record high value of the power factor (PF) of 2300 $\mu W/K^2/cm$ at around 10 K in single crystal samples, which may make this material a potential candidate for the Peltier cooling applications at very low temperature near 10 K. Despite the huge PF value, the dimensionless figure of merit (ZT) values for single crystal samples are limited by a very high thermal conductivity $\kappa \sim 500$ W/m/K at ~10 K. In our earlier work,[6] we were able to reduce the thermal conductivity by three orders of magnitude to 0.5 W/m/K in achieving a peak ZT value of ~0.013 at ~50 K in nanocomposite samples. However, the Seebeck coefficient in the nanocomposites is severely degraded at low temperatures when compared with that of the single crystal counterpart. For optimized samples with $\kappa = 0.40$ W/m/K and $\rho = 1.2 \times 10^{-4}$ Ω m at 50 K, a Seebeck coefficient of –970 μV/K is required to achieve a ZT value of 1. Unfortunately, the measured value of the Seebeck coefficient at 50 K was only –109 μV/K. Therefore, it is important to know the origin of the large Seebeck coefficient in this system to further improve ZT.

The classical theory of thermoelectricity is based on the assumption that the flow of charge carriers and phonons can be treated independently. Under this assumption, the Seebeck coefficient arises due solely to spontaneous electron diffusion. However, when the two flows are linked, the effect of electron–phonon scattering should be taken into account. Hence, in general, the Seebeck coefficient is given as the sum of two independent contributions[7]

$$S = S_{\mathrm{d}} + S_{\mathrm{p}}, \tag{1}$$

where S_d is the conventional electron-diffusion part and S_p is the phonon-drag contribution. The diffusion part is caused by the spatial variation of the electronic occupation in the presence of a thermal gradient, whereas the drag part arises due to the interaction between anisotropic lattice vibrations and mobile charge carriers. Herring[7] showed that the higher than expected value of thermopower in germanium[8] and other semiconductors could be explained assuming that the carriers are preferentially scattered by the phonons toward the cold end of the sample. The dragging of some of the charge carriers along the thermal gradient gives rise to an additional thermoelectric electromotive force (emf). Because the additional emf and the emf induced by diffusion have the same sign, the overall phonon-drag effect is to increase the Seebeck coefficient. Generally, this effect becomes stronger at lower temperatures where the phonon mean free path becomes longer.

The origin of the colossal Seebeck coefficient in $FeSb_2$ at low temperature is not completely understood yet. Several authors[5,9–12] suggested a strong electron–electron correlation as a possible cause. Other authors,[13,14] however, surmised that the origin of the colossal value of the Seebeck coefficient is not due to electron–electron correlations but due to the phonon drag effect. In this paper, we study the thermoelectric properties of $FeSb_2$ nanocomposites and present evidence of

a substantial phonon-drag contribution to the Seebeck coefficient in $FeSb_2$.

Experimental

Nanostructured $FeSb_2$ samples were synthesized by first forming an ingot through melting and solidification. The ingot was ball milled and hot pressed at different temperatures to obtain the nanocomposite samples with different grain sizes ranging from nanometers to micrometers. The labels given to the different samples and the corresponding processing parameters are shown in Table I. The Seebeck coefficient (S), electrical resistivity (ρ), thermal conductivity (κ), and Hall coefficient (R_H) were measured on a Physical Property Measurement System (PPMS) from Quantum Design Inc. (San Diego, CA). Sample preparation and measurements were performed in the manner described in Ref. 6.

Results and discussions

Figure 1 shows the temperature dependence of the Seebeck coefficient for our four nanocomposite samples. Sample S-600 was measured both in magnetic fields of 0 and 9 T. The Seebeck coefficients of all samples are significantly smaller than that of a single crystal at low temperature, whereas at high temperature the values are comparable. A room temperature value of $S \sim 26$ μV/K was observed for all our samples. This value is comparable to $S \sim 31$ μV/K reported for the single crystal.[15] A decrease in the Seebeck coefficient at low temperature in polycrystal,[11] thin films[16] and arsenic-substituted $FeSb_2$ single crystals[9] was reported earlier. As shown in the inset of Fig. 1, the peak value of the Seebeck coefficient (S_{max}) decreases with decreasing grain size. This is expected for the phonon-drag effect, because the non-electronic scattering (grain boundary scattering in the case of nanocomposites) reduces the phonon mean free path, which in turn decreases the phonon-drag contribution. A similar conclusion was drawn in Ref. 14. Yet another example of the reduction of phonon mean free path decreasing phonon drag contribution was shown by Weber et al.[17] It was demonstrated, using point contacts, that when the contact size becomes comparable to the mean free path of the relevant phonons, the phonon-drag part of the thermopower is suppressed by the boundary scattering. Here, we also note that the temperature profile of the Seebeck coefficient for the samples with larger grains follows the typical behavior of phonon-drag system as suggested by Blatt.[18]

Table 1. Assigned IDs, processing temperature, and average grain sizes estimated from the SEM images for the four nanocomposite $FeSb_2$ samples.

Sample code	Hot pressing temperature (°C)	Average grain size (nm)
S-300	300	30
S-400	400	100
S-500	500	350
S-600	600	20,000

The Seebeck peaks shift to the higher temperature when the grain size decreases (inset of Fig. 1). This type of size-dependent shift in the Seebeck peak is one of the characteristics of the phonon-drag-dominated systems, as pointed out previously.[8,19,20]

Usually, a small magnetothermopower is expected for the phonon-drag dominated system. For sample S-600 at 25 K, we observed a relative change in the Seebeck coefficient, $(S(9T) - S(0T))/S(0T) = 0.059$. This small value supports the non-electronic origin of the large Seebeck coefficient in this sample.

Figure 2 shows the temperature dependence of the thermal conductivity (κ) for the four samples. Calculations based on the Wiedemann–Franz law show that below 50 K, more than 97% of the total thermal conductivity comes from the lattice contribution. For large-grained samples, a temperature dependence of the form $\kappa \sim T^2$ is nearly obeyed at temperatures below 50 K. Weber et al.[21] reported a similar T^2 behavior in silicon below 20 K that they attribute to strong electron-phonon scattering. As the grain size decreases, we find a gradual deviation from the T^2 law. This can be understood as follows: for a large-grained sample, the number of available phonons interacting with the carriers is large which causes significant phonon-drag. As the grain size decreases the number of relevant phonons decreases and as a result the preferential scattering of electrons by phonons becomes weaker. Evidence for electron–phonon coupling in $FeSb_2$ single crystals was also reported by Perucchi et al.[22] who found a large change in phonon lifetimes using optical spectroscopy. Lazarevic et al.[23] later suggested that the electron–phonon coupling is temperature dependent below 40 K.

The inset of Fig. 2 shows the change in the Seebeck coefficient with thermal conductivity for 25 and 50 K. At 25 K, the Seebeck coefficient increases linearly with the thermal conductivity. The linear relationship is expected because in a phonon-drag dominated system S_p is expected to follow the same temperature dependence as the phonon heat capacity so that S_p and the lattice thermal conductivity (κ_l) are linearly related. This indicates that phonons play a significant role in determining the Seebeck coefficient values of our samples at around 25 K. At 50 K, however, the Seebeck coefficient decreases with increasing thermal conductivity without any obvious trend. This is an indication that the phonon-mean free path decreases and the phonon-drag effect becomes weak at higher temperature.

Significant phonon drag effects are expected to occur when the dominant phonons acquire sufficient momentum to scatter carriers across the Fermi surface.[24] In a rough approximation, $T_{max} \approx \frac{1}{10}\theta_D$, where T_{max} is the temperature at which the phonon drag peak occurs and θ_D is the Debye temperature. For rutile TiO_2,[25] θ_D is 450–780 K and the Seebeck peak occurs at 10–30 K. For bismuth,[20] another well-known

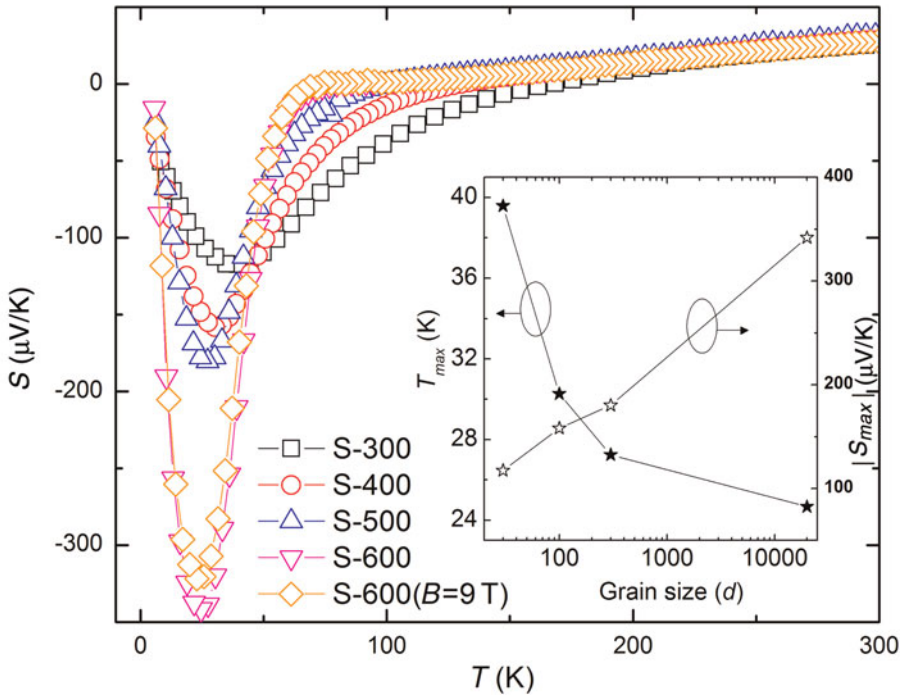

Figure 1. Temperature dependence of the Seebeck coefficient for the four samples. Sample S-600 was measured both at 0 and 9 T magnetic fields. Inset: The grain size dependence of the peak value (S_{max}) and the peak position (T_{max}) of the Seebeck coefficient.

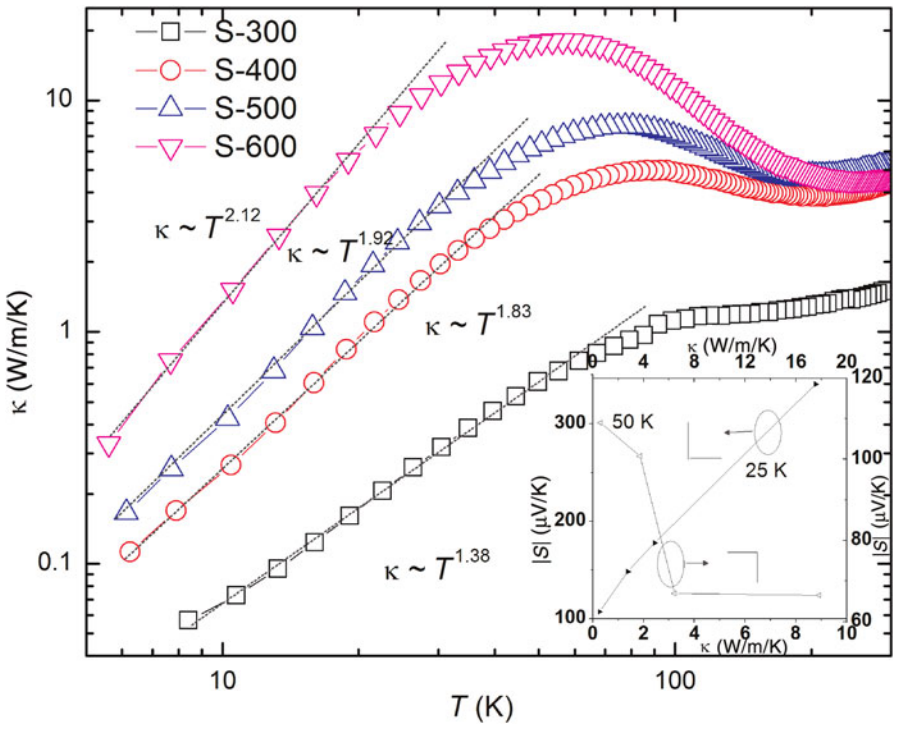

Figure 2. Temperature dependence of the thermal conductivity for the four samples. Fitting to the power law was done for all the samples below 50 K. Inset: Seebeck coefficient as a function of thermal conductivity at 25 and 50 K.

phonon drag system, θ_D is 119 K, whereas the Seebeck peak occurs at 2–3 K. For the $FeSb_2$ polycrystal, $\theta_D \approx 330 - 350$K was reported in Ref. 11 and 256 K in Ref. 26. The Seebeck peak in single crystal occurs at around 10 K. For our sample S-600, the peak occurs at 25 K. Hence, comparing with the other phonon drag systems, the scaling between T_{max} and θ_D in $FeSb_2$ is consistent with the phonon-drag picture.

Following Herring,[7] the electron-diffusion part of the Seebeck coefficient, in μV/K, for a semiconductor is given by

$$S_d = \mp 86.2\left[\ln\frac{4.7\times10^{15}}{n} + \frac{3}{2}\ln\frac{m^*}{m} + \frac{|\Delta E|}{kT} + \frac{3}{2}\ln T\right], \quad (2)$$

where n is the charge carrier density expressed in cm^{-3}, m and m^* are the bare and effective masses of the electron, respectively, and ΔE is the average energy of the transported electrons relative to the band edge. In Eq. (2), the upper and lower signs are for n-type and p-type materials, respectively.

For the case of lattice scattering by long wavelength phonons, $|\Delta E|/kT$ can be approximated by[7]

$$\left|\frac{\Delta E}{kT}\right| = \frac{5}{2} + r, \quad (3)$$

where the scattering parameter r is taken to be $-1/2$. S_d was calculated taking $m^* = m$ and using the charge carrier density (n) calculated from the Hall-coefficient measurements. The diffusion part was then subtracted from the total measured Seebeck coefficient to obtain the drag contribution shown in Fig. 3. For S-600 at 25 K, we find the diffusion value, $S_d = -110$ μV/K. Using Eq. (1), S_p was calculated to be -238 μV/K. However, for S-300 the calculated diffusion contribution turned out to be slightly larger than the measured values. Hence, no significant phonon drag contribution is expected for this sample. This is understandable, because the phonon mean free path for sample S-300 is drastically reduced so that the dominant phonons do not carry sufficient momentum to scatter carriers. Moreover, the phonon drag is expected to weaken with increasing carrier concentration and, in fact, it has been proposed that a saturation effect occurs at high concentration level. The overestimation of the diffusion part of the Seebeck coefficient in S-300 is probably due, in part, to the approximations made in the above calculations.

The phonon-drag thermopower for semiconductors, in the first-order approximation, can be written as[7]

$$S_p = \frac{\beta v_s \lambda_p n e}{\sigma T}, \quad (4)$$

where v_s is the velocity of sound, λ_p the mean free path of the interacting phonons, n the charge carrier density, σ the electrical conductivity, T is the absolute temperature, and β is the dimensionless parameter with its value ranging from 0 to 1 depending upon the strength of the interaction. Equation (4) can be used to find approximate values of the mean free path of t phonons interacting with the electrons. The mean free path of an average phonon can also be estimated from the lattice thermal conductivity based on kinetic theory[27]

$$K_l = \frac{1}{3} c_V \tilde{\lambda}_P v_S, \quad (5)$$

where K_l is the lattice thermal conductivity and c_V the phonon contribution to the total specific heat capacity. The lattice contribution of the total thermal conductivity was calculated assuming $\kappa_{total} = \kappa_l + \kappa_e$ and $\kappa_e = L\sigma T$, where κ_e is the electronic contribution to the total thermal conductivity. The Lorenz number in the free electron model, $L = 2.45\times10^{-8}$ $W/K^2/\Omega$ was used, c_V was calculated using $C_P - \gamma T = \beta T^3$ with $\gamma = 3.98\times10^{-3}/JK^2/mol$, as reported in Ref. 11, and the C_P values were obtained from the same reference. Figure 4 shows the temperature dependence of the two length scales for samples S-600. It turns out that with $\upsilon_s = 3116$ m/s and $\beta = 0.5$, the two length scales, which come from two independent calculations, are of the same order of magnitude and more importantly they behave roughly the same way as a function of temperature. This suggests that similar wavelength phonons are playing a role in both the thermal conductivity and the phonon-drag effect. A similar analysis was performed in Ref. 28 to describe the unusually large Seebeck coefficient in rutile TiO_2 at low temperature.

According to Keyes et al.[29] the value of the figure of merit (Z_p) that can be reached using phonon drag is rather low. Based on their argument, Goldsmid[30] shows that Z_pT is less than ¼ for a bulk thermoelectric material. Ivanov et al.[31] reported recently a similar conclusion for low-dimensional structures. These conclusions are consistent with our earlier work[6] where, despite the dramatic reduction in the thermal

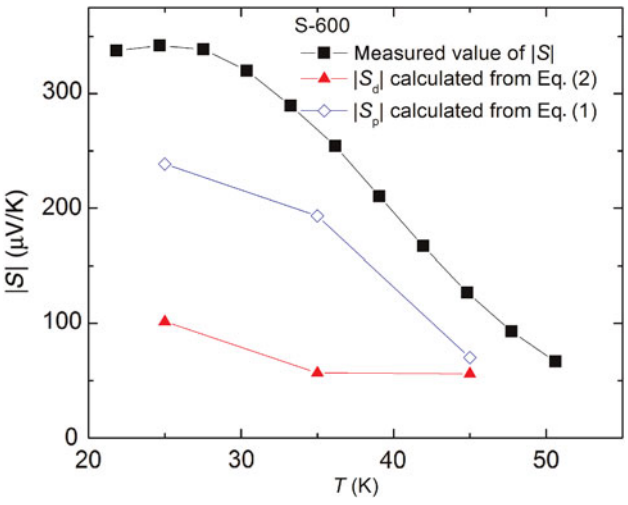

Figure 3. Temperature dependence of the calculated value of diffusion and drag part for the sample S-600 based on Eqs. (1) and (2). The carrier concentration obtained from the Hall coefficient data was used in the calculation. The measured total Seebeck coefficient is also plotted for comparison.

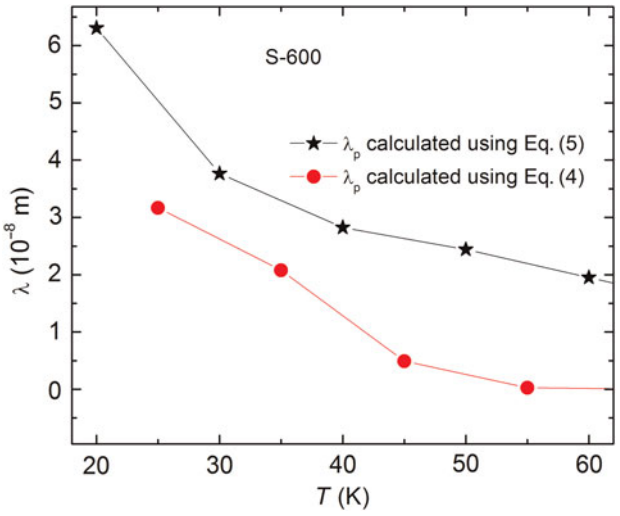

Figure 4. Temperature dependence of the phonon mean free paths calculated from two independent calculations using Eqs. (4) and (5).

conductivity by three orders of magnitude, *ZT* values were not improved significantly Fig. 3(d) in Ref. [6].

Finally, our nanocomposite data and analysis of phonon drag do not support other mechanisms that might explain the large Seebeck effects reported by Bentien et al.[5] Although one cannot preclude the presence of electron–electron correlation effects, their role in this phenomenon may be a minor one. The recent analysis of electron correlations using a hybrid functional approach of Becke[32] and Hegin's *GW* functional approach[33] by Tomczak et al.[14] suggest that the high thermopower in $FeSb_2$ should not be understood in the context of local correlations, but rather by utilizing vertex corrections to the transport coefficients. Such vertex corrections describe the phonon-drag effect. The phonon-drag effects in $FeSb_2$ are similar to those described in p-type Ge by Geballe and Hull.[8] In a similar vein the study of magnetoresistance and Hall effect by Takahashi et al.[13] concludes that the large Seebeck coefficient in $FeSb_2$ is unlikely to originate from electron–electron correlations because they have an insignificant effect on the Seebeck coefficient in the low-temperature insulating regime. Our data on $FeSb_2$ nanocomposite supports their conjecture that the phonon-drag effect plays an essential role in enhancing the Seebeck coefficient in the low-temperature regime, as shown in other semiconductor materials e.g., InSb[34] and weakly P doped Si.[21]

Conclusions

To summarize, in this paper we analyzed qualitatively and quantitatively several indicators of the presence of substantial electron–phonon interaction in $FeSb_2$ at low temperature. Our analysis indicates that a significant phonon-drag effect must take place in coarse-grained samples at low temperature. As the grain size decreases, the phonon drag effect becomes weaker, causing a much smaller peak value of the Seebeck coefficient in fine-grained samples. Based on these results we conclude that the phonon drag plays a significant role in the colossal value of the Seebeck coefficient in $FeSb_2$ single crystals. Therefore, the ZT values of $FeSb_2$ nanocomposite cannot be improved significantly even though the thermal conductivity can be drastically reduced.

Acknowledgments

The authors would like to thank J. Heremans, K. Kempa, and R. Farrell, S.J. for helpful discussions and comments on the manuscript. C.O. acknowledges financial support from the Trustees of Boston College. We gratefully acknowledge funding for this work by the Department of Defense, United States Air Force Office of Scientific Research, Multi-University Research Initiative (MURI) Program under Contract No. FA9550-10-1-0533.

References

1. H. Holseth and A. Kjekshus: Compounds with marcasite type of structure IV. The crystal structure of $FeSb_2$. *Acta Chem. Scand.* **23**, 3043 (1969).
2. A.K.L. Fan, G.H. Rosenthal, H.L. McKinzie, and A. Wold: Preparation and properties of $FeAs_2$ and $FeSb_2$. *J. Solid State Chem.* **5**, 136 (1972).
3. J. Steger and E. Kostiner: Mossbauer effect study of $FeSb_2$. *J. Solid State Chem.* **5**, 131 (1972).
4. C. Petrovic, J.W. Kim, S.L. Bud'ko, A.I. Goldman, and P.C. Canfield: Anisotropy and large magnetoresistance in the narrow-gap semiconductor $FeSb_2$. *Phys. Rev. B* **67**, 155205 (2003).
5. A. Bentien, S. Johnsen, G.K.H. Madsen, B.B. Iversen, and F. Steglich: Colossal Seebeck coefficient in strongly correlated semiconductor $FeSb_2$. *Euro. Phys. Lett.* **80**, 17008 (2007).
6. H. Zhao, M. Pokharel, G. Zhu, S. Chen, K. Lukas, J. Qing, C. Opeil, G. Chen, and Z. Ren: Dramatic thermal conductivity reduction by nanostructures for large increase in thermoelectric figure-of-merit of $FeSb_2$. *Appl. Phys. Lett.* **99**, 163101 (2011).
7. C. Herring: Theory of the thermoelectric power of semiconductors. *Phys. Rev.* **96**, 1163 (1954).
8. T.H. Geballe and G.W. Hull: Seebeck effect in silicon. *Phys. Rev.* **94**, 1134 (1954).
9. P. Sun, N. Oeschler, S. Johnsen, B.B. Iversen, and F. Steglich: Narrow band gap and enhanced thermoelectricity in $FeSb_2$. *Dalton Trans.* **39**, 1012 (2010).
10. P. Sun, N. Oeschler, S. Johnsen, B.B. Iversen, and F. Steglich: $FeSb_2$: prototype of huge electron-diffusion thermoelectricity. *Phys. Rev. B* **79**, 153308 (2009).
11. A. Bentien, G.K.H. Madsen, S. Johnsen, and B.B. Iversen: Experimental and theoretical investigations of strongly correlated $FeSb_{2-x}Sn_x$. *Phys. Rev. B* **74**, 205105 (2006).
12. P. Sun, M. Søndergaard, Y. Sun, S. Johnsen, B.B. Iversen, and F. Steglich: Unchanged thermopower enhancement at the semiconductor-metal transition in correlated $FeSb_{2-x}Te_x$. *Appl. Phys. Lett.* **98**, 072105 (2011).
13. H. Takahashi, R. Okazaki, Y. Yasui, and I. Terasaki: Low-temperature magnetotransport of narrow-gap semiconductor $FeSb_2$. *Phys. Rev. B* **84**, 205215 (2011).
14. J.M. Tomczak, K. Haule, T. Miyake, A. Georges, and G. Kotliar: Thermopower of correlated semiconductors: application to $FeAs_2$ and $FeSb_2$. *Phys. Rev. B* **82**, 085104 (2010).
15. N. Kh. Abrikosov and L.I. Petrova: The polythermal cross-section $FeSb_2$-$FeTe_2$ of the Fe-Sb-Te system. *Inorg. Mater.* **25**, 1087 (1989).
16. Y. Sun, S. Johnsen, P. Eklund, M. Sillassen, J. Bøttiger, N. Oeschler, P. Sun, F. Steglich, and B.B. Iversen: Thermoelectric transport properties of highly oriented $FeSb_2$ thin films. *J. Appl. Phys.* **106**, 033710 (2009).

17. L. Weber, M. Lehr, and E. Gmelin: Reduction of the thermopower in semiconducting point contacts. *Phys. Rev. B* **46**, 9511 (1992).
18. F.J. Blatt: *Physics of Electronic Conduction in Solids* (McGraw-Hill, New York, NY, 1968).
19. Q.R. Hou, B.F. Gu, Y.B. Chen, and Y.J. He: Phonon-drag effect of ultrathin $FeSi_2$ and $MnSi_{1.7}/FeSi_2$ films. *Mod. Phys. Lett. B* **25**, 1829 (2011).
20. J.P. Issi and J. Boxus: Phonon-drag low temperature refrigeration. *Cryogenics* **19**, 517 (1979).
21. L. Weber and E. Gmelin: Transport properties of silicon. *Appl. Phys. A* **53**, 136 (1991).
22. A. Perucchi, L. Degiorgi, R. Hu, C. Petrovic, and V.F. Mitrović: Optical investigation of the metal-insulator transition in $FeSb_2$. *Eur. Phys. J., B* **54**, 175 (2006).
23. N. Lazarević, Z.V. Popović, R. Hu, and C. Petrovic: Evidence for electron-phonon interaction in Fe_{1-x} M_xSb_2 (M = Co and Cr; $0 \leq x \leq 0.5$) single crystals. *Phys. Rev. B* **81**, 144302 (2010).
24. D.T. Morelli: Phonon-drag thermopower. Ph.D. Dissertation. University of Michigan, 1985., p. 82.
25. J. Tang, W. Wang, G.L. Zhao, and Q. Li: Colossal positive Seebeck coefficient and low thermal conductivity in reduced TiO_2. *J. Phys. Condens. Matter* **21**, 205703 (2009).
26. C. Petrovic, Y. Lee, T. Vogt, Dj.N. Lazarov, S.L. Bud'ko, and J. Canfield: Kondo insulator description of spin state transition in $FeSb_2$. *Phys. Rev. B* **72**, 045103 (2005).
27. J. Ziman: *Electrons and Phonons* (Oxford University Press, Oxford, UK, 2001).
28. W.R. Thurber and A.J.H. Mante: Thermal conductivity and thermoelectric power of rutile (TiO_2). *Phys. Rev.* **139**, A1655 (1965).
29. R.W. Keyes: *Thermoelectricity: Science and Engineering*, edited by R.R. Heikes and R.W. Ure Jr., (Interscience, New York, 1961).
30. H.J. Goldsmid: *Introduction to Thermoelectricity: Springer Series in Material Science* (Springer-Verlag, Berlin, Germany, 2010).
31. Y.U.V. Ivanov: *Thermoelectric Handbook: Macro to Nano*, edited by D.M. Rowe (CRC Taylor and Francis, Boca Raton, FL, 2006).
32. A.D. Becke: A new mixing of Hartree–Fock and local density – functional theories. *J. Chem. Phys.* **98**, 1372 (1993).
33. L. Hedin: New method for calculating the one-particle Green's function with application to the electron-gas problem. *Phys. Rev.* **139**, A796 (1965).
34. H.P.R. Frederikse and E.V. Mielczarek: Thermoelectric power of indium antimonide. *Phys. Rev.* **99**, 1889 (1955).

AIP | Applied Physics Letters

Dramatic thermal conductivity reduction by nanostructures for large increase in thermoelectric figure-of-merit of FeSb2

Huaizhou Zhao, Mani Pokharel, Gaohua Zhu, Shuo Chen, Kevin Lukas et al.

Citation: Appl. Phys. Lett. **99**, 163101 (2011); doi: 10.1063/1.3651757
View online: http://dx.doi.org/10.1063/1.3651757
View Table of Contents: http://apl.aip.org/resource/1/APPLAB/v99/i16
Published by the American Institute of Physics.

Dramatic thermal conductivity reduction by nanostructures for large increase in thermoelectric figure-of-merit of $FeSb_2$

Huaizhou Zhao,[1] Mani Pokharel,[1] Gaohua Zhu,[1] Shuo Chen,[1] Kevin Lukas,[1] Qing Jie,[1] Cyril Opeil,[1] Gang Chen,[2] and Zhifeng Ren[1,a)]
[1]*Department of Physics, Boston College, Chestnut Hill, Massachusetts 02467, USA*
[2]*Department of Mechanical Engineering, Massachusetts Institute of Technology, Cambridge, Massachusetts 02139, USA*

(Received 12 August 2011; accepted 26 September 2011; published online 17 October 2011; corrected 14 November 2011)

In this report, thermal conductivity reduction by more than three orders of magnitude over its single crystal counterpart for the strongly correlated system $FeSb_2$ through a nanostructure approach was presented, leading to a significant increase of thermoelectric figure-of-merit (*ZT*). For the samples processed with the optimal parameters, the thermal conductivity reached 0.34 Wm^{-1} K^{-1} at 50 K, leading to a *ZT* peak of about 0.013, compared to 0.005 for single crystal $FeSb_2$, an increase of about 160%. This work suggests that nanostructure method is effective and can be possibly extended to other strongly correlated low temperature thermoelectric materials, paving the way for future cryogenic temperature cooling applications. © *2011 American Institute of Physics*. [doi:10.1063/1.3651757]

Of the several strongly correlated semiconductors including FeSi,[1] $Ce_3Bi_4Pt_3$,[2] and $FeGa_3$,[3] $FeSb_2$ has recently stimulated extensive research efforts due to its colossal thermopower (Seebeck coefficient, *S*) at 10 K.[4] The thermopower *S* of $FeSb_2$ single crystals is on the order of tens of mV K^{-1} which contributes to the very large power factor (*PF*) of 0.23 Wm^{-1} K^{-2},[4,5] about 40 times of the best thermoelectric materials (Bi_2Te_3-based high-performance alloy ingots[6,7]). However, it is the figure of merit, $Z = S^2\sigma/\kappa$, where *S* is the Seebeck coefficient, σ the electrical conductivity, and κ the thermal conductivity, which determines the overall efficiency. To be practically useful, materials should have a dimensionless figure-of-merit (*ZT*) around 1. However, $FeSb_2$ single crystals have a peak *ZT* of around 0.005 at 12 K due to a large value of thermal conductivity of about 500 Wm^{-1} K^{-1}.[5] In order for $FeSb_2$ to become a useful material for thermoelectric cooling, *ZT* must be increased to a meaningful value.

The large lattice thermal conductivity of strongly correlated materials such as $FeSb_2$ at low temperatures limits their *ZT*. Zhang *et al.*[8] predicted that phonon size effects in nanostructured strongly correlated materials can be exploited to reduce phonon thermal conductivity while maintaining electron transport due to the long phonon mean free path and short electron mean free path. For example, it was estimated that single crystal $FeSb_2$ has an electron mean free path of less than 10 nm at all temperatures with a phonon mean free path around 40 μm at 15 K.[9] This large difference of mean free paths allows the opportunity to tune the electrical and thermal properties almost independently by either doping[10,11] or nano-engineering the grain size.[11] In principle, thermal conductivity suppression can be realized through several different methods such as the introduction of impurities, defects, or grain boundaries. Although substantial thermal conductivity reduction was achieved by doping, no improvements in *ZT* were reported due to altered electron transport properties in $FeSb_2$.[10,11]

Nanostructure approach has proven to be a very efficient way to reduce the lattice contribution to the thermal conductivity in many thermoelectric material systems.[12–15] The lower limit of the lattice thermal conductivity in $FeSb_2$ has been calculated[16] to be as low as 0.3 Wm^{-1} K^{-1} at 50 K through the model proposed by Cahill *et al.*[17] It will be shown in this report that the thermal conductivity of nanostructured $FeSb_2$ is drastically decreased leading to an improvement in *ZT*.

The nanostructured $FeSb_2$ were synthesized by first ingot formation through melting and solidification, and then followed by ball milling and hot pressing with different processing parameters. Scanning electron microscopy (SEM, JEOL 6340F) was used to investigate the grain size distributions of the above processed samples. Transmission electron microscopy (TEM, JEOL 2010F) observation was performed on the representative sample S15hr-200C. The electrical resistivity (ρ), Seebeck Coefficient (*S*), thermal conductivity (κ), and Hall coefficient (R_H) were all measured on a physical property measurement system (PPMS) from Quantum Design. Within the one-band model, the charge-carrier concentration was determined by $n = 1/(e/R_H/)$. The Hall mobility was determined by $\mu_H = /R_H//\rho$.

SEM images in Fig. 1 show how the grain size changes as a function of ball milling time and hot pressing temperature. From the images, it can be seen that samples pressed from powders ball milled for shorter times (Fig. 1(a)) or at higher temperatures (Fig. 1(d)) have much larger grains than those from powders ball milled for longer time (Figs. 1(b) and 1(c)) and at lower temperatures (Figs. 1(e) and 1(f)). It is also noticed that S15hr-200 C was composed of particles in which there are many smaller grains, which are around 20 ± 5 nm estimated from SEM images (Fig. 1(f)). TEM images shown in Fig. 2 indicate that the particles in sample S15hr-200C were indeed composed of smaller crystalline grains with different orientations, consistent with the SEM image (Fig. 1(f)).

a)Author to whom correspondence should be addressed. Electronic mail: renzh@bc.edu.

An enlarged area from Fig. 2(a) was shown in Fig. 2(b). It is clearly shown that the grains are well-crystallized with dimensions of 20×15 nm and a lattice spacing of 0.276 nm, which can be indexed to the (101) planes of orthorhombic *Pnnm* $FeSb_2$. The nano-sized grains and the boundaries between theses nano-sized crystals would contribute to the dramatic thermal conductivity reductions in the samples.

Figure 3(a) shows the temperature dependence of thermal conductivity for all samples and also the single crystals grown from vapor transport (VT) and self-flux (SF) methods.[5] A substantial decrease of thermal conductivity was found for all samples throughout the temperature range, decreasing as grain size decreases. The thermal conductivity of sample S15hr-600C is 17 Wm^{-1} K^{-1} at 40 K, compared with 0.34 Wm^{-1} K^{-1} for S15hr-200C at the same temperature due to a decrease in the lattice portion of the thermal conductivity. The peak positions of κ, which reveal the competition between the phonon-phonon (Umklapp) scattering or impurity scattering and the grain boundary scattering, shift to higher temperatures and nearly disappear on samples S15hr-200C and S15hr-room temperature. This demonstrates that grain boundary scattering is the dominant scattering mechanism in samples with smaller grain sizes. Moreover, fittings for all the curves below 100 K show a shift from $T^{2.04}$ to $T^{1.31}$ with the decreasing of grain sizes, as is also seen in nanocrystalline silicon[12] which indicates that other parameters besides C_V such as porosity, phonon frequency (ω), and the effective mean free path (Λ_{eff}) also play important roles in thermal conductivity reduction. When compared with single crystal $FeSb_2$, there is a reduction by more than three orders of magnitude in the thermal conductivity from

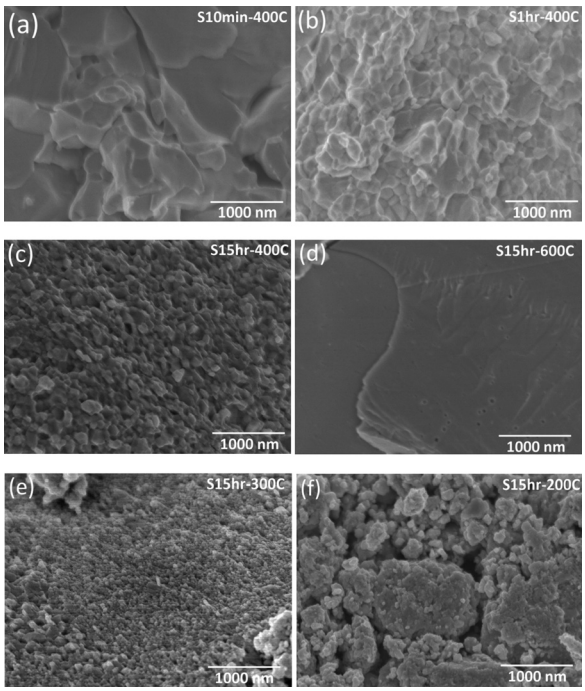

FIG. 1. SEM images for nanostructured samples that were prepared with different conditions. (a) hot pressed at 400 °C using powders ball milled for 10 min, (b) hot pressed at 400 °C using powders ball milled for 1 h, (c) hot pressed at 400 °C using powders ball milled for 15 h, (d) hot pressed at 600 °C using powders ball milled for 15 h, (e) hot pressed at 300 °C using powders ball milled for 15 h, and (f) hot pressed at 200 °C using powders ball milled for 15 h.

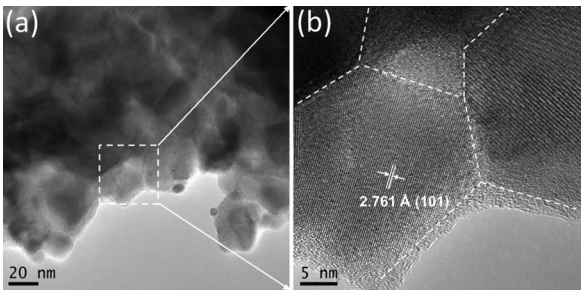

FIG. 2. TEM images for nanostructured sample S15hr-200C. (a) Lower magnification to show the average grain size and (b) higher magnification of the boxed area shown in (a) to show the crystalline orientation and defected boundaries.

500 Wm^{-1} K^{-1} down to around 0.1 Wm^{-1} K^{-1} at 20 K in the nanostructured sample S15hr-200C. Such a large thermal conductivity suppression by nanostructuring at low temperature is much larger than any other nanostructured thermoelectric materials at high temperatures. Nanostructured *p*-type BiSbTe bulk alloy achieved 83% thermal conductivity reduction compared with its ingot counterpart at 250 °C,[13] half-Heuslers achieved 33% in high temperature ranges,[15] and a 100% reduction for *p*-type silicon germanium alloy.[18]

Figure 3(b) shows the temperature dependence of electrical resistivity for all the samples. The data was fit using Arrhenius' law to find approximate energy gaps. Sample S15hrs-600C has two gaps of 28.2 meV and 4.2 meV. When the pressing temperature is lowered further, e.g., sample S15hrs-300C, only one gap appears with a value of 21 meV. The change in the band gaps corresponds to the increasing of crystal defects that are probably due to the decreased grain size and increased carrier concentration. It appears that the smaller energy gap located in the temperature range of 7-20 K was suppressed; and the larger band gap was decreased as can be seen in the sample pressed at room temperature whose band gap is reduced to 18 meV. Measurements of the carrier concentration, inset of Fig. 3(c) increased as well, confirming the narrowing of the energy gaps.

The temperature dependent Seebeck coefficients (S) are shown in Fig. 3(c). It shows that S decreases as grain size is decreased, which could mean that carriers are generated. This is not the case for S10min-400C, which has smaller grains than S15hr-600C. From the relationship of the electrical property and the quality of crystal, it is believed that S10min-400C has fewer defects than that of S15hr-600C due to the longer ball milling time of the latter. Defects typically increase carrier concentration, which decreases the S. An increase in the carrier concentration will also lead to a decrease in the resistivity, which is the case as seen in Fig. 3(b). Mobility and carrier concentration measurements are shown for two samples in the inset of Fig. 3(c). Carrier concentration at 25 K is higher for the S15hr-300C sample with a value of 9.75×10^{19} cm^{-3} and while its mobility is lower at 4.52 cm^2 $V^{-1}s^{-1}$, when compared to S15hr-600C at 25 K, whose carrier concentration is decreased to 8.36×10^{17} cm^{-3} while its mobility is as high as 160 cm^2 $V^{-1}s^{-1}$. These properties directly correlate to the increase seen in the S. There is a cross over between the two samples in the Seebeck coefficient found at 65 K. This cross over is also seen in the measurements for carrier concentration at 65 K while the mobility remains relatively constant

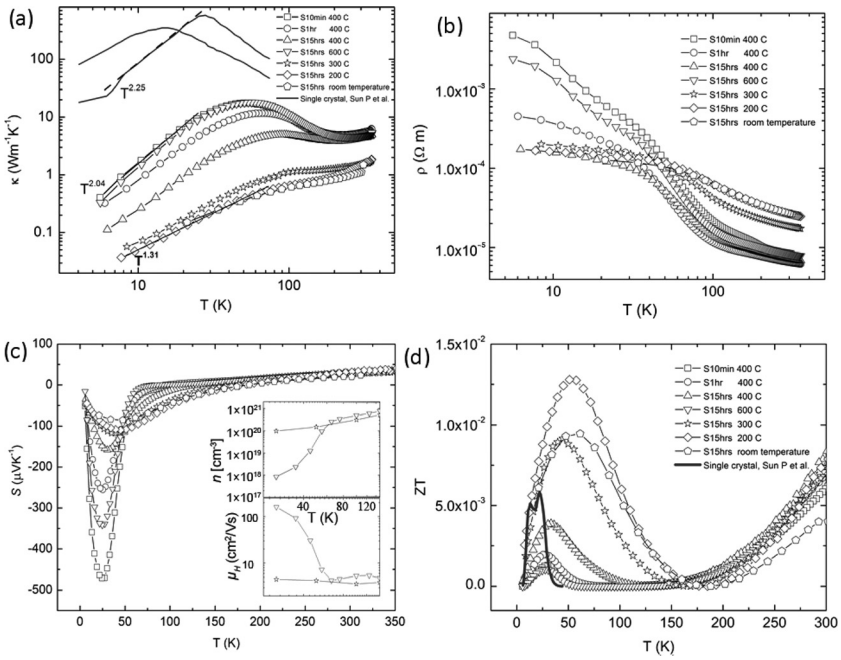

FIG. 3. Thermoelectric properties for nanostructured samples: (a) temperature dependence of thermal conductivity, fittings was applied to sample S10min-400C and S15hr-200C. Two solid curves correspond to thermal conductivity from single crystal samples (Ref. 5); (b) temperature dependence of resistivity; (c) temperature dependence of Seebeck coefficient, the insets indicate the temperature dependent carrier concentration and Hall mobility for S15hr-600C and S15hr-300C, respectively; (d) temperature dependence of *ZT*.

confirming both measurements. S15hr-600C has better crystallization and therefore a band gap of 4.2 meV in the temperature range 7-20 K, which is not seen in S15hr-300C and induces higher resistivity than that of S15hr-300C below 50 K. For the same reason, peak values of the Seebeck coefficient of S15hr-600C, which is 352 μV K^{-1} at 20 K, is much larger than 117 μV K^{-1} for S15hr-300C at 35 K. In $FeSb_2$ systems, the relation between carrier concentration and Seebeck coefficient has been intensively investigated recently by Sun *et al.*[9,11,19] It was found that an enhancement by a factor of 30 or larger could be applied to the calculated Seebeck coefficient based on the free-electron model. Due to this enhancement, it is quite likely that an increase in the Seebeck coefficient can be realized by tuning carrier concentration through doping or composition adjustment, providing the potential for much future work.

Figure 3(d) shows the temperature dependence of *ZT* for the nanostructured samples as well as those for single crystals. The *ZT* increases from 0.001 of sample S15hr-600C to 0.013 of S15hr-200C, which is an unambiguous indication of grain size effect. The optimal *ZT* value reaching 0.013 at 50 K in S15hr-200C is much higher than $ZT = 0.005$ at 10 K for single crystal samples. Though the power factor is much less than that of single crystal, the drastic reduction in thermal conductivity contributes to the increase in *ZT*. One feature worth pointing out is that the *ZT* curve in nanostructured $FeSb_2$ is broadened significantly over that of the single crystal counterpart, which is much more useful for applications between 10 and 150 K.

In conclusion, substantial thermal conductivity suppression for the strongly correlated system $FeSb_2$ through a nanostructure approach was reported in this letter. Thermal conductivity was reduced by more than three orders of magnitude over its single crystal counterpart. As grain size decreases from tens of microns to around 20 nm, the corresponding thermal conductivity decreases by 50 times, reaching 0.34 Wm^{-1} K^{-1} at 50 K. *ZT* was found to be 0.013, compared to 0.005 for single crystal $FeSb_2$, an increase of 160%. Although this is still far from the state-of-art requirement of $ZT = 1$, nanostructure to reduce thermal conductivity in $FeSb_2$ is clearly the right way, and a combination with other methods of *ZT* enhancement including doping or composition adjustment is expected to further increase the *ZT*.

The work is sponsored by Air Force MURI program under Contract FA9550-10-1-0533.

[1]B. C. Sales, E. C. Jones, B. C. Chakoumakos, J. A. Fernandez-Baca, H. E. Harmon, J. W. Sharp, and E. H Volckmann, Phys. Rev. B: Condens. Matter. **50**(12), 8207 (1994).
[2]M. F. Hundley, P. C. Canfield, J. D. Thompson, and Z. Fisk, Phys. Rev. B **50**(24), 18142 (1994).
[3]Y. Hadano, S. Narazu, M. A. Avila, T. Onimaru, and T. Takabatake, J. Phys. Soc. Jpn. **78**(1), 013702 (2009).
[4]A. Bentien, S. Johnsen, G. K. H. Madsen, B. B. Iversen, and F. Steglich, Europhys. Lett. **80**, 17008 (2007).
[5]P. Sun, N. Oeschler, S. Johnsen, B. B. Iversen, and F. Steglich, J. Phys.: Conf. Ser. **150**, 012049 (2009).
[6]O. Yamashita, S. Tomiyoshi, and K. Makita, J. Appl. Phys. **93**, 368 (2003).
[7]S. Paschen, in *Thermoelectric Handbook*, edited by D. M. Rowe (CRC Press, Taylor & Francis Group, Boca Raton, 2006), Chap. 15.
[8]Y. Q. Zhang, M. S. Dresselhaus, Y. Shi, Z. F. Ren, and G. Chen, Nano Lett. **11**(3), 1166 (2011).
[9]P. Sun, N. Oeschler, S. Johnsen, B. B. Iversen, and F. Steglich, Phys. Rev. B **79**(15), 153308 (2009).
[10]A. Bentien, G. K. H. Madsen, S. Johnson, and B. B. Iversen, Phys. Rev. B **74**(20), 205105 (2006).
[11]P. Sun, M. Søndergaard, Y. Sun, S. Johnsen, B. B. Iversen, and F. Steglich, Appl. Phys. Lett. **98**, 072105 (2011).
[12]Z. Wang, J. E. Alaniz, W. Jang, J. E. Garay, and C. Dames, Nano Lett. **11**(6), 2206 (2011).
[13]B. Poudel, Q. Hao, Y. Ma, Y. Lan, A. Minnich, B. Yu, X. Yan, D. Wang, A. Muto, D. Vashaee, X. Chen, J. Liu, M. S. Dresselhaus, G. Chen, and Z. F. Ren, Science **320**(5876), 634 (2008).
[14]Y. C. Lan, A. J. Minnich, G. Chen, and Z. F. Ren, Adv. Funct. Mater. **20**, 357 (2010).
[15]X. Yan, G. Joshi, W. S. Liu, Y. C. Lan, H. Wang, S. Lee, J. W. Simonson, S. J. Poon, T. M. Tritt, G. Chen, and Z. F. Ren, Nano Lett. **11**, 556 (2011).
[16]S. Zhu, W. Xie, D. Thompson, T. Holgate, M. Zhou, Y. Yan, and T. M. Tritt, J. Mater. Res. **26**(15), 1894 (2011).
[17]D. G. Cahill, S. K. Watson, and R. O. Pohl, Phys. Rev. B **46**(10), 6131 (1992).
[18]G. Joshi, H. Lee, Y. Lan, X. Wang, G. Zhu, D. Wang, R. W. Gould, D. C. Cuff, M. Y. Tang, M. S. Dresselhaus, G. Chen, and Z. F. Ren, Nano Lett. **8**(12), 4670 (2008).
[19]P. Sun, N. Oeschler, S. Johnsen, B. B. Iversen, and F. Steglich, Dalton Trans. **39**, 1012 (2010).

AIP | Applied Physics Letters

Thermoelectric property enhancement by Cu nanoparticles in nanostructured FeSb2

Machhindra Koirala, Huaizhou Zhao, Mani Pokharel, Shuo Chen, Tulashi Dahal et al.

Citation: Appl. Phys. Lett. **102**, 213111 (2013); doi: 10.1063/1.4808094
View online: http://dx.doi.org/10.1063/1.4808094
View Table of Contents: http://apl.aip.org/resource/1/APPLAB/v102/i21
Published by the American Institute of Physics.

Thermoelectric property enhancement by Cu nanoparticles in nanostructured $FeSb_2$

Machhindra Koirala,[1] Huaizhou Zhao,[1,a)] Mani Pokharel,[2] Shuo Chen,[1] Tulashi Dahal,[1] Cyril Opeil,[2] Gang Chen,[3] and Zhifeng Ren[1,a)]
[1]*Department of Physics and TcSUH, University of Houston, Houston, Texas 77204, USA*
[2]*Department of Physics, Boston College, Chestnut Hill, Massachusetts 02467, USA*
[3]*Department of Mechanical Engineering, Massachusetts Institute of Technology, Cambridge, Massachusetts 02139, USA*

(Received 8 March 2013; accepted 14 May 2013; published online 29 May 2013)

We present the thermoelectric figure-of-merit (*ZT*) improvement in nanostructured $FeSb_2$ by Cu nanoparticles of ~5 nm as a modulation dopant. Because of the similar work functions between $FeSb_2$ and Cu and the high electrical conductivity of Cu, the Kondo insulator-like electrical resistivity of $FeSb_2$ at low temperatures was dramatically reduced. Both carrier concentration and mobility of the nanocomposites were improved over pure $FeSb_2$ without degrading the Seebeck coefficient. Overall, an improvement of ~90% in power factor was achieved for the optimized nanocomposite $FeSb_2Cu_{0.045}$. Combined with the reduced thermal conductivity by Cu/$FeSb_2$ interfaces, *ZT* was improved by ~110%. These results clearly demonstrate the potential of modulation doping to enhance the thermoelectric performance of $FeSb_2$. A similar approach could be applied to other Kondo insulators or previously known thermoelectric materials to improve *ZT*.
 [http://dx.doi.org/10.1063/1.4808094]

Cryogenic cooling (~77 K) using thermoelectric materials remains challenging so far, Kondo insulator and heavy fermion systems, such as CeB_6,[1] $YbAl_3$,[2] FeSi,[3] $FeSb_2$,[4–10] and $CrSb_2$ (Ref. 11) have been investigated for cryogenic cooling applications. However, the figure-of-merit (*ZT*), which determines the cooling efficiency, is much lower than those thermoelectric materials working at or above room temperatures. It is known that $ZT = (s^2\sigma/\kappa)T$, where *S*, σ, κ, and T are the Seebeck coefficient, electrical conductivity, thermal conductivity, and absolute temperature, respectively. Due to the large Seebeck *S* and high electrical conductivity σ observed in highly doped Kondo insulators and heavy fermions, large power factors (*PF*) have been reported. For example, $FeSb_2$ single crystals have a *PF* around $78 \times 10^{-4}\,W\,m^{-1}\,K^{-2}$ (Ref. 12) that is about twice the highest known *PF* when compared to other systems though it decreases to $5.5 \times 10^{-4}\,W\,m^{-1}\,K^{-2}$ for poly-crystal samples.[13] Most recently, it was reported $CrSb_2$ single crystal has *S* of $-5000\,\mu V\,K^{-1}$,[11] and p-type poly-crystal FeSi of $\sim 1200\,\mu V\,K^{-1}$.[3] In addition, doped FeSe[14] and $CeCu_6$ (Ref. 15) have also received attention for potential cryogenic application.

In addition to exploring new thermoelectric materials for cryogenic cooling applications, new approaches or strategies that can substantially improve the performance of the existing thermoelectric materials are also compelling. Recently, the approaches, such as nanostructures,[13,16–18] resonant doping,[19–21] band engineering at the Fermi level,[22,23] modulation doping that provides more charge carriers for higher electrical conductivity,[24,25] as well as metal/semiconductor interfacial engineering providing barrier to scatter phonons or improve *PF*[26–31] have been proved to be helpful in several material systems. In the case of strongly correlated materials, such as $FeSb_2$, nanostructures have been proved to be able to significantly increase *ZT*.[6,7,13]

In this report, inspired by the recent results, we achieved in $FeSb_{2-x}Ag_x/Ag_{1-y}Sb_y$ nanocomposite by adding Ag nanoparticles (NPs) into the system[32] and our early work on modulation doping in SiGe alloys,[24,25] we found that modulation doping approach substantially increases the *ZT* by ~110% through adding Cu NPs to make nanocomposite $FeSb_2$/Cu in which Cu nanoparticles act as the charge donor. This is a clear demonstration of modulation doping since the Cu does not diffuse into $FeSb_2$, this is distinct from our earlier study of SiGe alloys where significant amounts of B or P diffused easily into the parent compound,[24,25] which weakened the role of modulation doping. Similar work functions of the (100) planes in $FeSb_2$ and Cu facilitate the electron transfer from Cu to $FeSb_2$ at their interfaces to increase the electrical conductivity.

The $FeSb_2/Cu_x$ nanocomposites were synthesized by two procedures. For the synthesis of nanocomposites with ≤5 nm Cu nanoparticle inclusions, a total of 25 grams of Fe, Sb, and Cu with the stoichiometry of $FeSb_2Cu_y$ (y = 0.0225, 0.045, and 0.09) were mixed and sealed in vacuum in a quartz tube. Following a high temperature melt, quenching and 12 h of ball milling as previously reported,[13] 3 g of the ball milled powders with various amount of Cu nanoparticles (NPs) were pressed at 200 °C and 80 MPa for 2 min using direct current (dc) induced hot pressing method. For the synthesis of nanocomposites with ~100 nm Cu nanoparticle inclusion, $FeSb_2$ nanopowders were first prepared, then Cu NPs (~100 nm, Aldrich) were added into the powder with a final nominal composition of $FeSb_2Cu_{0.045}$. The mixed powders of ~5 g were further ball milled for 3 h. After this 3 h ball milling, some of the ~100 nm Cu particles may be milled to smaller nanoparticles, but should still be larger than ~5 nm. Disk samples were prepared by the same method mentioned above.

a)Authors to whom correspondence should be addressed. Electronic addresses: zhz0600@hotmail.com and zren@uh.edu

All the hot pressed samples with the same nominal composition $FeSb_2Cu_{0.045}$, but different sizes of Cu NPs, were characterized by high-resolution transmission electron microscopy (HRTEM) (JEOL 2010 F) for detailed structure and composition studies. The HRTEM samples were prepared by hand grinding and then dispersed in methanol, and the obtained suspension was dropped onto a typical carbon-coated Au grid, which can be used for HRTEM observation after drying. The edge area of the grains was selected for observations.

The temperature dependent electrical resistivity (ρ), Seebeck coefficient (S) and thermal conductivity (k) were measured on a Physical Property Measurement System (PPMS) from Quantum Design using the Thermal Transport Option (TTO). Gold leads were soldered onto samples with dimensions of $3 \times 3 \times 5$ mm^3. The normal 2-point TTO option of the PPMS for transport measurements was used. All the properties were measured in the direction perpendicular to the hot pressing direction.

The schematic band alignment between $FeSb_2$ and Cu, and the structure of $FeSb_2Cu_y$ nanocomposite are shown in Figs. 1(a) and 1(b), respectively. Since $FeSb_2$ is n-type semiconductor with a band gap of ~28 meV,[13] and its Fermi level located at the conduction band edge, the difference between the conduction band edge and vacuum level can be regarded as the same as the work functions for $FeSb_2$ at different crystal orientations. The work functions of $FeSb_2$ have been calculated to be 4.514 eV for (001) plane, 4.852 eV for (010) plane, and 4.723 eV for (100) plane.[32] According to the alignment of Fermi levels, the band bend for (001) and (010) planes, leaving an energy barrier in the range of 0.15–0.2 eV at their interfaces. However, due to the similar work functions between the (100) plane and Cu, which is 4.7 eV, the electron transfer between them would be much easier. It is reasonable to expect that Cu NPs can donate electrons from its conduction band to $FeSb_2$, which will increase the carrier concentration in the $FeSb_2$ host. Based on our early study, it appeared that the higher carrier concentration in nanostructured $FeSb_2$ mostly originated from its high defect density as compared to single crystal or micro sized samples.[13] As a result of the high defect density, the electrical conductivity of the nano sized $FeSb_2$ is significantly higher than the micro sized poly-crystal samples in the low temperature range (roughly $\leq$200 K), but the Seebeck coefficient is also significantly lower, which makes the power factor much lower. How to make the electrical conductivity in nanostructured $FeSb_2$ high without degrading the Seebeck coefficient is very challenging. We realized that localized Cu NPs can provide a large number of free electrons for higher electrical conductivity without changing the band structure of $FeSb_2$ for high Seebeck coefficient due to modulation doping similar to what was observed in SiGe alloy system.[24,25]

Fig. 2 shows the TEM images for both samples with the nominal composition of $FeSb_2Cu_{0.045}$. Figs. 2(a)–2(c) are for the samples prepared by mixing $FeSb_2$ nanopowder and ~100 nm Cu NPs, and Figs. 2(d) and 2(e) refer to samples in which Cu was incorporated by high temperature alloying resulting in very small Cu nanoparticles ~5 nm. In Fig. 2(a), we see the similar grain size and morphology for $FeSb_2$ host as we have shown in our previous reports.[13,32] It can be seen that the particle are composed of small size grains. Fig. 2(b) shows EDS (Energy Dispersive X-ray Spectroscopy) analysis of four selected areas. From regions A to D shown in Fig. 2(a), we see a transition from $FeSb_2$ to Cu, regions B and C are Cu dominated, and region D is approximately 200 nm, showing a slight aggregate of Cu. This indicates that Cu NPs are uniformly distributed in the composites. Region C in Fig. 2(a) is enlarged in Fig. 2(c), the measured lattice spacing from HRTEM images are 0.22 nm and 0.19 nm, which can be indexed to (111) and (200) planes of FCC Cu, respectively. Inverse Fast Fourier transform (IFFT) of the lattice image is also consistent with the Cu FCC structure with the [011] zone axis orientation. In Figs. 2(d) and 2(e), we observed that the size of Cu NPs is reduced to less than ~5 nm, while the $FeSb_2$ kept the similar size and morphology as that in Fig. 2(a). In terms of the volume ratio in both cases, Cu is about 0.9% in the host. The lattice spacing measurement and IFFT show that the $\sim 3 \times 3$ nm particle located at the edge area of $FeSb_2$ grains is Cu, due to the small size, EDS cannot focus on the Cu targets to confirm the composition. It is reasonable to assume that for the nanocomposites with smaller Cu particles, the Cu was first uniformly melted together with Fe and Sb when heated up to 1350 K. During cooling, Cu precipitates out as isolated nanoparticles due to the very limited solubility of Cu in $FeSb_2$.

The measured TE properties are shown in Fig. 3. Fig. 3(a) shows temperature dependence of thermal conductivity for all $FeSb_2Cu_y$ composites as well as the pure nanostructured $FeSb_2$. First, owing to the interfaces between Cu NPs and $FeSb_2$, reduced thermal conductivity was observed for

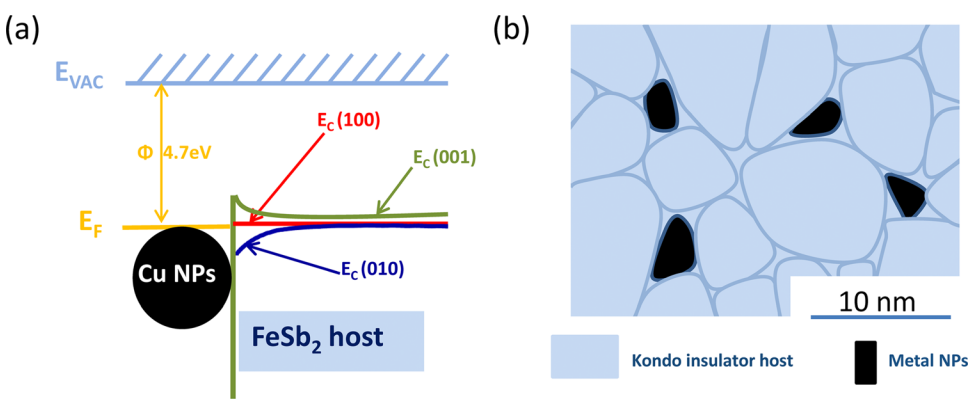

FIG. 1. Schematics of the band alignment between $FeSb_2$ and Cu (a); distribution of Cu NPs in the nanocomposite (b), scale bar indicates that the grains of $FeSb_2$ are around 50 nm on average and ~5 nm for Cu NPs.

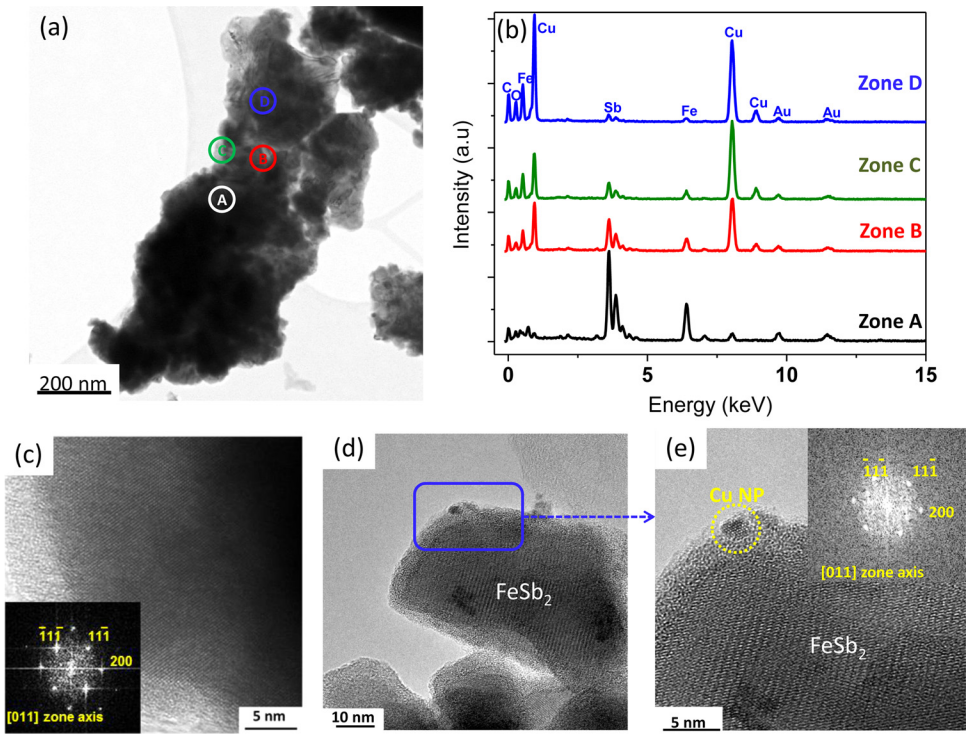

FIG. 2. TEM image (a) for $FeSb_2Cu_{0.045}$ nanocomposite prepared by mixing $FeSb_2$ nanopowder and 100 nm Cu NPs; (b) EDS for the selected zones in (a); (c) HRTEM for zone C shown in (a), inset shows IFFT for (c); (d) TEM image for $FeSb_2Cu_{0.045}$ nanocomposite prepared by melting Fe, Sb, and Cu at 1350 K and solidifying; and (e) is the enlarged area in (d), inset is the IFFT of the Cu nanoparticle area in (d).

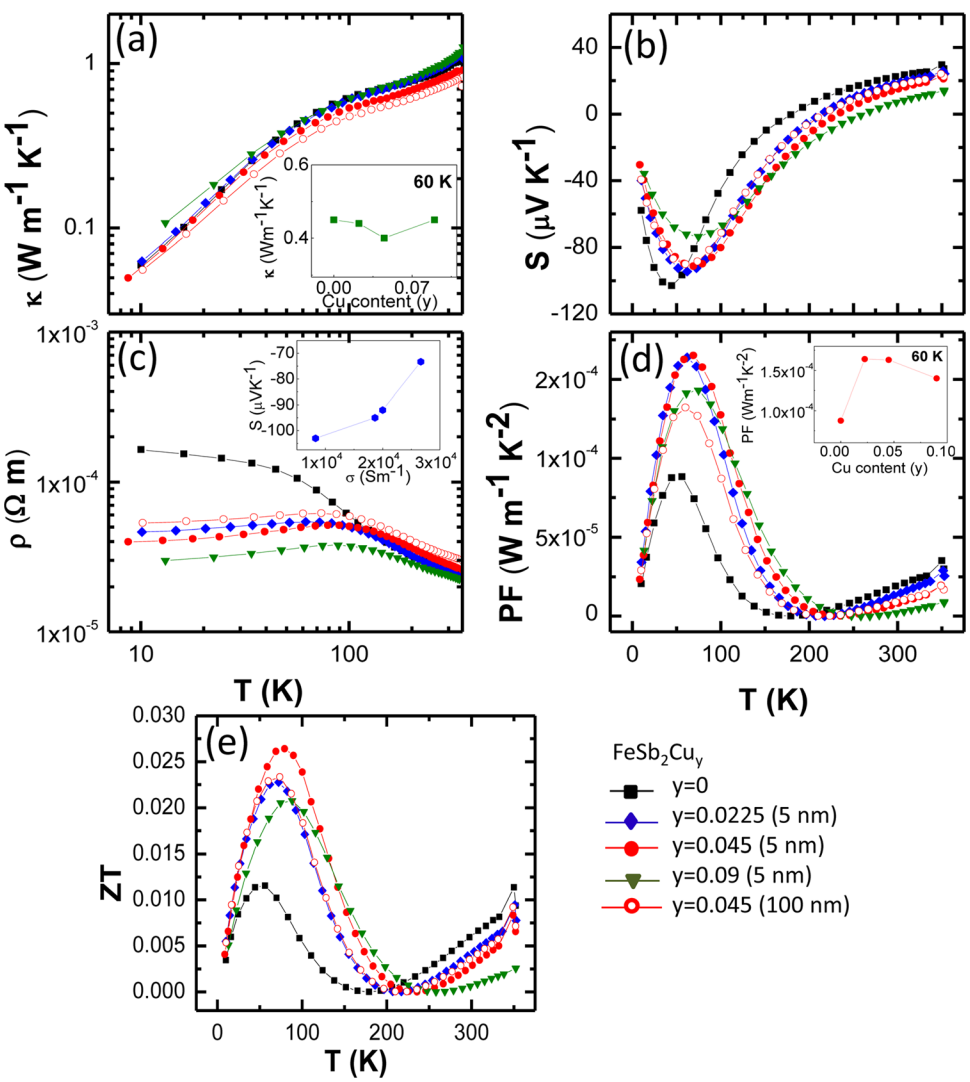

FIG. 3. Thermoelectric properties of $FeSb_2Cu_y$ ($y = 0$, 0.0225, 0.045, 0.09) samples: (a) temperature dependence of thermal conductivity, inset shows the measured thermal conductivity versus Cu content at 60 K; (b) temperature dependence of Seebeck coefficients; (c) temperature dependence of electrical resistivity, inset shows the peak Seebeck coefficient versus electrical conductivity at corresponding temperatures; (d) temperature dependence of power factor, inset shows the peak value of power factor at 60 K versus Cu content; and (e) temperature dependence of *ZT* for $FeSb_2$ and $FeSb_2Cu_y$ nanocomposites.

most samples. However, a notable difference between two $FeSb_2Cu_{0.045}$ samples was found, the one with larger Cu NPs (~100 nm) shows 20% lower thermal conductivity than that of pure $FeSb_2$ and 10% lower than the one with smaller Cu NPs (~5 nm). The former is understandable due to the interface phonon scattering, but the latter is very surprising and hard to understand at the moment. We guess the most possible reason is the subtle porosity difference between the two samples since our nanocomposites have relative density of 76% to 78%, as we have reported.[32]

As for all nanocomposites with ~5 nm Cu NPs, it is seen that with the increase of Cu content (inset of Fig. 3(a)), thermal conductivity at 60 K decreased slowly to a minimum of $0.39\,W\,m^{-1}\,K^{-1}$ for $FeSb_2Cu_{0.045}$ from $0.44\,W\,m^{-1}\,K^{-1}$ for the pure nanostructured $FeSb_2$. We believe that this is due to the phonon scattering at the interface of $FeSb_2$ and Cu. The minimum lattice thermal conductivity of $FeSb_2$ was reported to be $0.25\,W\,m^{-1}\,K^{-1}$ at 60 K,[33] indicating potential for further thermal conductivity reduction. When the Cu volume ratio reaches 1.8% for sample $FeSb_2Cu_{0.09}$, thermal conductivity becomes comparable to the pure nanostructured $FeSb_2$ and even larger below 50 K, which shows the contribution of increased electron thermal conductivity outweighs the decrease of the lattice thermal conductivity.

Seebeck coefficient results were shown in Fig. 3(b). Interestingly, the Seebeck coefficient only slightly decreases from $-102\,\mu V\,K^{-1}$ to $-93\,\mu V\,K^{-1}$ even though the electrical conductivity is increased by a factor of ~2 as shown is Fig. 3(c) for the $FeSb_2Cu_{0.045}$ sample with ~5 nm Cu NPs comparing to pure $FeSb_2$. The relatively high Seebeck coefficients at different concentrations of Cu nanoparticles can be understood as the result of modulation doping since the matrix $FeSb_2$ is not significantly affected.

Regarding the electrical conductivity shown in Fig. 3(c), we have achieved significant improvement by incorporating Cu NPs to the nanostructured $FeSb_2$. First, as temperature decreases, all the samples incorporated with Cu NPs show reduced electrical resistivity with metal-like features below 100 K compared to pure $FeSb_2$. Increasing the Cu content leads to reduced resistivity, while sample $FeSb_2Cu_{0.09}$ has the lowest resistivity. Clearly the $FeSb_2Cu_{0.045}$ sample having ~5 nm Cu NPs is more conductive than the samples with ~100 nm Cu NPs, probably due to better electron transfer from Cu to $FeSb_2$ when Cu is smaller and well dispersed in $FeSb_2$. Inset in Fig. 3(c) shows a peak Seebeck coefficient dependence of electrical conductivity for all nanocomposites with ~5 nm Cu NPs inclusion.

Because of the increased electrical conductivity and slightly reduced Seebeck coefficient for the $FeSb_2Cu_y$ nanocomposites, we observe a significant power factor *PF* improvement below 200 K for all Cu NPs incorporated nanocomposites compared to pure $FeSb_2$. As can be seen from Fig. 3(d)), a maximum $PF \sim 1.64 \times 10^{-4}\,W\,m^{-1}\,K^{-2}$ at 60 K was obtained for $FeSb_2Cu_{0.0225}$ before decreasing to $1.39 \times 10^{-4}\,W\,m^{-1}\,K^{-2}$ for $FeSb_2Cu_{0.045}$. Such a large improvement (~90%) over the pure $FeSb_2$ is comparable with the results achieved by other approaches such as resonant doping,[19–21] band engineering,[22,23] and modulation doping.[24,25] Combined with the slight decrease of thermal conductivity shown in Fig. 3(a), *ZT* of ~0.027 has been achieved, that is ~110% enhancement over ~0.013 achieved in the nanostructured pure $FeSb_2$ at 60 K.

In summary, we observed the figure-of-merit (*ZT*) improvement in nanostructured $FeSb_2Cu_y$ by modulation doping of Cu nanoparticles. Because of the favorable work functions between $FeSb_2$ and Cu nanoparticles, and the high electrical conductivity of Cu, the insulator-like electrical resistivity for $FeSb_2$ at low temperatures was reduced. It was found that the power factor was improved by ~90% and *ZT* ~110% for the optimized nanocomposite $FeSb_2Cu_{0.045}$ over the nanostructured pure $FeSb_2$. Our results suggest that a similar strategy could be extended to other Kondo insulators to enhance their TE properties if the modulation dopant does not severely react with the matrix.

The work was sponsored by Air Force Office of Scientific Research's MURI program under Contract No. FA9550-10-1-0533.

[1]S. R. Harutyunyan, V. H. Vardanyan, A. S. Kuzanyan, V. R. Nikoghosyan, S. Kunii, K. S. Wood, and A. M. Gulian, Appl. Phys. Lett. **83**(11), 2142 (2003).
[2]D. M. Rowe, M. Gao, and V. L. Kuznestsov, Philos. Mag. Lett. **77**(2), 105 (1998).
[3]B. C. Sales, O. Delaire, M. A. McGuire, and A. F. May, Phys. Rev. B **83**, 125209 (2011).
[4]A. Bentien, G. K. H. Madsen, S. Johnson, and B. B. Iversen, Phys. Rev. B **74**(20), 205105 (2006).
[5]A. Bentien, S. Johnsen, G. K. H. Madsen, B. B. Iversen, and F. Steglich, Europhys. Lett. **80**, 17008 (2007).
[6]P. Sun, N. Oeschler, S. Johnsen, B. B. Iversen, and F. Steglich, Phys. Rev. B **79**(15), 153308 (2009).
[7]P. Sun, N. Oeschler, S. Johnsen, B. B. Iversen, and F. Steglich, Dalton Trans. **39**, 1012 (2010).
[8]P. Sun, M. Søndergaard, Y. Sun, S. Johnsen, B. B. Iversen, and F. Steglich, Appl. Phys. Lett. **98**, 072105 (2011).
[9]M. S. Diakhate, R. P. Hermann, A. Möchel, I. Sergueev, M. Søndergaard, M. Christensen, and M. J. Verstraete, Phys. Rev. B **84**(12), 125210 (2011).
[10]A. Mani, J. Janaki, A. T. Satya, T. G. Kumary, and A. Bharathi, J. Phys.: Condens. Matter **24**, 075601 (2012).
[11]B. C. Sales, A. F. May, M. A. McGuire, M. B. Stone, D. J. Singh, and D. Mandrus, Phys. Rev. B **86**, 235136 (2012).
[12]Q. Jie, R. Hu, E. Bozin, A. Llobet, I. Zaliznyak, C. Petrovic, and Q. Li, Phys. Rev. B **86**(11), 115121 (2012).
[13]H. Z. Zhao, M. Pokharel, G. H. Zhu, S. Chen, K. Lukas, Q. Jie, C. Opeil, G. Chen, and Z. F. Ren, Appl. Phys. Lett. **99**, 163101 (2011).
[14]E. L. Thomas, W. Wong-Ng, D. Phelan, and J. N. Millican, J. Appl. Phys. **105**, 073906 (2009).
[15]A. Amato, D. Jaccard, J. Flouquet, F. Lapierre, J. L. Tholence, R. A. Fisher, S. F. Lacy, J. A. Olsen, and N. E. Phillips, J. Low Temp. Phys. **68**(5–6), 371 (1987).
[16]K. F. Hsu, S. Loo, F. Guo, W. Chen, J. S. Dyck, C. Uher, T. Hogan, E. K. Polychroniadis, and M. G. Kanatzidis, Science **303**(5659), 818 (2004).
[17]B. Poudel, Q. Hao, Y. Ma, Y. Lan, A. Minnich, B. Yu, X. Yan, D. Wang, A. Muto, D. Vashaee, X. Chen, J. Liu, M. S. Dresselhaus, G. Chen, and Z. F. Ren, Science **320**(5876), 634 (2008).
[18]X. Yan, G. Joshi, W. S. Liu, Y. C. Lan, H. Wang, S. Lee, J. W. Simonson, S. J. Poon, T. M. Tritt, G. Chen, and Z. F. Ren, Nano Lett. **11**, 556 (2011).
[19]J. P. Heremans, V. Jovovic, E. S. Toberer, A. Saramat, K. Kurosaki, A. Charoenphakdee, S. Yamanaka, and G. J. Snyder, Science **321**, 554 (2008).
[20]Q. Y. Zhang, H. Wang, W. S. Liu, H. Z. Wang, B. Yu, Q. Zhang, Z. T. Tian, G. Ni, S. Lee, K. Esfarjani, G. Chen, and Z. F. Ren, Energy Environ. Sci. **5**, 5246 (2012).
[21]J. P. Heremans, B. Wiendlocha, and A. M. Chamoire, Energy Environ. Sci. **5**, 5510 (2012).
[22]Y. Z. Pei, X. Y. Shi, A. LaLonde, H. Wang, L. D. Chen, and G. J. Snyder, Nature **473**, 66 (2011).
[23]Q. Zhang, F. Cao, W. S. Liu, K. Lukas, B. Yu, S. Chen, C. Opeil, D. Broido, G. Chen, and Z. F. Ren, J. Am. Chem. Soc. **134**, 10031 (2012).

[24]M. Zebarjadi, G. Joshi, G. H. Zhu, B. Yu, A. Minnich, Y. C. Lan, X. W. Wang, M. S. Dresselhaus, Z. F. Ren, and G. Chen, Nano Lett. **11**, 2225 (2011).
[25]B. Yu, M. Zebarjadi, H. Wang, K. Lukas, H. Z. Wang, D. Z. Wang, C. Opeil, M. S. Dresselhaus, G. Chen, and Z. F. Ren, Nano Lett. **12**, 2077 (2012).
[26]J. P. Heremans, C. M. Thrush, and D. T. Morelli, J. Appl. Phys. **98**, 063703 (2005).
[27]W. Kim, J. Zide, A. Gossard, D. Klenov, S. Stemmer, A. Shakouri, and A. Majumdar, Phys. Rev. Lett. **96**(4), 045901 (2006).
[28]S. V. Faleev and F. Léonard, Phys. Rev. B. **77**(21), 214304 (2008).
[29]M. Zebarjadi, K. Esfarjani, A. Shakouri, J.-H. Bahk, and Z. X. Bian, Appl. Phys. Lett. **94**, 202105 (2009).
[30]S. Sumithra, N. J. Takas, D. K. Misra, W. M. Nolting, P. F. P. Poudeu, and K. L. Stokes, Adv. Energy Mater. **1**, 1141 (2011).
[31]D. K. Ko, Y. J. Kang, and C. B. Murray, Nano Lett. **11**, 2841 (2011).
[32]H. Z. Zhao, M. Pokharel, S. Chen, B. Liao, K. Lukas, C. Opeil, G. Chen, and Z. F. Ren, Nanotechnology **23**, 505402 (2012).
[33]S. Zhu, W. J. Xie, D. Thompson, T. Holgate, M. H. Zhou, Y. G. Yan, and T. M. Tritt, J. Mater. Res. **26**(15), 1894 (2011).

NANO LETTERS

Letter

pubs.acs.org/NanoLett

Nanostructured $YbAgCu_4$ for Potentially Cryogenic Thermoelectric Cooling

Machhindra Koirala,[†] Hui Wang,[†] Mani Pokharel,[‡] Yucheng Lan,[†] Chuanfei Guo,[†] Cyril Opeil,[‡] and Zhifeng Ren[†,*]

[†]Department of Physics and TcSUH, University of Houston, Houston, Texas 77204, United States

[‡]Department of Physics, Boston College, Chesnut Hill, Massachusetts 02467, United States

ABSTRACT: We have studied the thermoelectric properties of nanostructured $YbAgCu_4$ materials. A high power factor of ~131 μW cm^{-1} K^{-2} has been obtained at 22 K for nanostructured samples prepared by ball milling the arc melted ingot into nanopowder and hot pressing the nanopowder. The implementation of nanostructuring method decreased the thermal conductivity at 42 K by 30−50% through boundary scattering comparing with the previously reported value of polycrystalline $YbAgCu_4$. A peak dimensionless thermoelectric figure-of-merit, ZT, of 0.11 has been achieved at 42 K, which may find potential applications for cryogenic cooling below 77 K. The nanostructuring approach can be extended to other heavy Fermion materials to achieve high power factor and low thermal conductivity and ultimately higher ZT.

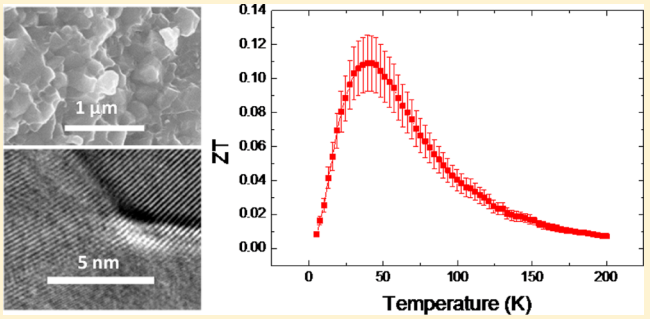

KEYWORDS: *Thermoelectric, heavy Fermions, Kondo lattice, boundary scattering, $YbAgCu_4$*

The ability of thermoelectric (TE) materials for converting heat into electricity and vice versa is very important for power generation[1,2] as well as solid-state cooling.[3] For the aerospace program where the weight and size compatibility of the devices is important, thermoelectric devices are more useful for cryogenic application in comparison to other heavy cooling devices. The power generation efficiency or coefficient of performance of thermoelectric devices are determined by the dimensionless figure of merit, $ZT = [(S^2\sigma)/\kappa]T$, where S is the Seebeck coefficient, σ is the electrical conductivity, κ is the thermal conductivity, and T is the absolute temperature.[4−6] All of these quantities are related to each other and changing one affects the others, so increasing ZT is really challenging. In the recent years, the development of new techniques for controlling the material properties through nanostructuring,[7] modulation doping,[8,9] resonant doping,[10,11] and band engineering near Fermi level[12,13] have helped to enhance ZT significantly. The rapid development of technologies enabled to increases ZT above 1 for cooling applications at around room temperature and power generation at high temperatures but at the low-temperature (cryogenic) range, the existing ZT is far below the application requirement.

For low-temperature thermoelectric materials, most of the focus is toward narrow band gap semiconductors and Kondo insulators. In different temperature ranges below room temperature, there are many materials that are being investigated. The well-known low-temperature thermoelectric material is single crystal $Bi_{1-x}Sb_x$ with ZT ~ 0.5 at ~150 K.[14] Encapsulating Ce in clathrate has enhanced ZT to 0.1 at 150 K.[15] Doping on extremely high mobility materials CuAgSe has enhanced ZT to 0.1 at 100 K.[16] Doped FeSi have been reported to have peak ZT of 0.12 at 120 K.[17] However, the operating temperature for these materials is above 100 K, which is above liquid nitrogen temperature, 77 K. For temperature below 77 K, ZT is very low because the temperature T is very small.

The current trend for cryogenic thermoelectric materials involves mostly Kondo insulators like $FeSb_2$,[18−20] $CrSb_2$,[21] and some rare earth Kondo systems like $YbAl_3$,[22] $CeCu_6$,[23] $Ce_{0.5}La_{0.5}Al_3$,[24] YbCuAl,[25] $CeAl_3$,[25] $CePd_3$,[26] and so forth. Rare earth metallic heavy Fermions like $YbAl_3$, $CePd_3$[26] have been investigated to the temperature range of 150 K and a peak ZT ~ 0.23 have been reported for both n- and p-type. Our focus in this work is to study materials having good ZT at below 77 K. $FeSb_2$ was studied for its giant Seebeck coefficient below 77 K by Bentein.[18] Much effort have been made on that materials but the optimized ZT is not more than 0.026.[18−20,27] In phonon drag systems like $FeSb_2$[28] and $CrSb_2$, it is very difficult to decouple the electrical and phonon part and the value of ZT remains low. There are some rare earth Kondo systems with good power factor at temperature below 77 K, but they have high thermal conductivity so the overall ZT is low. Maintaining that high power factor and reducing thermal conductivity is really challenging.

Received: April 17, 2014
Revised: July 17, 2014
Published: July 31, 2014

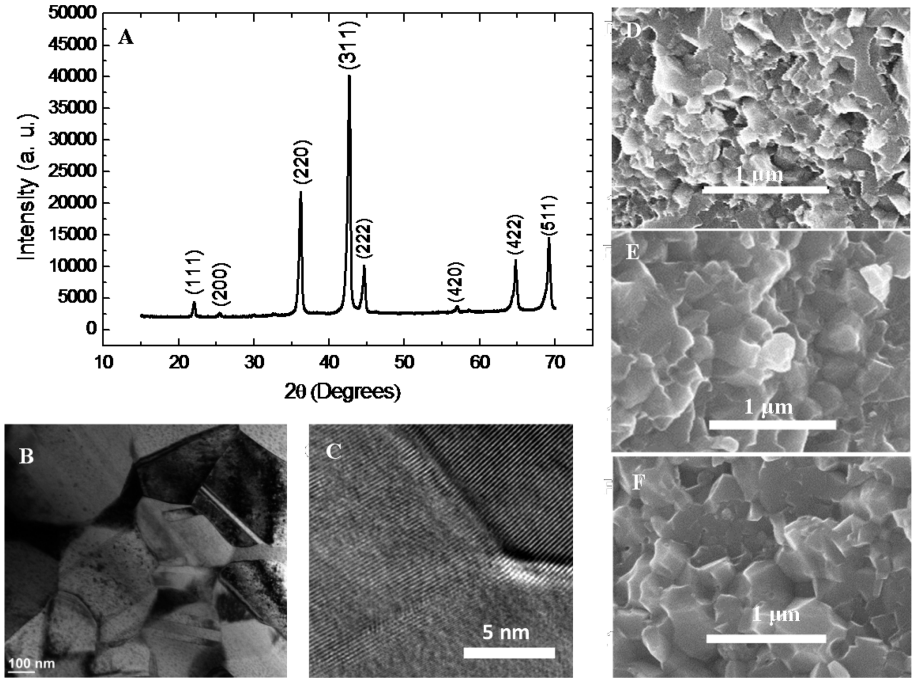

Figure 1. XRD pattern (A) and TEM images (B,C) for $YbAgCu_4$ samples hot pressed at 750 °C, SEM images for $YbAgCu_4$ samples hot pressed at temperatures of 550 (D), 650 (E), and 750 °C (F).

Here, we present the synthesis and characterization of the thermoelectric properties of nanostructured $YbAgCu_4$. This material was discovered as heavy Fermion materials in 1987 by Rossel[29] with moderate effective mass. $YbAgCu_4$ comes from the family of parent compound $YbCu_5$ that is nonmagnetic and metallic with hexagonal structure.[30−32] The replacing of one Cu atom by Ag makes a dramatic change in crystal structure and turns it into face-centered cubic (fcc) structure.[33] The spin exchange interaction between f orbital and conduction electron is much stronger than the intersite Ruderman−Kittel−Kasuya−Yosida (RKKY) interaction and any other possible crystalline field splitting effect.[29,34] There is the presence of the giant Seebeck peak at 45 K which is due to Kondo scattering of conduction electron from almost the full f band.[35] The thermal conductivity of $YbAgCu_4$ is unusually low below 50 K in comparison to other heavy Fermion systems,[36] which makes this material worth for investigation as TE materials. This material has been noted by Mahan[25] as having a high power factor of ∼235 μW cm^{-1} K^{-2} on the basis of two earlier published papers[35,37] by inappropriately using the electrical resistivity data from Graf[37] and Seebeck coefficient data from Casanova.[35] Nevertheless, we endeavor to study the thermoelectric properties of a series of samples to determine whether such a high power factor can be achieved. It is also intended to study whether lower thermal conductivity can be achieved in this material by nanostructuring while maintaining the high power factor.

Experimental Section. Nanostructured $YbAgCu_4$ was prepared by arc melting followed by ball milling process. The stoichiometric ratio of 99.9% pure Ag and 99.9% Cu granular from Alfa Aesar is kept in an arc melting hearth and melted to make the single piece. Pure Yb pieces (99.9%) with 10 % extra form stoichiometric ratio is kept in the arc melting hearth with the Ag−Cu piece and melted together. The main idea for this melting approach is to avoid the direct contact of arc with Yb, which is volatile in nature. The melting process was repeated 8 times by monitoring the total weight loss at each time. The ingot was polished with metal brush and ball milled for 6 h in high energy ball milling machine. The powder was dc hot pressed at 550, 650, and 750 °C and a pressure of 100 MPa for 5 min. The samples were characterized by X-ray diffraction (Panalytical X'pert), high-resolution transmission electron microscope (HRTEM, JEOL 2100F), and scanning electron microscope (SEM, LEO 1525) to characterize the phase formation, crystallinity, homogeneity, grain size distribution, and grain boundary. Samples of 3 × 3 × 5 cm^3 were measured for temperature-dependent electrical conductivity, Seebeck coefficient, and thermal conductivity using thermal transport option by physical properties measurement system (Quantum design, PPMS with TTO).

Results and Discussion. Figure 1A presents the XRD pattern of the sample hot pressed at 750 °C for 5 min. The sample is single phase within the detection limit of the XRD machine and can be indexed by $AuBe_5$-type face-centered cubic structure. The TEM images shown in Figure 1B,C indicate that the grains are closely packed and the crystallinity of the grains is good and the grain boundaries are clean. The samples hot pressed at different temperatures were analyzed using SEM to study the effect of hot pressing temperature on the grain size and distribution. Figure 1D−F shows that the average grain size is 100 ± 25, 175 ± 25, and 225 ± 25 nm for the samples hot pressed at 550, 650, and 750 °C, respectively.

We have measured the thermoelectric properties of $YbAgCu_4$ samples and the results are presented in Figures 2 and 3. Electrical resistivity data are presented in Figures 2A and 3A. It is clearly seen that the samples show pretty strong metallic behavior below 75 K and a weak semiconductor behavior above 75 K. The electrical transport data can be explained in the basis of phenomenological method which is being used for many heavy Fermion systems.[38−40] The dominant contribution to electrical resistivity is due to electron−phonon interaction and scattering of electron between conduction band and

dx.doi.org/10.1021/nl501436w | Nano Lett. 2014, 14, 5016−5020

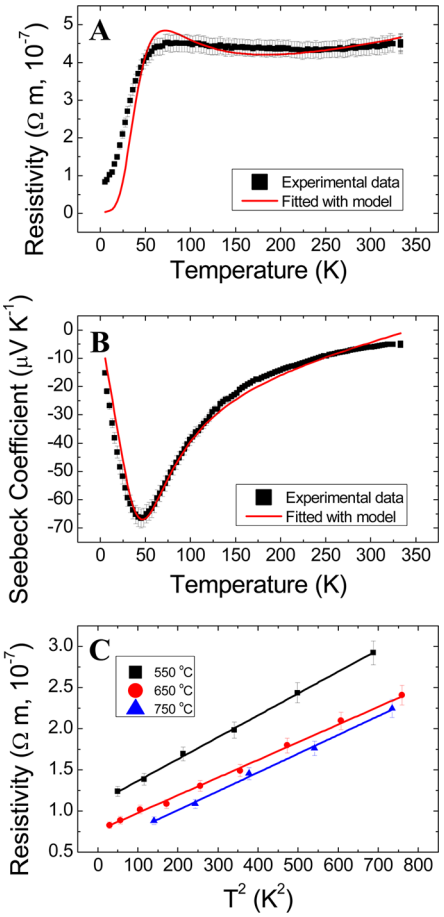

Figure 2. Temperature-dependent resistivity (A) and Seebeck coefficient (B) fitted with phenomenological model for samples hot pressed at 650 °C. Plot of electrical resistivity ρ versus T^2 below 27 K for $YbAgCu_4$ (C).

Lorentzian-shaped 4f band. Using the Mott's analogy, resistivity due to scattering of electron of conduction band and f band is proportional to the density of states of f states at Fermi level.[41] Hence, electrical resistivity can be written as[38,39]

$$\rho = aT + \frac{bW(T)}{(T_o^2 + (W(T))^2)} \quad (1)$$

where $W(T) = T_f \exp(-T_f/T)$ is the width of f band and T_o ($k_\beta T_o = \varepsilon_F - \varepsilon_f$ where ε_F is the Fermi energy and ε_f the is energy corresponding to center of gravity of 4f peak) is the central position of 4f band from Fermi level. The term T_f is a temperature-dependent parameter and related to quasi-elastic line width of neutron spectra. The coefficients a and b represent the strength of electron phonon scattering and the strength of hybridization between s and f bands, respectively. The quasi-elastic line width for $YbAgCu_4$ is reported to be invariant with temperature[42] and the value of T_f is reported to be 100 K.[42,43] The coefficients a and b are obtained from fitting the resistivity curve and found to be 6.51×10^{-10} Ω m K^{-1} and 2.02×10^{-5} Ω m K, respectively. From Figure 2A, we have seen that experimental data can be fitted with model very well with T_o = 23 K. The difference between the experimental and fitted data near the resistivity maxima temperature could be due to defects and the grain boundary presented in the sample.

In the range of 75 to 200 K, there is formation of dilute Kondo system. In that temperature range, there is an increase of electrical resistivity with decreasing temperature. This is due to Kondo scattering of electrons between conduction and f bands. When the temperature goes below 75 K, the dilute Kondo system transformed to Kondo lattice system with sharp decrease in electrical resistivity. Electrical resistivity for samples hot pressed at different temperatures is presented in Figure 3A. The electrical resistivity of a sample hot pressed at 550 °C is higher compared to the other two samples. This can be understood as conduction electron scattering by the weakly linked grain boundary that resulted from the low hot press temperature.

At the very low temperature, the system behaves as Fermi liquid system with resistivity linear to square of the temperature of the system as discussed in refs 33 and 44. At that temperature range, it is not reasonable to expect the matching of experimental data with phenomenological model. Figure 2C shows that the electrical resistivity of all samples can be fitted with Fermi liquid theory below 27 K. The slope of the resistivity with T^2 is proportional to the density of states of conduction electron. In our samples, we have seen that the Fermi liquid behavior can be seen up to 27 K indicating that the electronic motion is not much affected by grain size. Therefore, the nanostructures do not affect the electronic contribution arising from band hybridization of the 4f and conduction bands.

Using the Lorentzian density of states of f band at Fermi level, the Seebeck coefficient can be expressed as

$$S = c_1 T + \frac{c_2 T T_o}{(T_o^2 + (W(T))^2)} \quad (2)$$

where the first term gives the nonmagnetic contribution to Seebeck coefficient and the second term gives the magnetic contribution to Seebeck coefficient. We have used the same value T_f (100 K) and extracted value for T_o (23 K) using resistivity relation and fitted the Seebeck coefficient. Our Seebeck coefficient data match with the phenomenological model with c_1 = 0.175 μV K^{-2} and c_2 = −46.713 μV K^{-1} showing that most of the contribution on the Seebeck coefficient is from the magnetic scattering of conduction electron by the f band. From the extracted value of T_o (23 K), we have found that the center of the f band is 1.9 meV below the Fermi level giving the negative slope of density of states of the f band at Fermi level which makes the negative Seebeck coefficient of $YbAgCu_4$. The presence of a flat f band could enhance the density of states near the Fermi level, which enhances Seebeck coefficient.[45] From Figure 3B, for our nanostructured sample we have achieved absolute maximum Seebeck coefficient of 66 μV K^{-1} at 45 K. From this analysis, we can conclude that the simple phenomenological model can explain Seebeck coefficient of $YbAgCu_4$.

Figure 3C shows the power factor of the $YbAgCu_4$ samples hot pressed at different temperatures. Because the absolute maxima of Seebeck coefficient and resistivity minimum occur at two different temperatures, we observed the highest power factor of 131 μW cm^{-1} K^{-2} at 22 K. Even though it is much lower than 235 μW cm^{-1} K^{-2} calculated by Mahan[25] on the basis of the previously published papers,[35,36] it is already much higher than most of the other good TE materials such as Bi_2Te_3[46] and $Bi_{1-x}Sb_x$.[14] Although very high power factors have been reported for the $FeSb_2$ single crystal,[18] it cannot be maintained in nanostructured samples with very lower thermal conductivity. Thermal conductivity decreases with grain size but also the peak Seebeck coefficient and hence the power

dx.doi.org/10.1021/nl501436w | Nano Lett. 2014, 14, 5016−5020

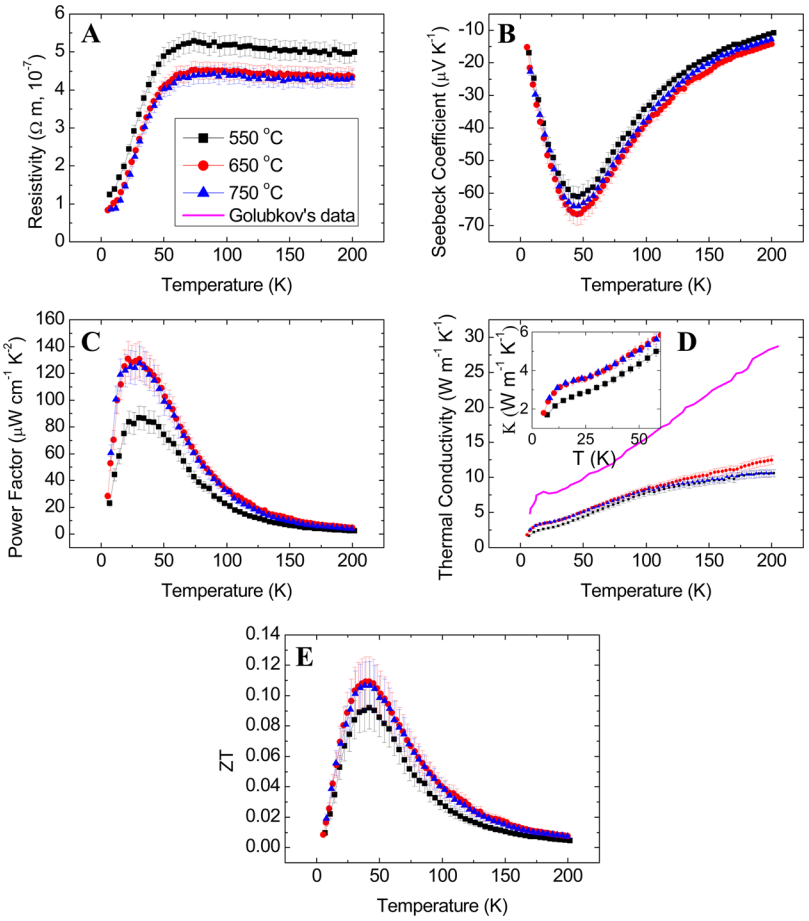

Figure 3. Thermoelectric properties of nanostructured $YbAgCu_4$ samples hot pressed at different temperatures. Temperature-dependent electrical resistivity (A), Seebeck coefficient (B), power factor (C), thermal conductivity with the reference data from Golubkov et al.[36] for comparison (D), and ZT with 15% uncertainty in measurement (E).

factor and overall ZT enhancement is not significant. For our system, we did not notice a big decrease of Seebeck coefficient with grain size. The samples hot pressed at 650 and 750 °C have nearly the same power factors and are higher than that of the sample hot pressed at 550 °C.

Figure 3D shows the thermal conductivity of these samples. They all show a similar trend: decrease with temperature. The thermal conductivity of the samples hot pressed at 550 °C is a little bit smaller than the other two samples hot pressed at a higher temperature. Because the grain size of the samples hot pressed at 650 and 750 °C is not much different, hence the thermal conductivity is also similar. In heavy Fermions systems, the formation of gap due to hybridization of bands enhances the phonon mean free path and hence the thermal conductivity of these materials is very high.[4] In many heavy Fermion systems, the lattice thermal conductivity of doped samples is of the same magnitude of undoped sample[26] suggesting point defect scattering is not effective to decrease thermal conductivity. Short intrinsic electronic mean free path of heavy Fermions suggests that boundary scattering of phonon is one of the promising ways to decrease the thermal conductivity without significantly affecting the electrical properties of such systems.[47] We did not find any report for thermal conductivity of single crystal $YbAgCu_4$ for comparison of boundary scattering. There are a couple of reports on thermal conductivity of polycrystalline $YbAgCu_4$.[36,48] In comparison, the nanostructure reduces the thermal conductivity by 30−50% through boundary scattering of phonons comparing with the earlier reported value for polycrystalline sample (data from ref 36 is plotted in Figure 3D for comparison). Although, the grain size information on the refs 36 and 48 is not available, from their synthesis method it could be speculated that the grain size of their polycrystalline samples should be in the order of several microns.

Figure 3E shows the thermoelectric figure of merit ZT of $YbAgCu_4$ samples. We note a peak ZT of 0.11 at 42 K has been achieved for samples hot pressed at 650 and 750 °C. This is pretty high at this low temperature, which will take us one step further to the cooling applications at this temperature.

In conclusion, we have synthesized and characterized nanostructured $YbAgCu_4$ using ball milling the arc melted ingot and hot pressing method. The Seebeck coefficient in Yb-based heavy Fermions is due to Kondo scattering of electrons between conduction band and 4f band. The electrical resistivity and Seebeck coefficient of nanostructured sample can be explained in terms of the well-known phenomenological model. The good electrical conductivity of $YbAgCu_4$ leads to a high power factor of 131 $\mu W\ cm^{-1}\ K^{-2}$ at 22 K. We have maintained the high power factor with a significantly lower thermal conductivity. The high power factor is clearly advantageous for higher ZT. A peak ZT of 0.11 has been achieved at 42 K, suitable for cooling down to this temperature. Our results bring us one step closer for using TE materials for Peltier cooling purpose below liquid nitrogen temperature. We believe that this

dx.doi.org/10.1021/nl501436w | *Nano Lett.* 2014, 14, 5016−5020

result will attract more research effort for this and other similar material systems to make the TE cooling below liquid nitrogen temperature a reality.

AUTHOR INFORMATION

Corresponding Author

*E-mail: zren@uh.edu.

Notes

The authors declare no competing financial interest.

ACKNOWLEDGMENTS

The work was financially supported by Air Force Office of Scientific Research's MURI program under Contract No. FA9550-10-1-0533.

REFERENCES

(1) Ioffe, A. F. *Physics of Semiconductors*; Academic Press: New York, 1960.
(2) Slack, G. A.; Hussain, M. A. *J. Appl. Phys.* **1991**, *70*, 2694.
(3) Taylog, R. A.; Solbrekken, G. L. *IEEE Trans. Compon. Packag. Technol.* **2008**, *31*, 23.
(4) Rowe, D. M. *CRC Handbook of Thermoelectrics*; CRC Press: Boca Raton, 1995.
(5) Goldsmid, H. J *Thermoelectric Refrigeration*; Plenum: New York, 1964.
(6) Tritt, T. M. *Semiconductor and Semimetals, Recent Trends in Thermoelectric Materials Research, Part 1−3*; Academic: San Diego, CA, 2001; Vol. *69−71*.
(7) Poudel, B.; Hao, Q.; Ma, Y. C.; Lan, Y.; Minnich, A.; Yu, B.; Yan, X.; Wang, D. Z.; Muto, A.; Vashaee, D.; Chen, X.; Liu, J.; Dresselhaus, M. S.; Chen, G.; Ren, Z. F. *Science* **2008**, *320*, 634.
(8) Zebarjadi, M.; Joshi, G.; Zhu, G.; Yu, B.; Minnich, A.; Lan, Y. C.; Wang, X.; Dresselhaus, M.; Ren, Z. F.; Chen, G. *Nano Lett.* **2011**, *11*, 2225.
(9) Yu, B.; Zerbarjadi, M.; Wang, H.; Lukas, K.; Wang, H.; Wang, D.; Opeil, C.; Dresselhaus, M.; Chen, G.; Ren, Z. F. *Nano Lett.* **2012**, *12*, 2077.
(10) Heremans, J. P.; Jovovic, V.; Toberer, E. S.; Saramat, A.; Kurosaki, K.; Charoenphakdee, A.; Yamanaka, S.; Snyder, G. J. *Science* **2008**, *321*, 554.
(11) Heremans, J. P.; Wiendlocha, B.; Chamoire, A. M. *Energy Environ. Sci.* **2012**, *5*, 5510.
(12) Pei, Y. Z.; Shi, X. Y.; LaLonde, A.; Wang, H.; Chen, L. D.; Snyder, G. J. *Nature* **2011**, *473*, 66.
(13) Zhang, Q.; Cao, F.; Liu, W. S.; Lukas, K.; Yu, B.; Chen, S.; Opeil, C.; Broido, D.; Chen, G.; Ren, Z. F. *J. Am. Chem. Soc.* **2012**, *134*, 10031.
(14) Smith, G. E.; Wolfe, R. *J. Appl. Phys.* **1962**, *33*, 841.
(15) Prokofiev, A.; Sidorenko, A.; Hradil, K.; Ikeda, M.; Svagera, R.; Waas, M.; Winkler, H.; Neumaier, K.; Paschen, S. *Nat. Mater.* **2013**, *12*, 1096.
(16) Ishiwata, S.; Shiomi, Y.; Lee, J. S.; Bahramy, M. S.; Suzuki, T.; Uchida, M.; Arita, R.; Taguchi, Y.; Tokura, Y. *Nat. Mater.* **2013**, *12*, 512.
(17) Sales, B. C.; Delaire, O.; McGuire, V. L.; May, A. F. *Phys. Rev. B* **2011**, *83*, 125209.
(18) Bentien, A.; Johnson, S.; Madsen, G. K. H.; Iverson, B. B.; Steglich, F. *Europhys. Lett.* **2007**, *80*, 17008.
(19) Zhao, H. Z.; Pokharel, M.; Zhu, G.; Chen, S.; Lukas, K.; Jie, Q.; Opeil, C.; Chen, G.; Ren, Z. F. *Appl. Phys. Lett.* **2011**, *99*, 163101.
(20) Koirala, M.; Zhao, H. Z.; Pokharel, M.; Chen, S.; Dahal, T.; Opeil, C.; Chen, G.; Ren, Z. F. *Appl. Phys. Lett.* **2013**, *102*, 213111.
(21) Sales, B. C.; May, A. F.; McGuire, M. A.; Stone, M. B.; Singh, D. J.; Mandrus, D. *Phys. Rev. B* **2012**, *86*, 235136.
(22) Lehr, G. J.; Morelli, D. T. *J. Electron. Mater.* **2013**, *42*, 1697.
(23) Ocko, M.; Miljak, M.; Kost, I.; Park, J.-G.; Roy, S. B. *J. Phys.: Condens. Matter* **1995**, *7*, 2979.
(24) Van Aken, P. B.; Van Daal, H. J.; Buschow, K. H. J. *Phys. Lett. A* **1974**, *49*, 201.
(25) Mahan, G. D. *Solid State Physics* **1998**, *51*, 81.
(26) Mahan, G. D.; Sales, B.; Sharp, J. *Phys. Today* **1997**, *50* (3), 42.
(27) Sun, P.; Sondergaard, M.; Sun, Y.; Johnsen, S.; Iversen, B. B.; Steglich, F. *Appl. Phys. Lett.* **2011**, *98*, 072105.
(28) Pokharel, M.; Zhao, H.; Lukas, K.; Ren, Z. F.; Opeil, C.; Mihaila, B. *MRS Commun.* **2013**, *3*, 31.
(29) Rossel, C.; Yang, K. N.; Maple, M. B.; Fisk, Z.; Zirngiebl, E.; Thompson, J. D. *Phys. Rev. B* **1987**, *35*, 1914.
(30) Tsujii, N.; He, J.; Amita, F.; Yoshimura, K.; Kosuge, K.; Michor, H.; Hilscher, G.; Goto, T. *Phys. Rev. B* **1997**, *56*, 8103.
(31) Mitsuda, A.; Yamauchi, K.; Tsujii, N.; Yoshimura, K.; Isikawa, Y.; Yamada, Y. *J. Phys. Soc. Jpn.* **2007**, *76*, 78.
(32) Yamaoka, H.; jarrige, I.; Tsujii, N.; Hiraoka, N.; Ishii, H.; Tuesi, K.-D. *Phys. Rev. B* **2009**, *80*, 035120.
(33) Tsujii, N.; He, J.; Yoshimura, K.; Kosuge, K.; Michor, H.; Kreiner, K.; Hilscher, G. *Phys. Rev. B* **1997**, *55*, 1032.
(34) Schlottmann, P. *J. Appl. Phys.* **1993**, *73*, 5412.
(35) Casanova, R.; Jaccard, D.; Marcenat, C.; Hamdaoui, C.; Besnus, M. J. *J. Magn. Magn. Mater.* **1990**, *90 & 91*, 587.
(36) Golubkov, A. V.; Parfen'eva, L. S.; Smirnov, I. A.; Misiorek, H.; Mucha, J.; Jezowski, A. *Phys. Solid State* **2001**, *43*, 218.
(37) Graf, T.; Lawrence, J. M.; Hundley, M. F.; Thompson, J. D.; Lacerda, A.; Haanappel, E.; Torikachvili, M. S.; Fisk, Z.; Canfield, P. C. *Phys. Rev. B* **1995**, *51*, 15053.
(38) Freimuth, A. *J. Magn. Magn. Mater.* **1987**, *68*, 28.
(39) Grade, C. S.; Ray, J. *Phys. Rev. B* **1995**, *51*, 2960.
(40) Gumeniuk, R.; Sarkar, R.; Geibel, C.; Schnelle, W.; Paulmann, C.; Beanitz, M.; Tsirlin, A. A.; Guritanu, V.; Sichelschmidt, J.; Grin, Y.; Leithe-Jasper, A. *Phys. Rev. B* **2012**, *86*, 235138.
(41) Mott, N. F. *Proc. Phys. Soc.* **1935**, *47*, 571.
(42) Severing, A.; Murani, A. P.; Thompson, J. D.; Fisk, Z.; Loong, C.- K. *Phys. Rev. B* **1990**, *41*, 1739.
(43) Luthi, B. *Physical Acoustics in the Solid State*; Springer Series in Solid-State Sciences; Springer-Verlag, Berlin Heidelberg, 2005; p 148.
(44) Bauer, E.; Hausser, R.; Gratz, E.; Payer, K. *Phys. Rev. B* **1993**, *48*, 15873.
(45) Sun, P.; Ikeno, T.; Mizushima, T.; Isikawa, Y. *Phys. Rev. B* **2009**, *80*, 193105.
(46) Goncalves, L. M.; Couto, C.; Alpuimb, P.; Rolo, A. G.; Völkleinc, F.; Correia, J. H. *Thin Solid Films* **2009**, *518*, 2816.
(47) Zhang, Y.; Dresselhaus, M.; Shi, Y.; Ren, Z. F.; Chen, G. *Nano Lett.* **2011**, *11*, 1166.
(48) Bauer, E.; Gratz, E.; Hutflesz, G.; Bhattacharjee, A. K.; Coqblin, B. *Phys. B* **1993**, *186 − 188*, 494.

nature COMMUNICATIONS

ARTICLE

Received 10 Aug 2013 | Accepted 4 Feb 2014 | Published 25 Feb 2014

DOI: 10.1038/ncomms4377

Carrier localization and electronic phase separation in a doped spin-orbit-driven Mott phase in $Sr_3(Ir_{1-x}Ru_x)_2O_7$

Chetan Dhital[1], Tom Hogan[1], Wenwen Zhou[1], Xiang Chen[1], Zhensong Ren[1], Mani Pokharel[1], Yoshinori Okada[1], M. Heine[1], Wei Tian[2], Z. Yamani[3], C. Opeil[1], J.S. Helton[4], J.W. Lynn[4], Ziqiang Wang[1], Vidya Madhavan[1] & Stephen D. Wilson[1]

Interest in many strongly spin-orbit-coupled *5d*-transition metal oxide insulators stems from mapping their electronic structures to a $J_{eff} = 1/2$ Mott phase. One of the hopes is to establish their Mott parent states and explore these systems' potential of realizing novel electronic states upon carrier doping. However, once doped, little is understood regarding the role of their reduced Coulomb interaction *U* relative to their strongly correlated 3*d*-electron cousins. Here we show that, upon hole-doping a candidate $J_{eff} = 1/2$ Mott insulator, carriers remain localized within a nanoscale phase-separated ground state. A percolative metal–insulator transition occurs with interplay between localized and itinerant regions, stabilizing an anti-ferromagnetic metallic phase beyond the critical region. Our results demonstrate a surprising parallel between doped 5*d*- and 3*d*-electron Mott systems and suggest either through the near-degeneracy of nearby electronic phases or direct carrier localization that *U* is essential to the carrier response of this doped spin-orbit Mott insulator.

[1] Department of Physics, Boston College, Chestnut Hill, Massachusetts 02467, USA. [2] Quantum Condensed Matter Division, Oak Ridge National Laboratory, Oak Ridge, Tennessee 37831-6393, USA. [3] Chalk River Laboratories, Canadian Neutron Beam Centre, National Research Council, Chalk River, Ontario, Canada K0J 1P0. [4] NIST Center for Neutron Research, National Institute of Standards and Technology, Gaithersburg, Maryland 20899-6102, USA. Correspondence and requests for materials should be addressed to S.D.W. (email: stephen.wilson@bc.edu).

Iridium^{4+} ions with a half-filled $5d$ shell in a cubic octahedral oxygen coordination occupy a unique region in relative energy scales: one where a model of crystal field splitting combined with strong spin-orbit coupling (SOC) breaks the fivefold degeneracy of electronic states into fully occupied $J_{\rm eff}=3/2$ and half-filled $J_{\rm eff}=1/2$ bands[1,2]. The resulting bandwidth-narrowed $J_{\rm eff}=1/2$ states allow the relatively modest $U(\sim 1.5$–$2\,{\rm eV})$ inherent to these $5d$-transition metal elements[3] to split the band and generate a charge gap. A SOC-assisted Mott phase results, allowing an unexpected manifestation of correlation-driven physics in materials with extended $5d$-electron wave functions. Doping this spin-orbit Mott phase has since generated predictions of stabilizing states analogous to those found in doped strongly correlated $3d$-electron Mott insulators such as the high-temperature cuprate superconductors[4]. To date however, the role of Coulomb interactions in the doped $J_{\rm eff}=1/2$ Mott phase remains contentious with no direct observations of correlated electronic phase behaviour.

Two prototypical spin-orbit Mott materials are the $n=1$ and $n=2$ members of the iridate Ruddelsden–Popper series $Sr_{n+1}Ir_nO_{3n+1}$ (refs 5,6). Here the bilayer system $Sr_3Ir_2O_7$ (Sr-327) possesses a low-temperature charge gap of $E_g=130\,{\rm meV}$,[7] roughly reduced by a factor of four from the gap of its single-layer cousin Sr_2IrO_4 (ref. 8). This reduced gap renders the Sr-327 system a fortuitous starting point for perturbing the spin-orbit Mott phase and exploring carrier-induced electronic phase behaviour as the system is driven toward the metallic regime. To this end, in this work Ru^{4+} $(4d^4)$ ions are substituted onto the Ir^{4+} $(5d^5)$ sites of $Sr_3(Ir_{1-x}Ru_x)_2O_7$ with the known end point, $Sr_3Ru_2O_7$, possessing a Fermi liquid ground state in close proximity to a magnetic instability[9]. Our combined transport, magnetization, neutron scattering and scanning-tunnelling spectroscopy (STS) studies show that the Mott insulating state of $Sr_3Ir_2O_7$ is remarkably robust as the in-plane doped holes remain largely localized within a nanoscale phase-separated ground state and only generate a metal–insulator transition (MIT) near the two-dimensional (2D) percolation threshold. The resulting electronic phase diagram also reveals the surprising persistence of antiferromagnetic (AF) order deep into the metallic phase and suggests emergent itinerant magnetism at the interface between the AF-ordered spin-orbit Mott phase of $Sr_3Ir_2O_7$ and the nearly magnetic Fermi liquid electronic phase of $Sr_3Ru_2O_7$.

Results

Electronic phase diagram and bulk electronic properties. The resulting electronic phase diagram determined via our combined transport, bulk magnetization and neutron-scattering measurements is plotted in Fig. 1a. The most prominent feature of the phase diagram is that the transition from the insulating ground state of $Sr_3Ir_2O_7$ to the low-temperature metallic phase takes place only beyond the critical concentration of $x=0.35$. This suggests that the Ir^{4+} $(5d^5)$ valence is protected by the Mott gap that blocks the charge transfer of doped holes from the in-plane substituted Ru^{4+} $(4d^4)$ ions, a phenomenon of 'Mott blocking'. The corresponding resistivity $\rho(T)$ is plotted as a function of temperature in Fig. 2a for $Sr_3(Ir_{1-x}Ru_x)_2O_7$ concentrations spanning the phase diagram. Concentrations near the phase boundary also show a thermally driven MIT as illustrated in the inset of Fig. 2a for $x=0.33$ with $T_{\rm MIT}=135\,{\rm K}$ (see also Supplementary Fig. 1). As an initial window into the corresponding evolution of the magnetic order, the high-temperature inflection in $\rho(T)$ in the $x=0$ parent compound is known to identify the onset of canted AF order at $T_{\rm AF}=280\,{\rm K}$. This feature in $\rho(T)$ is gradually suppressed to lower temperatures upon Ru doping, where the anomaly vanishes in the metallic regime.

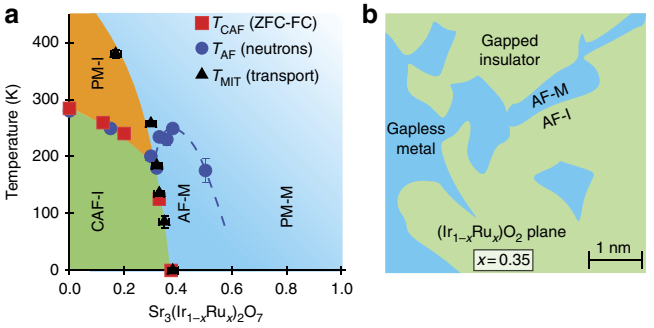

Figure 1 | Electronic phase diagram of $Sr_3(Ir_{1-x}Ru_x)_2O_7$. (**a**) Evolution of electronic phases of $Sr_3(Ir_{1-x}Ru_x)_2O_7$ as a function of Ru concentration. CAF-I denotes the insulating canted AF phase, PM-I denotes the paramagnetic insulating phase, AF-M denotes the AF ordered metallic state and PM-M indicates the paramagnetic metallic regime. Squares indicate the onset of canted AF order determined with bulk susceptibility measurements, circles denote the onset of AF order as observed via neutron direction measurements, and triangles indicate the transition temperatures for thermally driven MITs near the phase boundary. (**b**) Illustration of the basal-plane showing phase-separated metallic puddles near the percolative threshold, which nucleate within the spin-orbit Mott insulating background of $Sr_3Ir_2O_7$. Error bars in all plots represent 1 s.d.

Low-temperature magnetoresistance (MR) data with the magnetic field applied perpendicular to the *ab* plane are plotted in Fig. 2b. The negative magnetoresistance previously reported in the parent material[10] and indicative of suppressed spin fluctuations or magnetic domain scattering persists in lightly doped, insulating samples; however, as the system transitions into the metallic phase, the MR smoothly switches sign from negative to positive values that increase in magnitude with continued Ru doping. This suggests that orbital (Lorentz force) effects begin to dominate across the MIT phase boundary as the carrier concentration is enhanced while fluctuation/domain effects from AF order are damped. Further illustrating this, bulk magnetization measurements of the in-plane susceptibility were performed on select samples, shown in Fig. 2c. As Ru is doped into Sr-327, the onset temperature of the net ferromagnetism, arising from the canted AF order and denoted via the irreversibility temperature ($T_{\rm irr}$), is reduced. Close to the critical regime, the $x=0.33$ sample exhibiting a thermally driven MIT with $T_{\rm MIT}=135\,{\rm K}$ (Fig. 2a inset) shows an onset of canted AF order at the same temperature. This suggests that near the MIT phase boundary the two transitions ($T_{\rm MIT}$ and $T_{\rm CAF}$) become coupled and that this coupling diminishes in lightly doped samples deeper within the insulating regime. Samples with Ru doping $x>0.33$ show no irreversibility in magnetization, and concentrations with a metallic ground state show only local moment behaviour within resolution. The only exception is that the highest doped sample with $x=0.75$ shows the reemergence of $T_{\rm irr}$ at low temperature (Supplementary Fig. 2); however, the origin of this may simply be an extrinsic perturbation of the nearby Fermi liquid phase of $Sr_3Ru_2O_7$.

Through direct analogy with $Sr_3Ru_2O_7$ (ref. 11), Ru nominally enters the Sr-327 iridate lattice in the low spin state of Ru^{4+} and subsequently introduces $S=1$ impurities into the $J_{\rm eff}=1/2$ magnetic background. Unlike its single-layer cousin Sr_2IrO_4 (ref. 12), the parent Sr-327 iridate shows no Curie–Weiss behaviour up to 400 K[13]; however, as Ru ions are introduced into the lattice a paramagnetic upturn begins to build in the low-temperature magnetization data for the lowest doping measured ($x=0.13$). Immediately upon doping Ru, the known low-temperature downturn in $\chi(T)$ in the parent system[10,14]

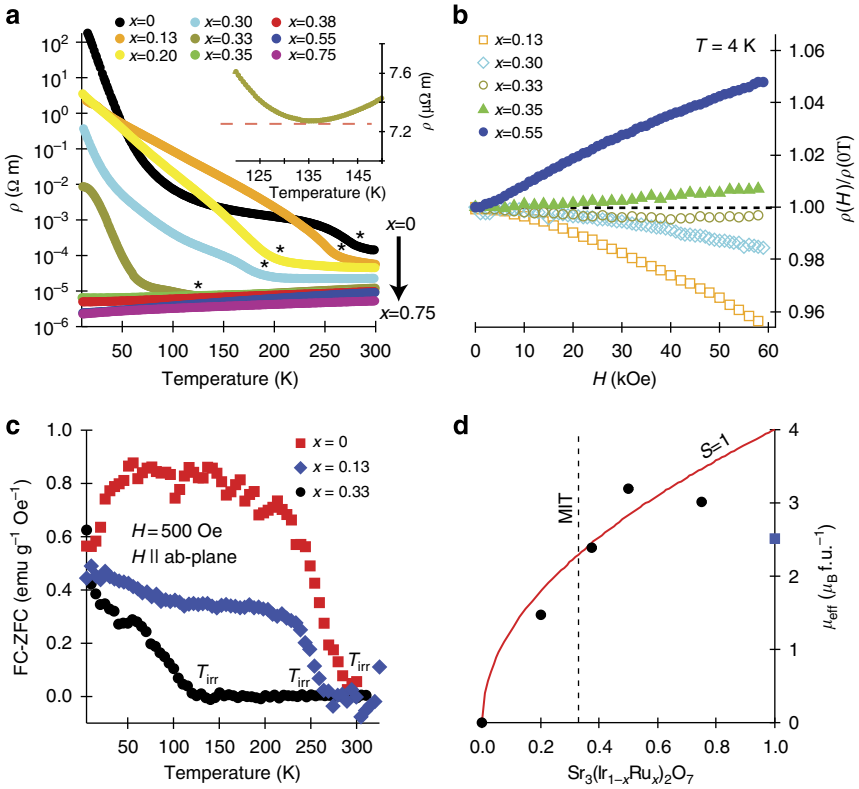

Figure 2 | Bulk transport and magnetization measurements of $Sr_3(Ir_{1-x}Ru_x)_2O_7$. (**a**) Resistivity plotted as a function of temperature for Ru concentrations spanning the MIT. Inset shows thermally driven transition at $T_{MIT} = 135$ K for $x = 0.33$. (**b**) 4 K magnetoresistance plotted as a function of applied field for Ru concentrations spanning the MIT. (**c**) Field-cooled (FC) minus zero-field cooled (ZFC) magnetization as a function of temperature for select Ru dopings. (**d**) Local moments extracted from Curie–Weiss fits plotted as a function of Ru concentration. Solid line denotes the expected full moment value for $S = 1$ impurities. The blue square denotes data taken from Ikeda *et al.*[11] $1\,\text{emu}\,\text{g}^{-1}\,\text{Oe}^{-1} = 4\pi \times 10^{-3}\,\text{m}^3\,\text{kg}^{-1}$. Error bars in all plots represent 1 s.d.

(Fig. 2c) rapidly vanishes and is replaced by a weak paramagnetic upturn. The resulting local moments, extracted via Curie–Weiss fits to the susceptibility, are plotted in Fig. 2d. For low Ru-dopant levels, the effective local moments extracted from each concentration track the expectation for contributions solely arising from local $S = 1$ impurities, which build continuously across the MIT. This suggests Ru ions remain largely localized at low Ru dopings within the insulating background of $Sr_3Ir_2O_7$ and that their survival into the metallic regime demonstrates robust correlation effects on either side of the MIT. For doping levels beyond $x = 0.5$, the local moments are screened and smoothly connect to the high-temperature susceptibility of metallic $Sr_3Ru_2O_7$ (ref. 11).

Neutron-scattering measurements. In order to more directly elucidate the evolution of the ordered AF phase across the MIT in this system, neutron-scattering measurements were performed. The results plotted in Fig. 3a show that, for insulating samples, the onset of long-range AF order coincides with the T_{irr} determined via the magnetization curves in Fig. 2. Upon increased doping, however, the AF phase surprisingly survives across the MIT at the same Q positions as the insulating phase[10,15], and the resulting order parameters for metallic samples are plotted in Fig. 3b. From the limited number of magnetic peaks observable in our neutron measurements ((1, 0, L); $L = 1, 2, 3, 4$), the spin structure remains consistent with that of the parent system across the MIT in the phase diagram, albeit the small degree of spin canting present in the insulating parent system is necessarily eliminated or strongly suppressed in the metallic regime. The persistent AF order remains long-range within resolution with a minimum correlation length $\xi \approx 200$ Å ($\xi = 2\sqrt{2\ln(2)}\frac{1}{w}$, where w is obtained by fits of radial scans to the form $I = I_0 + Ae^{-\frac{1}{2}\left(\frac{(x-c)}{w}\right)^2}$). Keeping a model of c axis-aligned moments across the MIT[5], Fig. 3c, shows a nearly linear suppression of the AF moment in the lightly Ru-doped insulating regime due to the dilution of ordered Ir ions by localized Ru $S = 1$ impurities, and deep in the metallic regime the ordered moment is quickly screened. In close proximity to the MIT phase boundary however, an anomalous enhancement in the ordered AF moment appears (Fig. 3 and Supplementary Fig. 3), suggesting the potential of induced ordering of $S = 1$ moments from doped $4d^4$ electrons in this range or potentially a partial relaxation of the octahedral distortion resulting in enhanced magnetic exchange.

The intrinsic crystal structure of $Sr_3Ir_2O_7$ remains an active area of investigation with superlattice reflections violating the tetragonal space group I4/*mmm* reported in single-crystal studies[14,16]. Previously, our neutron studies resolved high-temperature Bragg scattering[10] at positions forbidden by both the recently reported I4/*mmm* (ref. 15) and *Bbcb* (ref. 5) space groups. In order to clarify the origin of this high-temperature superlattice, we also performed polarized neutron diffraction measurements with the results plotted in Fig. 3d. Radial scans through $Q = (1, 0, 3)$ show that the (1, 0, L)-type superlattice reflections at 300 K appear only in the non-spin-flip channel with the neutron guide field applied parallel to Q. This demonstrates

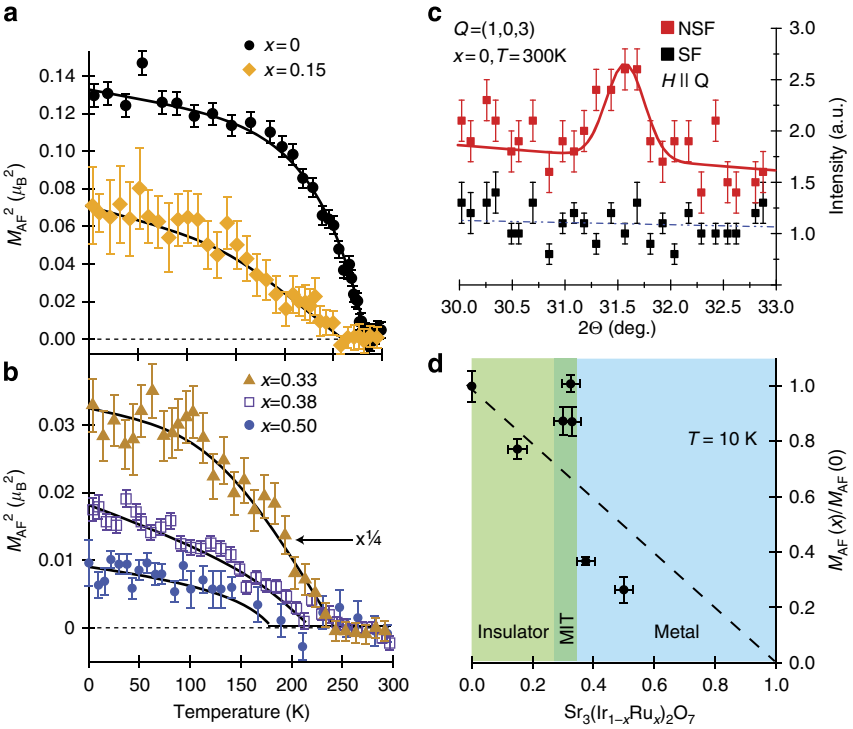

Figure 3 | Neutron scattering characterization of $Sr_3(Ir_{1-x}Ru_x)_2O_7$. (**a**) Temperature evolution of the square of the AF order parameter ($M_{AF}^2(T)$) for fully insulating $x=0$ (from ref. 10) and $x=0.15$. (**b**) $M_{AF}^2(T)$ for metallic $x=0.5$ and $x=0.38$ samples as well as for $x=0.33$ at the phase boundary. The data for $x=0.33$ have been scaled by $\frac{1}{4}$ for clarity. (**c**) Ordered AF moments for $Sr_3(Ir_{1-x}Ru_x)_2O_7$ scaled relative to the parent $Sr_3Ir_2O_7$ insulator. Shaded areas denote boundaries between insulating, metallic and critical MIT regimes. (**d**) Polarized neutron diffraction measurements of $Sr_3Ir_2O_7$ showing radial scans through the $Q=(1, 0, 3)$ superlattice peak at 300 K in both spin-flip (SF) and non-spin-flip (NSF) channels. The magnetic guide field was applied parallel to the momentum transfer Q. Error bars in all plots represent 1 s.d.

the structural origin of the superlattice and mandates a space group symmetry lower than *Bbcb*. The resulting high-temperature (1, 0, *L*)-type peaks argue for oxygen octahedral tilting as well as in-plane rotation in this system. A tilt already necessarily exists for the *c* axis-aligned moments in the canted AF phase, and the strong spin-lattice coupling in perovskite iridates[17] supports the notion of an accompanying structural tilt. Such a tilt likely renders Sr-327 isostructural to $Ca_3Ru_2O_7$ (space group: $Bb2_1m$)[18]; however, a full neutron data set and structural refinement have yet to be carried out.

STS measurements. In order to better understand the formation of the metallic phase, low-temperature (4 K) STS measurements were performed on two concentrations: samples with $x=0.35$ in close proximity to the MIT and samples deep within the metallic regime with $x=0.5$. Figure 4a shows the resulting topography of STS measurements exploring the local density of states (LDOS) in the $x=0.35$ concentration. Strong inhomogeneity across nanometre-length scales in this sample is immediately apparent from the topography and reveals the coexistence of two distinct local environments whose representative tunnelling spectra are plotted in Fig. 4c. Dark regions with low LDOS in the corresponding map show a fully gapped spectra paralleling that of the parent $Sr_3Ir_2O_7$ insulating phase[7] reproduced in Fig. 4f, while the bright regions reveal metallic regions with an enhanced LDOS. The striking nanoscale coexistence of both fully gapped and gapless metallic regions in this sample demonstrates that the sample segregates into electronically distinct regions. The low-temperature MIT phase line in Fig. 1a therefore does not represent a thermodynamic phase transition but rather the percolation threshold of metallic puddles localized within a spin-orbit Mott phase.

In exploring the extent of this segregation between electronic phases or doped carriers further, we performed STS measurements on the metallic $x=0.5$ concentration. These measurements reveal this sample to be globally gapless; however, the spectra also resolve a substantial degree of electronic inhomogeneity within this nominal metal, as illustrated by a representative topography in Fig. 4b. Correspondingly, the spectra plotted in Fig. 4d again show two distinct shapes representing different local environments: one with suppressed V-shaped LDOS and the second with enhanced LDOS and a spectrum that strongly resembles that of $Sr_3Ru_2O_7$ (ref. 19). To better illustrate this, a comparison with $Sr_3Ru_2O_7$ is provided as shown in Fig. 4e. The similarity between the hole-rich regions of the metallic $x=0.5$ sample and the pure bilayer ruthenate system is particularly striking, with the tunnelling data resembling a thermally broadened version of a qualitatively similar electronic structure. This combined with the strong inhomogeneity of this metallic state indicates that even the fully metallic compounds continue to remain electronically segregated over nanometre-length scales.

Discussion

Our combined experimental results, viewed globally, paint a picture of a nanoscale, electronically phase-separated ground state for in-plane carriers doped within a spin-orbit-driven Mott phase, $Sr_3Ir_2O_7$ (Fig. 1). Since the meaning of 'electronic phase separation' is rather subtle at the nanoscale in doped transition metal oxides, we define its use explicitly here simply as the observation of two different local environments with distinct electronic properties. This general scenario of nanoscale phase separation, either via the coexistence of distinct electronic phases or the direct segregation of holes, results in the stabilization of

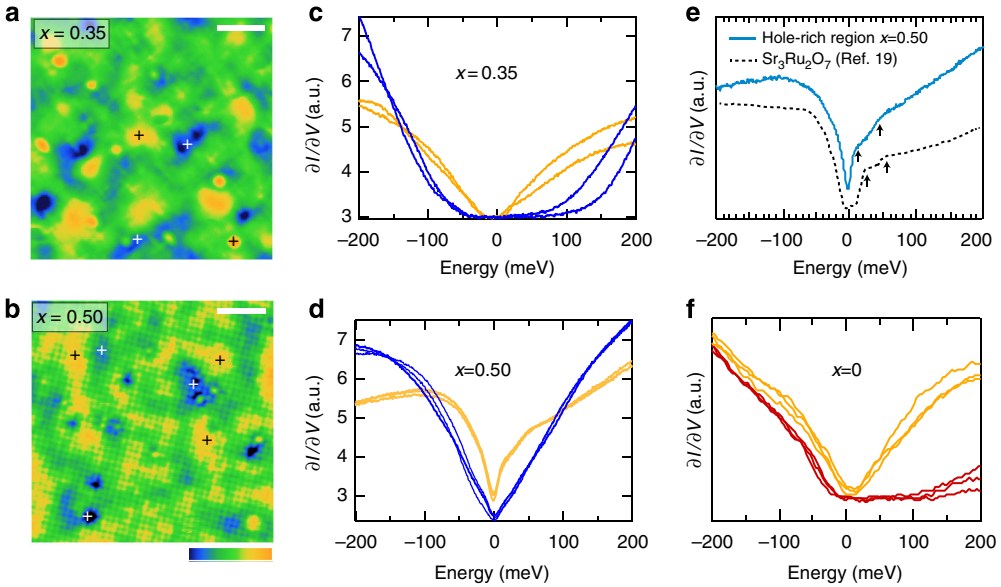

Figure 4 | STS measurements of $Sr_3(Ir_{1-x}Ru_x)_2O_7$. (**a**) Topography at a bias voltage of −100 mV for the $x = 0.35$ concentration near the MIT. (**b**) Topography at a bias voltage of −100 mV for the $x = 0.5$ metallic concentration. Intensity scales for topography in (**a**) and (**b**) are unique to each plot and their relative variation is shown via the colour bar below the panels. White bars in each plot denote the length scale of 3 nm. Colour bar denotes the relative scale of LDOS ranging from low (blue) to high (orange) values. (**c**) Tunnelling spectra collected in gapped and gapless phase-separated regions denoted by blue and yellow curves collected at white and black crosses in the corresponding map. (**d**) Spectra for $x = 0.5$ within two regions denoted by yellow and blue curves collected at black and white crosses respectively in the topography. (**e**) High-resolution tunnelling data collected within a bright region of the $x = 0.5$ sample in (**b**). Dashed line is low-temperature STS data for $Sr_3Ru_2O_7$ reproduced from ref. 19. (**f**) Spectra collected for $Sr_3Ir_2O_7$ in regions with enhanced LDOS due to oxygen defects (yellow curves) and spectra collected away from defects showing the full charge gap (red curves). We note here that the inhomogeneity observed within the parent insulating system stems from relatively rare regions of oxygen defects and that the majority of the surface showed fully gapped behaviour (red curves), whereas for the $x = 0.35$ and $x = 0.5$ systems the entirety of the samples showed strong electronic inhomogeneity across nanometre-length scales.

two different local environments and a percolating conduction network sensed by our earlier transport measurements. Bare charge accumulation into puddles of 1–2 nanometre-length scales may not be energetically favourable due to unscreened long-range Coulomb interactions. Without knowing the effective screening length for the Coulomb interaction and the pinning potential for carriers, it is hard to quantify what the length scale should be in $Sr_3Ir_2O_7$. An alternative of phase separation into electrically neutral, yet electronically distinct, phases separated by a first-order phase transition is instead a likely mechanism; however, we are unable to differentiate this from the pure carrier segregation scenario. Regardless of which scenario dominates, the carriers within metallic patches remain initially localized across ~1–2 nm-length scales, and at the critical concentration where transport measurements show a MIT ($x \sim 0.35$), this leads to the formation of metallic patches percolating within the fully gapped, spin-orbit Mott insulating background. At Ru substitution levels below $x = 0.35$, the thermally driven MIT is therefore the likely result of the expansion of these metallic puddles due to thermal shifts in their free energy relative to insulating host phase. Phase inhomogeneity continues deep into the metallic regime, where our STS data directly demonstrate nanometre-scale texture in metallic Sr_3IrRuO_7 comprising two distinct regions: (1) large LDOS regions with an electronic response mirroring the $4d^4$ electronic spectrum of isostructural $Sr_3Ru_2O_7$ (ref. 19) and (2) regions with V-shaped spectra with LDOS suppressed close to the Fermi energy.

Since their valence states are rather far from the Fermi level, A-site doping in perovskite oxides is historically envisioned as controlling the filling of *d*-bands on the B-sites by donating their valence electrons to the entire system. The resulting doping mechanism gives rise to a rapid suppression of the Mott phase such as in A-site-doped Sr_2IrO_4 (ref. 20) and $Sr_3Ir_2O_7$ (ref. 21). Our B-site doping in Sr-327, however, reveals that holes nominally added via Ru substitution remain localized within the IrO_2 planes until ~35% of the Ir 5*d* ions have been replaced, close to the classical 2D percolation threshold of 41% (ref. 22). Even beyond this threshold at 50% replacement, hole-rich regions remain phase separated. Given that Ru doping is nominally a strong perturbation to the weakly insulating ground state of Sr-327, this observation is striking and suggests that Coulomb interactions and correlation effects remain essential across the majority of the phase diagram of this system.

Our combined neutron scattering and STS data reveal that the AF-ordered state that survives across the MIT has a spin–spin correlation length ($\xi > 200$ Å) that spans across the phase-separated puddles of gapped and metallic regions—revealing a globally AF-ordered phase. Furthermore, in concentrations doped close to the MIT, the recovery of the ordered AF moment to values nearly equalling that of the undoped parent $Sr_3Ir_2O_7$ rules out any trivial superposition of chemically distinct phases. A magnetically ordered, metallic state beyond the MIT is reminiscent of the phase diagrams of $(Ca_{1-x}Sr_x)_3Ru_2O_7$ (ref. 23) and $Ca_{2-x}Sr_xRuO_4$ (ref. 24); however, from our current measurements of $Sr_3(Ir_{1-x}Ru_x)_2O_7$ the structural symmetry appears identical for concentrations spanning the MIT, suggesting that the critical point is not directly tied to a structural phase transition. AF metallic states have also been proposed in disordered and binary alloy Mott phases as an intermediate state prior to the onset of Anderson localization[25,26]. The global picture our data provide shows that the physics here is more complex than that of a trivially diluted AF system with

percolative transport. The percolating metallic network seemingly can be induced to order by the host AF matrix, which may explain why the ordered AF moment is actually enhanced near the region of maximum heterogeneous interface area at the MIT as well as why AF order survives across the percolation threshold where no infinite domain of the AF host persists. Local antiferromagnetism does however naively persist across the critical concentration and can continue to influence the metallic phase into the heavily Ru-doped regime. Eventually this gives way to a globally gapless AF phase in the $x = 0.5$ sample.

We propose the following picture of magnetic interactions within this system: when they are dilute within the matrix, Ru-doped holes behave in a manner consistent with isolated ions in the $S = 1$ low spin state giving rise to the local moment response; however, increasing the Ru-doping level increases the density of these isolated magnetic impurities, eventually nucleating clusters of metallic regions (resolved directly in our STS measurements). Within these metallic puddles, whose percolation generates the MIT, the local moment should be quenched at low temperatures in a Fermi liquid ground state; however, these puddles may still be magnetically ordered due to proximity of local AF order in neighbouring regions and a large spin susceptibility arising from their nested Fermi surface pockets. Such an instability is indeed known to be present along the $Q = (\pi, \pi)$ in-plane wave vectors of $Sr_3Ru_2O_7$ (ref. 27) where an enhanced density of states is nested at the Fermi level due to the $\sqrt{2}\times\sqrt{2}$ structural zone folding. In this regard, this suggests similarities to the thermally driven MIT in the prototypical Mott system VO_2, where percolating metallic puddles display significant correlation effects[28]. More broadly, the survival of an ordered magnetic moment into the metallic state of the system demonstrates that electron–electron correlations remain relevant across the MIT of this system and argues against the picture of $Sr_3Ir_2O_7$ as a trivial band-insulator simply driven by the zone folding that occurs at the onset of AF order.

The evolution of AF order across the MIT in the phase diagram of this hole-doped spin-orbit Mott insulator demonstrates that a rich interplay can be realized at the boundary between a novel $J_{\rm eff} = 1/2$ insulator and a correlated metal. The localization of Ru-doped carriers into a phase-separated ground state surprisingly parallels the strongly correlated phase behaviour of 3*d*-transition metal oxide systems such as the B-site-doped correlated manganites[29–32] and reveals that correlation physics can play a dominant role in the electronic phase formation of a doped spin-orbit Mott insulator. Our findings demonstrate that correlation effects felt by carriers introduced within in a 5*d* Mott phase remain robust enough to drive electron localization, a key ingredient in emergent phenomena such as high-temperature superconductivity and enhanced ferroic behaviour. This opens up a new frontier for exploring correlated electron phases within the presence of strong SOC effects inherent to a 5*d*-electron setting.

Methods

Materials and crystal growth. The single crystals of $Sr_3(Ir_{1-x}Ru_x)_2O_7$ were grown by conventional flux methods similar to earlier reports[10,14] using a $SrCl_2$ flux. Crystals were grown in platinum crucibles using IrO_2 (99.98%, Alfa Aesar), RuO_2 (99.98%, Alfa Aesar), $SrCO_3$ (99.99%, Alfa Aesar) and anhydrous $SrCl_2$ (99.5%, Alfa Aesar) in a 2:3:15 molar ratio. Starting powders were partially sealed inside the crucible with a Pt lid and further contained inside alumina crucibles. Mixtures were heated up to 1,380 °C, cooled to 850 °C at a rate of 3.5 °C per hour, and then furnace-cooled to room temperature. The resulting boule was etched with deionized water and shiny, black $Sr_3(Ir_{1-x}Ru_x)_2O_7$ crystals with typical dimensions $2 \times 2 \times 0.1$ mm were removed.

Ru concentrations were determined to match target values within ~2% via energy-dispersive X-ray spectroscopy (EDS) measurements. EDS measurements were performed on numerous samples across different regions of samples from each growth batch, and measurements were also collected across different length scales to verify chemical homogeneity. Multiple crystals were tested from every batch, and from point to point on a given sample, we were able to resolve a Ru distribution homogenous within a central value ± 1% (2% spread). The central value of Ru concentrations between crystals from a single growth batch would vary no more than ± 2% from a central value (4% spread). Error bars on the reported phase diagram in the main text reflect this uncertainty—in many cases they are within the symbol size. The actual crystals measured via transport and magnetization measurements and almost all of the crystals for the neutron measurements were first characterized (only the $x = 0.20$ and $x = 0.15$ samples were not, although crystals from the same batch were characterized) via EDS measurements to determine/verify the precise Ru content.

X-ray diffraction measurements. Single crystals from a single batch of each concentration were ground into a powder and measured via X-ray powder diffraction within a Bruker D2 Phaser diffractometer. X-ray powder diffraction and refinement revealed no impurity phases within instrument resolution (~2–3%). Lattice parameters and unit cell volumes were refined within the I4/*mmm* space group and showed both *a*- and *c* axes that reduce continuously with increased Ru substitution (Supplementary Fig. 4)—as expected, because the smaller Ru^{4+} ions are introduced into the lattice. We note here that laboratory-based powder X-ray measurements typically lack the intensity to resolve the known orthorhombic superlattice reflections in this material, so each concentration was instead refined within the tetragonal I4/*mmm* space group.

Bulk property measurements. Magnetotransport measurements were performed via standard four-wire measurements within a Quantum Design PPMS. Magnetization measurements were collected within a Quantum Design SQUID MPMS magnetometer.

MIT determined via resistivity. The MIT depicted in the phase diagram of Fig. 1a was determined via the temperature at which the slope of the sample's resistance versus temperature changed sign from $\delta R/\delta T > 0$ to $\delta R/\delta T < 0$ upon cooling. Data showing the MIT for all samples where an MIT was reported are shown in the inset of Fig. 2a and in Supplementary Fig. 1.

Bulk spin susceptibility. Local moments were determined via Curie–Weiss fits to the form $1/\chi(T) = \Theta/C + T/C$, where Θ is the Weiss constant and C is the Curie constant (results plotted in Supplementary Fig. 2). Here $C = \frac{N_A}{3k_B}\mu_{\rm eff}^2$, with N_A as Avogadro's number and k_B is Boltzman's constant. Fits render a negative Weiss constant for $x < 0.75$ consistent with the observation of AF correlations. For $x = 0.75$, low-temperature susceptibility shows the reemergence of an irreversibility temperature ($T_{\rm irr}$) below 20 K. The reentrance of a net ferromagnetic signal in this heavily doped regime is likely the result of the fragility of the nearly magnetic ground state of $Sr_3Ru_2O_7$ where small levels of impurity substitution or pressure are known to stabilize magnetic order[11]. As similar effects are known to occur in $Sr_3Ru_2O_7$, for the purposes of our study we treat the ground state of $x = 0.75$ as qualitatively similar to that of the ruthenate bilayer end point. We have not performed neutron diffraction measurements exploring the presence of AF order in this concentration.

Neutron-scattering measurements. The unpolarized neutron diffraction experiments were performed on HB1-A triple-axis spectrometer at the High Flux Isotope Reactor (HFIR) at Oak Ridge National Laboratory (ORNL) and at N-5 triple-axis spectrometer at Canadian Neutron Beam Center, Chalk River Canada. For HB1-A the incident beam was monochromated by the $Q = (0, 0, 2)$ reflection of a double-bounce pyrolitic-graphite (PG) monochromator with a fixed incident energy of $E_i = 14.65$ meV, and a PG(002) analyser crystal was used on the scattered side. Two PG filters were placed before the sample, and collimations of 40′–40′–40′–80′ were used before the monochromator, sample, analyser and detector, respectively. Experiments on N5 were performed with a PG monochomator and $E_i = 14.5$ meV and PG analyser with one PG filter placed after the sample. Collimations of 30′–60′–33′–144′ were used before the monochromator, sample, analyser and detector, respectively. The polarized neutron experiment was carried out on the BT7 triple-axis spectrometer at the NIST Center for Neutron Research using PG(002) monochromator, ^{3}He polarizers, PG filters before and after the sample, radial collimation and a position-sensitive detector on the scattered side. A guide field allowed the magnetic field to be tuned along the scattering vector (horizontal field) and perpendicular to the scattering plane (vertical field) configuration. For all experiments, the crystals were aligned in the (H, 0, L) scattering plane.

STS measurements. $Sr_3(Ir_{1-x}Ru_x)_2O_7$ single crystals were cleaved at ~77 K in ultra-high vacuum before being directly transferred to the STM head held at 4 K. From previous data, cleaving at low temperatures is critical for obtaining flat clean samples. Tips were prepared by annealing etched W-tips in vacuum and then checking the quality on metallic (copper single crystal) surfaces. The quality of all tips used in this study was checked by imaging standing waves on Cu and performing spectroscopy. The tips thus prepared showed atomic resolution on the iridate samples and were stable, allowing us to obtain high-quality $\delta I/\delta V$ maps.

Measurement statistics. For transport measurements, each batch with a unique Ru concentration was tested at a minimum of three times (in most cases more) on different crystals. Phase transitions determined via transport measurements reproduced within the error bars shown within the phase diagram of Fig. 1a. The most sensitive batches were those with Ru contents close to the sharp MIT phase boundary with $x = 0.35$ where the same slight deviations in Ru content resulted in a larger sample-to-sample variation in T_{MIT}. The resulting uncertainty is encompassed by the horizontal error bars in Fig. 1a, often within the symbol size.

For neutron measurements, every data point for T_{AF} on the phase diagram in Fig. 1a represents a measurement on one unique sample. The anomalous regions such as those near the phase boundary with an enhanced moment ($x = 0.33$–0.35) and deep within the metallic regime ($x = 0.5$) were checked with additional experiments on additional samples grown in different batches. The magnetic behaviour reproduced in both instances and those data points are not shown.

For our magnetization measurements, only a few select samples, well characterized by transport and EDS, were chosen for measurement. Only one measurement was taken for each concentration reported.

For STS measurements, for each doping, at least three different tips and samples were studied. The spectral shapes for any given doping were consistent and repeatable. We checked the tip height dependence for the insulating regions of the parent compound and the $x = 0.35$ compound and found no obvious changes in spectral shape with height. We have measured three samples at the $x = 0.35$ concentration and found the reported nanoscale phase coexistence completely reproducible. Three samples with $x = 0.5$ have also been measured and with completely reproducible spectra and surfaces.

References

1. Kim, B. J. *et al.* Phase-sensitive observation of a spin-orbital mott state in Sr_2IrO_4. *Science* **323,** 1329–1332 (2009).
2. Kim, B. J. *et al.* Novel $J_{eff} = 1/2$ Mott state induced by relativistic spin-orbit coupling in Sr_2IrO_4. *Phys. Rev. Lett.* **101,** 076402 (2008).
3. Wang, Q. *et al.* Dimensionality-controlled Mott transition and correlation effects in single-layer and bilayer perovskite iridates. *Phys. Rev. B* **87,** 245109 (2013).
4. Wang, F. & Senthil, T. Twisted Hubbard model for Sr_2IrO_4: magnetism and possible high temperature superconductivity. *Phys. Rev. Lett.* **106,** 136402 (2011).
5. Kim, J. W. *et al.* Dimensionality driven spin-flop transition in layered iridates. *Phys. Rev. Lett.* **109,** 037204 (2012).
6. Moon, S. J. *et al.* Dimensionality-controlled insulator-metal transition and correlated metallic state in 5*d*transition metal oxides $Sr_{n+1}Ir_nO_{3n+1}$ ($n = 1$, 2, and ∞). *Phys. Rev. Lett.* **101,** 226402 (2008).
7. Okada, Y. *et al.* Imaging the evolution of metallic states in a spin-orbit interaction driven correlated iridate. *Nat. Mater.* **12,** 707–713 (2013).
8. Dai, J., Calleja, E., Cao, G. & McElroy, K. Local density of states study of a spin-orbit-coupling induced Mott insulator Sr_2IrO_4. Preprint at http://arXiv:1303.3688 (2013).
9. Grigera, S. A. *et al.* Magnetic field-tuned quantum criticality in the metallic ruthenate $Sr_3Ru_2O_7$. *Science* **294,** 329–332 (2001).
10. Dhital, C. *et al.* Spin ordering and electronic texture in the bilayer iridate $Sr_3Ir_2O_7$. *Phys. Rev. B* **86,** 100401(R) (2012).
11. Ikeda, S. I., Maeno, Y., Nakatsuji, S., Kosaka, M. & Uwatoko, Y. Ground state in $Sr_3Ru_2O_7$: Fermi liquid close to a ferromagnetic instability. *Phys. Rev. B* **62,** 6089(R) (2000).
12. Kini, N. S., Strydom, A. M., Jeevan, H. S., Geibel, C. & Ramakrishnan, S. Transport and thermal properties of weakly ferromagnetic Sr_2IrO_4. *J. Phys. Condens. Matter* **18,** 8205 (2006).
13. Nagai, I. *et al.* Canted antiferromagnetic ground state in $Sr_3Ir_2O_7$. *J. Phys. Condens. Matter* **19,** 136214 (2007).
14. Cao, G. *et al.* Anomalous magnetic and transport behavior in the magnetic insulator $Sr_3Ir_2O_7$. *Phys. Rev. B* **66,** 214412 (2002).
15. Boseggia, S. *et al.* Antiferromagnetic order and domains in $Sr_3Ir_2O_7$ probed by X-ray resonant scattering. *Phys. Rev. B* **85,** 184432 (2012).
16. Matsuhataa, H. *et al.* Crystal structure of $Sr_3Ir_2O_7$ investigated by transmission electron microscopy. *J. Solid State Chem.* **177,** 3776 (2004).
17. Jackeli, G. & Khaliullin, G. Mott insulators in the strong spin-orbit coupling limit: from Heisenberg to a quantum compass and Kitaev Models. *Phys. Rev. Lett* **102,** 017205 (2009).
18. Yoshida, Y. *et al.* Crystal and magnetic structure of $Ca_3Ru_2O_7$. *Phys. Rev. B* **72,** 054412 (2005).
19. Iwaya, K. *et al.* Local tunnelling spectroscopy across a metamagnetic critical point in the bilayer ruthenate $Sr_3Ru_2O_7$. *Phys. Rev. Lett.* **99,** 057208 (2007).
20. Ge, M. *et al.* Lattice-driven magnetoresistivity and metal-insulator transition in single-layered iridates. *Phys. Rev. B* **84,** 100402(R) (2011).
21. Li, L. *et al.* Tuning the $J_{eff} = 1/2$ insulating state via electron doping and pressure in the double-layered iridate $Sr_3Ir_2O_7$. *Phys. Rev. B* **87,** 235127 (2013).
22. Shante, V. K. S. & Kirkpatrick, S. An introduction to percolation theory. *Adv. Phys.* **20,** 325–357 (1971).
23. Qu, Z. *et al.* Unusual heavy-mass nearly ferromagnetic state with a surprisingly large Wilson ratio in the double layered ruthenates $(Sr_{1-x}Ca_x)_3Ru_2O_7$. *Phys. Rev. B* **78,** 180407(R) (2008).
24. Nakatsuji, S. *et al.* Heavy-mass Fermi liquid near a ferromagnetic instability in layered ruthenates. *Phys. Rev. Lett.* **90,** 137202 (2003).
25. Paris, N., Baldwin, A. & Scalettar, R. T. Mott and band-insulator transitions in the binary-alloy Hubbard model: Exact diagonalization and determinant quantum Monte Carlo simulations. *Phys. Rev. B* **75,** 165113 (2007).
26. Heidarian, D. & Trivedi, N. Inhomogeneous metallic phase in a disordered Mott insulator in two dimensions. *Phys. Rev. Lett* **93,** 126401 (2004).
27. Tamai, A. *et al.* Fermi surface and van Hove singularities in the itinerant metamagnet $Sr_3Ru_2O_7$. *Phys. Rev. Lett.* **101,** 026407 (2008).
28. Qazilbash, M. M. *et al.* Mott transition in VO_2 revealed by infrared spectroscopy and nano-imaging. *Science* **318,** 1750–1753 (2007).
29. Uehara, M., Mori, S., Chen, C. H. & Cheong, S.-W. Percolative phase separation underlies colossal magnetoresistance in mixed-valent manganites. *Nature* **399,** 560–563 (1999).
30. Elbio D., Takashi, H. & Moreo, A. Colossal magentoresistance materials: the key role of phase separation. *Phys. Rep.* **344,** 1–153 (2001).
31. Pradhan, K., Mukherjee, A. & Majumdar, P. Exploiting B-site disorder for phase control in the manganites. *Euro. Phys. Lett.* **84,** 37007 (2008).
32. Machida, A., Moritomo, Y., Ohoyama, K., Katsufuji, T. & Nakamura, A. Phase separation and ferromagnetic transition in B-site substituted $Nd_{1/2}Ca_{1/2}MnO_3$. *Phys. Rev. B* **65,** 064435 (2002).

Acknowledgements

The work at Boston College was supported by NSF CAREER-Award DMR-1056625 (S.D.W), DOE DE-SC0002554 (Z.W.) and NSF DMR-1305647 (V.M.). The work at the ORNLs High Flux Isotope Reactor was sponsored by the Scientific User Facilities Division, Office of Basic Energy Sciences, US DOE. The identification of any commercial product or trade name does not imply endorsement or recommendation by the National Institute of Standards and Technology.

Author contributions

C.D., T.H., Z.Y., J.S.H., J.W.L. and S.D.W. performed neutron-scattering measurements. W.Z., M.H., Y.O. and V.M. performed STM measurements. C.D., Z.R., T.H., X.C., M.P. and C.O. performed transport and magnetization measurements. Z.W., V.M., C.D. and S.D.W. analysed the data. Z.W., V.M., J.W.L. and S.D.W. wrote the paper.

Additional information

Supplementary Information accompanies this paper at http://www.nature.com/naturecommunications

Competing financial interests: The authors declare no competing financial interests.

Reprints and permission information is available online at http://npg.nature.com/reprintsandpermissions/

How to cite this article: Dhital, C. *et al.* Carrier localization and electronic phase separation in a doped spin-orbit-driven Mott phase in $Sr_3(Ir_{1-x}Ru_x)_2O_7$. *Nat. Commun.* 5:3377 doi: 10.1038/ncomms4377 (2014).

PHYSICAL REVIEW B **86**, 100401(R) (2012)

Spin ordering and electronic texture in the bilayer iridate $Sr_3Ir_2O_7$

Chetan Dhital,[1] Sovit Khadka,[1] Z. Yamani,[2] Clarina de la Cruz,[3] T. C. Hogan,[1] S. M. Disseler,[1] Mani Pokharel,[1] K. C. Lukas,[1] Wei Tian,[3] C. P. Opeil,[1] Ziqiang Wang,[1] and Stephen D. Wilson[1,*]

[1]*Department of Physics, Boston College, Chestnut Hill, Massachusetts 02467, USA*

[2]*Chalk River Laboratories, Canadian Neutron Beam Centre, National Research Council, Chalk River, Ontario, Canada K0J 1P0*

[3]*Neutron Scattering Science Division, Oak Ridge National Laboratory, Oak Ridge, Tennessee 37831-6393, USA*

(Received 7 June 2012; published 7 September 2012)

Through a neutron scattering, charge transport, and magnetization study, the correlated ground state in the bilayer iridium oxide $Sr_3Ir_2O_7$ is explored. Our combined results resolve scattering consistent with a high temperature magnetic phase that persists above 600 K, reorients at the previously defined $T_{AF} = 280$ K, and coexists with an electronic ground state whose phase behavior suggests the formation of a fluctuating charge or orbital phase that freezes below $T^* \approx 70$ K. Our study provides a window into the emergence of multiple electronic order parameters near the boundary of the metal to insulator phase transition of the $5d$ $J_{\text{eff}} = 1/2$ Mott phase.

DOI: 10.1103/PhysRevB.86.100401 PACS number(s): 75.25.Dk, 75.50.Ee, 72.20.Ht

There has been considerable interest recently in studying the phase behavior of correlated $5d$-electron transition metal oxides due to the potential of realizing electronic phenomena possible only when electron hopping, spin-orbit coupling, and Coulomb interaction energy scales are almost equivalent.[1–3] Of particular focus has been members of the iridium oxide Ruddelsden-Popper (RP) series $Sr_{n+1}Ir_nO_{3n+1}$, where an experimental picture of a spin-orbit induced $J_{\text{eff}} = 1/2$ Mott insulating state has been proposed.[4,5] Upon increasing the dimensionality of the iridate RP series to higher n, optical[6] and transport measurements[7,8] have shown that the effective bandwidth increases and the system transitions from a quasi-two-dimensional insulating state to a metallic phase in the three-dimensional limit.

Specifically, the reported optical gap in the $n = 2$ member $Sr_3Ir_2O_7$ (Sr-327) shifts considerably downward relative to the $n = 1$ Sr_2IrO_4 system into what should be a weakly insulating phase,[6] demonstrating that Sr-327 occupies a unique position in the iridate RP phase diagram near the boundary of the metal to insulator phase transition in the RP series. Given this framework, $Sr_3Ir_2O_7$ exhibits a number of anomalous features in its magnetic properties: Bulk magnetization measurements of Sr-327 reveal a rich behavior possessing three distinct energy scales,[8,9] and recent muon spin rotation (μSR) measurements have revealed the presence of highly disordered local spin behavior,[10] both supporting the notion of multiple coexisting or competing magnetic phases. However, the details of how spin order evolves in this material and interfaces with the energy scales identified in both transport and bulk susceptibility measurements remains largely unexplored.

In this Rapid Communication, we utilize neutron scattering, bulk magnetization, and transport techniques to explore the phase behavior in $Sr_3Ir_2O_7$ (Sr-327). At high temperatures, a phase appears with $T_{\text{onset}} > 600$ K followed by a second magnetic transition at $T_{AF} = 280$ K. Scattering from this high temperature phase is consistent with a magnetic origin, provides an explanation for the absence of Curie-Weiss paramagnetism in this material above 280 K,[11] and also suggests an origin for the recently reported anomalous 93 meV magnon gap.[12] At low temperatures, the spin order is decoupled within resolution from a second upturn in the bulk spin susceptibility at $T_O = 220$ K, suggestive of the formation of an electronic glass that freezes below $T^* \approx 70$ K. Below this freezing energy scale, charge transport demonstrates a localized ground state that can be biased into a regime of field enhanced conductivity (FEC) consistent with collective transport above a threshold electric field. Our combined results demonstrate the coexistence of spin order with an unconventional, electronically textured, phase in an inhomogeneous ground state near the boundary but on the insulating side of the $J_{\text{eff}} = 1/2$ Mott transition.

Single crystals of $Sr_3Ir_2O_7$ (Sr-327) were grown via flux techniques similar to earlier reports.[13,14] The resulting Sr:Ir ratio was confirmed to be 3:2 via energy dispersive spectroscopy (EDS) measurements, and a number of Sr-327 crystals were also ground into a powder and checked via x-ray diffraction in a Bruker D2 Phaser system. No coexisting Sr_2IrO_4 phase was observed and the resulting pattern was refined to the originally reported $I4/mmm$ structure—we note, however, that, due to the small scattering signal from oxygen, we are unable to distinguish between this and the various reported orthorhombic symmetries.[8,11,13] For the remainder of this Rapid Communication, we will index the unit cell using the pseudotetragonal unit cell with $a = b = 5.50$ Å, $c = 20.86$ Å.

Neutron measurements were performed on the HB-1A triple-axis spectrometer at the High Flux Isotope Reactor (HFIR) at Oak Ridge National Laboratory and on the C5 spectrometer at the Canadian Neutron Beam Centre at Chalk River Laboratories. Experiments on C5 were performed with a vertically focusing pyrolitic graphite (PG-002) monochromator and analyzer, an $E_f = 14.5$ meV, two PG filters after the sample, and collimations of 33′-48′-51′-144′ before the monochromator, sample, analyzer, and detector, respectively. On HB-1A, a double bounce PG monochromator was utilized with fixed $E_i = 14.7$ meV, two PG filters before the sample, and collimations of 48′-48′-40′-68′. Magnetization measurements were performed on a Quantum Design MPMS-XL system and resistivity data was collected in a series of four-wire setups: (1) Zero field resistance from 300 to 12 K was collected

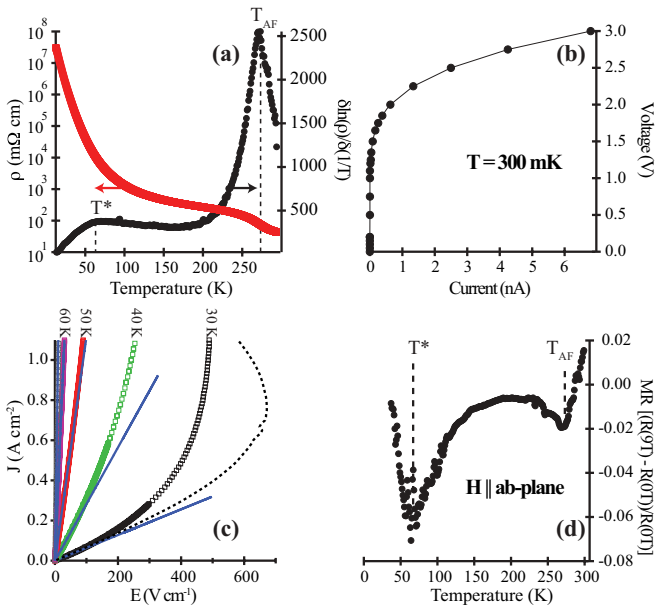

FIG. 1. (Color online) (a) Temperature dependence of the *ab*-plane resistivity for Sr-327. Also plotted is the $\frac{\partial \ln \rho}{\partial (1/T)}$ vs T showing two peaks at T_{AF} and T^*. (b) I-V curve of *ab*-plane transport at 300 mK showing voltage biasing into a FEC regime. (c) Current driven, pulsed, I-V measurements as a function of temperature. Solid lines show linear fits to the Ohmic regime at each temperature. The dashed line is a Joule heating model at 30 K as described in the text. (d) Magnetoresistance (MR) ratio as described in the text plotted as a function of temperature showing two well defined minima at the T^* and T_{AF} transitions.

with a Keithley 2182A voltmeter, (2) data from 12 to 0.3 K was collected in a ^{3}He absorption refrigerator with an Keithley Model 617 electrometer, and (3) magnetoresistance data was collected in a 9 T Quantum Design PPMS.

Looking first at the results of our *ab*-plane transport measurements under low (1 μA) current, Fig. 1(a) shows the zero field resistivity as a function of temperature. The sample's resistivity increases from several mΩ cm at room temperature to beyond 10 MΩ cm below 20 K, and begins to show saturation behavior below 2 K.[14] There is no substantial interval of constant activation energy, as illustrated by the overplot of $\frac{\partial \ln \rho}{\partial (1/T)}$ versus T in this same panel. Instead, $\frac{\partial \ln \rho}{\partial (1/T)}$ shows two peaks suggestive of two phase transitions coupling to charge carriers: the first near the known magnetic phase transition at $T_{AF} = 280$ K (Ref. 8) and the second indicating a lower temperature phase formation at $T^* \approx 70$ K.

In order to investigate further the transport properties of this lower temperature, T^* phase, the charge transport was characterized via a voltage driven I-V sweep at 300 mK shown in Fig. 1(b). A pronounced nonlinearity appears, where with increasing field strength the system switches from a linear, Ohmic regime with near zero conductance into a highly non-Ohmic FEC regime. To determine the temperature evolution of this FEC feature, a separate sample was mounted and probed with 600 μs current pulses to minimize heating effects [Fig. 1(c)]. While it is difficult to completely preclude all heating effects within the rise and sample time of the pulse, these pulsed measurements show that the nonlinear bend in the I-V curve persists and eventually vanishes below resolution at $T \approx 60$ K.

A separate (rough) check for discriminating the nonlinear conduction from simple Joule heating can be performed by looking at the 30 K data in Fig. 1(c). The Ohmic regime $R(30\text{ K}) = 42$ kΩ and the maximum pulsed current (2 mA) during the 600 μs pulse delivers a maximum $\Delta Q = 10.1 \times 10^{-5}$ J. While low temperature heat capacity data are needed for Sr-327, as a lower estimate, the heat capacity of Sr_2IrO_4 at 30 K can be used (≈14 J/K),[15] giving a maximum $\Delta T = 5.5$ K (for a 1.32×10^{-6} mol sample). In carrying out a similar analysis for each current value pulsed at 30 K and assuming *perfect* thermal isolation, the measured Ohmic $R(T)$ can be used to determine the lowest fields possible due to pure Joule heating as a function of the pulsed current density. This limiting case is plotted as a dashed line in Fig. 1(c), demonstrating that the nonlinear feature at 30 K is intrinsic.[16]

In looking at the magnetoresistance of the same sample plotted in the Fig. 1(d), the MR $= [R(9\text{ T}) - R(0\text{ T})]/R(0\text{ T})$ ratio is negative and shows two minima at $T^* \approx 70$ K and $T_{AF} = 280$ K. The lower minimum appears approximately at the temperature where the onset of FEC emerges and coincides with the low-T peak in $\frac{\partial \ln \rho}{\partial 1/T}$. The origin of the negative magnetoresistance is likely the removal of spin disorder scattering due to biased magnetic domain populations which will be discussed later, and the inflection below T^* supports the idea of a field coupled order parameter freezing below 70 K. The suppression of enhanced fluctuations originating from an additional electronic instability, however, may also account for the overall negative MR.

Magnetization data shown in Fig. 2(a) supports the idea of a bulk phase transition below 70 K where a downturn in the dc susceptibility originally reported by Cao *et al.*[8] begins, suggestive of a glassy freezing process. Consistent with earlier reports,[8,9] three energy scales are apparent in the field cooled magnetization data: a canted AF phase transition at $T_{AF} = 280$ K, a sharp upturn at $T_O = 220$ K, and an eventual decrease in susceptibility below $T^* = 70$ K. Both field cooled (FC) and zero field cooled (ZFC) data show similar downturns near T^* and an irreversibility temperature near T_O. At 300 K, however,

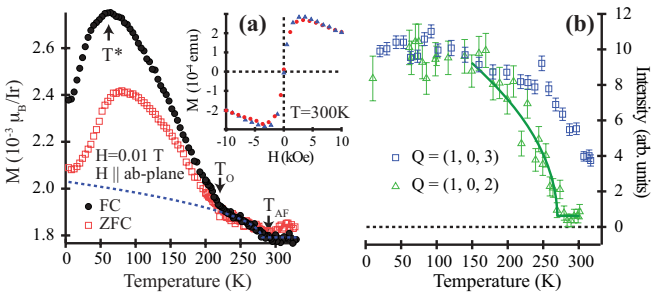

FIG. 2. (Color online) (a) dc-magnetization data for Sr-327 with $H = 0.01$ T aligned parallel to the *ab* plane for both FC (solid symbols) and ZFC temperature sweeps (open symbols). The dashed line shows the mean-field order parameter fit to the net moment from the 280 K transition. The inset shows M vs H sweep at 300 K. (b) Temperature dependence of the peak intensities at (1,0,3) and (1,0,2) magnetic reflections. The solid line is a power law fit to the (1,0,2) order parameter.

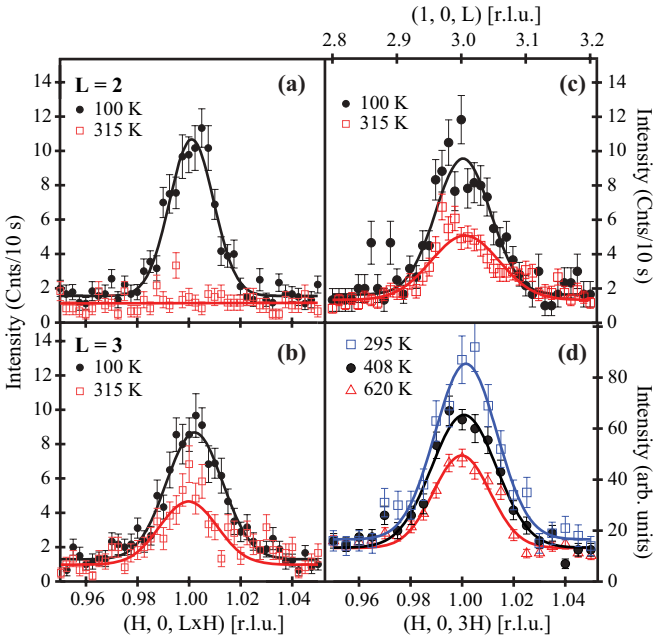

FIG. 3. (Color online) Radial **Q** scans at 100 and 315 K through the (a) **Q** = (1,0,2) and (b) **Q** = (1,0,3) reflections. Solid lines are Gaussian fits to the data. (c) *L* scans across the (1,0,3) peak position showing three-dimensional (3D) superlattice peaks at 100 and 315 K. (d) **Q** scans showing the temperature dependence of the (1,0,3) peak.

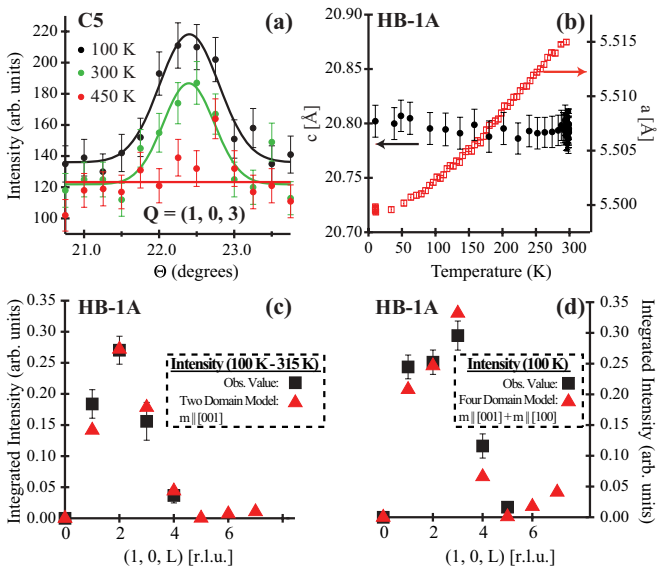

FIG. 4. (Color online) (a) Rocking scans on a separate crystal showing the temperature dependence of the (1,0,3) peak above 300 K. (b) Temperature dependence of the *a*- and *c*-axis lattice parameters measured at the (2,0,0) and (0,0,4) reflections. Integrated intensities plotted as (c) 100 K with 315 K data subtracted and (d) the total scattering data at 100 K. Data is compared with two simple collinear spin models described in the text.

field sweeps plotted in the inset of Fig. 2(a) reveal a rapid saturation of the spin response, suggesting the persistence of magnetic correlations above T_{AF}.

In order to further investigate the spin order, neutron diffraction measurements were performed on a 7 mg single crystal Sr-327 sample with the results plotted in Figs. 3 and 4. $[H,0,L]$, $[H,K,0]$, and $[H,H,L]$ zones were explored and magnetic reflections were observed only at the $(1,0,L)$ positions for $L = 1,2,3,4,5$. The correlated order is three dimensional with $\xi_L = \sqrt{2\ln(2)} \times 1/w = 147 \pm 10$ Å, where $w(\text{Å}^{-1})$ is the peak's Gaussian width [Fig. 3(c)]. The appearance of both $L =$ even and $L =$ odd reflections in a simple collinear picture of the spin structure is therefore consistent with recent x-ray results resolving the presence of two magnetic domains.[9] attributable to in-plane structural twinning in an orthorhombic symmetry.

Looking at the order parameters for both the $L = 3$ and $L = 2$ reflections in Fig. 2(b), the magnetic intensities show that the $L = 2$ peak disappears at T_{AF} while substantial intensity remains at 280 K in the $L = 3$ reflection. **Q** scans plotted in Fig. 3(b) demonstrate this more explicitly. The peak remaining above 280 K is long-range ordered with a minimum correlation length of 93 ± 18 Å, comparable to the correlation length observed at 10 K (97 ± 5 Å). Due to the rather coarse collimations used, both these values and those of all magnetic Bragg reflections are resolution limited. At 300 K peaks remain at the $(1,0,L)$ $L = 1,3,4$ positions, all forbidden in the reported structural space groups to date. This same crystal was then loaded into a furnace and measured at higher temperatures, where, upon warming, the remnant peaks continue to decrease in intensity as illustrated in Fig. 3(d); however, they notably remain present beyond 600 K. The continued temperature dependence of these peaks above 300 K and the absence of peaks at higher order *L* and *H* strongly imply that this remnant scattering is magnetic and that an additional magnetic phase persists beyond 280 K.

In order to verify this in a second sample, a 2 mg crystal from a separate batch was explored on the C5 spectrometer with the results plotted in Fig. 4(a). Again, a clear temperature dependence above 300 K was observed with the remnant (1,0,3) peak vanishing within the error of the measurement by 450 K. The earlier disappearance of this high temperature AF peak is likely due to the poorer statistics in the measurement of this second sample; however, variable oxygen stoichiometry between samples may also play a role in diminishing the effective transition temperature.

Due to the presence of two magnetic domains[9] and the rapid attenuation due to the Ir magnetic form factor, it is difficult to uniquely determine a model of the spin structure in both the high and low temperature magnetic phases. If we assume that the scattering seen at 315 K is a separate, saturated, order parameter, then the additional intensity due to the 280 K transition is plotted in Fig. 4(c). The rapid disappearance of magnetic peaks for $L > 5$ suggests a sizable component of the moment directed along the *c* axis, and the best symmetry bound two-domain model matching the data is a *G*-type arrangement of AF-coupled bilayers with moments directed along the (0,0,1) axis, consistent with a recent x-ray report.[14,17] The ordered moment using this model is $\mu = 0.52 \pm 0.08 \mu_B$.

Looking instead at the total scattering observed at 100 K in Fig. 4(d), no simple collinear model captures all of the major reflections well. Nevertheless, if we again use a twinned *G*-type spin structure, a model comprising four magnetic domains with

two different moment orientations can be constructed. If the two twin domains added to the previous model have moments directed along the (1,0,0) axis, this four domain model roughly fits the data.[14] This added domain would comprise the high temperature phase in a two domain picture, however, future polarized measurements are required to differentiate between this multidomain picture, a potential noncollinear spin structure with an accompanying spin reorientation at 280 K, and to confirm the magnetic nature of the high temperature phase.

Our combined data demonstrate the presence of canted 3D antiferromagnetic domains whose phase evolution is decoupled within resolution from the fluctuation and freezing behavior at T^* and T_O [Fig. 2(b)], precluding any additional major spin reorientations at these temperatures. This suggests that there remain additional moments weakly coupling[8,9] to fluctuations below T_O and eventually freezing below T^*. Our measurements in their entirety therefore suggest a picture of three distinct order parameters driving the phase behavior of Sr-327: (1) a high temperature phase (of likely magnetic origin) with $T_{onset} > 620$ K, (2) a canted AF magnetic transition at 280 K, followed by (3) the freezing of the T^* phase into an electronically textured ground state.

The T^* transition is nominally suggestive of a charge density wave (CDW) or collective transport mechanism which becomes depinned above a threshold field, leading to an avalanche process in the carrier number. The structural lattice parameters [Fig. 4(b)], however, evolve smoothly as the system is cooled from 315 to 10 K and, to date, no structural distortion associated with a conventional CDW formation has been observed below 300 K,[11,18] although, high temperature structural measurements are a promising avenue for future studies. An alternative scenario of exchange coupled metallic islands condensing below T^* with a substantial Coulomb barrier for tunneling may also address the transport mechanism below T^*.[19,20] Similar non-Ohmic behavior has also been reported in other correlated iridates,[21,22] suggesting an electronic inhomogeneity intrinsic to these 5*d*-correlated materials.

Curiously, X-ray measurements on a Sr-327 sample with a qualitatively similar bulk spin susceptibility have reported the onset of AF order at T_O.[9] This resonant x-ray scattering (RXS) study speculated about the presence of short-range order setting in at T_{AF} and diverging at T_O as the reason for the discrepancy,[9] however, our measurements reveal no appreciable change in the correlation length upon cooling through T_O. Given that more recent RXS measurements show the onset of magnetism at the expected $T_{AF} = 285$ K,[17] variation in sample quality is likely the cause for the variance reported between these two RXS studies.

To summarize, our studies have illustrated a complex electronic ground state in the $Sr_3Ir_2O_7$ system with multiple electronic order parameters. Our observation of scattering consistent with an AF phase extending beyond 600 K is supported by the absence of Curie-Weiss behavior above the previously identified T_{AF} (Ref. 11) and also by the rapid field-induced saturation of the magnetization at 300 K. The system then transitions through a magnetic transition at $T_{AF} =$ 280 K, and exhibits multiple magnetic domains or alternatively noncollinear spin order in its ground state. The spin order appears decoupled from two additional energy scales appearing in transport and bulk susceptibility measurements, suggesting a fluctuating charge/orbital state that freezes into an inhomogeneous electronic ground state where tunneling and sliding effects manifest under increasing electric field strength.

S.D.W. acknowledges helpful discussions with Ying Ran and Stefano Boseggia, and Michael Graf for use of a ^{3}He refrigerator. The work at BC was supported by NSF Award DMR-1056625 and DOE DE-SC0002554. Part of this work was performed at ORNL's HFIR, sponsored by the Scientific User Facilities Division, Office of Basic Energy Sciences, US DOE.

*stephen.wilson@bc.edu

[1] B.-J. Yang and Y. B. Kim, Phys. Rev. B **82**, 085111 (2010).
[2] D. A. Pesin and L. Balents, Nat. Phys. **6**, 376 (2010).
[3] F. Wang and T. Senthil, Phys. Rev. Lett. **106**, 136402 (2011).
[4] B. J. Kim *et al.*, Phys. Rev. Lett. **101**, 076402 (2008).
[5] B. J. Kim *et al.*, Science **323**, 1329 (2009).
[6] S. J. Moon *et al.*, Phys. Rev. Lett. **101**, 226402 (2008).
[7] J. M. Longo, J. A. Kafalas, and R. J. Arnott, J. Solid State Chem. **3**, 174 (1971).
[8] G. Cao, Y. Xin, C. S. Alexander, J. E. Crow, P. Schlottmann, M. K. Crawford, R. L. Harlow, and W. Marshall, Phys. Rev. B **66**, 214412 (2002).
[9] S. Boseggia, R. Springell, H. C. Walker, A. T. Boothroyd, D. Prabhakaran, D. Wermeille, L. Bouchenoire, S. P. Collins, and D. F. McMorrow, Phys. Rev. B **85**, 184432 (2012).
[10] I. Franke, P. J. Baker, S. J. Blundell, T. Lancaster, W. Hayes, F. L. Pratt, and G. Cao, Phys. Rev. B **83**, 094416 (2011).
[11] I. Nagai *et al.*, J. Phys.: Condens. Matter **19**, 136214 (2007).
[12] J. Kim *et al.*, arXiv:1205.5337.
[13] M. A. Subramarian, M. K. Crawford, and R. L. Harlow, Mater. Res. Bull. **29**, 645 (1994).
[14] See Supplemental Material at http://link.aps.org/supplemental/10.1103/PhysRevB.86.100401 for additional details.
[15] N. S. Kini *et al.*, J. Phys.: Condens. Matter **18**, 8205 (2006).
[16] Both higher field pulsed measurements and dc measurements show pronounced regions of negative differential resistance; however, for the purpose of this Rapid Communication, we limit our discussion to only measurements where the effect of Joule heating has been minimized.
[17] J. W. Kim, Y. Choi, J. Kim, J. F. Mitchell, G. Jackeli, M. Daghofer, J. van den Brink, G. Khaliullin, and B. J. Kim, Phys. Rev. Lett. **109**, 037204 (2012).
[18] H. Matsuhata *et al.*, J. Solid State Chem. **177**, 3776 (2004).
[19] D. P. Arovas, F. Guinea, C. P. Herrero, and P. San Jose, Phys. Rev. B **68**, 085306 (2003).
[20] P. San-Jose, C. P. Herrero, F. Guinea, and D. P. Arovas, Eur. Phys. B **54**, 309 (2006).
[21] G. Cao, J. Bolivar, S. McCall, J. E. Crow, and R. P. Guertin, Phys. Rev. B **57**, R11039 (1998).
[22] G. Cao *et al.*, Solid State Commun. **113**, 657 (2000).